

## ABSTRACT

Title of dissertation:       **DYNAMIC FORCE MEASUREMENT IN  
HYPERSONIC WIND TUNNELS**

**John Draper III, Doctor of Philosophy, 2019**

Dissertation directed by:   **Professor Sung W. Lee**  
                                      **Department of Aerospace Engineering**

In this dissertation, dynamic force measurement methodologies are developed and implemented for use in hypersonic wind tunnel testing. The chief application is implementation into Arnold Engineering Development Complex's Hypervelocity Wind Tunnel No. 9. The Sum of Weighted Accelerations Technique, Time Domain Deconvolution Method, and Frequency Domain Inverse Method are of particular interest for this study due to their implementation feasibility within Tunnel 9.

The formulation of each "conventional" method is presented in its most basic or commonly used form. Then several modifications are made to improve the results of the various methods. Much of this work focuses on the specific alterations performed on each method and the consequences of each change. To improve the Sum of Weighted Accelerations Technique, modal separation and a damping matrix are added to the formulation. This allows for higher frequency accuracy and successful reconstructions on highly damped setups. A novel Time Domain Deconvolution Method is formulated in this dissertation which exhibits several advantages over the typical time domain approaches. Examples include elimination of inversion regularization, smooth reconstructions, and improved computational efficiency via response segmentation. The Frequency Domain Inverse Method was

reformulated to solve directly for the frequency response function. This direct solution also allows for the use of multiple calibration tests during solution which improves accuracy.

Each alteration is validated on numerical, bench top, and wind tunnel systems to provide a full theory to implementation understanding. Linked spring-mass-damper models are used for all of the numerical investigations with additive Gaussian noise and are used to draw early conclusions about each method and alteration. Bench top studies are performed on three separate support structures to build confidence in the methods on a more complex, experimental system. Finally, data obtained by tests performed in a transonic wind tunnel are used to demonstrate the capabilities and highlight some of the advantages of each method.



# DYNAMIC FORCE MEASUREMENT IN HYPERSONIC WIND TUNNELS

by

John Draper III

Dissertation submitted to the Faculty of the Graduate School of the  
University of Maryland, College Park in partial fulfillment  
of the requirements for the degree of  
Doctor of Philosophy  
2019

Advisory Committee:  
Professor Sung W. Lee, Chair/Advisor  
Professor Amr Baz  
Professor Inderjit Chopra  
Professor Norman Wereley  
Professor Stuart Laurence

© Copyright by  
John Draper III  
2019

## Acknowledgments

This work would not have been possible without the generous support of the AEDC Tunnel 9, the Air Force Office of Scientific Research (AFOSR) Center of Testing Excellence (CoTE), and The University of Maryland Department of Aerospace Engineering. I would like to sincerely thank each of them for their support and encouragement.

I would also like to thank my advisor Dr. Sung W. Lee. He has been an outstanding mentor and friend throughout the duration of my time at University of Maryland. Even before my graduate tenure, he provided me with one-on-one senior level instruction on his own time which made my internship at Tunnel 9 a truly enriching experience. Our long discussions about vibrations, history, and life have made my graduate experience much more than just a job.

My mentor Dr. Eric Marineau and many others at tunnel 9 deserve a huge amount of credit for the completion of this dissertation. Countless technical discussions with Eric, George Moraru, Dan Lewis, John Lafferty, and many others have helped develop my knowledge from a clueless farm boy into an aerospace engineer. Many members of the Tunnel 9 staff were always ready and willing to help me with anything from mounting test articles to soldering electronics. I am very appreciative of their generosity.

Fellow graduate students Ananth Virakthi, Jonathon Brooks, John Juliano, and Bernadine Passe also hold a special place in my heart for all of their intellectual guidance and general support throughout my graduate study. Conversations with each of them have been integral to my success. Many late nights, phone calls, and code collaborations have enhanced my experience and performance. I owe them a great thanks for their friendship.

Of course my family has been integrally important to my success. From a teddy bear-stealing, chicken nugget loving kid to an aerospace engineer, you all have loved and supported me through it all. Mom, Dad, Ellen, Mommom, Bubba, and the rest of my family, I love you all and appreciate the life you have given me.

## Table of Contents

Acknowledgements	ii
Table of Contents	vi
List of Tables	vii
List of Figures	x
1 Introduction	1
1.1 AEDC Tunnel 9 Overview . . . . .	2
1.2 Research Objectives and Scope of Research . . . . .	3
1.3 Conventional Force Reconstruction Technologies . . . . .	4
1.3.1 Forward Solution Techniques . . . . .	5
1.3.1.1 Six-Component Strain Gage Force Balance . . . . .	5
1.3.1.2 Sum of Weighted Accelerations Technique . . . . .	6
1.3.1.3 Free Flying Force Measurement . . . . .	6
1.3.1.4 Surface Pressure Integration . . . . .	7
1.3.2 Inverse Solution Techniques . . . . .	8
1.3.2.1 Time Domain Deconvolution Method . . . . .	8
1.3.2.2 Frequency Domain Inverse Method . . . . .	9
1.4 Instrumentation Considerations . . . . .	10
1.4.1 Frequency Response . . . . .	11
1.4.2 Temperature Sensitivity . . . . .	11
1.4.3 Capacitive Drift . . . . .	12
2 Dynamic Force Measurement Methodology Development	14
2.1 SWAT . . . . .	14
2.1.1 SWAT Overview . . . . .	14
2.1.2 Novel SWAT Alterations . . . . .	18
2.1.2.1 Modal Separation . . . . .	18
2.1.2.2 Damping Force Term . . . . .	19

2.1.3	Numerical Example of the SWAT . . . . .	20
2.1.3.1	Static Calibration . . . . .	21
2.1.3.2	Modal Separation . . . . .	22
2.1.3.3	Damping Force Term . . . . .	24
2.1.4	SWAT Limitations . . . . .	26
2.2	TDDM . . . . .	27
2.2.1	TDDM Overview . . . . .	27
2.2.2	Novel TDDM Alterations . . . . .	32
2.2.2.1	Constraint Matrix Method . . . . .	33
2.2.2.2	Generalized Draper-Lee Method . . . . .	43
2.2.2.3	Linear, Quadratic, and Cubic Distributions of GDLM . . . . .	48
2.2.2.4	Extension to Multiple Outputs . . . . .	55
2.2.2.5	Averaging of Calibration Sets . . . . .	58
2.2.2.6	Segmentation . . . . .	60
2.2.2.7	Acceleration Deconvolution . . . . .	62
2.2.3	Numerical Example of TDDMs . . . . .	64
2.2.3.1	SISO Example of the CMM . . . . .	66
2.2.3.2	SISO Example of the GDLM . . . . .	69
2.2.3.3	Noise Discussion . . . . .	72
2.2.3.4	Conventional Method Comparison . . . . .	73
2.2.3.5	SIMO Example of GDLM . . . . .	75
2.2.3.6	MIMO Example of GDLM . . . . .	78
2.2.3.7	Averaging of Calibration Sets . . . . .	80
2.2.3.8	Segmentation . . . . .	84
2.2.3.9	Acceleration Deconvolution . . . . .	86
2.2.4	TDDM Limitations . . . . .	88
2.3	FDIM . . . . .	89
2.3.1	FDIM Overview . . . . .	89
2.3.2	Novel FDIM Alterations . . . . .	92
2.3.2.1	FRF Solution . . . . .	93
2.3.2.2	Averaging of Calibration Sets . . . . .	93
2.3.2.3	Acceleration Deconvolution . . . . .	94
2.3.3	Numerical Examples of FDIM . . . . .	97
2.3.3.1	SISO Example of the Conventional FDIM . . . . .	97
2.3.3.2	SISO Example of FDIM with Solved FRF . . . . .	98
2.3.3.3	Averaging Calibration Sets . . . . .	100
2.3.3.4	SIMO Example . . . . .	101
2.3.3.5	MIMO Example . . . . .	105
2.3.3.6	Acceleration Deconvolution . . . . .	107
2.3.4	FDIM Limitations . . . . .	109

3	Experimental Validation on No-Flow Test Article	111
3.1	Experimental Setups	111
3.1.1	Support Structures	111
3.1.2	Sensors	115
3.1.3	Data Acquisition	118
3.2	Experimental Results	119
3.2.1	SWAT Results	119
3.2.1.1	Static Calibration Results	119
3.2.1.2	Dynamic Calibration Results	125
3.2.2	TDDM Results	134
3.2.2.1	SIMO CMM Experimental Results	135
3.2.2.2	SIMO GDLM Experimental Results	139
3.2.2.3	MIMO GDLM Experimental Results	142
3.2.2.4	Acceleration Deconvolution	148
3.2.3	FDIM Results	151
3.2.3.1	SIMO FDIM Experimental Results	151
3.2.3.2	MIMO FDIM Experimental Results	153
3.2.3.3	Acceleration Deconvolution	156
4	Dynamic Force Reconstruction Demonstration in Wind Tunnels	159
4.1	Aerodynamic Forcing Considerations	159
4.1.1	Distributed Loading	159
4.1.2	Aeroelastic Effect	163
4.1.2.1	Aeroelastic System Description	163
4.1.2.2	Dynamic Calibration Discussion	166
4.1.2.3	Force Reconstruction Example	167
4.2	Transonic Demonstration	170
4.2.1	Test Setup	171
4.2.2	Force Reconstruction Results	172
4.2.2.1	GDLM Results	173
4.2.2.2	FDIM Results	180
5	Conclusions, Contributions, Recommendation, and Future Work	186
A	Ill-Posed Problem Explanation	192
B	Properties of Convolution	194
B.1	Commutativity	194
B.2	Fourier Transform	195
B.3	Differentiability	196

C	Standard Operating Procedures	199
C.1	Data Acquisition . . . . .	199
C.2	Static Calibration . . . . .	206
C.3	Dynamic Calibration . . . . .	210
C.3.1	SWAT - Drop Testing . . . . .	210
C.3.2	TDDM/FDIM - Hammer Testing . . . . .	213
	Bibliography	216

## List of Tables

2.1	Back Calculated Residuals for Numerical MDOF SWAT Example . . . . .	22
3.1	Strain and accelerometer sensor specifications . . . . .	117
3.2	BCR for 6-component strain gage calibration . . . . .	124
3.3	BCR for piezoelectric strain gage calibration . . . . .	124
3.4	Original SWAT modal reduction percentages . . . . .	132
3.5	Modally separate SWAT modal reduction percentages . . . . .	133
3.6	Modally separate with damping SWAT modal reduction percentages . . . .	134
3.7	Input Pulse Reconstruction Error Analysis . . . . .	138
3.8	Error metrics for experimental linear GDLM acceleration deconvolution results . . . . .	149
3.9	Error metrics for experimental FDIM acceleration deconvolution results . .	157
4.1	Numerical system parameters for 2DOF aeroelastic model. . . . .	168
4.2	Sensor specifications for AFRL transonic wind tunnel experiment . . . . .	172
4.3	Input Pulse Reconstruction Error Analysis for AFRL tests using third order GDLM . . . . .	175
4.4	Input Pulse Reconstruction Error Analysis for AFRL tests using FDIM . . .	181



## List of Figures

2.1	MDOF lumped mass system . . . . .	20
2.2	Modally separated SWAT force reconstruction numerical result . . . . .	23
2.3	Frequency comparison of modally separated force reconstruction numerical result . . . . .	24
2.4	Modally separated, damping term SWAT numerical result with increasing system damping. . . . .	25
2.5	Typical IRF solution using scaling and time shifting of the displacement. . .	28
2.6	Mock L-Curve Output . . . . .	31
2.7	Segment of IRF showing value and slope at end points . . . . .	52
2.8	Nonzero initial condition force reconstruction numerical result using GDLM	61
2.9	SDOF spring mass damper system. . . . .	65
2.10	SISO IRF construction numerical result for the CMM . . . . .	67
2.11	Advantage of resolution increase for the CMM SISO numerical force re- construction . . . . .	68
2.12	SISO sinusoidal force reconstruction numerical result using the CMM . . .	69
2.13	SISO IRF construction numerical result using the GDLM . . . . .	70
2.14	SISO force reconstruction numerical result using the GDLM . . . . .	71
2.15	SISO demonstration of SNR influence on IRF construction accuracy . . . .	72
2.16	SISO IRF construction numerical result comparison of conventional TDDM and GDLM . . . . .	74
2.17	SISO force reconstruction numerical result comparison of conventional TDDM and GDLM for varying SNRs . . . . .	75
2.18	SIMO force reconstruction numerical result for the GDLM . . . . .	76
2.19	SIMO force reconstruction error numerical result using GDLM and an in- creasing number of outputs . . . . .	77
2.20	MIMO force reconstruction numerical result using GDLM . . . . .	79
2.21	MIMO force reconstruction error numerical result using GDLM with an increasing number of outputs . . . . .	80
2.22	SISO example of overfitting problem using CMM . . . . .	81
2.23	Sine reconstruction using overfit IRF and CMM . . . . .	82
2.24	SISO IRF construction error and condition number numerical result with increasing number of calibration tests using the CMM . . . . .	83
2.25	SISO sinusoidal force reconstruction using segmented CMM . . . . .	84

2.26	Computation time comparison between CMM and segmented CMM . . . . .	85
2.27	GDLM acceleration deconvolution SISO example . . . . .	87
2.28	GDLM SISO displacement-only, acceleration-only, and combined acceleration-displacement deconvolution comparison . . . . .	88
2.29	Conventional FDIM noiseless force reconstruction . . . . .	97
2.30	Conventional FDIM noisy force reconstruction . . . . .	98
2.31	FRF solved FDIM noiseless force reconstruction . . . . .	99
2.32	FRF solved FDIM noisy force reconstruction . . . . .	99
2.33	FDIM SISO IRF construction accuracy versus number of calibration tests .	100
2.34	FDIM SIMO noiseless force reconstruction . . . . .	101
2.35	FDIM SIMO IRF/FRF construction result . . . . .	102
2.36	FRF solved SIMO FDIM noisy force reconstruction . . . . .	103
2.37	SIMO FDIM noisy force reconstruction with ten calibration tests . . . . .	104
2.38	Peak and Area Difference versus number of calibration tests for FDIM SIMO numerical studies . . . . .	104
2.39	MIMO force reconstruction numerical result using FRF solved FDIM . . .	106
2.40	MIMO noisy force reconstruction numerical result using FRF solved FDIM	107
2.41	Peak and Area Difference versus number of calibration tests for FDIM MIMO numerical studies . . . . .	108
2.42	SISO FDIM force reconstruction using acceleration deconvolution . . . . .	109
2.43	FDIM SISO displacement-only, acceleration-only, and combined acceleration-displacement deconvolution comparison . . . . .	110
3.1	CAD representation of dynamic calibration bench top test article . . . . .	112
3.2	Calibration test article mounted on support structure 1. . . . .	113
3.3	Calibration test article mounted on support structure 2. . . . .	114
3.4	Static calibration support structure . . . . .	114
3.5	3-2-2 Accelerometer Array . . . . .	116
3.6	Static calibration experiment mock up . . . . .	121
3.7	BCR for foil and piezoelectric strain static force calibration . . . . .	122
3.8	BCR for foil and piezoelectric strain static moment calibration . . . . .	123
3.9	Original SWAT force and moment reconstruction example . . . . .	128
3.10	Modally separated SWAT force and moment reconstruction example . . . . .	129
3.11	Modally separated with damping SWAT force and moment reconstruction example . . . . .	130
3.12	Amplitude spectra comparison for SWAT reconstruction . . . . .	131
3.13	CMM Experimental Force Reconstruction with full scale output . . . . .	136
3.14	CMM Experimental Force Reconstruction: X-Direction . . . . .	136
3.15	CMM Experimental Force Reconstruction: Y-Direction . . . . .	137
3.16	CMM Experimental Force Reconstruction: Z-Direction . . . . .	137
3.17	CMM average condition numbers for IRF and impulse reconstruction in-versions . . . . .	138

3.18	CMM average error metrics vs constraint parameter . . . . .	139
3.19	GDLM experimental force reconstruction; first and third order . . . . .	140
3.20	GDLM peak and area difference versus constraint parameter for first and third order . . . . .	141
3.21	GDLM average condition numbers for IRF and impulse reconstruction in- versions . . . . .	142
3.22	MIMO GDLM point force reconstruction experimental result . . . . .	144
3.23	MIMO GDLM force and moment reconstruction experimental result . . . .	145
3.24	MIMO GDLM reconstruction error versus number of calibration locations .	147
3.25	Acceleration deconvolution experimental result . . . . .	149
3.26	MIMO GDLM reconstruction error versus number of calibration locations using acceleration outputs . . . . .	150
3.27	FDIM SIMO force reconstruction experimental example result . . . . .	151
3.28	SIMO FDIM reconstruction error versus number of calibration tests . . . .	152
3.29	MIMO FDIM point force reconstruction experimental result . . . . .	153
3.30	MIMO FDIM reconstruction error versus number of calibration locations .	155
3.31	FDIM SIMO acceleration deconvolution force reconstruction experimental example result . . . . .	156
3.32	SIMO FDIM reconstruction error versus number of calibration tests for acceleration deconvolution . . . . .	158
4.1	Abaqus FEM with distributed pressure loading on flap . . . . .	161
4.2	First order GDLM flap force reconstruction numerical example . . . . .	162
4.3	FDIM flap force reconstruction numerical example . . . . .	162
4.4	2DOF model wing section . . . . .	163
4.5	IRF construction for 2DOF wing model . . . . .	168
4.6	Input force reconstruction for 2DOF wing model . . . . .	169
4.7	AFRL transonic wind tunnel test setup . . . . .	171
4.8	Cubic GDLM calibration pulse force reconstruction at AFRL . . . . .	174
4.9	SIMO GDLM transonic force reconstruction at forward station . . . . .	176
4.10	SIMO GDLM transonic force reconstruction at middle station . . . . .	177
4.11	SIMO GDLM transonic force reconstruction at aft station . . . . .	178
4.12	FDIM calibration pulse force reconstruction at AFRL . . . . .	180
4.13	SIMO FDIM transonic force reconstruction at forward station . . . . .	182
4.14	SIMO FDIM transonic force reconstruction at middle station . . . . .	183
4.15	SIMO FDIM transonic force reconstruction at aft station . . . . .	184

## Chapter 1: Introduction

This dissertation focuses on the problem of dynamic force and moment measurement in wind tunnels. Conventional force and moment (henceforth generalized to "force") measurement in wind tunnels utilizes the assumption that the applied aerodynamic load and the test article under load come to a static equilibrium[1–3]. In such cases, the measured strain of the test article is proportional to the applied load. However, for certain scenarios this condition cannot be met but the applied aerodynamic load is still of interest. This scenario is henceforth referred to as dynamic force measurement.

Hypersonic wind tunnel tests in particular, often exhibit dynamic applied loads due to their short test times. It is difficult and often impossible to bring a test article to static equilibrium with respect to the flow in the test times of interest. To combat this, moving averages or filters are often employed to remove the undesirable transience present in the strain response. This approach may be sufficient for aerodynamic coefficient measurement but is unable to obtain important forcing features such as rise time and peak magnitude. Additionally, a wealth of testing scenarios exist where only the transient force application is of interest. Examples include jet-flow interaction[4, 5], scramjet engine unstart[6, 7], and control surface deployment[8, 9].

Our sponsor, Arnold Engineering Development Complex (AEDC) Hypervelocity Wind Tunnel No. 9 is a facility with just such a motivation. Their current force measurement methodology utilizes a static approach as discussed. However, they seek to improve this measurement capability by developing a dynamic force measurement method applicable to

Tunnel 9.

## 1.1 AEDC Tunnel 9 Overview

Tunnel 9 is a large scale hypervelocity wind tunnel owned and operated by the Air Force and is located in White Oak, Maryland[10]. This facility is capable of unique conditions, not capable by any other wind tunnel. In particular, its large scale test section (5' diameter) is particularly uncommon for the high Mach and Reynold's number capabilities. Aerodynamic measurement for Tunnel 9 is truly a multi-physics endeavor. The information of interest during a tunnel run may include force, surface pressure, surface heat transfer, and flowfield visualization. The breadth of measurement is an advantage of this facility. However, these additional measurements must be considered when determining an applicable dynamic force measurement technique.

Tunnel 9 is a blowdown facility which utilizes a working fluid of pure Nitrogen. Current nozzle capability includes Mach numbers of 7, 8, 10, and 14. The Mach 7 nozzle is capable of duplicating a large range of flight conditions including unit Reynold's numbers of  $0.05 \cdot 10^6/\text{ft}$  to  $48 \cdot 10^6/\text{ft}$ . Many other flight conditions can be simulated using the other nozzles.

Temperature Sensitive Paint (TSP) is another premier measurement capability at Tunnel 9[11]. A thin TSP layer is often applied to the surface of test article which allows for the computation of heat transfer rates over the entire imaged area. The TSP cameras and light sources are located above the test section. On the sides of the test section, large viewing windows are present for advanced Schlieren flow visualization. For best use of these capabilities, the test article must remain fixed. However, a pitch system is also present which is capable of rotating the test article about its center of gravity. Therefore, pitch sweeps may be performed without sacrificing visualization capability.

Finally, the test articles are often outfitted with a number of surface pressure taps and thermocouples. The latter is used to calibrate the TSP data and to provide discrete temperature measurements at critical locations. With all of this instrumentation, the force measurement options are fairly limited. However, as discussed previously, Tunnel 9 uses a six component strain gage roll balance to measure the quasi-static forces and moments applied to the test article. This force balance is constrained between the test article and the support arm ("sting") to ensure all applied loads travel across the balance.

The following sections present an overview of current force measurement methodologies and their applicability to Tunnel 9. Upon review of this section, the selection of the methods discussed in this dissertation are made clear. Following the discussion of methodologies, brief consideration is given to sensor selection; another practical option that must be considered for the Tunnel 9 application.

## 1.2 Research Objectives and Scope of Research

The scope of this research is to identify and improve dynamic force measurement techniques applicable to Tunnel 9. There are many methods available for dynamic force measurement in hypersonic wind tunnels. However, a select few are applicable to the size and test times common in Tunnel 9. Therefore, the scope is limited to only the methods practical to Tunnel 9.

Although applicable methods exist, simple implementation may not be sufficient. Therefore a full investigation into each applicable method is of interest in this research. Identification of weaknesses and methodology improvement is of primary interest in this work.

More specifically, the research objectives are as follows:

1. Identify dynamic force measurements applicable to the AEDC Tunnel 9 facility
2. Identify weaknesses in the conventional implementation of the conventional applica-

ble methods

3. Modify the applicable methods to improve their performance
4. Validate each modification on numerical and experimental systems
5. Demonstrate methods in wind tunnel tests as able

Upon successful completion of the above research objectives, a practical and concise recommendation for future Tunnel 9 implementation should be provided.

### 1.3 Conventional Force Reconstruction Technologies

Two branches of force measurement methodologies are discussed in this dissertation: forward and inverse[12]. In forward problems, an operation may be performed to a measured quantity to derive the desired quantity. This may be written as

$$\mathcal{L}\{\mathbf{y}\} = \mathbf{f} \quad (1.1)$$

where  $\mathcal{L}$  is some operation being performed on the measured quantity  $\mathbf{y}$  to derive the desired quantity  $\mathbf{f}$ .

Inverse problems, on the other hand, are posed in the opposite manor. In such problems, an operation is being performed on the desired quantity to result in the measurement, i.e.

$$\mathbf{y} = \mathcal{L}\{\mathbf{f}\}. \quad (1.2)$$

In such problems, the operation must be inversely performed on the measured quantity to derive the desired one.

Each solution methodology discussed hereafter can be cast in such a form.

### 1.3.1 Forward Solution Techniques

Forward solution approaches are the most desirable force measurement techniques due to their relative simplicity as compared to inverse approaches. Some of the more commonly used approaches and their applicability to Tunnel 9 are discussed in this section.

#### 1.3.1.1 Six-Component Strain Gage Force Balance

As discussed in Section 1.1, this is the most commonly used methodology and is currently used at Tunnel 9. In this technique, the physics of the force measurement problem are cast as

$$S_S \mathbf{C}_S = F_{\text{rec}} \quad (1.3)$$

where  $S_S$  is a 1 by  $ns$  row vector of strain measurements,  $\mathbf{C}_S$  is an  $ns$  by 6 matrix of scaling constants, and  $F_{\text{rec}}$  is a 1 by 6 row vector of reconstructed forces and moments ( $F_x$ ,  $F_y$ ,  $F_z$ ,  $M_x$ ,  $M_y$ , and  $M_z$ )[13]. To solve this problem, the user must hang weights at various locations over the test article and record the strain balance output voltages. After many tests have been performed, the user may solve for  $C_S$  as

$$\mathbf{C}_S = [\mathbf{S}_S^T \mathbf{S}_S]^{-1} \mathbf{S}_S^T \mathbf{F}_{\text{app}} \quad (1.4)$$

where  $\mathbf{S}_S$  is a matrix of stacked strain output row vectors and  $\mathbf{F}_{\text{app}}$  is a matrix of stacked known applied load row vectors. Note that a least squares solution is employed.

This is an accurate method and has been trusted and utilized by the wind tunnel industry for many decades. However, this method assumes quasi-static equilibrium between the test article and applied aerodynamic flow. In the dynamic case, structural restoring forces are present in the strain response and this method will fail.



### 1.3.1.2 Sum of Weighted Accelerations Technique

An extension of the strain gage roll balance technique is the sum of weighted accelerations technique (SWAT)[14–17]. This method is sometimes referred to as acceleration compensation but is spiritually equivalent to the SWAT. The SWAT aims to remove the unwanted structural restoring forces from the scaled response by measuring the inertial forces of the test article. As the name suggests, accelerometers are used to measure acceleration and the response is scaled and combined with the previous method. The SWAT can be depicted as

$$S_A \mathbf{C}_A + S_S \mathbf{C}_S = F_{\text{rec}} \quad (1.5)$$

where Eq. (1.3) has been expanded to include  $S_A$ , the acceleration measurements, and  $C_A$ , the acceleration scaling constants. To solve this problem, a static calibration is first performed. This is represented by Eq. (1.4). In such cases, loads are applied smoothly and no dynamics are excited. After the static scaling terms ( $C_S$ ) are obtained, a dynamic calibration is performed. First, a known dynamic load is applied to the test article. Next, the elastic force contributions are subtracted from that known force. Finally, a least squares solution is again employed as

$$\mathbf{C}_A = [S_A^T S_A]^{-1} S_A^T [F_{\text{app}} - S_S \mathbf{C}_S] \quad (1.6)$$

### 1.3.1.3 Free Flying Force Measurement

A technique more commonly used in shock tunnels to measure applied forcing is free flying force measurement. Since the model is unconstrained, the acceleration of the test article is directly proportional to the applied loads. Therefore, the physics can be posed

using Newton's Second Law, i.e.

$$S_A C_A = F_{\text{rec}} \quad (1.7)$$

where  $S_A$  are the acceleration measurements and  $C_A$  is a matrix of scaling constants containing the mass properties of the system. This calibration matrix is obtained via experiments and supplemented using derived inertial quantities of the test article.

Initial tethers must be present to hold the test article in a position prior to flow initiation. Additionally, for safety reasons, a capture mechanism must be present to recover the test article after the usable flow time has passed[18]. Alternatively, very soft boundary conditions could be employed so the support structure has very little influence on the test article over the experiment duration[19]. Due to the scale of test articles at Tunnel 9, these considerations make this method undesirable. Firstly, test articles can be on the order of a hundred pounds. Therefore, sturdy tethers must be initially present prior to flow initiation. However, when the flow impacts the system, these tethers need to break to ensure no affect on the test article. Ensuring that these tethers are strong enough to support large test articles but break with little influence after flow initialization would be difficult.

Additionally, Tunnel 9 can have test times on the order of seconds. These methods are typically employed in shock tunnels due to their short (few millisecond) test times. This allows the tunnel operators to place the capture mechanism very close to the test article as it should only move a few millimeters. However, if the desirable test times are on the order of seconds, the capture mechanism would need to allow a much wider span of motion which presents further safety concerns. For these reasons, such a technique is not investigated.

#### 1.3.1.4 Surface Pressure Integration

Surface pressure measurement is becoming more and more popular as imaging capability becomes more advanced. These and recent advances in pressure sensitive paint (PSP)

have made the pressure measurement of an entire visible surface possible[20]. With the surface pressure known, the applied forces can be computed as

$$\iint_S p(t) dS = F_{\text{rec}}(t) \quad (1.8)$$

where the surface pressure,  $p$ , at time  $t$  is known everywhere on the surface,  $S$ . Integrating over the entire surface, the applied force can be obtained.

Although this is a promising method, it requires an oxygen flow for the PSP to react[21]. As Tunnel 9 is a pure Nitrogen facility, this will not work. Furthermore, one of the premier measurements at Tunnel 9 is TSP. Since simultaneous TSP and PSP is not currently possible, this would sacrifice a key measurement capability. Finally, in some sensitive cases, this paint layer can be intrusive to the measurements of interest[22] so it may be of interest to use an internal force measurement mechanism.

### 1.3.2 Inverse Solution Techniques

Inverse solution methodologies are historically less popular than their forward counterparts[12]. Reasons include high levels of noise contamination due to the inverse formulation and high computational expense due to the commonly used convolution relationship.

#### 1.3.2.1 Time Domain Deconvolution Method

The first inverse technique discussed is the time domain deconvolution method (TDDM). This name is not universal for the technique described below, however, many methods can be categorized as a variant of this. It should also be noted that this is one of the most popular force reconstruction techniques in hypersonic wind tunnel testing[23–26].

In this method, the system under investigation must be linear and time-invariant (LTI).

If this condition is satisfied, any input-output (e.g. force-strain) pair can be related via the convolution integral, i.e.

$$y(t) = \int_0^t h(t - \tau)u(\tau) d\tau \quad (1.9)$$

where  $u$  is the applied force,  $y$  is a measured output (e.g. strain or acceleration), and  $h$  is the impulse response function (IRF) of the system. If the IRF is known, then this equation can be discretized and assembled into a matrix expression as

$$\mathbf{y} = \mathbf{H}\mathbf{u}. \quad (1.10)$$

Finally, one may *invert* the impulse response matrix (IRM) and premultiply it by the measured response to obtain the applied force at a particular location.

The inverse formulation makes this problem ill-posed. However, there are many approaches to improving the conditioning of the formulation. As this is a methodology-imposed hindrance, it is not considered a Tunnel 9 application problem. Therefore, this method is considered. One possible drawback of these methods is the point-to-point formulation. In the discussed forward methods, the center of gravity forces and moments are computed as an end product. However, in TDDM, only the forcing contribution at a particular point is reconstructed. This may or may not be a drawback depending on the application of interest.

### 1.3.2.2 Frequency Domain Inverse Method

The frequency domain inverse method (FDIM) is a frequency domain couple to the TDDM. The physics behind this formulation are identical to the TDDM, i.e. input-output location pairs are related via the continuous convolution integral given in Eq. (1.9). However, FDIM utilizes the fact that when a Fourier Transform is performed on a time domain

convolution, it simply becomes a multiplication in the frequency domain, i.e.

$$\mathcal{F}\{y(t)\} = \mathcal{F}\{h * u(t)\} \quad (1.11a)$$

$$Y(\omega) = H(\omega) \cdot U(\omega) \quad (1.11b)$$

where  $\mathcal{F}\{\cdot\}$  denotes the Fourier transform, the  $*$  operator denotes convolution and capital variable names represent frequency domain couples of the original time domain variables. This is proven in Appendix B.2.

By transforming this equation to the frequency domain, the cumulative nature of convolution is no longer present. Instead of the response depending on the entire time history of the IRF from 0 to  $t$ , it is only a function of the particular frequency of interest,  $\omega$ . Instead of inverting a large IRM, one may simply perform a point wise division of the frequency response function (FRF),  $H(\omega)$ .

Few examples of this approach are available in wind tunnel testing[27–29]. However, the computational efficiency and physical similarity to TDDMs make it an attractive option for longer duration wind tunnel force measurement.

## 1.4 Instrumentation Considerations

This dissertation primarily focuses on methodology improvements for dynamic force measurement. However, it is also important to remember the physical sensor challenges inherent to force measurement. Measurement errors due to temperature sensitivity, thermal drift, and others may lead to unreasonable errors in the reconstructed force.

### 1.4.1 Frequency Response

Due to the constraints of current Tunnel 9 operation, the scope of this dissertation is limited to the SWAT, TDDM, and FDIM. However, proper measurement recording must be ensured to test and validate each method. This selection also drives the model design for wind tunnel tests.

The SWAT requires measurement of strain and acceleration. However, current strain gage technology utilizes flexures in various direction to isolate the strain measurements to a particular direction. The use of the flexures limits the stiffness of the balance and causes a resonant frequency of approximately 30 Hz[30]. Due to the high frequency response present in some dynamic events, this bandwidth is not sufficient. To circumvent this limitation, an additional strain measurement using piezoelectric strain sensors is recorded. These sensors are far stiffer and therefore exhibit a much higher resonant peak above 10 kHz.

Additionally, acceleration must be recorded for the SWAT. Therefore, uniaxial piezoresistive accelerometers are placed over the test articles. They too, must have high bandwidth and the selected models exhibit resonant peaks of greater than 10kHz.

As noted, TDDM and FDIM can use strain or acceleration output. However, the dynamic input must be precisely known for dynamic calibration. Therefore, an impulse hammer, instrumented with a piezoelectric load cell and dynamically calibrated by the manufacturer is used to supply the known applied loads.

### 1.4.2 Temperature Sensitivity

Physical sensors such as strain gages or accelerometers have temperature sensitivity. This means that the measured response is also a function of the temperature of the sensor (e.g. Model 356A32 accelerometers[31]). The validation studies performed in this dissertation are all at room temperature, however, it is important to recognize the full picture.

Temperature sensitivity is of particular importance to hypersonic wind tunnel testing. Due to the high flow velocities in these tunnels, temperatures can reach much higher levels than in other typical measurement applications. More recently, sensors specifically designed for wind tunnel measurement are starting to account for this thermal sensitivity by adding a sensor temperature measurement to the sensor and providing a temperature calibration in addition to the typical calibration. For example, Kulite now provides a five wire model high frequency pressure gage to account for temperature sensitivity[32].

There are a few ways to circumvent this thermal effect. The first is to simply only test in room temperature. This is what is done in this dissertation to validate methodologies but is obviously not possible in many wind tunnel testing applications. The second, as discussed previously, is to measure the temperature of the sensor and use a previously derived calibration curve to correct the sensor response. Finally, one may attempt to fix the sensor temperature at a desired temperature through the use of thermal insulation or a cooling jacket. For example, NASA Langley uses cooling jackets on many of its strain gage roll balances to prevent the negative effects of thermal drift.

### 1.4.3 Capacitive Drift

This final sensor consideration is of particular interest to piezoelectric sensors. These sensors often have very high frequency response due to the high stiffness. However, these sensors are capacitive in nature, meaning any constant load applied will generate a response voltage which will decay to zero over time. This decay is repeatable and is characterized by the time constant provided by the sensor manufacturer.

The capacitive drift can cause many errors to the various methods discussed in this dissertation. For example, the SWAT requires a static calibration where a constant load is applied to the test article. Unfortunately, due to this capacitive drift, the voltage output from

the piezoelectric sensors will decay with time preventing ideal steadying of the applied load. Additionally, this drift affects the low frequency response of these sensors, ultimately lower band limiting the response. However, this is far lower than what is of interest in most wind tunnel applications.

Since this drift is repeatable, the tester could apply a correction to the measured data prior to applying any methodology. However, these corrections are not considered in this methodology development to limit the complexity of the various discussions.



## Chapter 2: Dynamic Force Measurement Methodology Development

In this chapter, an overview of the three force measurement techniques that are applicable for Tunnel 9 is presented. These are the SWAT, TDDM, and FDIM. Additionally, novel changes made to each method and the extension to multiple input-output systems are presented. Next, a brief numerical example of each method is shown. Finally, the limitations of each method under investigation is discussed.

### 2.1 SWAT

The first method under investigation is the SWAT. This method bears the most resemblance to typical static calibration methodologies and therefore is easiest to understand and implement. Additionally, examples of the conventional version of this method have been employed by researchers at CALSPAN-University of Buffalo Research Center (CUBRC)[14, 15] for axial and normal force measurement in a hypersonic wind tunnel. The alterations described in this dissertation were first presented in our AIAA conference paper[16].

#### 2.1.1 SWAT Overview

The basic SWAT is composed of two steps: a static and dynamic calibration. The static calibration step is analogous to what has been done for decades with conventional strain gage force balances. To create an accurate static calibration matrix, begin with Eq. (1.3).

Next, one must apply a constant load to the test article. This is most commonly done using some sort of a weight hanger and double knife edge to ensure point loading. Next, the weight can be settled and the tester can utilize gravity to ensure the directionality of the applied static load. When the weight is steady, the applied load can be assumed to be coincident with the gravity direction and the voltage reading from the strain gages can be recorded. Next, one may remove the weight and reapply them at a new location and repeat.

Each test will form an equation of the form

$$\begin{bmatrix} F_x^i & F_y^i & F_z^i & M_x^i & M_y^i & M_z^i \end{bmatrix} = \begin{bmatrix} S_1^i & S_2^i & \dots & S_{ns}^i \end{bmatrix} \mathbf{C}_S \quad (2.1)$$

where the superscript,  $i$ , denotes the test number,  $ns$  is the number of strain channels measured, and  $\mathbf{C}_S$  is an  $m$  by 6 static calibration matrix.

Additional tests will further contribute to the solution of  $\mathbf{C}_S$  and can simply be stacked onto Eq. (2.1) as

$$\begin{bmatrix} F_x^1 & F_y^1 & F_z^1 & M_x^1 & M_y^1 & M_z^1 \\ F_x^2 & F_y^2 & F_z^2 & M_x^2 & M_y^2 & M_z^2 \\ \vdots & \vdots & \vdots & \vdots & \vdots & \vdots \\ F_x^P & F_y^P & F_z^P & M_x^P & M_y^P & M_z^P \end{bmatrix} = \begin{bmatrix} S_1^1 & S_2^1 & \dots & S_{ns}^1 \\ S_1^2 & S_2^2 & \dots & S_{ns}^2 \\ \vdots & \vdots & \ddots & \vdots \\ S_1^P & S_2^P & \dots & S_{ns}^P \end{bmatrix} \mathbf{C}_S \quad (2.2)$$

where  $P$  is the number of calibration tests performed. Equation (2.2) may be written in matrix form as

$$\mathbf{F}_{app} = \mathbf{S}_S \mathbf{C}_S. \quad (2.3)$$

Provided  $P > ns$  (i.e. there are more calibration tests performed than number of strain

channels), this equation can be uniquely solved using a least squares pseudo inverse

$$\mathbf{C}_S = [\mathbf{S}_S^T \mathbf{S}_S]^{-1} \mathbf{S}_S^T \mathbf{F}_{\text{app}}. \quad (2.4)$$

The least squares pseudo inverse will henceforth be written as

$$\mathbf{S}_S^+ = [\mathbf{S}_S^T \mathbf{S}_S]^{-1} \mathbf{S}_S^T \quad (2.5)$$

for compactness.

It is common practice to encompass all loading magnitudes and directions in your static calibration. This will help prevent extrapolation of the calibration matrix. Additionally, static calibrations occasionally apply multiple loads simultaneously (e.g. side force and normal force). As this is not possible with our current test setup, it will not be utilized.

The next step of the SWAT is a dynamic calibration. In this step, the acceleration response will be scaled to the elastic force contributions present in the statically calibrated strain measurement. This is done by adding an additional term to Eq. (1.3) as is shown in Eq. (1.5). This step of the analysis is a bit more computationally expensive than the static calibration. This is due to the time dependence of the formulation. Rather than just a single value per channel, many cycles of structural resonances are required.

Start by expanding Eq. (1.5) for a given time,  $t_j$

$$\begin{bmatrix} F_x^i & F_y^i & F_z^i & M_x^i & M_y^i & M_z^i \end{bmatrix}_{t_j} = \begin{bmatrix} S_{s,1}^i & S_{s,2}^i & \dots & S_{s,ns}^i \end{bmatrix}_{t_j} \mathbf{C}_S + \begin{bmatrix} S_{a,1}^i & S_{a,2}^i & \dots & S_{a,na}^i \end{bmatrix}_{t_j} \mathbf{C}_A \quad (2.6)$$

where the subscript  $s$  denotes a strain measurement,  $a$  denotes an acceleration measurement, and  $na$  denotes the number of accelerometer channels.

Consider an applied dynamic load where the force and moment contributions are known

as a function of time. This would be the case for a step load applied at a known location. If the load is applied suddenly, inertial oscillations and structural restoring forces will ensue. This results in a time varying response of both the accelerometers and the strain sensors. Similarly to Eq. (2.2), Eq. (2.6) is stacked for all sampled points of interest as

$$\mathbf{F}_{\text{app}}^i = \mathbf{S}_s^i \mathbf{C}_S + \mathbf{S}_a^i \mathbf{C}_A. \quad (2.7)$$

This process is repeated at a new or different location and this creates a new data set that should utilize the same calibration matrices. Therefore, Eq. (2.7) is stacked for multiple tests as

$$\begin{bmatrix} \mathbf{F}_{\text{app}}^1 \\ \mathbf{F}_{\text{app}}^2 \\ \vdots \\ \mathbf{F}_{\text{app}}^P \end{bmatrix} = \begin{bmatrix} \mathbf{S}_s^1 \\ \mathbf{S}_s^2 \\ \vdots \\ \mathbf{S}_s^P \end{bmatrix} \mathbf{C}_S + \begin{bmatrix} \mathbf{S}_a^1 \\ \mathbf{S}_a^2 \\ \vdots \\ \mathbf{S}_a^P \end{bmatrix} \mathbf{C}_A \quad (2.8)$$

or in matrix form as

$$\hat{\mathbf{F}}_{\text{app}} = \hat{\mathbf{S}}_s \mathbf{C}_S + \hat{\mathbf{S}}_a \mathbf{C}_A \quad (2.9)$$

where the hat signifies all tests stacked together. Since the static calibration matrix is known, the applied load is known, and the strain and acceleration data are measured, the dynamic calibration matrix is solved as

$$\mathbf{C}_A = \hat{\mathbf{S}}_a^+ [\hat{\mathbf{F}}_{\text{app}} - \hat{\mathbf{S}}_s \mathbf{C}_S]. \quad (2.10)$$

With both calibration matrices known, any dynamic response of the test article can be measured and inserted into to Eq. (2.7) to construct the applied force. Since both calibrations are done a priori, this multiplication can be performed directly on the measured data as it is recorded. This means one can have a live estimate of the applied forces during a

tunnel run.

## 2.1.2 Novel SWAT Alterations

### 2.1.2.1 Modal Separation

The SWAT is a straightforward method that aims to build on a trusted method to improve accuracy in the dynamic regime. However, this methods simplicity is also a source of weakness. In a typical modal response of a structural system, the presence of the first mode will be the dominant amplitude. The consequence of this on the SWAT is that the dynamic calibration matrix tends to be weighted towards removing the first (or rather the most dominant) mode of the system. This bias will prevent extensive removal of higher order dynamics and is a case of high frequency error.

In the first alteration to the SWAT, higher frequency accuracy is sought. To achieve this, modal isolation of the acceleration response is proposed. During dynamic calibration, if each mode of vibration is scaled separately and removed from the dynamic strain response, higher order removal of modal dynamics is possible.

Begin by filtering the measured signals around the first mode of interest,  $l$ . Equation (2.9) then becomes

$$\hat{\mathbf{F}}_{\text{app},l} = \hat{\mathbf{S}}_{s,l} \mathbf{C}_S + \hat{\mathbf{S}}_{a,l} \mathbf{C}_{A,l} \quad (2.11)$$

where a new dynamic calibration matrix,  $\mathbf{C}_{A,l}$  is defined that is specific to mode  $l$ .

Just as in the non-modally separated case, each dynamic calibration matrix can be solved using Eq. (2.10) for the filtered data as

$$\mathbf{C}_{A,l} = \hat{\mathbf{S}}_{a,l}^+ [\hat{\mathbf{F}}_{\text{app},l} - \hat{\mathbf{S}}_{s,l} \mathbf{C}_S] . \quad (2.12)$$

One may repeat this for all  $L$  modes of interest. When the solution of each dynamic

calibration matrix is obtained, they can be applied to the strain response via a summation over all modes, i.e.

$$\hat{\mathbf{F}}_{\text{app}} = \hat{\mathbf{S}}_s \mathbf{C}_S + \sum_{l=1}^L (\hat{\mathbf{S}}_{a,l} \mathbf{C}_{A,l}). \quad (2.13)$$

By modally separating the inertial response, higher order accuracy that is not biased by first mode contributions should be achievable.

### 2.1.2.2 Damping Force Term

Another observation made is the clear resemblance that Eq. (2.9) bears to the equation of motion of a structural system, i.e.

$$m\ddot{y} + c\dot{y} + ky = F_{\text{app}} \quad (2.14)$$

where  $m$ ,  $c$ , and  $k$  are the mass, damping, and stiffness of the single degree of freedom (SDOF) spring-mass-damper system. However, in the SWAT, any damping force has not been considered. Therefore, the addition of a damping force term into the SWAT is proposed.

Begin by adding a term to Eq. (2.9) which scales a measured velocity as

$$\hat{\mathbf{F}}_{\text{app}} = \hat{\mathbf{S}}_s \mathbf{C}_S + \hat{\mathbf{S}}_v \mathbf{C}_V + \hat{\mathbf{S}}_a \mathbf{C}_A. \quad (2.15)$$

Now this equation is very similar to Eq. (2.14). Note that  $\mathbf{C}_V$  and  $\mathbf{C}_A$  must be simultaneously solved as

$$\begin{bmatrix} \mathbf{C}_V & \mathbf{C}_A \end{bmatrix} = \begin{bmatrix} \hat{\mathbf{S}}_v & \hat{\mathbf{S}}_a \end{bmatrix}^+ [\hat{\mathbf{F}}_{\text{app}} - \hat{\mathbf{S}}_s \mathbf{C}_S] \quad (2.16)$$

Similarly to the first alteration, modal isolation is maintained and the applied force is

solved as

$$\hat{\mathbf{F}}_{\text{app}} = \hat{\mathbf{S}}_s \mathbf{C}_S + \sum_{l=1}^L (\hat{\mathbf{S}}_{v,l} \mathbf{C}_{v,l} + \hat{\mathbf{S}}_{a,l} \mathbf{C}_{A,l}) \quad (2.17)$$

where simultaneous solution for each  $\mathbf{C}_{v,l}$  and  $\mathbf{C}_{a,l}$  is required as

$$\begin{bmatrix} \mathbf{C}_{V,l} & \mathbf{C}_{A,l} \end{bmatrix} = \begin{bmatrix} \hat{\mathbf{S}}_{v,l} & \hat{\mathbf{S}}_{a,l} \end{bmatrix}^+ [\hat{\mathbf{F}}_{\text{app},l} - \hat{\mathbf{S}}_{s,l} \mathbf{C}_S]. \quad (2.18)$$

The addition of this term may improve accuracy when the damping force is large.

### 2.1.3 Numerical Example of the SWAT

Consider a multiple degree of freedom (MDOF) spring-mass-damper model as shown in Figure 2.1. A system such as this has  $n$  DOF or  $n$  modes of vibration. This will allow us

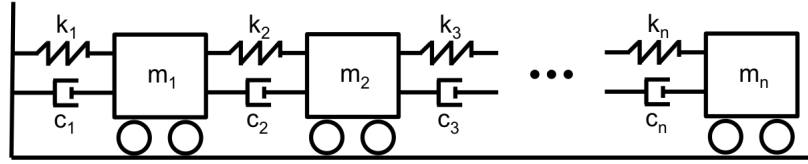


Figure 2.1: MDOF lumped mass system

to display the biasing of the SWAT to dominant modes.

For this study,  $n = 10$  is chosen. The stiffness properties are chosen randomly from 0 to 10000 with some separation to encourage spacing of the modes. This is done by adding each stiffness value by the previous values. The mass properties are all set to one and the damping values range from 0 to 100. Since  $n = 10$ , up to ten modes of vibration are present in the elastic response. A numerical integration scheme (e.g. fourth order Runge-Kutta) is used to solve for the kinematics (displacement, velocity, and acceleration) of each mass as a function of time in response to a prescribed applied load. In reality, the measurement of the kinematics of every DOF is not feasible, therefore, the measured DOFs (i.e. strain sensor and accelerometer locations) are restricted to only three DOFs. Similarly, it is unrealistic

to supply inputs at every DOF so the applied inputs are restricted to only the odd DOFs. Therefore,  $ns = na = 3$  and  $P = 5$ .

For the static calibrations, a 10 N step load with a ten second rise time is used. The displacement data will be collected at the end of the simulation to ensure any dynamics have ceased. For dynamic calibrations, a 10 N step load with a 0.1 second rise time is used. The speed of this load application will prevent static equilibrium over the test time of interest.

Finally, note that for a numerical system such as this, there is no transverse or rotational motion allowed. Therefore, the output forces and moments (i.e.  $F_x, F_y, F_z, M_x, M_y$ , and  $M_z$ ) will no longer be relevant and are instead replaced with a single force contribution,  $F$ .

### 2.1.3.1 Static Calibration

A static calibration need first be performed. First the quasi-static step loads is applied at the odd input locations. A numerical integration code (e.g. ode45) can then be used to approximate the kinematics under that load. Assuming positive damping and the slow rise time, the dynamics should be small towards the end of the time history. Therefore, extract the displacement values at each of the three output locations at this time. These serve as the outputs ( $S^i$ ) in Eq. (2.1). Progressing to the various input locations, the other rows of Eq. (2.2) are filled in identical fashion. Finally, Eq. (2.4) is used to solve for the static calibration matrix.

To determine the accuracy of this static calibration, the commonly used Back Calculated Residuals (BCR)[13] is used. This is defined as

$$\text{BCR} = \mathbf{S}_S \mathbf{C}_S - \mathbf{F}_{\text{app}}. \quad (2.19)$$

This is effectively a measure of how well Eq. (2.3) holds for this static calibration. For



the example shown in this discussion, the BCR are shown in Table 2.1. Additionally, the percentage error, computed as

$$\varepsilon = \frac{\text{BCR}}{F_{\text{app}}} \cdot 100\% \quad (2.20)$$

are also displayed.

Table 2.1: Back Calculated Residuals for Numerical MDOF SWAT Example

Input DOF	BCR	$\varepsilon$
1	-0.4012	-4.01%
3	0.6541	6.54%
5	-0.5242	-5.24%
7	-0.0070	-0.07%
9	0.1885	1.89%

The errors are fairly low and are on average less than 5%. Better results could be achieved with more input and output locations, but this level of error is deemed acceptable for this investigation.

### 2.1.3.2 Modal Separation

The next step is to perform a dynamic calibration. For simplicity, the same input and output locations as in the static calibration are chosen. As mentioned, a 10 N step load is applied with a 0.1 second rise time to onset a dynamic response. Again, a numerical integration code is used to simulate the kinematics of the system.

The dynamic calibration matrix is first computed using Eq. (2.10), the standard way. Next, compute dynamic calibration matrices using Eq. (2.12) with three frequency ranges. These ranges are  $0 - 2f_1$ ,  $2f_1 - 1.5f_2$ , and  $1.5f_2 - 2f_{10}$ . Due to the close proximity and low magnitude of the higher modes, only one calibration matrix is used for modes 3-10.

An example of the dynamic calibrations can be seen in Figure 2.2. The elastic force, computed using Eq. (2.3), is also shown. Immediately, it is clear that a dynamic calibration

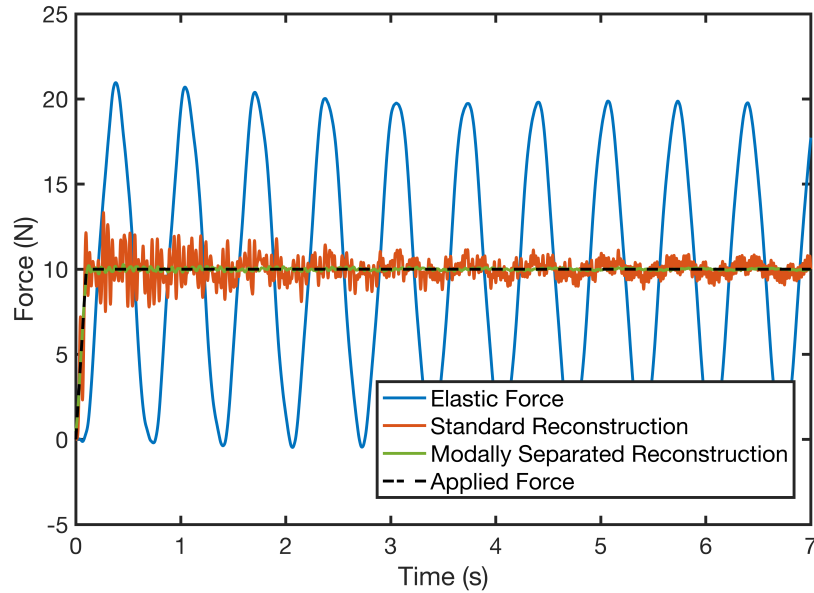


Figure 2.2: SWAT Force Reconstruction using standard (red) and modally separated (green) methods.

is necessary as the elastic forces dominate the response. After applying the standard SWAT, the reconstruction improves, however, there still exists high frequency error. Finally, after applying the modally separated approach, the reconstruction very closely matches the applied load.

Further insight can be gained by investigating each reconstruction in the frequency domain. This is shown in Figure 2.3.

In the standard method, the only modal contributions that have decreased in magnitude are the first mode. All higher order modes have actually increased in magnitude beyond what was present in the elastic response. The biasing of first mode contributions has actually caused an amplification of the higher mode dynamics. In the modally separated method however, these high mode contributions are very small and our reconstruction matches the applied load very well. In particular, the two truly isolated modes, (i.e. modes 1 and 2) were completely removed and the reconstruction nearly perfectly matches the applied load over these two frequency ranges.

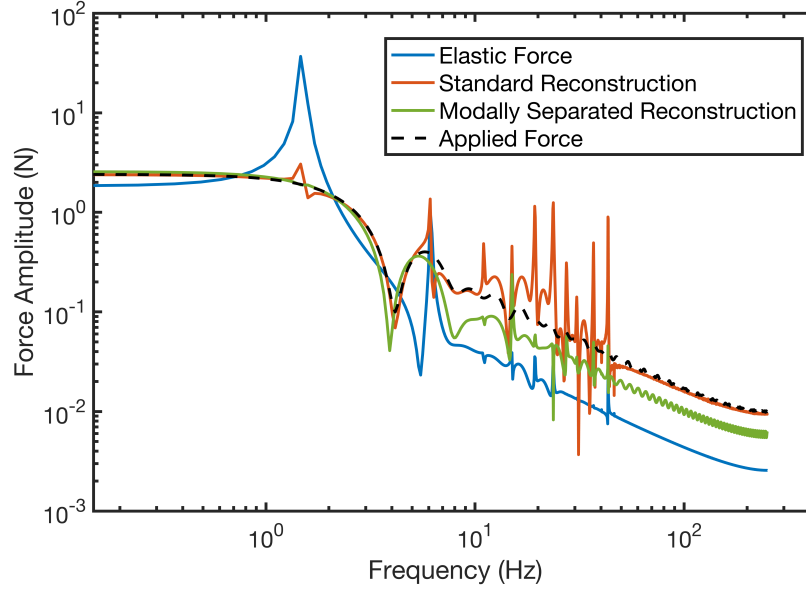


Figure 2.3: Frequency contribution of SWAT Force Reconstruction using standard (red) and modally separated (green) methods.

Clearly, allowing separate dynamic calibration matrices for various frequency ranges can result in more accurate reconstructions.

### 2.1.3.3 Damping Force Term

Finally, consider the addition of the damping force term. Only Eq. (2.17) is discussed but the advantages are analogous to the non-modally separated case.

For this study, all numerical parameters (including filtering ranges for modal separation) remain the same. However, the magnitude of the damping matrix is varied to observe the accuracy of each method as a function of the damping force. The results are presented in Figure 2.4.

Four cases are depicted, each with increased damping. Begin with Figure 2.4a. In this example, the damping matrix has been multiplied by zero to represent an undamped system. For this case, this method has little effect on the result and performs as well as the

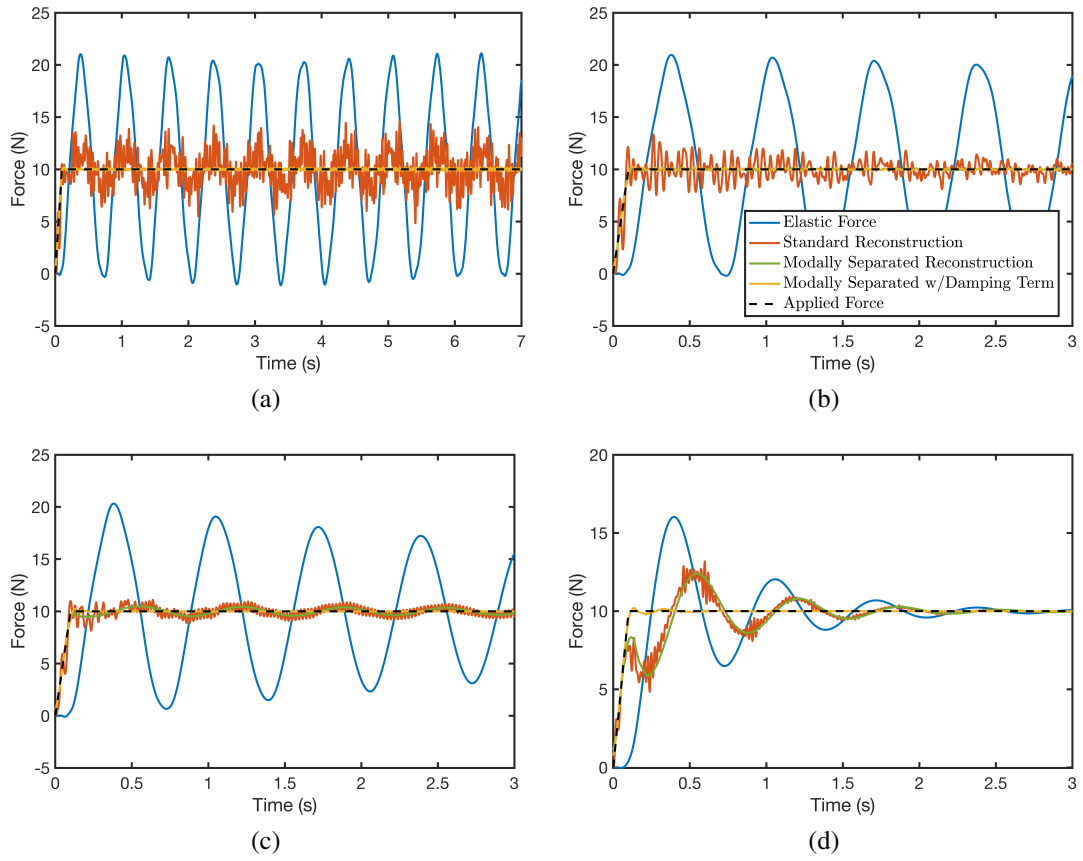


Figure 2.4: Example force reconstruction using modally separated damping force SWAT. 0x (a), 1x (b), 10x (c), and 100x (d) damping are all shown.

modally separated method.

In Figure 2.4b, the damping is chosen to match the previous analysis. Again for this lightly damped case, little improvement is observed and this performs as well as the modally separated method.

In Figure 2.4c, the damping is increased by an order of magnitude. This is done to make the damping force more significant. Observing this figure, the advantages of the damped method begin to show. The damped method more accurately rejects the structural oscillations than the other two methods. Additionally since the modally separated formulation was maintained, high frequency accuracy is also achieved.

Finally, in Figure 2.4d, the damping is increased by two orders of magnitude as compared to the case shown in Figure 2.4b. In this study, the damping force is extremely significant. This is reflected in the accuracy of the various methods. Due to the large damping force, the standard SWAT and modally separated versions are ineffective at removing the structural oscillations of even the first mode. However, since Eq. (2.17) considers a damping force, this method very accurately reconstructs the applied step loading.

#### 2.1.4 SWAT Limitations

The SWAT appears to be an elegantly simple method that builds on techniques that have been used for decades. Additionally, two major limitations (i.e. high frequency error and neglecting damping force) have been alleviated with the proposed alterations. However, there are still inherent limitations with this method when considering a physical system.

The first problem is the measurement of point velocity. For the displacement measurement, strain gages are used. For the acceleration measurement, accelerometers are used. However, there is no way to measure the velocity at a particular point within the test article. This leaves us with two options: integrating the acceleration response or differentiating the strain response. The latter will amplify any noise in the system while the former will amplify any sensor bias. Therefore, neither approach is optimal.

Another major limitation of this method is the inability to account for phase shifts in the system response. Since this method simply scales the measurements, there is no way to account for phase shifts between the acceleration, velocity, and displacement/strain response. In theory, this is acceptable as there should be no phase delay for strain, velocity, and acceleration recorded at the same location. However, in reality, it is impossible to measure the response at exactly the same location. Therefore, there will always be some amount of phase lag due to real stress wave propagation. Furthermore, more significant phase lag

occurs due to varying sensor response time. Due to a myriad of factors such as sensor operation and electrical connections, real sensor delay exists in a physical measurement. Since this cannot be accounted for in the problem formulation, this is an unavoidable limitation.

These phase shift effects are expected to be small. Therefore, this limitation should only band-limit the effectiveness of SWAT meaning it will still be useful at reconstructing these forces up to the frequency at which these system delays become significant.

## 2.2 TDDM

Next the TDDM is analyzed. This method relates an input and output via time domain convolution with the IRF. The primary motivation for looking into TDDMs is the phase delay limitation of the SWAT. Any repeatable phase shift in sensor response can be directly accounted for in the IRF. Therefore, higher frequency accuracy is expected to be possible.

### 2.2.1 TDDM Overview

For LTI systems, the relationship between an input,  $u(t)$ , and output,  $y(t)$ , can be described by the convolution of the input and IRF,  $h(t)$ , of the system. This relationship can be expressed as

$$y(t) = \int_0^t h(t - \tau)u(\tau)d\tau. \quad (2.21)$$

Typical solution of the inverse problem using Eq. (2.21) invokes the assumption that system response to a finite pulse is approximately the impulse response[24]. If the response is scaled by the area and time shifted by half the width of the impulse, this is a decent assumption. Any output response can be deconvolved with this impulse response to reconstruct the input. To realize this, observe Figure 2.5. The unaltered output (red) from the applied finite impulse does not appear to match the analytical IRF. However, when the

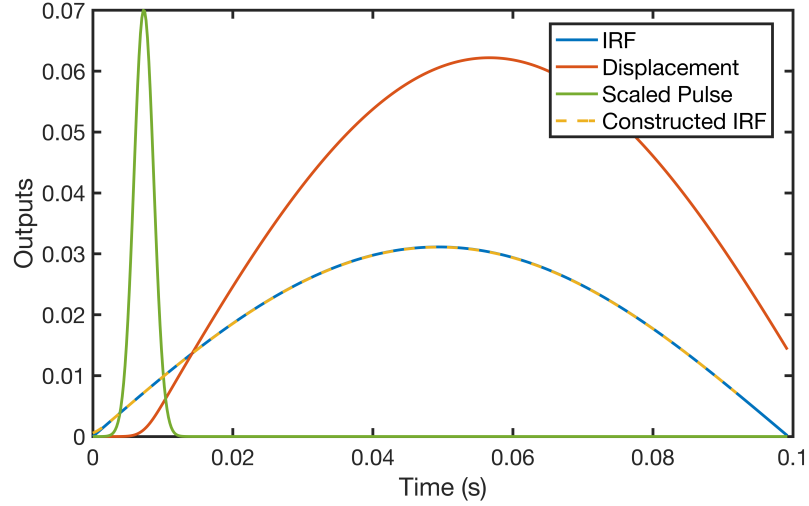


Figure 2.5: Typical IRF solution using scaling and time shifting of the displacement.

displacement is scaled by the area under the impulse and shift it by half of the width of the impulse, it nearly perfectly matches the analytical IRF. Note that the magnitude of the impulse has been reduced considerably for visualization purposes.

Alternatively, Eq. (2.21) could be solved given a measured input and output. However, the former approach is usually taken for simplicity. Additionally, instrumented impulse hammers are commercially available and therefore the determination of area and pulse width is simple.

The next step is to discretize Eq. (2.21). Since real signals are sampled, a discrete equation must be formulated. Begin by breaking up the continuous integral into a summation of integrals over each sampling time as

$$y(t_k) = \sum_{i=0}^{k-1} \int_{i\Delta t_s}^{(i+1)\Delta t_s} h(t_k - \tau) u(\tau) d\tau \quad (2.22)$$

where  $\Delta t_s$  is the sampling time and  $t_k = k\Delta t_s$ . Next, zero order sampling is typically assumed. This is the assumption that a sampled value remains constant until the next sampled time. Although this would be a step-like representation of the signal, it allows for easy

solution of the integral. Subbing this assumption into Eq. (2.22) results in

$$y_k = \sum_{i=0}^{k-1} h_{k-i} \left[ \int_{i\Delta t_s}^{(i+1)\Delta t_s} d\tau \right] u_{i+1} \quad (2.23)$$

where the subscripts denote the sampling index (i.e.  $u_i = u(i\Delta t_s)$ ). This integral can be easily solved as

$$y_k = \sum_{i=0}^{k-1} h_{k-i} u_{i+1} \Delta t_s \quad (2.24)$$

and assembled into matrix form for all  $L$  points as

$$\mathbf{y} = \mathbf{H}\mathbf{u}\Delta t_s. \quad (2.25)$$

Since all  $h_i$  points were solved for during impulse testing and  $\mathbf{y}$  is measured, the unknown applied input can be solved by inverting the impulse response matrix (IRM),  $\mathbf{H}$ , i.e.

$$\mathbf{u} = \mathbf{H}^{-1}\mathbf{y} \cdot \frac{1}{\Delta t_s}. \quad (2.26)$$

Although constructing the IRM is fairly straight forward, the inversion is not. During the inversion, small amounts of noise present in the measurements become large errors in the reconstruction and can often cause the response to erroneously blow up. For an in depth discussion of this problem, review Appendix A. If  $\mathbf{H}$  has any small singular values, any noise in the measured output can become large errors in the reconstructed input.

To solve this ill-posed problem, regularization is typically used. This is the process of introducing additional information into the problem to improve the conditioning of the inversion. Arguably the most common regularization technique is the Tikhonov method[33, 34]. This is effectively an extension of least squares method. Consider a matrix  $\mathbf{A}$ , an  $m \times n$



matrix with  $m \geq n$  where

$$\mathbf{y} = \mathbf{A}\mathbf{u}. \quad (2.27)$$

The Least Squares method provides a unique approximation by minimizing

$$F = \|\mathbf{y} - \mathbf{A}\mathbf{u}\|_2^2, \quad (2.28)$$

the square of the  $L_2$  norm of the difference of each side, with respect to  $\mathbf{u}$ . If one carries out this minimization (i.e.  $\partial F / \partial \mathbf{u} = 0$ ), they obtain the expression used throughout this paper, i.e.

$$\mathbf{u} \approx (\mathbf{A}^T \mathbf{A})^{-1} \mathbf{A}^T \mathbf{y}. \quad (2.29)$$

However, this solution does not guarantee an accurate solution. Tikhonov suggested supplementing the objective function (i.e.  $F$  from Eq. (2.28)) with an additional term

$$F_T = \|\mathbf{y} - \mathbf{A}\mathbf{u}\|_2^2 + \|\Gamma \mathbf{u}\|_2^2 \quad (2.30)$$

where  $\Gamma$  is an arbitrary matrix. If  $F_T$  is minimized with respect to  $\mathbf{u}$ , the result is

$$\mathbf{u} \approx (\mathbf{A}^T \mathbf{A} + \Gamma^T \Gamma)^{-1} \mathbf{A}^T \mathbf{y}. \quad (2.31)$$

This formulation can be further simplified by assuming

$$\Gamma = \sqrt{\alpha} \mathbf{I} \quad (2.32)$$

where  $\alpha$  is a positive, user supplied regularization parameter and  $\mathbf{I}$  is the identity matrix of

dimension  $n$ . Plugging Eq. (2.32) into Eq. (2.31) results in

$$\mathbf{u} \approx (\mathbf{A}^T \mathbf{A} + \alpha \mathbf{I})^{-1} \mathbf{A}^T \mathbf{y}. \quad (2.33)$$

Provided the user supplies an appropriate regularization parameter,  $\alpha$ , an accurate solution of  $\mathbf{u}$  may be obtained.

Much of the research into the solution of inverse problems focuses on regularization and the solution of regularization parameters[35]. One widely accepted approach is known as the L-Curve method and is applicable to many regularization schemes[36, 37]. This method is most easily understood graphically. Consider Figure 2.6. Using Tikhonov as an

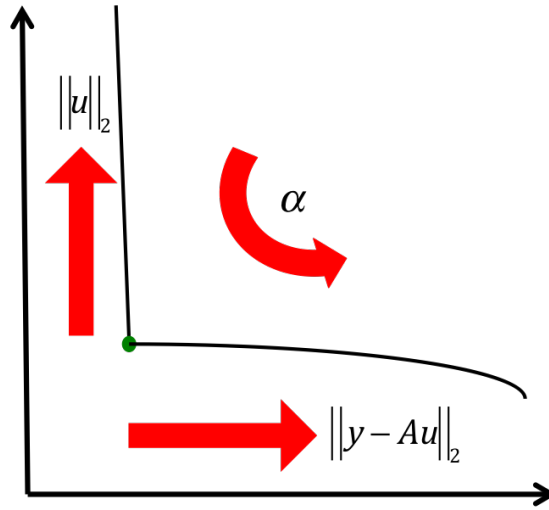


Figure 2.6: Mock L-Curve Output

example, the user can supply various  $\alpha$  parameters to try and influence the answer. Too small of  $\alpha$  will allow the noise to corrode the response and hence the norm of the input,  $\mathbf{u}$ , will grow. This is depicted in the left of the graph. However, as  $\alpha$  is increased, the influence of this noise will decrease and the solution will become more accurate, as depicted in the bottom of the graph. The creators of the L-Curve method noted that there is an optimal regularization parameter that considers both norms and occurs at the bend of this function.

This optimal is displayed by the green dot in Figure 2.6.

Countless methods exist to regularize this inversion and even more exist to select a parameter for the various methods. For this work, the two common approaches discussed above are of interest. For added clarity, the "standard" TDDM used in this work is summarized below:

1. Apply an impulse at the input location of interest and record the dynamic response at the output of interest.
2. To obtain the IRF, divide the response magnitude by the area under the pulse and time shift it (backwards) by half of the impulse width.
3. Record the dynamic response of a new input at the same location.
4. Assemble Eq. (2.25) using the measured output and constructed IRF.
5. Approximate the input by evaluating Eq. (2.33) where  $\alpha$  is chosen using the L-Curve method.

### 2.2.2 Novel TDDM Alterations

While working with the conventional TDDM, two problems were initially identified:

1. Solution of the IRF requires impulse testing and
2. Selection of regularization parameter is often difficult and requires multiple attempts.

A more general method was sought that (1) could utilize any dynamic calibration load available to testers to solve for the IRF. Since the convolution is commutative, as proved in Appendix B.1, any solution methodology utilized for solution of an unknown applied dynamic force, could also be used to solve for the IRF if the load is known.

Additionally, a simpler method was sought that (2) didn't require selection of a regularization parameter than imparts arbitrary smoothness into the solution.

To remedy these two shortcomings, a completely new TDDM was developed. The formulation is as follows. Two new methods have been developed:

1. Constraint Matrix Method (CMM) and
2. Generalized Draper-Lee Method (GDLM).

The CMM is a linear version of the GDLM, formulated in a simpler way. The CMM was first presented in our Journal of Sound and Vibration (JSV) article[38] and the GDLM was first presented in our following JSV article[39].

#### 2.2.2.1 Constraint Matrix Method

Consider a linear, time-invariant (LTI) system. The relationship between an input,  $u(t)$ , and output,  $y(t)$ , for such a system can be described by the convolution of the input and IRF,  $h(t)$ , of the system. This relationship can be expressed as Eq. (2.21) and mirrored here for clarity as

$$y(t) = \int_0^t h(t - \tau)u(\tau)d\tau. \quad (2.34)$$

As discussed above, typical solution of the inverse problem using Eq. (2.21) invokes the assumption that system response to a finite pulse is approximately the impulse response[24]. If the response is scaled by the area and time shifted by the width of the impulse, this is a decent assumption. Any output response can be deconvolved with this impulse response to reconstruct the input.

Instead of this approach, the commutative property of the convolution integral is in-

voked and Eq. (2.21) is rewritten as

$$y(t) = \int_0^t u(t - \tau)h(\tau)d\tau. \quad (2.35)$$

For discrete measurement signals the integral in Eq. (2.35) can be segmented into a summation of integrals over each pair of sampling points:

$$y(t_k) = \sum_{i=1}^{k-1} \int_{t_i}^{t_{i+1}} u(t_k - \tau)h(\tau)d\tau. \quad (2.36)$$

Many discrete representations of the convolution integral utilize the assumption that a sampled point holds constant until the next point is sampled, as is done in Eq. (2.24). However, here it is assumed that  $u(t)$  and  $h(t)$  are piecewise linear over the sampling time segment,  $\Delta t_s$ , as follows:

$$u(t) = (1 - s)u_i + su_{i+1} \quad t \in [t_i, t_{i+1}] \quad (2.37a)$$

$$h(t) = (1 - s)h_i + sh_{i+1} \quad t \in [t_i, t_{i+1}] \quad (2.37b)$$

$$s = \frac{t - t_i}{\Delta t_s} \quad t \in [t_i, t_{i+1}] \quad (2.37c)$$

From Eq. (2.37c), it is assumed that  $dt = \Delta t_s ds$ . Note that for convenience of formulation, the sampling frequencies are assumed to be the same for  $u(t)$  and  $h(t)$ . However, a larger time segment for  $h(t)$  is subsequently assumed through a linear constraint. Applying this constraint significantly improves the conditioning of the problem, for solution via the least squares method. For compactness, the expressions in Eq. (2.37) may be written in matrix

form as follows:

$$u(t) = \begin{bmatrix} u_i & u_{i+1} \end{bmatrix} \begin{Bmatrix} N_1 \\ N_2 \end{Bmatrix} \quad t \in [t_i, t_{i+1}] \quad (2.38a)$$

$$h(t) = \begin{bmatrix} N_1 & N_2 \end{bmatrix} \begin{Bmatrix} h_i \\ h_{i+1} \end{Bmatrix} \quad t \in [t_i, t_{i+1}] \quad (2.38b)$$

where  $N_1 = 1 - s$  and  $N_2 = s$ . Substituting this into Eq. (2.36) and transforming the integral from  $\tau$  to  $s$  results in:

$$y_k = \sum_{i=1}^{k-1} \begin{bmatrix} u_{k-i+1} & u_{k-i} \end{bmatrix} \int_{s=0}^{s=1} \begin{bmatrix} N_1^2 & N_1 N_2 \\ N_1 N_2 & N_2^2 \end{bmatrix} \Delta t_s ds \begin{Bmatrix} h_i \\ h_{i+1} \end{Bmatrix} \quad (2.39)$$

Next, Eq. (2.39) is assembled into matrix form over all time segments. For illustration, consider the first few points of a signal and how Eq. (2.39) evolves with time.

$$y_2 = \begin{bmatrix} u_2 & u_1 \end{bmatrix} \mathbf{N} \Delta t_s \begin{Bmatrix} h_1 \\ h_2 \end{Bmatrix} \quad (2.40a)$$

$$y_3 = \begin{bmatrix} u_3 & u_2 \end{bmatrix} \mathbf{N} \Delta t_s \begin{Bmatrix} h_1 \\ h_2 \end{Bmatrix} + \begin{bmatrix} u_2 & u_1 \end{bmatrix} \mathbf{N} \Delta t_s \begin{Bmatrix} h_2 \\ h_3 \end{Bmatrix} \quad (2.40b)$$

$$y_4 = \begin{bmatrix} u_4 & u_3 \end{bmatrix} \mathbf{N} \Delta t_s \begin{Bmatrix} h_1 \\ h_2 \end{Bmatrix} + \begin{bmatrix} u_3 & u_2 \end{bmatrix} \mathbf{N} \Delta t_s \begin{Bmatrix} h_2 \\ h_3 \end{Bmatrix} + \dots$$

$$+ \begin{bmatrix} u_2 & u_1 \end{bmatrix} \mathbf{N} \Delta t_s \begin{Bmatrix} h_3 \\ h_4 \end{Bmatrix} \quad (2.40c)$$

$$\text{where } \mathbf{N} = \int_{s=0}^{s=1} \begin{bmatrix} N_1^2 & N_1 N_2 \\ N_1 N_2 & N_2^2 \end{bmatrix} ds \quad (2.40d)$$

Even when only considering three time steps, the equations become complicated. Therefore, extraction of patterns is desirable to perform a faster matrix operation instead. One may notice that the multiplication of  $u_{k-i+1}$  and  $u_{k-i}$  with  $\mathbf{N}$  is reused every time step. Therefore let us define a row vector for the multiplication that occurs each time step as

$$\begin{bmatrix} a_{k-1,1} & a_{k-1,2} \end{bmatrix} = \begin{bmatrix} u_{k-1} & u_k \end{bmatrix} \mathbf{N}. \quad (2.41)$$

Using the above equation, the column vector of the output at all time segments can be related to a column vector of the IRF at all time segments as follows:

$$\begin{Bmatrix} y_2 \\ y_3 \\ \vdots \\ y_{N+1} \end{Bmatrix} = \begin{bmatrix} a_{1,1} & a_{1,2} & 0 & \dots & 0 \\ a_{2,1} & a_{2,2} + a_{1,1} & a_{1,2} & \dots & 0 \\ a_{3,1} & a_{3,2} + a_{2,1} & a_{2,2} + a_{1,1} & \dots & 0 \\ \vdots & \vdots & \vdots & \ddots & \vdots \\ a_{N,1} & a_{N,2} + a_{N-1,1} & a_{N-1,2} + a_{N-2,1} & \dots & a_{1,2} \end{bmatrix} \begin{Bmatrix} h_1 \\ h_2 \\ \vdots \\ h_N \end{Bmatrix} \Delta t_s \quad (2.42)$$

or in compact form as

$$\mathbf{y} = \mathbf{A}\mathbf{h}\Delta t_s \quad (2.43)$$

Note that the final column of  $\mathbf{A}$  has been truncated to ensure it is square. This is not required but is done to maintain similarity with previous methods.

For a given input and output, one may assemble  $\mathbf{A}$ , invert  $\mathbf{A}$ , and solve for  $\mathbf{h}$ . However, this inversion is ill-posed and a simple matrix inverse problem is not possible. Typical solution of this problem utilizes regularization to force a well-posed solution[40] in which the matrix is conditioned to remove any singularities.

However, a different approach is taken to improve the conditioning of the inverse prob-

lem. In this approach the assumption that a single linear segment of the resultant IRF holds for multiple segments of the input and output is made. Here the parameter

$$R_1 = \frac{\Delta t_h}{\Delta t_s}, \quad (2.44)$$

is defined where  $\Delta t_h$  is the new time segment of  $h(t)$  and  $\Delta t_s$  is the sampling time segment.

Next a linear constraint is invoked to account for this difference in time segment size. For the sake of illustration, assume  $R_1 = 3$  and consider the IRF over the first time segment of  $\Delta t_h$ . For all points in this segment  $h(t)$  can be expressed as follows:

$$h(t) = (1 - s_h)h(0) + s_h h(3\Delta t_s) \quad s_h \in [0, 1] \quad (2.45)$$

Therefore the first  $R_1$  points of the segment can be written as follows:

$$\begin{aligned} h(0) &= (1 - 0)h(0) + 0h(3\Delta t_s) = h(0) \\ h(\Delta t_s) &= (1 - \frac{1}{3})h(0) + \frac{1}{3}h(3\Delta t_s) \\ h(2\Delta t_s) &= (1 - \frac{2}{3})h(0) + \frac{2}{3}h(3\Delta t_s) \end{aligned}$$

or in matrix form

$$\begin{Bmatrix} h(0) \\ h(\Delta t_s) \\ h(2\Delta t_s) \end{Bmatrix} = \begin{bmatrix} 1 & 0 \\ \frac{2}{3} & \frac{1}{3} \\ \frac{1}{3} & \frac{2}{3} \end{bmatrix} \begin{Bmatrix} h(0) \\ h(3\Delta t_s) \end{Bmatrix} \quad (2.46)$$

Such a relationship also exists for the next truncated segment of the IRF, i.e.

$$\begin{Bmatrix} h(3\Delta t_s) \\ h(4\Delta t_s) \\ h(5\Delta t_s) \end{Bmatrix} = \begin{bmatrix} 1 & 0 \\ \frac{2}{3} & \frac{1}{3} \\ \frac{1}{3} & \frac{2}{3} \end{bmatrix} \begin{Bmatrix} h(3\Delta t_s) \\ h(6\Delta t_s) \end{Bmatrix} \quad (2.47)$$



Continuing this pattern for all  $N$  points in the IRF of interest, one may assemble all these relationships as

$$\left\{ \begin{array}{c} h(0) \\ h(\Delta t_s) \\ h(2\Delta t_s) \\ h(3\Delta t_s) \\ h(4\Delta t_s) \\ h(5\Delta t_s) \\ \vdots \\ h((N-3)\Delta t_s) \\ h((N-2)\Delta t_s) \\ h((N-1)\Delta t_s) \\ h(N\Delta t_s) \end{array} \right\} = \begin{bmatrix} 1 & 0 & 0 & \dots & 0 & 0 \\ \frac{2}{3} & \frac{1}{3} & 0 & \dots & 0 & 0 \\ \frac{1}{3} & \frac{2}{3} & 0 & \dots & 0 & 0 \\ 0 & 1 & 0 & \dots & 0 & 0 \\ 0 & \frac{2}{3} & \frac{1}{3} & \dots & 0 & 0 \\ 0 & \frac{1}{3} & \frac{2}{3} & \dots & 0 & 0 \\ \vdots & \vdots & \vdots & \ddots & \vdots & \vdots \\ 0 & 0 & 0 & \dots & 1 & 0 \\ 0 & 0 & 0 & \dots & \frac{2}{3} & \frac{1}{3} \\ 0 & 0 & 0 & \dots & \frac{1}{3} & \frac{2}{3} \\ 0 & 0 & 0 & \dots & 0 & 1 \end{bmatrix} \left\{ \begin{array}{c} h(0) \\ h(3\Delta t_s) \\ h(6\Delta t_s) \\ \vdots \\ h((N-3)\Delta t_s) \\ h(N\Delta t_s) \end{array} \right\} \quad (2.48)$$

Note the diagonal stitching of each segment of the IRF into the larger constraint matrix.

This expression can be written compactly as

$$\mathbf{h} = \mathbf{C}_h \mathbf{h}_c \quad (2.49)$$

where  $\mathbf{C}_h$  is a matrix assembled from the mapping matrix as shown Eq. (2.46), and  $\mathbf{h}_c$  is the constrained, IRF vector. Substituting Eq. (2.49) into Eq. (2.42) yields

$$\mathbf{y} = \mathbf{A} \mathbf{C}_h \mathbf{h}_c \Delta t_s = \hat{\mathbf{A}} \mathbf{h}_c \Delta t_s. \quad (2.50)$$

The multiplication of  $\mathbf{A}$  and  $\mathbf{C}_h$  is denoted  $\hat{\mathbf{A}}$  that is  $N$  by  $(N/R_1 + 1)$ . Using  $R_1 > 1$  results in many more rows than columns, which allows for a better conditioned least squares

inversion.

Applying the initial condition  $\mathbf{h}_c(0) = 0$ , Eq. (2.50) can be solved using least squares method as follows:

$$\mathbf{h}_c = \frac{1}{\Delta t_s} \left( \hat{\mathbf{A}}^T \hat{\mathbf{A}} \right)^{-1} \hat{\mathbf{A}}^T \mathbf{y} \quad (2.51)$$

With the IRF now determined, return to Eq. (2.21). Since the commutative property of convolution is invoked, the roles of the IRF and input can be simply switched in the final discretized equation as

$$y_k = \sum_{i=1}^{k-1} \begin{bmatrix} h_{k-i+1} & h_{k-i} \end{bmatrix} \int_{s=0}^{s=1} \begin{bmatrix} N_1^2 & N_1 N_2 \\ N_1 N_2 & N_2^2 \end{bmatrix} \Delta t_s ds \begin{Bmatrix} u_i \\ u_{i+1} \end{Bmatrix}, \quad (2.52)$$

and solve for any input.

Since  $h(t)$  is assumed linear over  $\Delta t_h$ , one may evaluate  $h(t)$  at any points corresponding the sampling rate of the output. A linear constraint is subsequently applied to the input to obtain a least squares solution of that input. One needs to select a new ratio

$$R_2 = \frac{\Delta t_i}{\Delta t_s} = \frac{f_s}{f_i} \quad (2.53)$$

between the sampling frequency ( $f_s$ ) of the measured output,  $y(t)$ , and that of the input,  $u(t)$ , to be constructed. The reconstructed input will be piecewise linear of time segments of length  $\Delta t_i$ . This ratio need not be related to that used to form the IRF ( $R_1 = f_s/f_h$ ) and therefore, various  $R_2$  values may be selected to determine the best solution. Note that selecting  $R_2 < R_1$  is not recommended as no additional information is given at a finer sampling interval than  $R_1 \Delta t_s$ . Recall that linear interpolation is used to obtain these points.

To solve for the input, the convolution needs to be formulated out of the new known: the IRF. Again a constraint matrix,  $\mathbf{C}_u$ , is applied, formed by using the prescribed  $R_2$  value.

Although this analysis is equivalent to the IRF solution, it is presented here for clarity.

Return to Eq. (2.52). For illustration, consider the first few points of a signal and how this equation evolves with time.

$$y_2 = \begin{bmatrix} h_2 & h_1 \end{bmatrix} \mathbf{N} \Delta t_s \begin{Bmatrix} u_1 \\ u_2 \end{Bmatrix} \quad (2.54a)$$

$$y_3 = \begin{bmatrix} h_3 & h_2 \end{bmatrix} \mathbf{N} \Delta t_s \begin{Bmatrix} u_1 \\ u_2 \end{Bmatrix} + \begin{bmatrix} h_2 & h_1 \end{bmatrix} \mathbf{N} \Delta t_s \begin{Bmatrix} u_2 \\ u_3 \end{Bmatrix} \quad (2.54b)$$

$$y_4 = \begin{bmatrix} h_4 & h_3 \end{bmatrix} \mathbf{N} \Delta t_s \begin{Bmatrix} u_1 \\ u_2 \end{Bmatrix} + \begin{bmatrix} h_3 & h_2 \end{bmatrix} \mathbf{N} \Delta t_s \begin{Bmatrix} u_2 \\ u_3 \end{Bmatrix} + \dots \\ + \begin{bmatrix} h_2 & h_1 \end{bmatrix} \mathbf{N} \Delta t_s \begin{Bmatrix} u_3 \\ u_4 \end{Bmatrix} \quad (2.54c)$$

$$\text{where } \mathbf{N} = \int_{s=0}^{s=1} \begin{bmatrix} N_1^2 & N_1 N_2 \\ N_1 N_2 & N_2^2 \end{bmatrix} ds \quad (2.54d)$$

Even when only considering three time steps, the equations become complicated. Therefore, extraction of patterns is desirable to perform a faster matrix operation. Just as in the IRF solution, one may notice that the multiplication of  $h_{k-i+1}$  and  $h_{k-i}$  with  $\mathbf{N}$  is reused every time step. Therefore let us define a row vector for the multiplication that occurs each time step as

$$\begin{bmatrix} b_{k-1,1} & b_{k-1,2} \end{bmatrix} = \begin{bmatrix} h_{k-1} & h_k \end{bmatrix} \mathbf{N}. \quad (2.55)$$

Using the above equation, the column vector of the output at all time segments can be

related to a column vector of the unknown input force at all time segments as follows:

$$\begin{Bmatrix} y_2 \\ y_3 \\ \vdots \\ y_{N+1} \end{Bmatrix} = \begin{bmatrix} b_{1,1} & b_{1,2} & 0 & \dots & 0 \\ b_{2,1} & b_{2,2} + b_{1,1} & b_{1,2} & \dots & 0 \\ b_{3,1} & b_{3,2} + b_{2,1} & b_{2,2} + b_{1,1} & \dots & 0 \\ \vdots & \vdots & \vdots & \ddots & \vdots \\ b_{N,1} & b_{N,2} + b_{N-1,1} & b_{N-1,2} + b_{N-2,1} & \dots & b_{1,2} \end{bmatrix} \begin{Bmatrix} u_1 \\ u_2 \\ \vdots \\ u_N \end{Bmatrix} \Delta t_s \quad (2.56)$$

or in compact form as

$$\mathbf{y} = \mathbf{B}\mathbf{u}\Delta t_s \quad (2.57)$$

Note that the final column of  $\mathbf{B}$  has been truncated to ensure it is square. This is not required but is done to maintain similarity with previous methods.

As in the IRF solution, one may apply a constraint to the unknown input force. For the

example case of  $R_2 = 3$ , the full constraint relationship is

$$\left\{ \begin{array}{c} u(0) \\ u(\Delta t_s) \\ u(2\Delta t_s) \\ u(3\Delta t_s) \\ u(4\Delta t_s) \\ u(5\Delta t_s) \\ \vdots \\ u((N-3)\Delta t_s) \\ u((N-2)\Delta t_s) \\ u((N-1)\Delta t_s) \\ u(N\Delta t_s) \end{array} \right\} = \begin{bmatrix} 1 & 0 & 0 & \dots & 0 & 0 \\ \frac{2}{3} & \frac{1}{3} & 0 & \dots & 0 & 0 \\ \frac{1}{3} & \frac{2}{3} & 0 & \dots & 0 & 0 \\ 0 & 1 & 0 & \dots & 0 & 0 \\ 0 & \frac{2}{3} & \frac{1}{3} & \dots & 0 & 0 \\ 0 & \frac{1}{3} & \frac{2}{3} & \dots & 0 & 0 \\ \vdots & \vdots & \vdots & \ddots & \vdots & \vdots \\ 0 & 0 & 0 & \dots & 1 & 0 \\ 0 & 0 & 0 & \dots & \frac{2}{3} & \frac{1}{3} \\ 0 & 0 & 0 & \dots & \frac{1}{3} & \frac{2}{3} \\ 0 & 0 & 0 & \dots & 0 & 1 \end{bmatrix} \left\{ \begin{array}{c} u(0) \\ u(3\Delta t_s) \\ u(6\Delta t_s) \\ \vdots \\ u((N-3)\Delta t_s) \\ u(N\Delta t_s) \end{array} \right\} \quad (2.58)$$

or written compactly as

$$\mathbf{u} = \mathbf{C}_u \mathbf{u}_c. \quad (2.59)$$

Plugging Eq. (2.59) into Eq. (2.57), yields the new discrete convolution relationship written as

$$\mathbf{y} = \hat{\mathbf{B}} \mathbf{u}_c \Delta t_s, \quad (2.60)$$

where  $\hat{\mathbf{B}} = \mathbf{B} \mathbf{C}_u$ . As mentioned previously, a different  $R_2$  value may be used and therefore  $\mathbf{C}_u$  may be different from  $\mathbf{C}_h$  from Eq. (2.49). Now an equation similar to Eq. (2.51) can be constructed as

$$\mathbf{u}_c = \frac{1}{\Delta t_s} (\hat{\mathbf{B}}^T \hat{\mathbf{B}})^{-1} \hat{\mathbf{B}}^T \mathbf{y} \quad (2.61)$$

to solve for the applied input.

### 2.2.2.2 Generalized Draper-Lee Method

One may wonder why a linear distribution was chosen in the CMM instead of some other order. Therefore, the formulation of a general method that allows for any user selected distribution of the unknown IRF or input is desirable. This is done in this section and is referred to as the Generalized Draper-Lee Method. To demonstrate this, reconsider the IRF construction. A new time interval is defined as

$$\Delta t_h = R_1 \cdot \Delta t_s \quad (2.62)$$

where  $\Delta t_h$  is the selected time segment of the unknown IRF,  $R_1$  is an integer number greater than one, and  $\Delta t_s$  is the sampling time segment of the known output. Equation (2.35) is rewritten as a summation over these intervals, i.e.

$$y(t) = \sum_{i=0}^{N-1} \int_{i\Delta t_h}^{(i+1)\Delta t_h} u(t - \tau) h(\tau) d\tau \quad (2.63)$$

where  $N = t/\Delta t_h$ . Over this segment, a form of the IRF where all points in the segment are a function of the IRF at the end points or nodal points is assumed, i.e.

$$h(t) = \mathbf{N}_h \mathbf{h}_i \quad (2.64)$$

where  $\mathbf{N}_h$  is a row vector of interpolation functions of the normalized time parameter,  $s_h$  ( $0 \leq s_h \leq 1$  for segment  $i$ ), and  $\mathbf{h}_i$  is a column vector of the unknown nodal values for segment  $i$ . Over every  $R_1$  sampling points, the IRF is assumed to have a distribution which is only a function of the nodal points. At this point, a general form of  $\mathbf{N}_h$  is maintained. For specific examples, refer to Eqs. (2.79) and (2.97).

Instead of choosing the same discretization for the measured input, all of the infor-

mation is extracted at each sampling point. One may plug Eq. (2.64) into Eq. (2.63) and separate the continuous integral into a summation of integrals over all  $\Delta t_s$  segments in a given  $\Delta t_h$  segment to obtain

$$y(t) = \sum_{i=0}^{N-1} \left[ \sum_{j=0}^{R_1-1} \int_{i\Delta t_h + j\Delta t_s}^{i\Delta t_h + (j+1)\Delta t_s} u(t - \tau) \mathbf{N}_h d\tau \right] \mathbf{h}_{i+1}. \quad (2.65)$$

Note that  $\mathbf{h}$  has been removed from the integral as this is a vector of discrete values and is constant for the interior summation. Next, assume a linear distribution of the input over a sampling interval, i.e.

$$u(t) = (1 - s_u)u_1 + s_u u_2 \quad \text{for } 0 \leq s_u \leq 1. \quad (2.66)$$

Expanding to matrix form, results in

$$u(t) = \begin{bmatrix} u_1 & u_2 \end{bmatrix} \begin{Bmatrix} N_{u1} \\ N_{u2} \end{Bmatrix} = \mathbf{u} \mathbf{N}_u \quad (2.67)$$

where  $N_{u1} = 1 - s_u$  and  $N_{u2} = s_u$ . Substituting this into Eq. (2.65) and evaluating at a given time  $t_k = (k - 1)\Delta t_s$  results in

$$y(t_k) = \sum_{i=0}^N \left[ \sum_{j=0}^M \begin{bmatrix} u_{k-i \cdot R_1 - j} & u_{k-i \cdot R_1 - j - 1} \end{bmatrix} \int_{i\Delta t_h + j\Delta t_s}^{i\Delta t_h + (j+1)\Delta t_s} \mathbf{N}_u \mathbf{N}_h d\tau \right] \mathbf{h}_{i+1} \quad (2.68)$$

where the variables in the upper bounds of the summations are

$$M = \begin{cases} R_1 - 1, & \text{for } i < N \\ \text{rem}\left(\frac{k-2}{R_1}\right), & \text{for } i = N \end{cases} \quad (2.69)$$

(note, rem is the remainder function, i.e. remainder after division) and  $N = \text{floor}\left(\frac{k-2}{R_1}\right)$  (note, floor is a function where the division is rounded down to the nearest integer number), the number of segments that fit into  $y$  without exceeding it. Note that the first point in the measured  $y$  corresponds to  $k = 1$ . As in the previous formulation, the starting point is the second entry in  $y$  (i.e.  $k = 2$ ). Also note that the discrete input nodal values,  $u_i$ , have been moved outside of the integral as they are constants.

Finally, the integral is evaluated. However, the integration is over  $\tau$  while  $\mathbf{N}_u$  and  $\mathbf{N}_h$  are a function of  $s_u$  and  $s_h$ , respectively. To evaluate this integral, one of these variables is chosen and the expressions of the other terms are changed. For convenience,  $s_u$  is chosen as the integration parameter. By doing this, the integration range is always from  $s_u = 0$  to  $s_u = 1$ . However,  $d\tau$  and  $\mathbf{N}_h$  must change. Since the time was mapped into non-dimensional time, i.e.

$$t = (1 - s_u)t_1 + s_ut_2 \quad \text{for } 0 \leq s_u \leq 1, \quad (2.70)$$

one may note that  $dt = \Delta t_s ds_u = d\tau$ . The input interpolation column vector  $\mathbf{N}_u$  is already a function of  $s_u$ . Finally note that

$$s_h = (j + s_u)/R_1 \quad (2.71)$$

and substitute this into our expressions in  $\mathbf{N}_h$ . This yields the expression

$$y(t_k) = \sum_{i=0}^N \left[ \sum_{j=0}^M \begin{bmatrix} u_{k-i \cdot R_1 - j} & u_{k-i \cdot R_1 - j - 1} \end{bmatrix} \int_{s_u=0}^{s_u=1} \mathbf{N}_u \hat{\mathbf{N}}_h ds_u \right] \mathbf{h}_{i+1} \Delta t_s \quad (2.72)$$

where  $\hat{\mathbf{N}}_h$  has been obtained by substituting Eq. (2.71) into  $\mathbf{N}_h$ .

Equation (2.72) is compact however, for clarity, the first few iterations are presented



below for  $R_1 = 3$ .

$$y_2 = \begin{bmatrix} u_2 & u_1 \end{bmatrix} \mathbf{N}_0 \mathbf{h}_1 \Delta t_s \quad (2.73a)$$

$$y_3 = \begin{bmatrix} u_3 & u_2 \end{bmatrix} \mathbf{N}_0 \mathbf{h}_1 \Delta t_s + \begin{bmatrix} u_2 & u_1 \end{bmatrix} \mathbf{N}_1 \mathbf{h}_1 \Delta t_s \quad (2.73b)$$

$$y_4 = \begin{bmatrix} u_4 & u_3 \end{bmatrix} \mathbf{N}_0 \mathbf{h}_1 \Delta t_s + \begin{bmatrix} u_3 & u_2 \end{bmatrix} \mathbf{N}_1 \mathbf{h}_1 \Delta t_s + \dots \\ + \begin{bmatrix} u_2 & u_1 \end{bmatrix} \mathbf{N}_2 \mathbf{h}_1 \Delta t_s \quad (2.73c)$$

$$y_5 = \begin{bmatrix} u_5 & u_4 \end{bmatrix} \mathbf{N}_0 \mathbf{h}_1 \Delta t_s + \begin{bmatrix} u_4 & u_3 \end{bmatrix} \mathbf{N}_1 \mathbf{h}_1 \Delta t_s + \dots \\ + \begin{bmatrix} u_3 & u_2 \end{bmatrix} \mathbf{N}_2 \mathbf{h}_1 \Delta t_s + \begin{bmatrix} u_2 & u_1 \end{bmatrix} \mathbf{N}_0 \mathbf{h}_2 \Delta t_s \quad (2.73d)$$

$$\text{where } \mathbf{N}_j = \int_{s_u=0}^{s_u=1} \mathbf{N}_u(s_u) \hat{\mathbf{N}}_h(s_u, j) ds_u \quad (2.73e)$$

Just over these four iterations, the equations become complicated and displaying more iterations becomes confusing. Up until the second segment of the IRF is displayed. For the example of  $R_1 = 3$  this occurs at the fourth point of interest (i.e.  $k = 5$ ). Additionally, one may note that Eq. (2.73e) has the same  $R_1$  variants as the equation only changes as a function of  $j$ . Therefore, all  $R_1$  matrices are computed before assembling into matrix form rather than recomputing this integration at every iteration.

For a selected form of the IRF, this process can be assembled into matrix form as

$$\mathbf{y} = \hat{\mathbf{A}} \mathbf{h} \Delta t_s, \quad (2.74)$$

where  $\mathbf{y}$  is a column vector of discrete measured outputs,  $\hat{\mathbf{A}}$  is a matrix generated by assembling Eq. (2.72) for all points,  $\mathbf{h}$  is the vector of unknown nodal values of the IRF, and  $\Delta t_s$  is the sampling interval of the input force.

If an  $R_1$  large enough such that  $\hat{\mathbf{A}}$  has many more rows than columns is chosen, the

nodal values of the IRF are solved using

$$\mathbf{h} = \frac{1}{\Delta t_s} \hat{\mathbf{A}}^+ \mathbf{y} \quad (2.75)$$

where the plus superscript denotes the least squares pseudo inverse.

Now with the IRF known, one may interpolate using Eq. (2.64) to evaluate  $h(t)$  at any points in time over the sampling event.

Identically to the Constraint Matrix Method discussed in Section 2.2.2.1, an unknown applied input is solved by invoking the commutative property of the convolution. Using the now known IRF, the roles of  $u$  and  $h$  are switched in all of the above equations to discretize Eq. (2.34). This results in

$$y(t_k) = \sum_{i=0}^N \left[ \sum_{j=0}^M \begin{bmatrix} h_{k-i \cdot R_2-j} & h_{k-i \cdot R_2-j-1} \end{bmatrix} \int_{s_h=0}^{s_h=1} \mathbf{N}_h \hat{\mathbf{N}}_u ds_h \right] \mathbf{u}_{i+1} \Delta t_s \quad (2.76)$$

where now  $h$  at each sampling point is known and  $u$  has a distribution over many sampled points. Note that the distribution of the IRFs at this stage is always assumed linear regardless of the form of the IRF selected in stage 1. This is a formulation convenience chosen by the authors to maintain the similarity with stage 1.

As before, Eq. (2.76) can be assembled into matrix form as

$$\mathbf{y} = \hat{\mathbf{B}} \mathbf{u} \Delta t_s, \quad (2.77)$$

and solved using a Least Squares psuedo inverse as

$$\mathbf{u} = \frac{1}{\Delta t_s} \hat{\mathbf{B}}^+ \mathbf{y}. \quad (2.78)$$

### 2.2.2.3 Linear, Quadratic, and Cubic Distributions of GDLM

To make this clearer, a linear, quadratic, and cubic example distribution is presented. Begin with linear. In such a case, the form of the unknown IRF is assumed to be

$$h(t) = (1 - s_h)h_i + s_h h_{i+1} \quad \text{for } 0 \leq s_h \leq 1 \quad (2.79)$$

over a given segment. Expanding to matrix form yields

$$h(t) = \begin{bmatrix} N_1 & N_2 \end{bmatrix} \begin{Bmatrix} h_i \\ h_{i+1} \end{Bmatrix} = \mathbf{N}_h \mathbf{h} \quad (2.80)$$

where  $N_1 = 1 - s_h$  and  $N_2 = s_h$ .

Plugging this linear distribution into Eq. (2.72) and applying Eq. (2.70) results in

$$y(t_k) = \sum_{i=0}^N \left[ \sum_{j=0}^M \begin{bmatrix} u_{k-i \cdot R_1-j} & u_{k-i \cdot R_1-j-1} \end{bmatrix} \int_{s_u=0}^{s_u=1} \mathbf{N}_u \hat{\mathbf{N}}_h ds_u \right] \begin{Bmatrix} h_{i+1} \\ h_{i+2} \end{Bmatrix} \Delta t_s. \quad (2.81)$$

For clarity, an example assembly into matrix form is presented. Consider Eqs. (2.73a-2.73d). Substitute Eq. (2.80) into these expressions. Note that the matrices  $\mathbf{N}_j$  have dimension of 2 by 2. For compactness, define

$$\begin{bmatrix} a_{k-i \cdot R_1-j,1}^j & a_{k-i \cdot R_1-j,2}^j \end{bmatrix} = \begin{bmatrix} u_{k-i \cdot R_1-j} & u_{k-i \cdot R_1-j-1} \end{bmatrix} \mathbf{N}_j \quad (2.82)$$

where the superscript on the  $a$  entries denotes which  $\mathbf{N}_j$  matrix was used to form it. Using

the example in Eqs. (2.73a-2.73d) (i.e.  $R_1 = 3$ ), are assembled into matrix form as

$$\begin{Bmatrix} y_2 \\ y_3 \\ y_4 \\ y_5 \end{Bmatrix} = \begin{bmatrix} a_{2,1}^0 & a_{2,2}^0 & 0 \\ a_{3,1}^0 + a_{2,1}^1 & a_{3,2}^0 + a_{2,2}^1 & 0 \\ a_{4,1}^0 + a_{3,1}^1 + a_{2,1}^2 & a_{4,2}^0 + a_{3,2}^1 + a_{2,2}^2 & 0 \\ a_{5,1}^0 + a_{4,1}^1 + a_{3,1}^2 & a_{5,2}^0 + a_{4,2}^1 + a_{3,2}^2 + a_{2,1}^0 & a_{2,2}^0 \end{bmatrix} \begin{Bmatrix} h_1 \\ h_2 \\ h_3 \end{Bmatrix} \Delta t_s \quad (2.83)$$

Since a single value is available at each node,  $R_1 > 1$  is required for a least squares solution to be applicable.

Equation (2.81) is equivalent to that given in Eq. (2.39), however, the constraint on the IRF has been integrated into the formation of  $\hat{\mathbf{A}}$  rather than multiplying by a constraint matrix after formation.

For the quadratic case, a quadratic interpolation function must be introduced. This results in a piecewise smooth curve where the derivatives at the ends of the segments will not be matched. However, this curvature between nodes may enhance the accuracy of the method.

For quadratic interpolation between nodes the form of the IRF will be

$$h = a_1 + a_2 s_h + a_3 s_h^2. \quad (2.84)$$

To utilize a quadratic interpolation over a segment requires three nodes. Therefore, a "segment" of the IRF is redefined as three points,  $h_1$ ,  $h_2$ , and  $h_3$ . Evaluating Eq. (2.84) at each node results in

$$h_1 = a_1$$

$$h_2 = a_1 + \frac{a_2}{2} + \frac{a_3}{4}$$

$$h_3 = a_1 + a_2 + a_3$$

Solving this for the unknown interpolation coefficients gives us

$$\begin{aligned}a_1 &= h_1 \\a_2 &= -3h_1 + 4h_2 - h_3 \\a_3 &= 2h_1 - 4h_2 + 2h_3\end{aligned}$$

Plugging these definitions into Eq. (2.84) results in

$$h = N_{h_1}h_1 + N_{h_2}h_2 + N_{h_3}h_3 \quad (2.85)$$

where

$$\begin{aligned}N_{h_1} &= 1 - 3s_h + 2s_h^2 \\N_{h_2} &= 4s_h - 4s_h^2 \\N_{h_3} &= -s_h + 2s_h^2\end{aligned}$$

Now expressions similar in form to Eq. (2.37b) are available, albeit a bit more complex. Equation (2.85) can be placed into matrix form, resulting in an expression similar to Eq. (2.80):

$$h(t) = \begin{bmatrix} N_{h_1} & N_{h_2} & N_{h_3} \end{bmatrix} \begin{Bmatrix} h_1 \\ h_2 \\ h_3 \end{Bmatrix} = \mathbf{N}_h^2 \mathbf{h}^2 \quad (2.86)$$

Note that the superscript, 2, denotes the quadratic interpolation form.

By formulating in this manner, this can be substituted into Eq. (2.72), i.e.

$$y(t_k) = \sum_{i=0}^N \left[ \sum_{j=0}^M \begin{bmatrix} u_{k-i \cdot R_1 - j} & u_{k-i \cdot R_1 - j - 1} \end{bmatrix} \int_{s_u=0}^{s_u=1} \mathbf{N}_u \hat{\mathbf{N}}_h^2 ds_u \right] \begin{Bmatrix} h_{i+1} \\ h_{i+1.5} \\ h_{i+2} \end{Bmatrix} \Delta t_s \quad (2.87)$$

where  $\hat{\mathbf{N}}_h^2$  has substituted Eq. (2.71) into  $\mathbf{N}_h^2$ .

For clarity, an example assembly into matrix form is presented. Consider Eqs. (2.73a-2.73d). Substitute Eq. (2.98) into these expressions. Note that the matrices  $\mathbf{N}_j$  will have dimension of 2 by 3. For compactness, define

$$\begin{bmatrix} a_{k-i \cdot R_1-j,1}^j & a_{k-i \cdot R_1-j,2}^j & a_{k-i \cdot R_1-j,3}^j \end{bmatrix} = \begin{bmatrix} u_{k-i \cdot R_1-j} & u_{k-i \cdot R_1-j-1} \end{bmatrix} \mathbf{N}_j \quad (2.88)$$

where the superscript on the  $a$  entries denotes which  $\mathbf{N}_j$  matrix was used to form it. Using the example in Eqs. (2.73a-2.73d) (i.e.  $R_1 = 3$ ), assembly into matrix form is performed as

$$\begin{Bmatrix} y_2 \\ y_3 \\ y_4 \\ y_5 \end{Bmatrix} = \begin{bmatrix} a_{2,1}^0 & a_{2,2}^0 & a_{2,3}^0 & 0 & 0 \\ a_{3,1}^0 + a_{2,1}^1 & a_{3,2}^0 + a_{2,2}^1 & a_{3,3}^0 + a_{2,3}^1 & 0 & 0 \\ a_{4,1}^0 + a_{3,1}^1 + a_{2,1}^2 & a_{4,2}^0 + a_{3,2}^1 + a_{2,2}^2 & a_{4,3}^0 + a_{3,3}^1 + a_{2,3}^2 & 0 & 0 \\ a_{5,1}^0 + a_{4,1}^1 + a_{3,1}^2 & a_{5,2}^0 + a_{4,2}^1 + a_{3,2}^2 & a_{5,3}^0 + a_{4,3}^1 + a_{3,3}^2 + a_{2,1}^0 & a_{2,2}^0 & a_{2,3}^0 \end{bmatrix} \begin{Bmatrix} h_1 \\ h_{1.5} \\ h_2 \\ h_{2.5} \\ h_3 \end{Bmatrix} \Delta t_s \quad (2.89)$$

Since now two additional values for each new segment are required,  $R_1 > 2$  is required for the IRF solution via Eq. (2.51). Note that since twice as many variables are requested as in the linear case, the  $R_1 = 2$  case will result in a square matrix.

As in the linear case, the roles of the IRF and input force are reversed to solve for an unknown applied load.

The cubic case is similar to that of the linear case except with a cubic interpolation function. This results in a smooth construction of the IRF. Consider a segment of the IRF displayed in Figure 2.7. In this figure, each segment has been assigned a value and slope at each end point or node. Note the notation

$$\theta_i = \left. \frac{dh}{dt} \right|_i \quad (2.90)$$

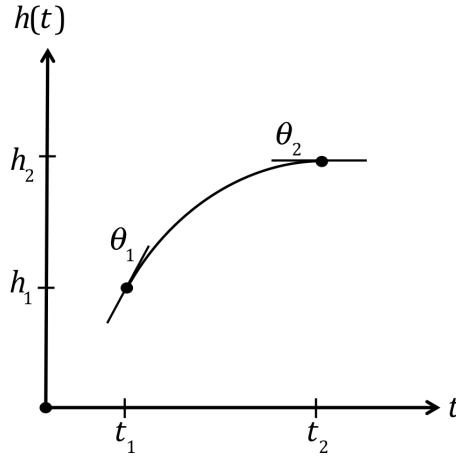


Figure 2.7: Segment of IRF showing value and slope at end points

is used for our time varying IRF. Therefore, matching the function values  $h_i$  and the time derivatives  $\theta_i$  at each node of the segments yields a continuous and differentiable reconstructed function over the entire IRF.

Note that the mapping into non-dimensional time is

$$t = (1 - s_h)t_1 + s_h t_2 \quad \text{for } 0 \leq s_h \leq 1 \quad (2.91)$$

and

$$\frac{dt}{ds_h} = t_2 - t_1 = \Delta t_h. \quad (2.92)$$

Since there are four unknowns for a segment,  $h_1$ ,  $\theta_1$ ,  $h_2$ , and  $\theta_2$ , four coefficients in our interpolation function are needed. Therefore, a cubic function is introduced of the form

$$h = a_1 + a_2 s_h + a_3 s_h^2 + a_4 s_h^3. \quad (2.93)$$

Plugging this into Eq. (2.90) yields

$$\theta = \frac{dh}{dt} = \frac{dh}{ds_h} \frac{ds_h}{dt} = \frac{1}{\Delta t_h} (a_2 + 2a_3 s_h + 3a_4 s_h^2). \quad (2.94)$$

Evaluating Eqs. (2.93) and (2.94) at each node gives us the following four equations:

$$\begin{aligned}
h_1 &= a_1 \\
\theta_1 &= \frac{1}{\Delta t_h} a_2 \\
h_2 &= a_1 + a_2 + a_3 + a_4 \\
\theta_2 &= \frac{1}{\Delta t_h} (a_2 + 2a_3 + 3a_4)
\end{aligned} \tag{2.95}$$

Solving this for the unknown interpolation coefficients gives us

$$\begin{aligned}
a_1 &= h_1 \\
a_2 &= \Delta t_h \theta_1 \\
a_3 &= -3h_1 - 2\Delta t_h \theta_1 + 3h_2 - \Delta t_h \theta_2 \\
a_4 &= 2h_1 + \Delta t_h \theta_1 - 2h_2 + \Delta t_h \theta_2
\end{aligned} \tag{2.96}$$

One may define  $\hat{\theta}_i = \Delta t_h \theta_i$  so that our interpolation function is purely a function of  $s_h$ .

Plugging these definitions and  $\hat{\theta}$  into Eq. (2.93) and rearranging gives us

$$h = N_{h_1} h_1 + N_{\hat{\theta}_1} \hat{\theta}_1 + N_{h_2} h_2 + N_{\hat{\theta}_2} \hat{\theta}_2 \tag{2.97}$$

where

$$\begin{aligned}
N_{h_1} &= 1 - 3s_h^2 + 2s_h^3 \\
N_{\hat{\theta}_1} &= s_h - 2s_h^2 + s_h^3 \\
N_{h_2} &= 3s_h^2 - 2s_h^3 \\
N_{\hat{\theta}_2} &= -s_h^2 + s_h^3
\end{aligned}$$

Now expressions similar in form to Eq. (2.37b) are available, albeit a bit more complex. Equation (2.97) can be placed into matrix form, resulting in an expression similar to



Eq. (2.80):

$$h(t) = \begin{bmatrix} N_{h_1} & N_{\hat{\theta}_1} & N_{h_2} & N_{\hat{\theta}_2} \end{bmatrix} \begin{Bmatrix} h_1 \\ \hat{\theta}_1 \\ h_2 \\ \hat{\theta}_2 \end{Bmatrix} = \mathbf{N}_h^3 \mathbf{h}^3 \quad (2.98)$$

Note that the superscript, 3, denotes the cubic interpolation form.

By formulating in this manner, this is simply substituted into Eq. (2.72), i.e.

$$y(t_k) = \sum_{i=0}^N \left[ \sum_{j=0}^M \begin{bmatrix} u_{k-i \cdot R_1-j} & u_{k-i \cdot R_1-j-1} \end{bmatrix} \int_{s_u=0}^{s_u=1} \mathbf{N}_u \hat{\mathbf{N}}_h^3 ds_u \right] \begin{Bmatrix} h_{i+1} \\ \hat{\theta}_{i+1} \\ h_{i+2} \\ \hat{\theta}_{i+2} \end{Bmatrix} \Delta t_s \quad (2.99)$$

where  $\hat{\mathbf{N}}_h^3$  is obtained by substituting Eq. (2.71) into  $\mathbf{N}_h^3$ .

For clarity, an example assembly into matrix form is presented. Consider Eqs. (2.73a-2.73d). Substitute Eq. (2.98) into these expressions. Note that the matrices  $\mathbf{N}_j$  have dimension of 2 by 4. For compactness, define

$$\begin{bmatrix} a_{k-i \cdot R_1-j,1}^j & a_{k-i \cdot R_1-j,2}^j & a_{k-i \cdot R_1-j,3}^j & a_{k-i \cdot R_1-j,4}^j \end{bmatrix} = \begin{bmatrix} u_{k-i \cdot R_1-j} & u_{k-i \cdot R_1-j-1} \end{bmatrix} \mathbf{N}_j \quad (2.100)$$

where the superscript on the  $a$  entries denotes which  $\mathbf{N}_j$  matrix was used to form it. Using

the example in Eqs. (2.73a-2.73d) (i.e.  $R_1 = 3$ ), matrix assembly proceeds as

$$\begin{Bmatrix} y_2 \\ y_3 \\ y_4 \\ y_5 \end{Bmatrix} = \begin{bmatrix} a_{2,1}^0 & a_{2,2}^0 & a_{2,3}^0 & & \\ a_{3,1}^0 + a_{2,1}^1 & a_{3,2}^0 + a_{2,2}^1 & a_{3,3}^0 + a_{2,3}^1 & \dots & \\ a_{4,1}^0 + a_{3,1}^1 + a_{2,1}^2 & a_{4,2}^0 + a_{3,2}^1 + a_{2,2}^2 & a_{4,3}^0 + a_{3,3}^1 + a_{2,3}^2 & & \\ a_{5,1}^0 + a_{4,1}^1 + a_{3,1}^2 & a_{5,2}^0 + a_{4,2}^1 + a_{3,2}^2 & a_{5,3}^0 + a_{4,3}^1 + a_{3,3}^2 + a_{2,1}^0 & & \\ & a_{2,4}^0 & 0 & 0 & \\ & a_{3,4}^0 + a_{2,4}^1 & 0 & 0 & \\ & a_{4,4}^0 + a_{3,4}^1 + a_{2,4}^2 & 0 & 0 & \\ & a_{5,4}^0 + a_{4,4}^1 + a_{3,4}^2 + a_{2,2}^0 & a_{2,3}^0 & a_{2,4}^0 & \end{bmatrix} \begin{Bmatrix} h_1 \\ \hat{\theta}_1 \\ h_2 \\ \hat{\theta}_2 \\ h_3 \\ \hat{\theta}_3 \end{Bmatrix} \Delta t_s \quad (2.101)$$

Since now two unknowns are assigned at each node (value and derivative),  $R_1 > 2$  is required for the IRF to be determined using Eq. (2.51). Note that since there are twice as many variables as in the linear case, the  $R_1 = 2$  case will result in a square matrix.

Solving this equation for the cubic case will result in a fully defined smooth curve. One may then evaluate Eq. (2.97) at any intermediate point to increase the resolution of the IRF while still maintaining the smooth curve.

#### 2.2.2.4 Extension to Multiple Outputs

In this section, an extension to multiple outputs (and inputs) will be presented. Although the notation is chosen to be consistent with the Constraint Matrix Method and the Generalized Draper-Lee Method, this formulation is applicable to any TDDM.

To begin, consider a system with many outputs. This is the case for many real systems where strain and acceleration may be measured at various locations over a model. Such

systems are classified as single input multiple output (SIMO). Additionally, one may consider a system with multiple inputs of interest. This may be the case on a test article with multiple thrusters or control surfaces. Assuming the system still has multiple outputs, these systems are classified as multiple input multiple output (MIMO). In either case, each input-output pair has a unique IRF. For the SIMO case, if one input and  $n$  outputs are available,  $n$  IRFs must be generated. Since each of these maps do not depend on each other, one may use Eq. (2.51),  $n$  times to generate the IRFs.

The reconstruction of the input, on the other hand, requires knowledge from all of output locations. Consider the response of a system to an input at location  $i$ . Following the form of Eq. (2.77), the map from input  $i$  to any output location  $j$  can be written as:

$$\mathbf{y}_j = \hat{\mathbf{B}}_{j,i} \mathbf{u}_i \Delta t_s \quad (2.102)$$

Each location  $j$ , has a similar relationship to input  $i$ . Therefore the problem is formulated as follows to construct an equation to solve for  $(\mathbf{u})_i$ .

$$\begin{Bmatrix} \mathbf{y}_1 \\ \mathbf{y}_2 \\ \vdots \\ \mathbf{y}_n \end{Bmatrix} = \begin{bmatrix} \hat{\mathbf{B}}_{1,i} \\ \hat{\mathbf{B}}_{2,i} \\ \vdots \\ \hat{\mathbf{B}}_{n,i} \end{bmatrix} \mathbf{u}_i \Delta t_s \quad (2.103)$$

This equation is condensed further as

$$\mathbf{Y} = \hat{\mathcal{B}}_i(\mathbf{u})_i \Delta t_s. \quad (2.104)$$

Extension to MIMO is also straightforward. Using the principle of superposition, the response of other inputs invokes response to all of the outputs in an additive fashion to

that of another input. Superimposing all  $p$  inputs, yields the following relationship for the MIMO case.

$$\begin{Bmatrix} \mathbf{y}_1 \\ \mathbf{y}_2 \\ \vdots \\ \mathbf{y}_n \end{Bmatrix} = \begin{bmatrix} \hat{\mathbf{B}}_{11} & \hat{\mathbf{B}}_{12} & \dots & \hat{\mathbf{B}}_{1p} \\ \hat{\mathbf{B}}_{21} & \hat{\mathbf{B}}_{22} & \dots & \hat{\mathbf{B}}_{2p} \\ \vdots & \vdots & \ddots & \vdots \\ \hat{\mathbf{B}}_{n1} & \hat{\mathbf{B}}_{n2} & \dots & \hat{\mathbf{B}}_{np} \end{bmatrix} \begin{Bmatrix} \mathbf{u}_1 \\ \mathbf{u}_2 \\ \vdots \\ \mathbf{u}_p \end{Bmatrix} \Delta t_s \quad (2.105)$$

Provided  $nN > pN/R_2$  for the linear case or  $nN > 2pN/R_2$  for the cubic case (twice as many unknowns), a least squares solution may be employed. Applying a ratio ensures that the solution will not tend to infinity. However, further analysis is required to determine if the problem is well-conditioned and the solution is acceptable.

It may be possible that the user is interested at the force contributions at each of the calibration locations. If this is the case, then extracting each input time history after solving Eq. (2.105) would suffice. However, in wind tunnel applications, it is more often the case that the experimentalist will be more interested in the forces and moments with respect to some center of moment. This is akin to the output of the SWAT (e.g.  $F_{\text{app}}$  in Eq. (2.7)). Additionally, this will provide easier comparison with the SWAT and static strain gage results.

If this latter result presentation is of interest, one needs to simply convert the result of point reconstruction into a total force and moment contribution. To do this, define a 1x6 scaling matrix,  $\mathbf{S}_h$  which is a function of the hole location and converts the hammer load into force and moment contributions. For example, a z-direction force applied 0.1 meters in front of the center of moment would have a scaling matrix of

$$\mathbf{S}_h = \begin{bmatrix} 0 & 0 & 1 & 0 & 0.1 & 0 \end{bmatrix}. \quad (2.106)$$

A general formula for  $\mathbf{S}_h$  requires generating a coordinate system and directionality of

applied load so this is neglected for this section.

With the scaling matrices defined, the contributions from each hole are added as

$$\mathbf{F}_{\text{app}} = \sum_{i=1}^p \mathbf{S}_h^i \mathbf{u}_i^T \quad (2.107)$$

where the super script  $i$  denotes which hole location was used to generate the scaling matrix. Note: if using a higher order version of the GDLM, the scaling should be done *after* the interpolation of the reconstructed force. In the third order method, slopes are reconstructed which should not be scaled and summed together. All interpolation for the third order case only holds for the reconstructed point force.

This should work well for point loadings at the various calibration locations. However, it remains to be seen if a distributed pressure load or a point load at a location other than the calibration locations could be accurately reconstructed using this approach.

#### 2.2.2.5 Averaging of Calibration Sets

In this section, the method is extended to account for repeat tests during dynamic calibration. One motivation for this is better noise rejection. As the noise is assumed random (i.e. non biased), its form will not be repeatable from test to test. Therefore, using multiple tests should not reflect its presence in the constructed IRF. Furthermore, this reduces the reliance on a single calibration test. If the user misses the application location or direction by a small distance or angle, this can negatively affect the IRF accuracy. However, over multiple tests the IRF may be more accurately reconstructed.

To begin, return to Eq. (2.74) where the IRF is solved using a single input from a particular test and the corresponding output. If the IRF also fits the noise characteristics of the applied input-output pair, this can result in poor accuracy when applying the IRF to other reconstructions. This process can be avoided by using a higher  $R_1$  ratio, however,

another way that does not compromise resolution is sought.

The IRF is a property of a system. It is the response of the system to a unit impulse of infinitesimal width. This means that by definition, it is not dependent on the input applied to the system. Therefore, any input applied to the same location should have an identical IRF when generating the output, i.e.

$$\mathbf{y}_k = \hat{\mathbf{A}}_k \mathbf{h} \Delta t_s, \quad (2.108)$$

where each input-output pair at the same location can be assembled using the procedure discussed in either of the two methods. So to exploit this fact, additional information is supplied to the IRF problem by simply performing repeat tests at the same location. Assembling Eq. (2.108) yields

$$\begin{Bmatrix} \mathbf{y}_1 \\ \mathbf{y}_2 \\ \vdots \\ \mathbf{y}_P \end{Bmatrix} = \begin{bmatrix} \hat{\mathbf{A}}_1 \\ \hat{\mathbf{A}}_2 \\ \vdots \\ \hat{\mathbf{A}}_P \end{bmatrix} \mathbf{h} \Delta t_s \quad (2.109)$$

where the subscript P denotes the number of repeat tests used in reconstruction. One may note a resultant equation that is very similar in spirit to Eq. (2.103). This is by design, as the further over determination of the problem tends to enhance the results.

One may note that this type of formulation would not be possible using the conventional method. Since that method assumes the IRF is simply a scaled multiple of the measured response to an applied hammer pulse, one may not use multiple tests. Rather, one may simply select the "best" test case.

Utilization of this type of formulation allows the user to use a variety of calibration inputs. Steps, hammer pulses, shaker testing, and many others could all be simultaneously

used to construct the most accurate IRF.

#### 2.2.2.6 Segmentation

One apparent drawback of TDDMs is the computation expense. As the entire time history is required (from time  $t = 0$ , defined as a time at rest) the IRM can become unwieldy when large test times are of interest. Observing Eq. (2.78) for example, requires the inversion of an  $(N/R_2) \times (N/R_2)$  matrix. For these experiments, dynamics of up to a few kilohertz are of interest. It is common practice to sample at ten times the frequency band of interest to ensure proper resolution. Therefore, a 25 kHz sampling rate was used for most of the experiments. For either TDDM, reconstruction of a two second long force would require the inversion of a 25,000x25,000 matrix for the case of  $R_2 = 2$ . Obviously, this is completely unreasonable and a better approach is required.

Instead of deconvolving the entire output,  $y$ , consider segmenting the output and deconvolving each segment separately. After each segment is deconvolved, they are assembled into the reconstruction over the entire time history. The problem with this is that the convolution integral, i.e. Eqs. (2.34) and (2.35) are only defined for a system starting from rest. This means that a system with nonzero initial conditions cannot be represented exactly using these equations. However, it may be of interest to observe magnitude of the error in our force reconstruction due to the presence of nonzero initial conditions.

Consider a dynamic LTI system subject to a sinusoidal forcing. Next imagine measuring the output of the system after the load has been applied. This is analogous to considering a segment of the response with nonzero initial conditions. Due to the linearity of LTI systems, the measured response ( $y_m$ ) in this scenario will be equivalent to the superposition of the response of the system subject to the sinusoidal forcing but starts from rest ( $y_1$ ) and the response of the system subject to those initial conditions ( $y_2$ ). Plugging this into

Eq. (2.34) yields

$$y_m = y_1 + y_2 = h * (u_1 + u_2) \quad (2.110)$$

where  $*$  denotes the continuous convolution operation,  $u_1$  is the sinusoidal applied load of interest and  $u_2$  is zero as there is no applied load in the unforced case.

Let's consider each equation separately to try and gain some additional insight, i.e.

$$y_1 = h * u_1 \quad (2.111a)$$

$$y_2 = h * u_2 \quad (2.111b)$$

Since Eq. (2.111a) has no initial conditions, this is solved using deconvolution techniques and reconstruct the desired applied load. This is given in Figure 2.8a.

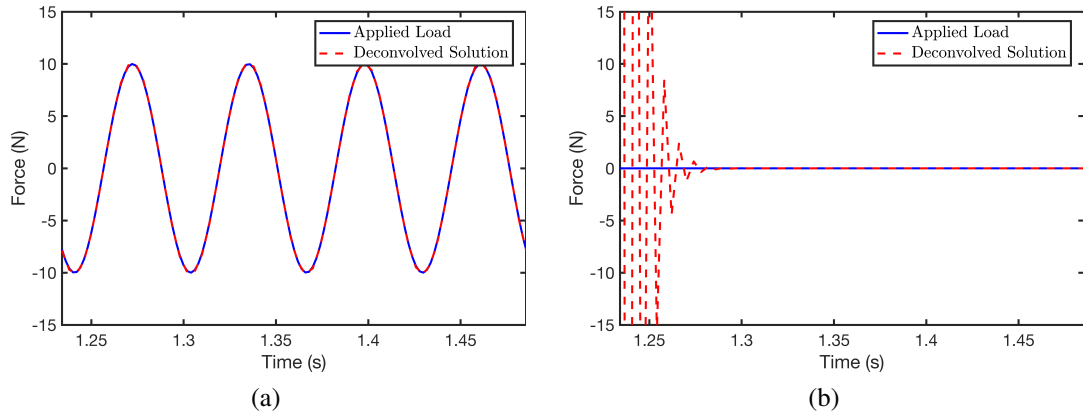


Figure 2.8: Force Reconstruction using Generalized Draper-Lee Method for sinusoidally forced system starting from rest (a) and unforced system with nonzero initial conditions (b).

As expected, the deconvolution algorithm works and the deconvolved solution exactly matches the applied load. Next, Eq. (2.111b) is solved using the same algorithm. However, due to the initial conditions, the results are not expected to be accurate. The interesting result is shown in Figure 2.8b. It seems as though the presence of the initial conditions



causes considerable error in the force reconstruction, however, the presence of this error reduces considerably in magnitude as time goes on until there is no evidence of it on the scale of interest. Therefore, deconvolution is applicable to systems with initial conditions, provided the beginning of the reconstruction is discarded.

One thing to note is that the IRF is lower band limited to the chosen segment length. The theoretical lower frequency band is computed as

$$f_{\min} = \frac{1}{t_{\max}} \quad (2.112)$$

where  $t_{\max}$  is the length of the signal in seconds. However, the realizable lower frequency (i.e. the frequency where one can realistically visualize a peak in the frequency domain) is usually about an order of magnitude higher than this. Therefore for a 100 ms segment, only frequencies above about 100 Hz are physically realizable. Therefore, any frequency content that is reconstructed lower than this realizable lower bound should be ignored.

#### 2.2.2.7 Acceleration Deconvolution

Although most of the examples in literature and in this dissertation utilize deconvolution of strain and displacement data, it should be noted that such a formulation also holds between applied force and acceleration. This work was first presented in an AIAA conference paper by Draper et al.[41].

Acceleration measurements are significantly easier to obtain than strain/displacement. For the latter, one typically needs to ensure all load can travel through the strain gages which often requires designing around these sensors. Alternatively, accelerometers need be simply placed on a surface of the body. This means that acceleration measurement is can be an afterthought which presents more design flexibility. Additionally, force measurement can theoretically be made without the need for complex strain balances. This may be

advantageous in smaller tunnels or small budget experiments.

Returning to the continuous convolution of displacement and applied force, and differentiating both sides twice yields

$$\ddot{y}(t) = \int_0^t \ddot{h}(t - \tau) u(\tau) d\tau \quad (2.113)$$

where time derivatives are represented using dots above the variables. For proof of this equation see Appendix B.3.

This is analogous to the previous study, however now the unknown is now the acceleration IRF ( $\ddot{h}(t)$ ) rather than the typical displacement/strain IRF ( $h(t)$ ). Using the constraint matrix method or generalized Draper-Lee method, one may construct the acceleration IRF and then use it to reconstruct an arbitrary applied dynamic force  $u(t)$ .

It also should be noted that all of the previously mentioned extensions to the developed methods are completely applicable to acceleration deconvolution as well.

Finally, one note should be made for extension to multiple outputs for acceleration deconvolution. It is true that if multiply acceleration measurements are made, one may utilize them all in the force reconstruction, analogously to what is done in Section 2.2.2.4 and given by Eq. (2.103). However, interestingly, the acceleration IRFs and strain/displacement IRFs can be combined to even further constrain the applied load reconstruction problem.

Such a problem looks like

$$\begin{Bmatrix} \mathbf{s}_1 \\ \mathbf{s}_2 \\ \vdots \\ \mathbf{s}_{\text{ns}} \\ \mathbf{a}_1 \\ \mathbf{a}_2 \\ \vdots \\ \mathbf{a}_{\text{na}} \end{Bmatrix} = \begin{bmatrix} \hat{\mathbf{B}}_{1,i}^s \\ \hat{\mathbf{B}}_{2,i}^s \\ \vdots \\ \hat{\mathbf{B}}_{\text{ns},i}^s \\ \hat{\mathbf{B}}_{1,i}^a \\ \hat{\mathbf{B}}_{2,i}^a \\ \vdots \\ \hat{\mathbf{B}}_{\text{na},i}^a \end{bmatrix} (\mathbf{u})_i \Delta t_s \quad (2.114)$$

where  $\mathbf{s}_j$  is a vector of discrete strain measurements from channel  $j$ ,  $\mathbf{a}_j$  is a vector of discrete acceleration measurements from channel  $j$ , the superscripts on the IRMs denote whether they are strain ( $s$ ) or acceleration ( $a$ ) IRFs, and ns and na denote the number of strain and accelerometer channels used, respectfully.

Using this, significant overdetermination the problem is achieved if acceleration measurement is made which allows for easier solution (i.e. smaller  $R_2$  parameter).

### 2.2.3 Numerical Example of TDDMs

Due to the more complex nature of these methods, begin with the more simple SISO numerical systems. This allows for concrete conclusions about each methodology without the complexity of multiple mode interaction. Experimental results are presented in the next chapter which serve as multiple output validation. An example single degree of freedom (SDOF) SISO system is given in Figure 2.9.

To be consistent with previous TDDM formulations, the output displacement and input force have been assigned the variables  $y(t)$  and  $u(t)$ , respectively. Assuming constant mass, stiffness, and damping values (i.e.  $m$ ,  $k$ , and  $c$ ) this system is subject to the differential

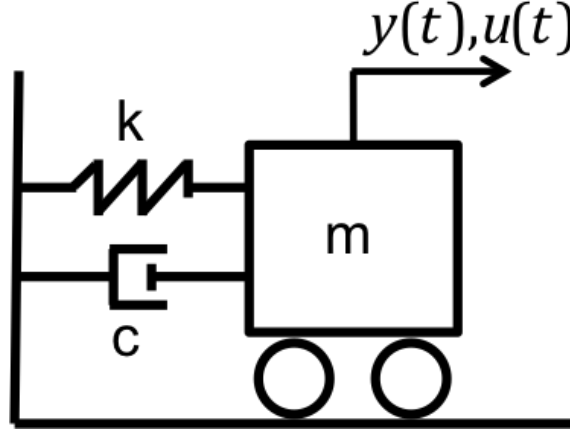


Figure 2.9: SDOF spring mass damper system.

equation

$$m\ddot{y} + c\dot{y} + ky = u(t) \quad (2.115)$$

where  $m = 1$  kg,  $k = 1000$  N/m, and  $c = 0.6325$  Ns/m. Additionally, the analytical IRF can be solved as

$$h(t) = \frac{1}{m\omega_d} \exp^{-\sigma t} \sin \omega_d t \quad (2.116)$$

where

$$\omega_d = \omega_n \sqrt{1 - \zeta^2} \quad (2.117a)$$

$$\sigma = \zeta \omega_n \quad (2.117b)$$

and  $\omega_n = \sqrt{k/m}$ , the natural frequency and  $\zeta = c/(2m\omega_n)$ , the critical damping factor.

For the TDDMs derived in this chapter, the selection of the input calibration force (i.e. the force measured when constructing the IRF) is arbitrary. However, the standard TDDM requires a hammer pulse calibration force. Furthermore, this load is easy to measure using an instrumented impulse hammer. Therefore, in these numerical studies, the chosen

calibration force is

$$F(t) = u(t) = \frac{b}{a\sqrt{\pi}} \exp^{-\left(\frac{t-0.5\varepsilon}{a}\right)^2}, \quad (2.118)$$

where  $a = 5 \cdot 10^{-4}$  controls the pulse width,  $b = \frac{1}{60}$  is a scaling constant used to select a desired area (and consequently peak magnitude), and  $\varepsilon$  is the pulse width used to shift the pulse from the  $t = 0$  axis. This simulates a steep hammer impulse force with an approximate width of 2 ms and height of 20 N.

Finally, to further replicate experimental studies, Gaussian numerical noise is added to the output data. This additive noise is defined as

$$\varepsilon = \frac{\sigma(\mathbf{y}_e)}{\text{SNR}} \mathbf{randn} \quad (2.119)$$

where  $\sigma(\cdot)$  is the standard deviation operator of the vector of interest,  $\mathbf{y}_e$  is the calculated exact output,  $\varepsilon$  is a vector of noise values to be added to  $\mathbf{y}_c$ , **randn** is a vector of points selected from a Gaussian distribution with a standard deviation equal to one, and SNR is the Signal to Noise Ratio defined as

$$\text{SNR} = \frac{\sigma(\mathbf{y}_e)}{\sigma(\mathbf{randn})_{\text{desired}}}. \quad (2.120)$$

Defining noise in this manner allows the user to supply unbiased noise to the "measured" signal as  $\mathbf{y} = \mathbf{y}_e + \varepsilon$  at a desired SNR.

### 2.2.3.1 SISO Example of the CMM

Begin with the validation of the Constraint Matrix Method derived in Section 2.2.2.1. This method is used to demonstrate some of the  $R_1$  and  $R_2$  parameters. However, as noted, this method is equivalent to the linear Draper-Lee Method.

Applying the approach discussed in Subsection 2.2.2.1, the impulse response was ob-

tained using a sampling frequency of 4 kHz and compared with the analytical solution as shown in Figure 2.10.

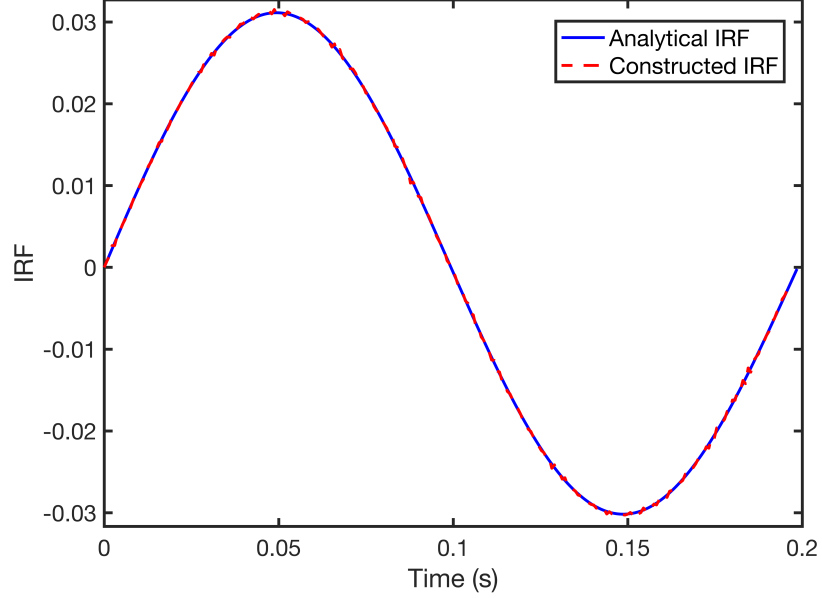


Figure 2.10: Comparison of Analytical and Constructed IRF using  $R_1 = 3$ , sampling frequency of 4 kHz, and SNR of 150.

The sampling frequency (4 kHz) is much higher than the natural frequency of the system (5 Hz). Therefore, applying the linear constraint on the IRF vector will have minimal effect on the IRF construction accuracy. Such a separation between sampling and natural frequency is not required but the former will dictate the bandwidth of the constructed IRF. If one considers a MDOF system with many natural frequencies, using a low sampling frequency may truncate important natural frequency contributions. However, for this simple SDOF case, this is not a concern. Overall, one may observe excellent IRF construction accuracy.

After this impulse response was obtained, more points were inserted into the IRF using linear interpolation to match the sampling frequency. The IRF was then used to solve Eq. (2.61) with a recorded output. To evaluate this, the numerically obtained  $y(t)$  corresponding to the applied force in Eq. (2.118) is used. The result of this force reconstruction

can be seen in Figure 2.11a. For this simulation,  $R_1 = R_2 = 3$ . Note that the only input information used in our reconstruction is displayed using the triangles. The smoothness of the actual input is plotted with a smooth curve, however, none of this information is available.

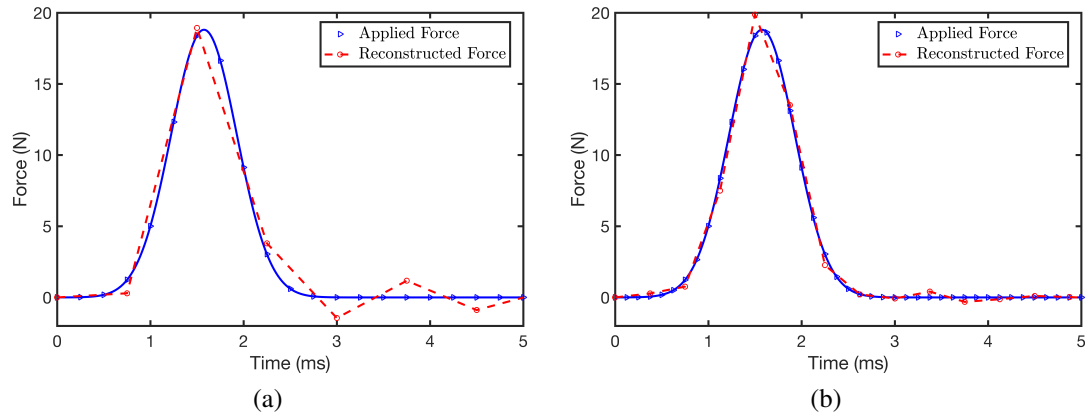


Figure 2.11: Hammer Pulse Force Reconstruction for a SDOF System using  $R_1 = R_2 = 3$  and  $\text{SNR} = 150$  with a sampling rate of 4 kHz (a) and 8 kHz (b)

Inadequate pulse resolution is observed. Furthermore, significant oscillations are observed after the pulse. However, the overall shape of the applied load is well recovered. If more resolution were available, the solution may be improved. For the 4 kHz case, there are approximately three data points in the reconstructed pulse; any less and the pulse may be underrepresented. To get sufficient resolution one may use a higher sampling frequency. Doubling the sampling frequency of the generated data and applying this method to this data set yields the result presented in Figure 2.11b. For this analysis,  $R_1 = R_2 = 3$ . As expected, by doubling the sampling frequency and maintaining  $R_2$ , better pulse resolution is achieved. Note that errors are still present in the reconstructed input. For this noisy SDOF case, this level of discrepancy is deemed acceptable.

This reconstruction also works on other loads, e.g. sinusoids, that were not used in the calibration. This same IRF was deconvolved with the output to a 100 Hz sinusoidal

input. The results of this reconstruction are shown in Figure 2.12. Once again, accurate reconstruction is achieved. Note that there exists slight discrepancy, however, the magni-

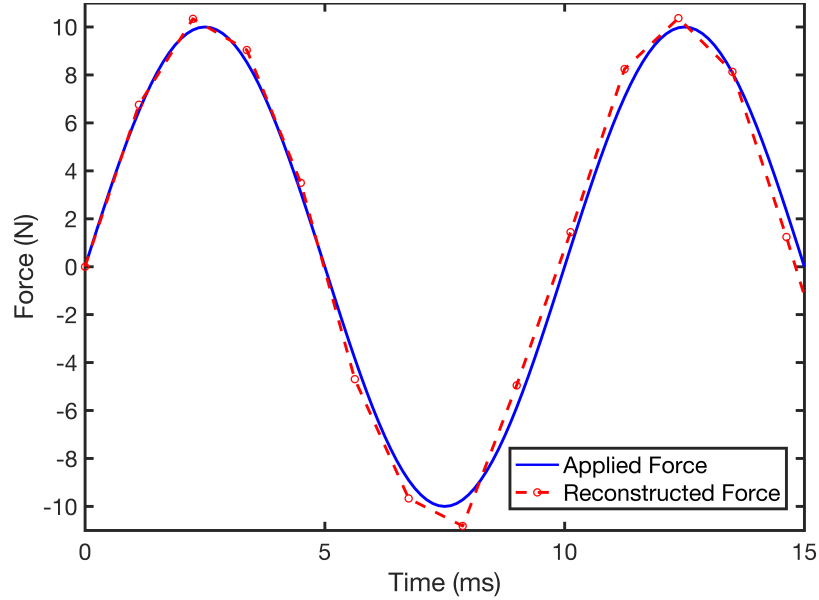


Figure 2.12: Reconstruction of Sinusoidal Forcing for a SDOF System with  $R_1 = 3$  and  $R_2 = 9$ , a sampling rate of 8 kHz, and  $\text{SNR} = 150$ .

tude and frequency recovery are excellent. For this analysis the higher sampling frequency (8 kHz) and  $R_2 = 9$  were used. In this case a higher  $R_2$  value is used since the resolution requirements are lower.

### 2.2.3.2 SISO Example of the GDLM

The Generalized Draper-Lee Method has similar conclusions to the Constraint Matrix Method. However, the ability to construct smooth signals is possible. For this investigation, the linear and cubic are compared for IRF construction and applied input force reconstruction accuracy. However, it is somewhat unfair to compare the methods using the same  $R_1$  and  $R_2$  parameters. For the cubic method, twice as many unknowns are assigned per node.



Therefore the term

$$\hat{R}_1 = \frac{L}{L_h} \quad (2.121)$$

is defined where  $L$  is the length of the measured output vector and  $L_h$  is the new length of the IRF to be solved. One may note that  $\hat{R}_1 = R_1$  for the linear case and  $\hat{R}_1 = 2R_1$  for the cubic case as there are twice as many unknowns.

Similarly,

$$\hat{R}_2 = \frac{L}{L_u} \quad (2.122)$$

is defined where  $L$  is the length of the measured output vector and  $L_u$  is the new length of the applied force to be solved.

Applying the approaches discussed in Section 2.2.2.2 with a known load given by Eq. (2.118), the IRF was obtained and compared with the analytical solution as shown in Figure 2.13. Note that a sampling rate of 250 Hz and a signal to noise ratio (SNR) of 25

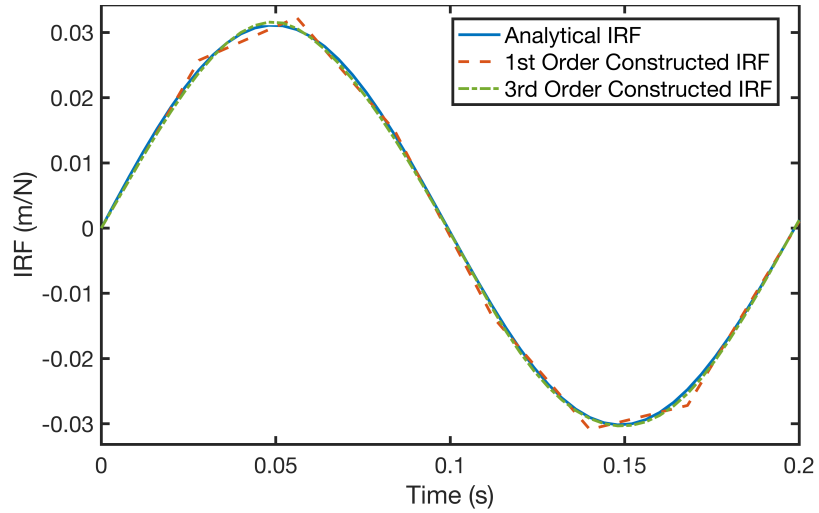


Figure 2.13: SDOF IRF construction using proposed method with first (red) and third (green) order IRF construction. A sampling rate of 250 Hz and a constraint parameter,  $\hat{R}_1 = 7$  were utilized for this demonstration.

(standard deviation of the output divided by standard deviation of the noise) was used for this analysis. However, the noise was determined to have little effect as compared to the

noiseless case.

From the results displayed in Figure 2.13, one may see that the desired result is obtained. For this low sampling rate and high  $\hat{R}_1$  case, poor resolution is obtained on the IRF construction for the linear case. However, when a third order formulation is utilized, the result more accurately approximates the exact IRF and results in a smooth curve (continuous and differentiable).

This method is also applicable when a smooth input is of interest (e.g. hammer pulse). Evaluating Eq. (2.51) for the cubic case the result shown in Figure 2.14 is obtained. Note that a low sampling frequency was chosen to highlight the advantages of the cubic formulation.

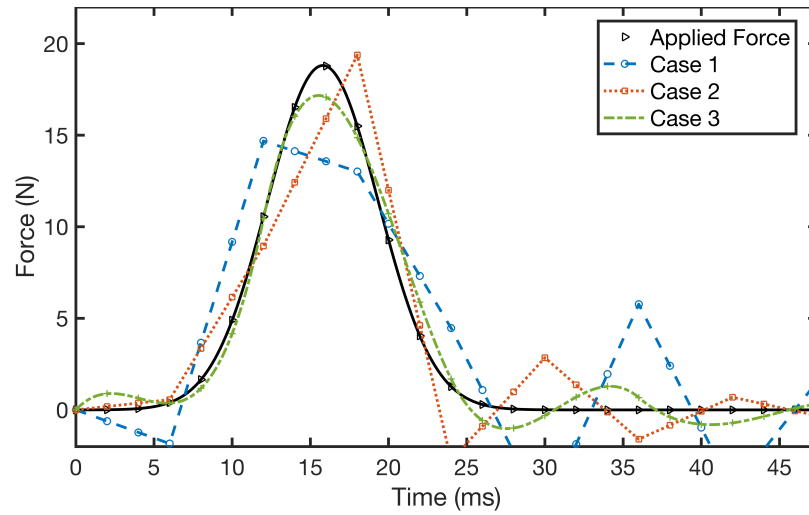


Figure 2.14: SDOF input force reconstruction using time domain deconvolution method with first (Case 1) and third (Case 3) order formulation. An additional case was presented where the IRF values from the third order IRF were used in conjunction with the first order method to reconstruct the applied load (Case 2). A sampling rate of 500 Hz, SNR of 25, and constraint parameters,  $\hat{R}_1 = \hat{R}_2 = 3$  were utilized for this demonstration.

In case 1, linear interpolation is assumed for both the construction of the IRF and the reconstruction of the applied force. In case 2, cubic interpolation is assumed for the IRF while linear interpolation is used for the reconstructed force. In case 3, cubic interpolation

is used for both the IRF construction and applied force reconstruction. The result for case 2 demonstrates that there is some benefit just from approximating a more accurate IRF.

### 2.2.3.3 Noise Discussion

Additionally, it would be prudent to investigate the effects of noise on this process. For these studies, the Constraint Matrix Method will be utilized. To observe the effects of noise, the constructed IRF for various SNRs is plotted in Figure 2.15a. However, an objective comparison is of interest. Therefore, the error metric

$$\epsilon = \frac{1}{N} |h_{\text{exact}} - h_{\text{rec}}|^2 \quad (2.123)$$

is used to compare the accuracy of the IRF for various SNR levels. This metric is also plotted versus  $R_1$  to see the effect of the constraint parameter on accuracy. This is shown in Figure 2.15b.

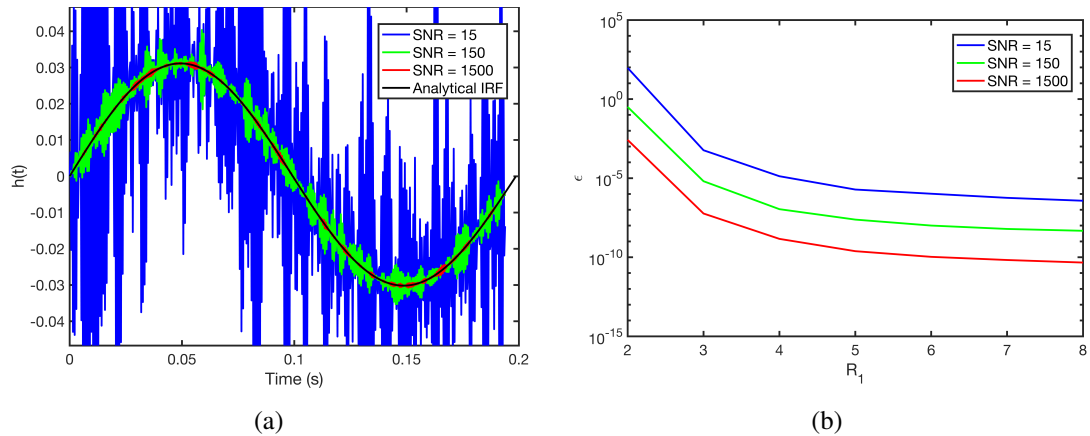


Figure 2.15: IRF constructions for various SNR values using  $R_1 = 3$  (a) and the error between analytical and constructed IRF for various SNR and  $R_1$  values (b).

As SNR increases, our construction tends to the analytical IRF. From Figure 2.15b, it is evident that the IRF construction is uniformly affected by the noise level. The error for a

particular  $R_1$  value tends to drop two orders of magnitude for every one order of magnitude increase in SNR. If a particular error level is desired, one may use either a higher  $R_1$  or SNR. Typically, one is constrained to a particular SNR and the constraint parameter must be altered instead.

This method performs well on a SDOF system, reconstructing a host of dynamic loading scenarios. The accuracy for a given ratio degrades as the SNR is decreased. As always, low noise measurements are still desirable. Note that the SDOF case is the worst case scenario. For a system with multiple outputs, more constraints can be introduced to the problem.

#### 2.2.3.4 Conventional Method Comparison

Thusfar, an in depth analysis of the two TDDMs developed in this chapter have been presented. However, it would be useful to compare these methods to the conventional TDDM described in Section 2.2.1. Begin with the IRF construction for a case with SNR=25. As discussed, the conventional method simply scales the measured output by the area under the supplied pulse. The result can be seen in Figure 2.16. As expected, all noise present in the measured output is present in the constructed IRF. This is exactly the undesirable outcome and is why solution of the IRF was performed. Clearly the GDLM better rejects the noise and more accurately constructs the IRF.

Although the IRF is important, it is an intermediate step in solving for the input force. Therefore, the input force reconstruction accuracies of each method are compared. In order to compare the reconstruction accuracy of the three methods, the following error metrics are considered:

$$AD = \left| 1 - \frac{\int_0^\epsilon f_{\text{rec}}(t) dt}{\int_0^\epsilon f_{\text{app}}(t) dt} \right| \cdot 100\% \quad (2.124)$$

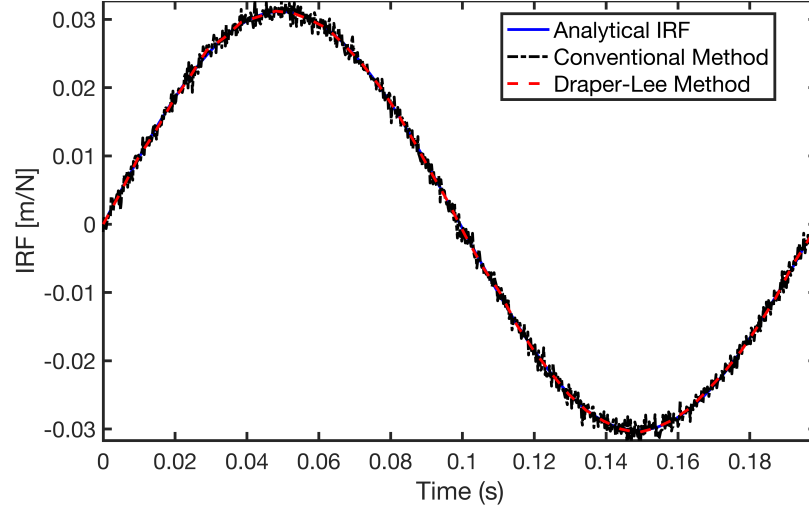


Figure 2.16: SDOF IRF construction using conventional method and third order Draper-Lee method with  $\hat{R}_1 = 12$  and  $\text{SNR}=25$ .

$$\text{PD} = \left| 1 - \frac{\max |f_{\text{rec}}(t)|}{\max |f_{\text{app}}(t)|} \right| \cdot 100\% \quad (2.125)$$

where AD and PD stand for Area Difference and Peak Difference, respectively. The symbols  $f_{\text{app}}(t)$  and  $f_{\text{rec}}(t)$  represent the discrete applied and reconstructed force, respectively. Finally,  $\varepsilon$  is the time width of the specific impulse under investigation; selected to be the location where the magnitude of the pulse drops below an arbitrarily chosen low value of 0.001 N. Note that for the cubic method, a smooth function is assumed and the area and maximum is computed exactly. For the first order and conventional methods, trapezoidal integration is used. These errors versus SNR are presented in Figure 2.17.

In these figures, it is clear that the proposed methods tend to outperform the conventional method. In some cases, this conventional method is better, however, the proposed methods more consistently reconstruct the applied pulse as displayed by the smaller bands of variation in the PD and AD plots. It is of course possible that the conventional method results could be improved with a different selection of the regularization parameter. However, it is not our intention to optimize this method but rather compare our methods to a

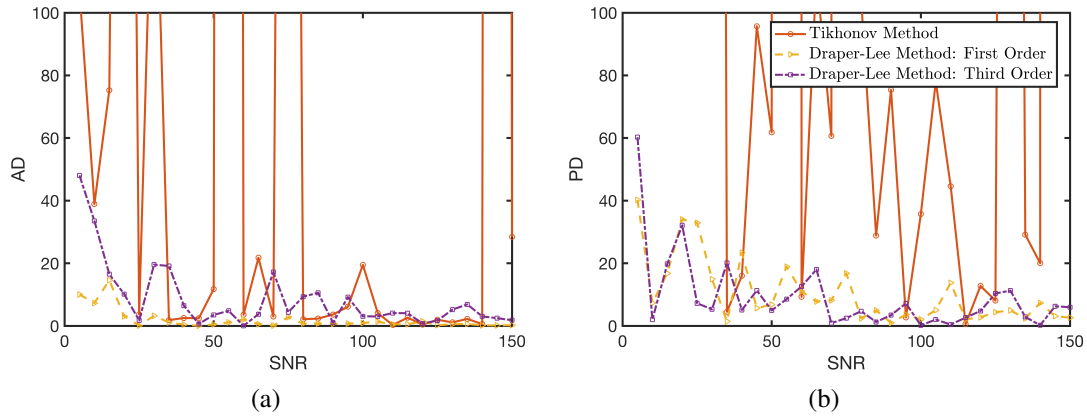


Figure 2.17: Area (a) and peak (b) differences versus SNR for conventional method and proposed first and third order methods. A sampling rate of 500 Hz and constraint parameters,  $\hat{R}_1 = \hat{R}_2 = 6$  were utilized for this demonstration.

conventional implementation (i.e. parameter selection via L-Curve).

Additionally, the results for our methods have all used the same parameter (i.e.  $\hat{R}_1 = \hat{R}_2 = 6$ ). It is possible that a more optimal parameter is present for each method at each SNR level. Automated determination of optimal parameters is a topic of future research.

### 2.2.3.5 SIMO Example of GDLM

In this section, the single-input-multiple-output extension of the GDLM is validated. This formulation is given in Section 2.2.2.4. Again consider a spring-mass-damper numerical system as was discussed at the beginning of Section 2.2.3. However, in this analysis, many of these SDOF systems are linked together as is done in Section 2.1.3.

As is stated in this section, each input-output pair have a unique IRF. Therefore, Eq. (2.102) is solved  $n$  times where  $p$  is the number of input locations and  $n$  is the number of output locations. Since this IRF construction was validated in Section 2.2.3.2, it is omitted in this section.

All constructed IRFs are needed to reconstruct a particular input location. This rela-

tionship is given in Eq. (2.103). For this analysis, consider a 10 DOF lumped mass system (i.e.  $n_{\max} = 10$ ) and an input location of 3 (i.e.  $i = 3$ ). This means the applied impulsive load is applied to the third mass. This location was arbitrarily chosen. Similar results are obtained at other input locations. A sampling frequency of 5 kHz was used. Additionally, the applied impulsive force is given by Eq. (2.118) with  $a = 10^{-3}$  and  $b = \frac{1}{30}$ . This generates a smooth pulse with a width of 6 ms and a height of 19 N. An SNR of 150 is chosen for this analysis. This is higher than in some of the previous studies due to the nature of the displacement. Because of the inertia of the connected masses, all displacements are positive for the time frame of interest. This results in a very large standard deviation of the output (i.e. the numerator of Eq. (2.120)). In order to avoid unrealistically high noise levels, the higher SNR was chosen.

In a real system, there are infinite DOFs and it is impossible to measure the displacement at each location. To simulate this, restrict output measurement to only the odd DOFs. The input force reconstruction and applied load can be seen in Figure 2.18 for the SIMO case. Clearly this method has done an excellent job of reconstructing the applied force.

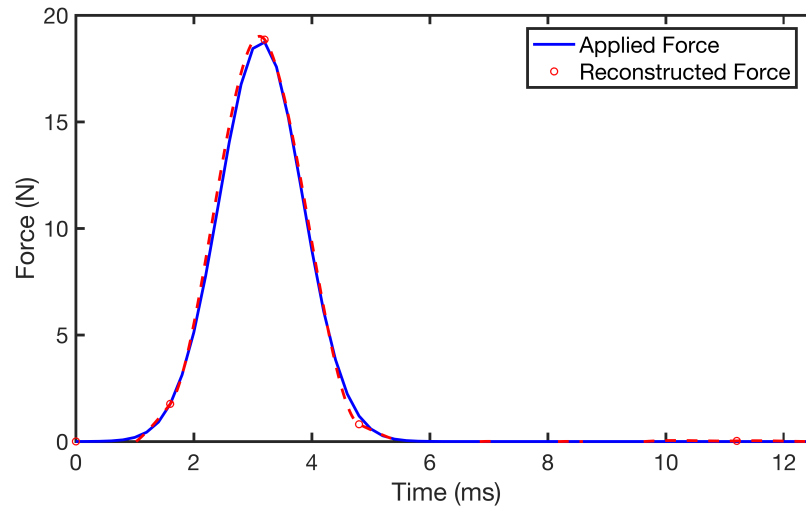


Figure 2.18: SIMO force reconstruction using ten DOF lumped mass system. SNR = 150,  $\hat{R}_1 = \hat{R}_2 = 4$ ,  $f_s = 5$  kHz, and the cubic GDLM were used in this analysis.

The reconstruction shows very little deviation from the applied load.

It may also be interesting to see the effect of the number of output DOFs on the reconstruction accuracy. To investigate this,  $n$  is varied from 1 to  $n_{\max}$  to see if any improvement on the accuracy is observed. There may be some correlation between the output location chosen with respect to the applied load. Therefore, to reduce this bias, the output locations are chosen randomly. Repeated investigations with different positions yielded characteristically similar results.

Again, Eqs. (2.124) and (2.125) are used to determine the area and peak difference, respectively. These error metrics versus the number of output DOFs used can be seen in Figure 2.19. A small increase in accuracy is seen as the number of outputs increases. This

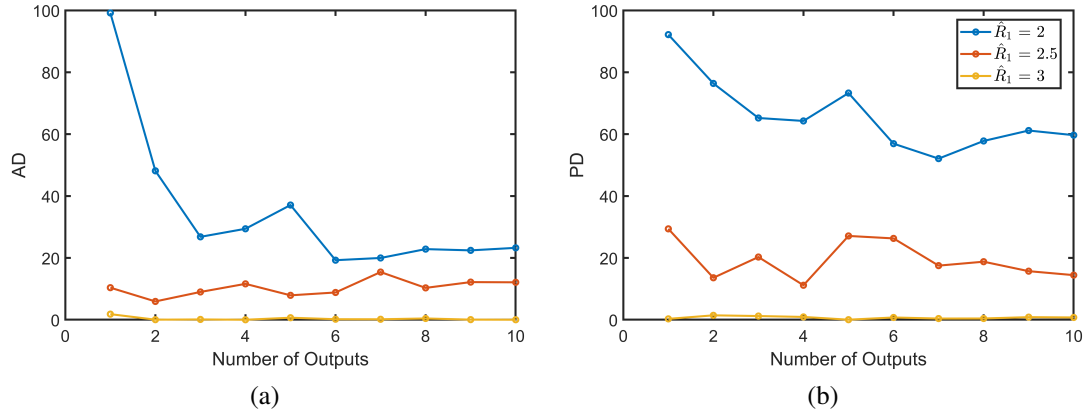


Figure 2.19: Area (a) and peak (b) differences versus number of outputs for SIMO cubic GDLM. A sampling rate of 5 kHz and constraint parameters, and varying  $\hat{R}_1 = \hat{R}_2$  were utilized for this demonstration.

shows that increased accuracy is possible simply by recording additional information (i.e. measuring more outputs).

Additionally, the constraint parameter is altered. One can see for more drastic improvements in accuracy, an increase in this parameter is still required. For the appropriate choice of  $\hat{R}_1$  and  $\hat{R}_2$ , the use of more outputs provides negligible improvement. The effect of increasing the number of outputs are more prevalent in the MIMO example.



### 2.2.3.6 MIMO Example of GDLM

In some scenarios, it may be possible for two forces to be applied simultaneously. In such scenarios, a MIMO approach is required. The SIMO approach assumes that a response is called by only a single input and therefore will not be applicable in these multi-load cases. In this case, the MIMO formulation presented in Section 2.2.2.4 is utilized. As in the SIMO formulation, each input-output pair has a unique IRF that can be computed using Eq. (2.102). Solving this equation  $pn$  times and assembling results in the IRM shown in Eq. (2.105). Note that after solving for the vector of applied forces, one needs to segment the result to obtain each applied load (as they are stacked).

For convenience, the same numerical system discussed in Section 2.2.3.5 is utilized. However, in this study, the responses to inputs at multiple locations are collected. Additionally, to better constrain the problem, all 10 DoFs are used. Lastly, multiple impulses are simultaneously applied to see how effectively the method can reconstruct each pulse. For this study,  $p = 4$ , meaning four input locations are chosen. Additionally, for the reconstruction, simultaneous impulses are supplied at three of the locations at slightly varying magnitudes. Therefore, one output is expected to be zero. The result of this study is shown in Figure 2.20.

Interestingly, this method is able to reconstruct the pulses at each location while reconstructing a zero applied load at the unloaded node (i.e. node 5). This validates that this method is capable of reconstructing simultaneous load application as well as showing when approximately no load is applied.

As in the SIMO case study, it may be interesting to investigate the effect of increasing output DOFs on the accuracy of the reconstruction. Again consider the system described above except vary the number of outputs used in the reconstruction as well as the constraint parameters. Note that since the accuracy of multiple input locations is of interest, a new set

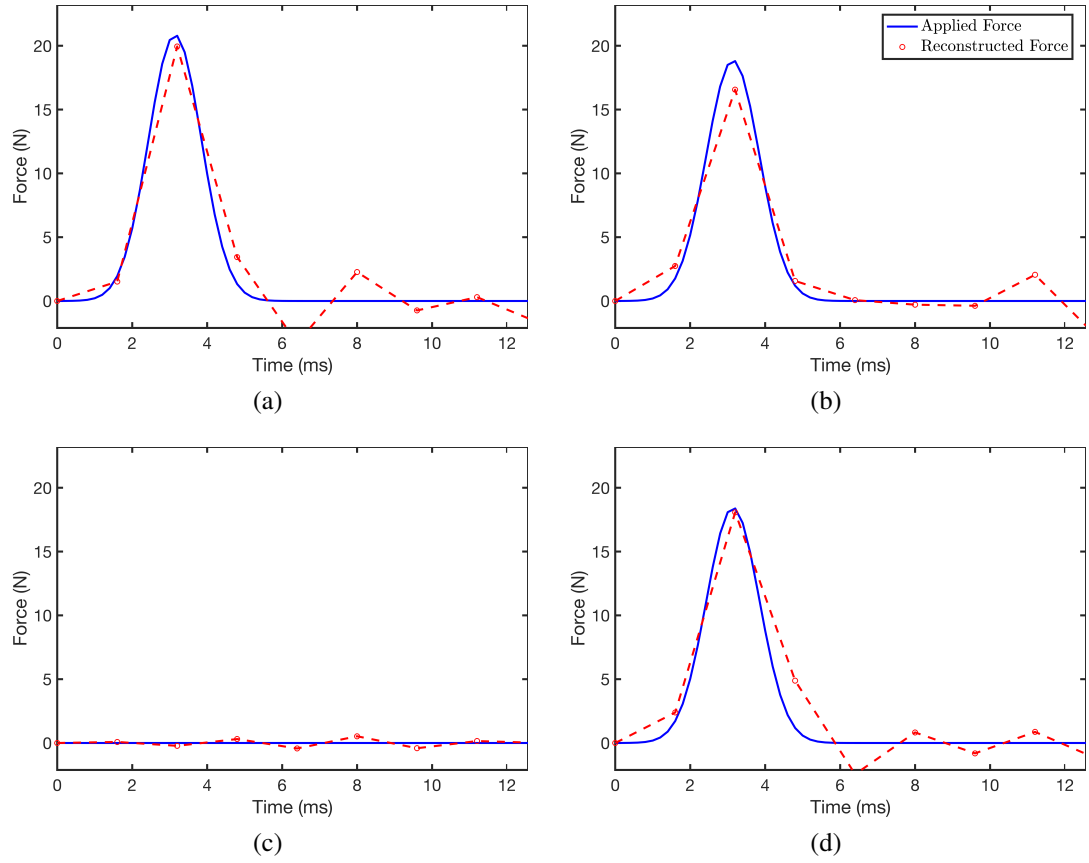


Figure 2.20: MIMO hammer pulse reconstruction for 10 DoF system. Applied force reconstruction at input nodes 1 (a), 3 (b), 5 (c), and 9 (d) are all shown. The linear GDLM,  $R_1 = R_2 = 8$ ,  $\text{SNR} = 150$ , and  $f_s = 5$  kHz were used for this study.

of error metrics are considered. These are defined as

$$\overline{\text{AD}} = \frac{1}{P_a} \sum_{i=1}^{P_a} \text{AD}_i \quad (2.126)$$

$$\overline{\text{PD}} = \frac{1}{P_a} \sum_{i=1}^{P_a} \text{PD}_i \quad (2.127)$$

where  $P_a$  is the number of locations where a force was applied. Therefore the accuracy of the zero load location is not considered. For the example case depicted in Figure 2.20,  $P_a = 3$ . For each of these locations, the area and peak difference are computed using

Eqs. (2.124) and (2.125), respectively and then the results are averaged. The resultant values for varying number of outputs (again chosen randomly) and constraint parameters is shown in Figure 2.21.

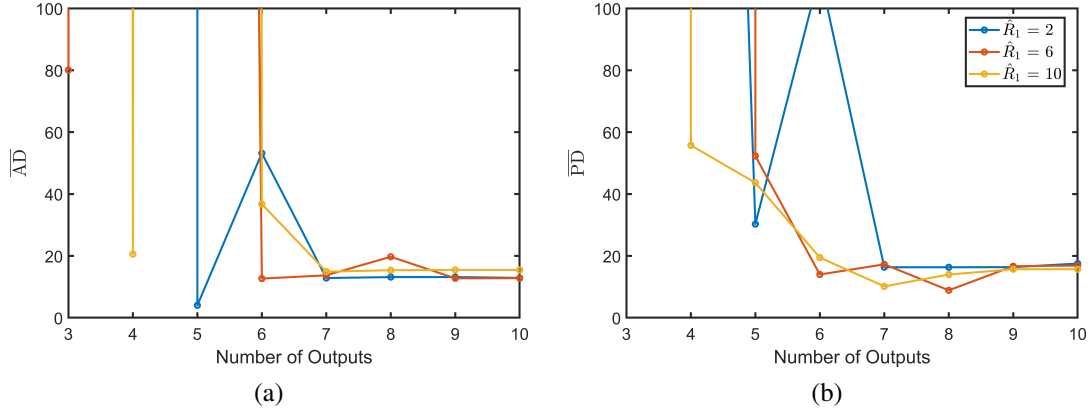


Figure 2.21: Average area (a) and peak (b) differences versus number of outputs for MIMO linear GDLM. A sampling rate of 5 kHz and constraint parameters, and varying  $\hat{R}_1 = \hat{R}_2$  were utilized for this demonstration.

As expected, increasing the number of outputs has a profound impact on the reconstruction accuracy. In fact, no noticeable trend can be seen by increasing the constrain parameter as was the case in the SIMO case. Increasing the number of outputs a bit beyond the number of inputs tends to yield the best result. A further increase of the number of outputs or constraint parameter value tends to have negligible effect on the accuracy. As predicted in the SIMO case study, the increase of number of outputs will have a much more profound impact on the accuracy of the MIMO reconstructions.

### 2.2.3.7 Averaging of Calibration Sets

Before validating this method, a discussion of the overfitting problem is discussed. When solving for the unknowns of a system, it is important to not over fit the results. This is a problem in many system identification investigations. For example, if trying to fit the

frequency response function of a signal, one might use 1000+ frequencies to do so. This may exactly match the Fourier transform result, but it will not be representative of the dynamics of the system as many of those peaks are likely from noise. A similarly spirited phenomenon can happen in this process.

Consider a SISO system subjected to a hammer pulse. Gaussian noise is added on top of the measured displacement data to simulate experimental noise. One of the TDDMs is then evaluated to obtain an IRF relating the noisy strain signal and input hammer force (also measured). Next, that IRF is utilized in conjunction with that same output response to solve for the calibration input. In this problem, the impulse should be replicated with great accuracy as the IRF has fit all the noise properties of the output signal. In reviewing Figure 2.22, this is exactly what happens. The IRF does not at all match the analytical IRF and yet this excessively over fit IRF still succeeds at reconstructing the impulse.

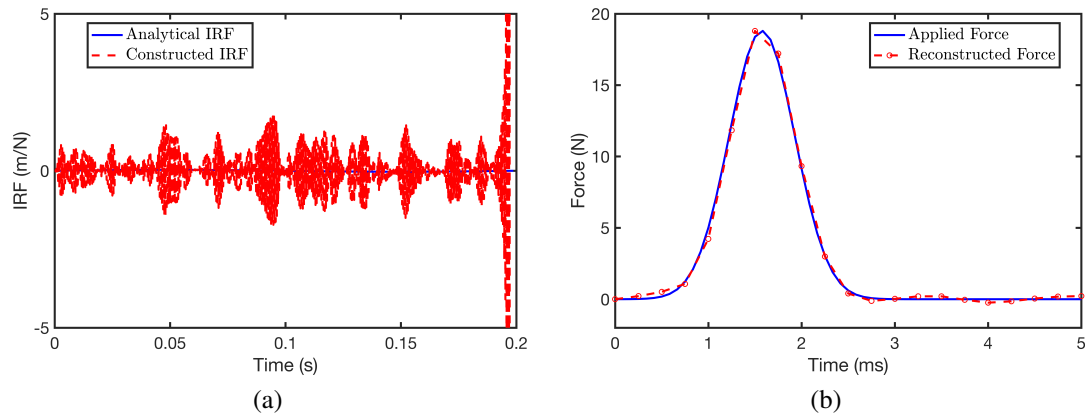


Figure 2.22: Constructed IRF (a) and Reconstructed applied force (b) using  $R_1 = R_2 = 3$  and the constraint matrix method.

This process fails, however, when trying to apply this erroneous IRF to other signals with slightly different noise. For example, consider an applied sinusoidal force on a SISO system. Once again, Gaussian noise is added on top of the displacement response and use this in conjunction with the constraint matrix method to reconstruct the sinusoidal

applied load. This can be seen in Figure 2.23. Although the overall shape of the sine

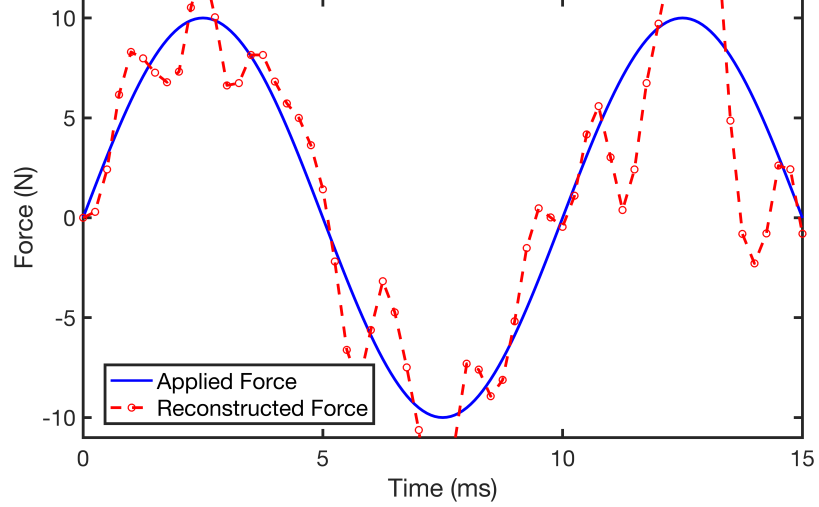


Figure 2.23: Sine force reconstruction using an over fit IRF and  $R_1 = R_2 = 3$  in the constraint matrix method.

wave is accurately captured, the noise that is modeled in the IRF causes large errors in the reconstruction. Clearly, the IRF is incorrect which propagates error onto reconstructions of other dynamic loads.

To reduce the effects of this, as discussed in the previous sections, multiple datasets are averaged in the formation of the IRF. To investigate the effects of this averaging, numerical studies are performed with this same SDOF system. To draw meaningful conclusions, the sampling rate, system parameters (i.e. mass, damping, stiffness), and noise level are fixed across all tests. To maintain similarity to real experiments, the pulse width and magnitude are varied with  $\pm 5\%$  variation. Additionally, the additive noise will be regenerated for every test. The independent variable is the number of repeat tests. However a metric to compare various experiments is needed.

To compare various repeat tests, two metrics: the condition number of matrix  $\hat{\mathbf{A}}^T \hat{\mathbf{A}}$  (i.e. the matrix being inverted from Eq. (2.51)) and the error between the analytical IRF and the reconstructed one are considered. The condition number is often used to display the

severity of the problem. Additionally, a reduction in the condition number often signifies a better solution. However, this is not guaranteed. The error is computed using Eq. (2.123), the sum square difference between the analytical and the constructed IRFs. These metrics are shown in Figure 2.24. Three different constraint ratios are also shown for comparison.

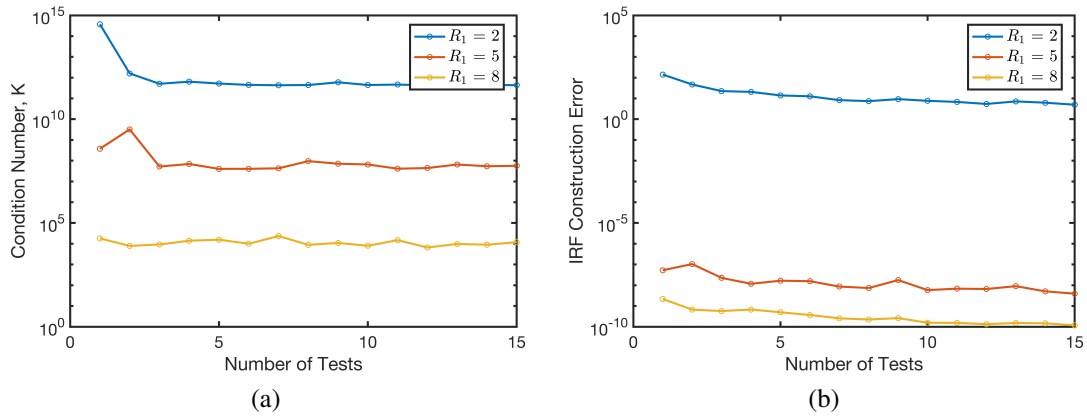


Figure 2.24: Condition number of  $\hat{\mathbf{A}}^T \hat{\mathbf{A}}$  (a) and IRF construction error (b) versus number of calibration tests used. The CMM was used for this analysis.

It appears as if using two tests in the IRF reconstruction improves the condition number of the inversion by two to four orders of magnitude. Additional repeat tests have minimal effects in improving the condition number. Two or three repeat tests have the greatest reduction of the error. Beyond this number of tests, minimal improvement is observed. Therefore, one is lead to conclude that two or three repeat tests is sufficient. For drastic changes in condition number or IRF accuracy beyond two or three repeat tests, a larger constraint parameter,  $R_1$ , is still required.

It is important to note that this is a very simplified study. For real systems, many significant modes of vibration are present. The excitation of these modes is largely depended on the applied load that is used. Therefore, the user could purposely use various pulse widths to intentionally excite various modes of vibration. For example, the tester may use a harder hammer tip to excite higher frequency modes. The averaging of all of these experiments

could result in even more significant improvements. This will be explored in subsequent chapters.

### 2.2.3.8 Segmentation

In this section, the segmentation of TDDMs is validated for use on long time histories. Although this is not as relevant for short duration loads such as hammer pulses, it may prove very useful in the reconstruction of persistent loading such as ramps or sinusoids. To maintain consistency with previous examples, the same numerical system described in the beginning of Section 2.2.3 is used. However, now the desired applied force is

$$u(t) = 10 \sin(2\pi 100t) \quad (2.128)$$

a 100 Hz sinusoidal load. The reconstruction of this force using the standard and segmented method is shown in Figure 2.25.

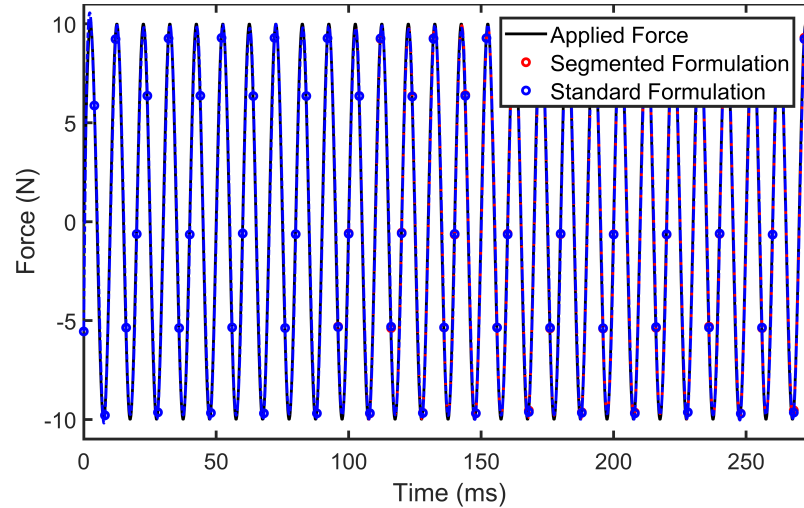


Figure 2.25: Sinusoidal force reconstruction using original (blue) and segmented (red) methods.  $R_1 = R_2 = 10$ ,  $olp = 25$ ,  $SNR = 150$ ,  $f_s = 5$  kHz, and three segments were used for this demonstration

For this study, it is clear that the segmented approach performs as well as the original

method. Only small deviation is seen towards the end of the signal and it is difficult to discern the difference. Note that for this investigation our normalized constraint parameters were 10, the first 25% of each segment was overlapped ( $olp = 25$ ) for the serial approach, and three segments were used over this entire time history.

As it is difficult to discern a difference by simply looking at the reconstruction, we've chosen two metrics. The first is the computation time of each method. The segmented method is expected to far outperform the original as data length increases. The second is the sum square of the error, i.e.

$$\epsilon = \frac{1}{N} \sum_{i=1}^L |u_{app,i} - u_{rec,i}|^2 \quad (2.129)$$

similar to Eq. (2.123) except now the applied force reconstruction accuracy is of interest.

The data length is increased to observe the affect on these two metrics. This is shown in Figure 2.26 where the data length is displayed as multiples of number of segments. As

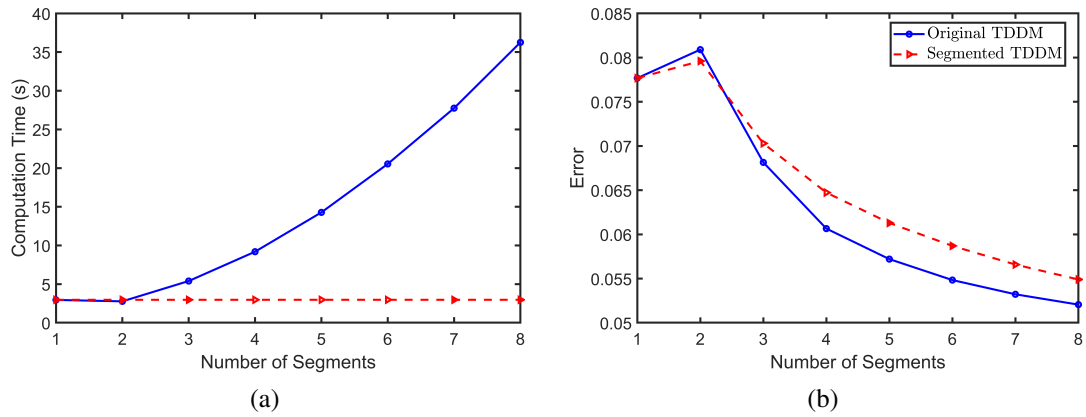


Figure 2.26: Computation time (a) and sum square sinusoidal force reconstruction error (b) versus length of output

shown in Figure 2.26a, a significant improvement in computation time as the data length increases is observed. For a signal that is eight times as long as the original signal, the segmented approach reconstructs it with negligible increase in computation time. Addi-



tionally, the sum square error, depicted in Figure 2.26b, displays that the error is comparable for both methods. Clearly significant computation time reduction is achieved without sacrificing much reconstruction accuracy.

### 2.2.3.9 Acceleration Deconvolution

Deconvolution of acceleration data is also possible. This section presents a brief numerical example of acceleration deconvolution on a SISO spring-mass-damper system. The GDLM is used but similar conclusions are observed for the CMM.

Begin by returning to the SISO numerical system presented in Section 2.2.3. To obtain the analytical acceleration IRF, Eq. (2.116) is differentiated twice with respect to time to obtain

$$\ddot{h}(t) = \frac{1}{m\omega_d} \exp^{-\sigma t} [(\sigma^2 - \omega_d^2) \sin \omega_d t - 2\sigma\omega_d \cos \omega_d t]. \quad (2.130)$$

Note that  $\ddot{h}(0) \neq 0$ . Therefore, the initial condition used in the previous formulation (i.e.  $h(0) = 0$ ) should no longer be used.

Using the third order GDLM on the acceleration response of the SDOF numerical system, the IRF construction and pulse force reconstruction shown in Figure 2.27 are obtained. A few interesting observations can be made from this figure. First, the reconstruction exhibits a large error at the beginning of the IRF construction. This error is consistent across all example cases performed. Even after applying the initial condition of

$$\ddot{h}(0) = -\frac{2\sigma}{m} \quad (2.131)$$

this start up error is still observed. It should be noted that this initial condition could not be obtained for an experimental system.

Despite this error in the IRF, the pulse is still reconstructed with high accuracy, as is

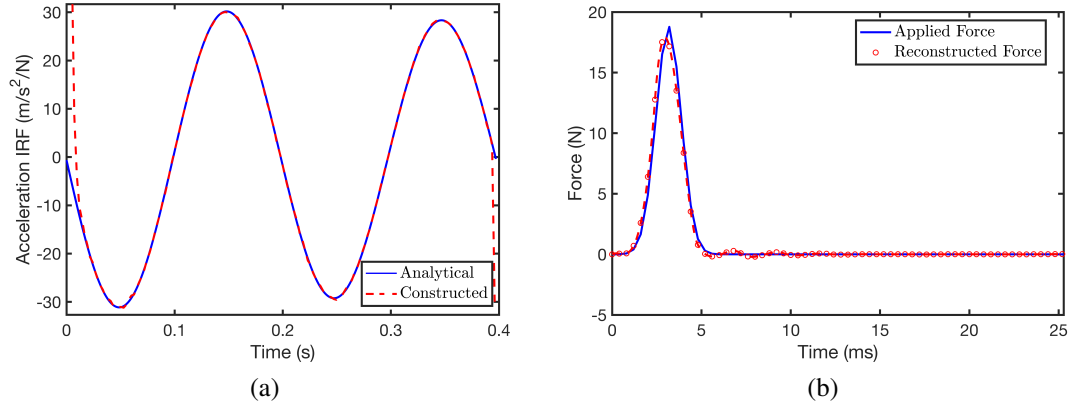


Figure 2.27: IRF construction (a) and pulse force reconstruction (b) for acceleration deconvolution SISO example.  $\hat{R}_1 = \hat{R}_2 = 3$ ,  $f_s = 2500$  Hz, and  $\text{SNR} = 150$  used for this example.

depicted in Figure 2.27b. Further research is required to determine the origin of this error in the IRF construction.

Next it may be of interest to compare the displacement-only, acceleration-only, and combined acceleration-displacement deconvolution approaches. To do this, the IRF and acceleration IRF of the SISO system are computed using a known applied pulse force. Then each IRF is used separately to reconstruct a new pulse force. Lastly, the acceleration and displacement signals are combined and used with Eq. (2.114) to reconstruct the new load. The result is shown in Figure 2.28.

Interestingly, the acceleration-only and combined acceleration-displacement deconvolution far outperform the displacement-only deconvolution. All methods perform well with no added noise. Therefore, the presence of noise appears to be more detrimental to the displacement deconvolution than acceleration. Future studies should be performed to determine the cause of this difference.

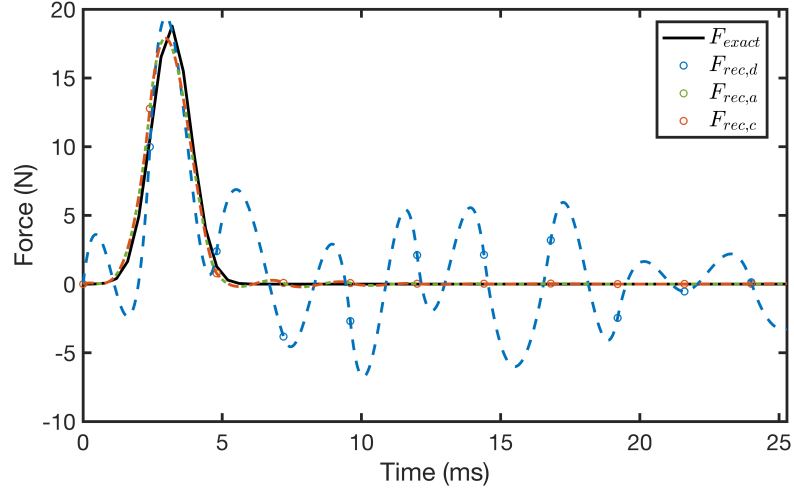


Figure 2.28: Pulse force reconstruction for acceleration-only, displacement-only, and combined acceleration-displacement deconvolution SISO example.  $\hat{R}_1 = \hat{R}_2 = 3$ ,  $f_s = 2500$  Hz, and  $\text{SNR} = 150$  used for this example.

#### 2.2.4 TDDM Limitations

The TDDM is a complex force reconstruction method that can generate extremely accurate results over very short time scales. Additionally, some of the drawbacks of these methods have been reduced or eliminated through our reformulation of the deconvolution problem and subsequent alterations. Although TDDMs do not possess the phase shift error present in the SWAT, it still some drawbacks which are worth noting.

The first is computation time. Formulating a deconvolution problem in the time domain is very computationally expensive. Although segmenting the formulation can reduce this burden, it also has its limits (i.e. due to overlapping there is a minimum reconstruction length per segment). If a very long time history (many samples) is of interest, this method may prove less desirable.

Additionally, there still exists some bit of subjectivity in selection of the constraint parameters. Although our formulation has reduced the number of possible choices and presents a clear resolution-accuracy trade off, there is not a clear single solution as is the

case in SWAT. This solution ambiguity may be viewed as a practical limitation.

Finally, TDDMs are formulated for a single input-output pair. That means loading is assumed to be concentrated at a single point. Often for wind tunnel applications, one cannot make this assumption. If the applied loading is expected to be largely distributed, this method again may prove suboptimal. In this dissertation, two solutions to this problem are presented: (1) pressure reconstruction (presented later) and (2) summation of point contributions. Further study is needed to determine if these solutions are adequate and the required density of calibration input locations.

## 2.3 FDIM

The FDIM is a frequency domain couple to the TDDM. This means it is based on the same physical relationship between input and output (i.e convolution), however, the solution is performed in the frequency rather than time domain. This method is commonly used to increase the computational efficiency of TDDMs. This consequently allows longer time histories to be reconstructed in a reasonable amount of time.

### 2.3.1 FDIM Overview

Begin with Eq. (2.21) relating a measured output and desired input force. In the TDDM, this equation is discretized and the system matrix is assembled. However, in the FDIM, a Fourier Transform is performed on Eq. (2.21). If this is done, the result is given by

$$Y(\omega) = H(\omega) \cdot U(\omega) \quad (2.132)$$

where capital variables signify frequency domain functions. This conversion from time to frequency domain is proven in Appendix B.2. Note that the complex convolution of two

time domain functions has become a more simple multiplication of two frequency domain functions.

As in the TDDM, the standard method for obtaining the IRF (i.e.  $h(t)$ ) is to supply a hammer pulse at the location of interest and record the response. Alternatively, some researchers choose to fit the IRF with the help of finite element models[27], however this is not considered here. To obtain the IRF, simply scale the response by the area under the pulse and time shift it by half of the impulse width. This is shown in Figure 2.5 and is discussed in further detail in Section 2.2.1. However, in the FDIM, the frequency domain couple to the IRF is of interest. This is commonly referred to as the Frequency Response Function (FRF).

With the IRF known, one may utilize the discrete Fourier Transform (DFT) to convert the IRF into the frequency domain. Next, one may measure a response caused by an applied dynamic load. Again using the DFT, one may obtain the frequency domain couple to the output (i.e.  $Y(\omega)$ ).

Finally, to obtain the unknown applied force, one may perform a piecewise division of the output by the FRF at every frequency, i.e.

$$U(\omega) = \frac{Y(\omega)}{H(\omega)}. \quad (2.133)$$

The time domain couple to this input force is obtained using the inverse discrete Fourier Transform (IDFT).

One may note that since a division is required rather than a matrix division, this operation requires  $\mathcal{O}(N)$  operations rather than  $\mathcal{O}(N^2)$  where  $N$  is the length of a measured channel. As expected, the computational efficiency has increased significantly and much longer time segments can be deconvolved.

As in the TDDM, many outputs and only a single input are available. In this SIMO case,

the solution is obtained in a very similar fashion to the conventional TDDM or either of the TDDMs developed in this dissertation. Begin by obtaining all FRFs between the input location and all output channels. For the conventional FDIM, this is obtained by performing a Fourier transform on the scaled and time shifted output to an applied hammer pulse. Each FRF at a frequency is denoted as  $(H_j)_\omega$  and the Fourier Transform of each measured output at a particular frequency  $(Y_j)_\omega$ , where the output location is denoted by the subscript  $j$  and the frequency of interest is denoted by the subscript  $\omega$ . As in the TDDMs, reconstruction of the input force requires information from all outputs. Therefore, Eq. (2.132) is stacked for all output locations to obtain

$$\begin{pmatrix} Y_1 \\ Y_2 \\ \vdots \\ Y_M \end{pmatrix}_\omega = \begin{pmatrix} H_1 \\ H_2 \\ \vdots \\ H_M \end{pmatrix}_\omega U(\omega) \quad (2.134)$$

or in compact form as

$$\mathbf{Y}(\omega) = \mathbf{H}(\omega)U(\omega) \quad (2.135)$$

which holds for every frequency,  $\omega$ . Note that  $M$  represents the arbitrary number of output channels used for the reconstruction.

Since this is a matrix equation, point wise division is no longer applicable. However, a simple least squares inversion can once again be used to solve for the input force as

$$U(\omega) = \mathbf{H}^+(\omega)\mathbf{Y}(\omega). \quad (2.136)$$

This is evaluated at each frequency which requires much less computation time compared to a typical TDDM.

Finally, a scenario where the force reconstruction at multiple input locations is of interest is considered. Such scenarios may be referred to as MIMO. As in the TDDMs, the MIMO formulation is simply a superposition of SIMO formulations. This is represented as

$$\begin{pmatrix} Y_1 \\ Y_2 \\ \vdots \\ Y_M \end{pmatrix}_\omega = \begin{bmatrix} H_{11} & H_{12} & \dots & H_{1P} \\ H_{21} & H_{22} & \dots & H_{2P} \\ \vdots & \vdots & \ddots & \vdots \\ H_{M1} & H_{M2} & \dots & H_{MP} \end{bmatrix}_\omega \begin{pmatrix} U_1 \\ U_2 \\ \vdots \\ U_P \end{pmatrix}_\omega \quad (2.137)$$

where  $P$  input locations are of interest. Again this is represented in compact form as

$$\mathbf{Y}(\omega) = \mathcal{H}(\omega)\mathbf{U}(\omega) \quad (2.138)$$

and solved using a least squares pseudo inverse as

$$\mathbf{U}(\omega) = \mathcal{H}^+(\omega)\mathbf{Y}(\omega) \quad (2.139)$$

provided  $M > P$ .

If  $N$  frequencies are of interest, this requires the pseudo inversion of  $N$   $M \times P$  matrices. Since inversion is  $\mathcal{O}(P^3)$  for this inversion, the MIMO computation is  $\mathcal{O}(N \cdot P^3)$ . The inversion for the typical MIMO TDDM is  $\mathcal{O}(N^3 \cdot P^3)$ , a factor of  $N^2$  larger. The computational efficiency of the FDIM is obvious as  $N$  becomes large.

### 2.3.2 Novel FDIM Alterations

In this section, the base FDIM formulation is improved to yield improved results.

### 2.3.2.1 FRF Solution

As in the TDDM alterations, the assumption of the IRF being equivalent to a multiple of the response to a hammer pulse is no longer made. Rather, the convolution relationship is solved (this time in the frequency domain) with a known applied load and measured response.

Return to Eq. (2.132) with  $U(\omega)$  known (measured) and the FRF unknown. As in the solution of an unknown applied force, the solution of the FRF is simply a division of the output by the input at each frequency, i.e.

$$H(\omega) = \frac{Y(\omega)}{U(\omega)}. \quad (2.140)$$

Although this formulation requires more computation than the typical one (i.e. assuming the measured response to a pulse loading is proportional to the FRF), this formulation is required for the next alteration. Additionally, this allows for a variety of calibration load types as opposed to just pulses.

### 2.3.2.2 Averaging of Calibration Sets

The next alteration made is very similar in spirit to what was changed in the TDDM and is discussed in Section 2.2.2.5. Again, the FRF of the system is not dependent on the applied load. That means that any applied load at a particular location should exhibit an identical FRF as any other load applied at the same location. This is capitalized upon to reduce the ill effects of noise amplification by performing multiple calibration tests.



Applying  $p$  input calibration tests at the same location results in

$$\begin{pmatrix} Y_1 \\ Y_2 \\ \vdots \\ Y_p \end{pmatrix}_{\omega} = \begin{pmatrix} U_1 \\ U_2 \\ \vdots \\ U_p \end{pmatrix}_{\omega} H(\omega) \quad (2.141)$$

at each frequency and written compactly as

$$\mathbf{Y}(\omega) = \mathbf{U}(\omega)H(\omega). \quad (2.142)$$

Since the noise is random from test to test, utilizing repeat tests will hopefully result in a more accurate FRF construction. As in Eq. (2.136), the FRF is solved using a least squares pseudo inverse as

$$H(\omega) = \mathbf{U}^+(\omega)\mathbf{Y}(\omega). \quad (2.143)$$

Since each FRF is unique, this technique can be repeated for solving for the FRF at each input-output pair when considering the SIMO or MIMO case.

### 2.3.2.3 Acceleration Deconvolution

As in the TDDM formulation, the convolution equation also holds between applied force and acceleration. Most of the discussions in this dissertation present examples with strain or displacement deconvolution. However there are some advantages to using acceleration data.

Acceleration measurements are significantly easier to obtain than strain/displacement. For strain, one typically needs to ensure all load can travel through the strain gages which often requires designing around sensors. Alternatively, accelerometers need be simply

placed on a surface of the body. Therefore acceleration measurement can be an afterthought which presents more design flexibility. Additionally, force measurement can theoretically be made without the need for complex strain balances. This may be advantageous in smaller tunnels or small budget experiments.

Returning to our continuous convolution of displacement and applied force, both sides are differentiated twice to obtain Eq. (B.21). For proof of this equation see Appendix B.3.

The unknown is now the acceleration FRF ( $\ddot{H}(\omega)$ ) rather than the typical displacement/strain FRF ( $H(t)$ ). Using the FDIM, one may construct the acceleration FRF and then use it to reconstruct an arbitrary applied dynamic force  $u(t)$ .

It also should be noted that all of the previously mentioned extensions to the developed FDIM variant are completely applicable to acceleration deconvolution as well. Therefore multiple input tests are used at the same location to solve for the acceleration FRFs. Therefore Eq. (2.141) becomes

$$\begin{pmatrix} \ddot{Y}_1 \\ \ddot{Y}_2 \\ \vdots \\ \ddot{Y}_p \end{pmatrix}_{\omega} = \begin{pmatrix} U_1 \\ U_2 \\ \vdots \\ U_p \end{pmatrix}_{\omega} \ddot{H}(\omega). \quad (2.144)$$

To solve for the unknown applied load, all of the FRFs are used in the solution. There-

fore, the SIMO form becomes

$$\begin{pmatrix} Y_1 \\ Y_2 \\ \vdots \\ Y_{ns} \\ \ddot{Y}_1 \\ \ddot{Y}_2 \\ \vdots \\ \ddot{Y}_{na} \end{pmatrix}_{\omega} = \begin{pmatrix} H_1 \\ H_2 \\ \vdots \\ H_{ns} \\ \ddot{H}_1 \\ \ddot{H}_2 \\ \vdots \\ \ddot{H}_{na} \end{pmatrix}_{\omega} U(\omega) \quad (2.145)$$

where  $ns$  denotes the number of strain sensors and  $na$  denotes the number of accelerometers. Additionally, the MIMO formulation becomes

$$\begin{pmatrix} Y_1 \\ Y_2 \\ \vdots \\ Y_{ns} \\ \ddot{Y}_1 \\ \ddot{Y}_2 \\ \vdots \\ \ddot{Y}_{na} \end{pmatrix}_{\omega} = \begin{bmatrix} H_{11} & H_{12} & \dots & H_{1P} \\ H_{21} & H_{22} & \dots & H_{2P} \\ \vdots & \vdots & \ddots & \vdots \\ H_{ns,1} & H_{ns,2} & \dots & H_{ns,P} \\ \ddot{H}_{11} & \ddot{H}_{12} & \dots & \ddot{H}_{1P} \\ \ddot{H}_{21} & \ddot{H}_{22} & \dots & \ddot{H}_{2P} \\ \vdots & \vdots & \ddots & \vdots \\ \ddot{H}_{na,1} & \ddot{H}_{na,2} & \dots & \ddot{H}_{na,P} \end{bmatrix}_{\omega} \begin{pmatrix} U_1 \\ U_2 \\ \vdots \\ U_P \end{pmatrix}_{\omega}. \quad (2.146)$$

Note that adding the acceleration measurements increases the row dimension of the inverted matrix. This in theory should improve performance for a least squares solution.

### 2.3.3 Numerical Examples of FDIM

In this section a few numerical examples of the FDIM solution approach are presented. This section presents a few of the considerations for the FDIM and demonstrates the advantages of the novel alterations presented in this dissertation.

#### 2.3.3.1 SISO Example of the Conventional FDIM

The most basic reconstruction problem is first considered. Consider the SISO spring-mass-damper system depicted in Figure 2.9. All definitions of noise and system properties are consistent with those defined in Section 2.2.3. Recall that the SISO case is much less desirable than the SIMO case. Only information from one location is available and one cannot over constrain the solution.

Applying the conventional FDIM (i.e. scaling and time shifting output to obtain IRF), the IRF and reconstructed pulse force shown in Figure 2.29 are obtained. Note that no noise was injected into this problem (aside from unavoidable numerical noise).

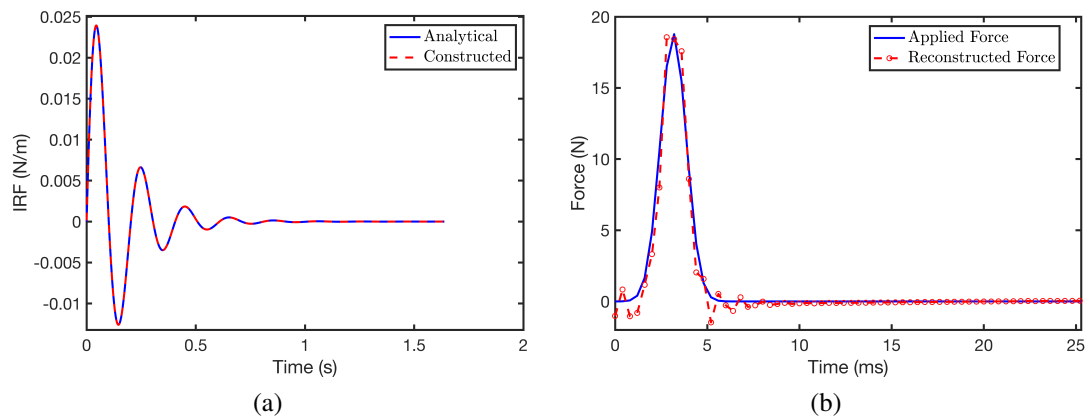


Figure 2.29: Conventional FDIM noiseless force reconstruction. IRF (a) and reconstructed force (b) are both shown.

As expected, the IRF matches very well with the analytical solution. Furthermore, when

this IRF is used to reconstruct a new load, the reconstruction matches well with the applied load. Note some small errors which can be attributed to numerical error accumulation and inability to perfectly shift the response by half of the impulse width.

Next it is important to observe the detrimental effects of noise to the reconstruction. Repeating the above analysis with  $\text{SNR} = 150$ , the results in Figure 2.30 are obtained. Although minimal influence is observed on the FRF solution, large error is present in the

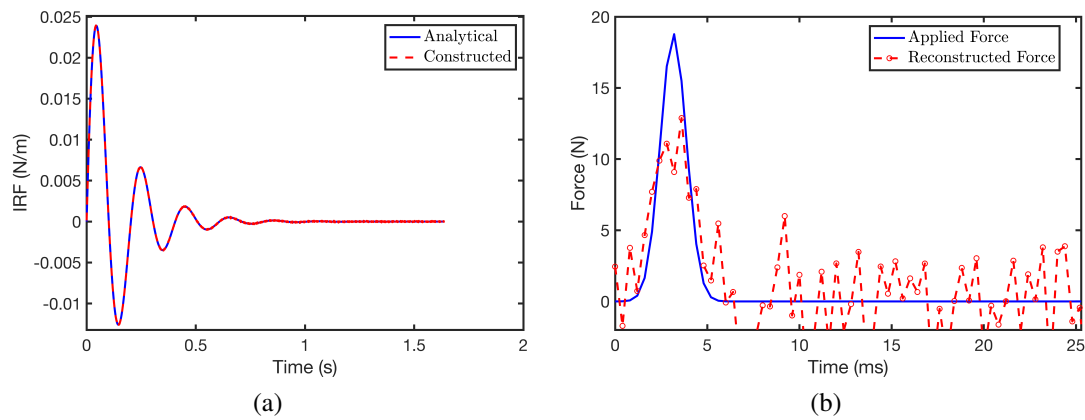


Figure 2.30: Conventional FDIM noisy force reconstruction. IRF (a) and reconstructed force (b) are both shown.

pulse force reconstruction. Unfortunately, with this conventional approach, there are no more knobs to turn and one is forced to accept this level of accuracy.

### 2.3.3.2 SISO Example of FDIM with Solved FRF

Next consider the solution of the FRF alteration suggested Section 2.3.2.1. Applying this approach, the IRF construction and pulse force reconstruction shown in Figure 2.31 are obtained.

Again, as expected, the FRF and pulse force are reconstructed with high accuracy. Interestingly, the results actually appear more accurate than the simple scaling of output approach (i.e. Figure 2.29b). It would seem that solving for the FRF is more accurate than

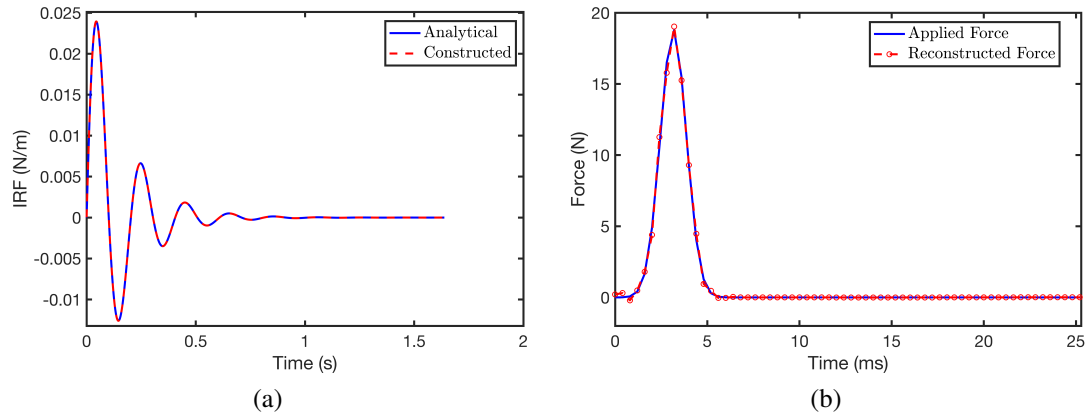


Figure 2.31: FRF solved FDIM noiseless force reconstruction. IRF (a) and reconstructed force (b) are both shown.

the conventional scaling and time shifting of the response.

Next it is important to observe the detrimental effects of noise to the reconstruction. Repeating the above analysis with SNR= 150, the results in Figure 2.32 are obtained.

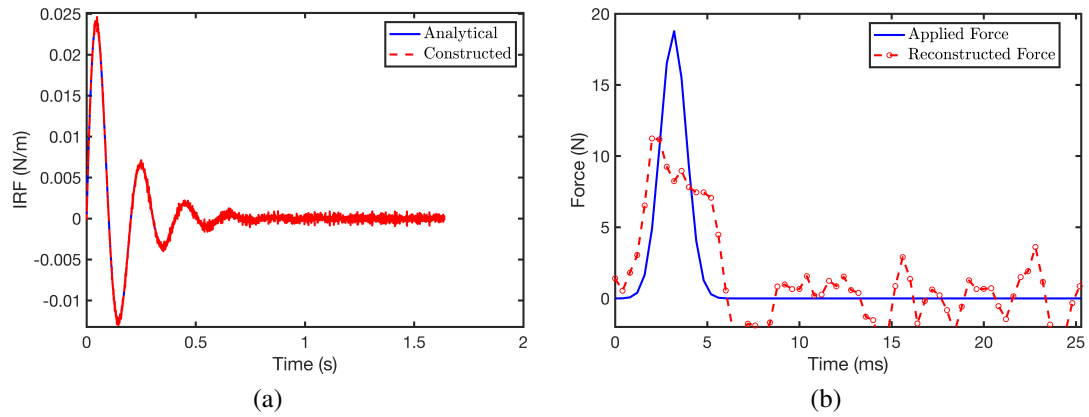


Figure 2.32: FRF solved FDIM noisy force reconstruction. IRF (a) and reconstructed force (b) are both shown.

Comparing Figure 2.32a with Figure 2.30, it is evident that the FRF solution is worse in the noisy case. Furthermore, if this noisy FRF is used to reconstruct a pulse force, the accuracy is once again unacceptable. The level of error in the reconstructions is comparable with that of the conventional FDIM. Again, no additional alterations are possible for this

stage of the method.

### 2.3.3.3 Averaging Calibration Sets

As with TDDMs, one possible way of increasing accuracy for the FRF construction is by utilizing multiple calibration sets in the FDIM formation. Since each input-output location pair has a unique FRF, one may perform multiple tests and use all of the information to construct the FRF. To compactly observe the influence of repeat tests on FRF construction accuracy, return to Eq. (2.123) and compute this accuracy versus number of calibration tests. A plot of this is shown in Figure 2.33. Since the FRF often displays high frequency error (e.g. Figure 2.35)b) computing an error metric based on the FRF is often less informative.

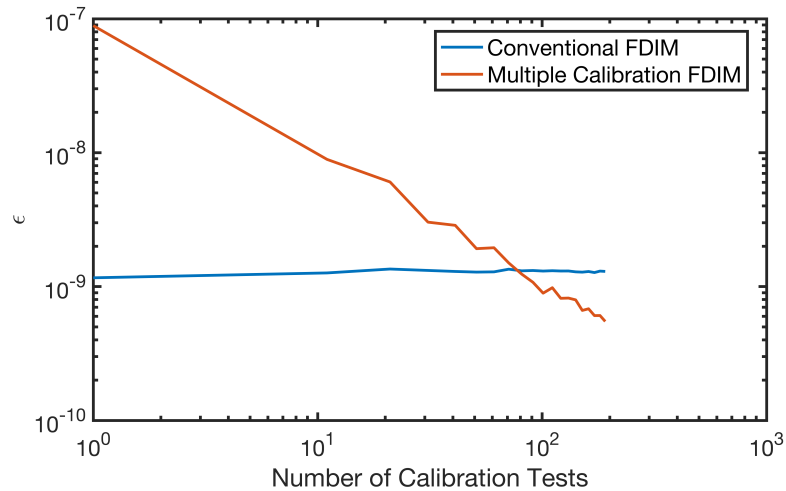


Figure 2.33: FDIM SISO IRF construction accuracy versus number of calibration tests

Since the FDIM is so efficient, one may perform many numerical studies with very little computational effort. Upon review of Figure 2.33, a very clear linear trend in log space is evident for the multiple calibration approach. One can achieve about an order of magnitude decrease in error by increasing the number of calibration tests by about an order

of magnitude. Although performing 100+ tests at the same hole location in real life may be unreasonable, it is useful to show that performing multiple tests can improve the accuracy.

Although higher accuracy than the conventional approach is achievable, this method still under performs for any practical number of tests on this SISO case study. Regardless, this at least gives the tester an option to change where previously they could not.

#### 2.3.3.4 SIMO Example

In this section SIMO force reconstruction is presented for a ten DOF lumped mass oscillator. This is same system form shown in Figure 2.1 with the stiffness and damping values selected randomly.

The FDIM presented in Section 2.3.2.1 is validated here. Using this more simplified method, one may observe the advantages of adding multiple calibration sets later in the section. Using this method, the pulse shown in Figure 2.34 is obtained.

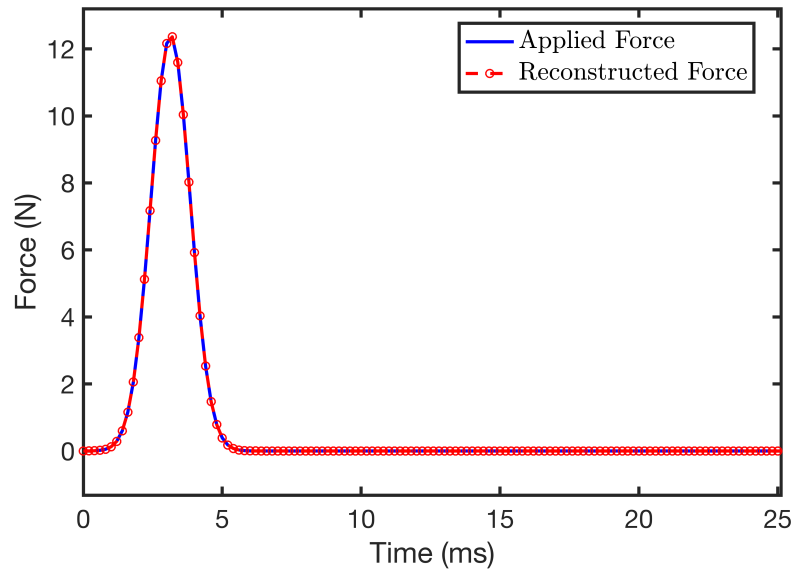


Figure 2.34: FDIM SIMO noiseless force reconstruction

As expected, excellent accuracy is achieved for the noiseless case. When reviewing the



various IRFs, a curious phenomenon is observed. This is shown in Figure 2.35a. Ringing is present in the beginning and end of the reconstruction. This is primarily due to the large high frequency error in the FRF which is shown in Figure 2.35b. However, this error does not materialize into large errors in the force reconstruction.

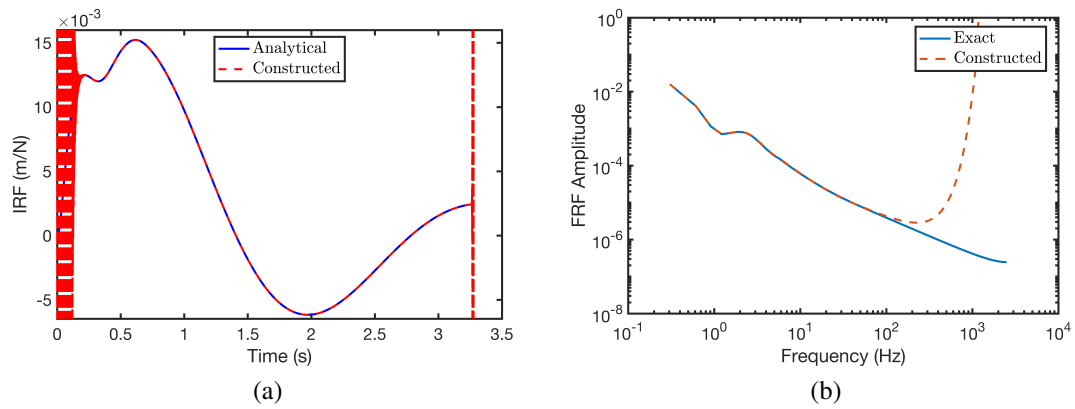


Figure 2.35: IRF (a) and FRF (b) construction at DOF 5 using FDIM with FRF solution.

This high frequency error in the FRF is due to the finite pulse used for calibration. The Fourier Transform of an infinitesimal width pulse is constant at a value of 1. When a finite pulse is used, this constant value drops off steeply at high frequencies. When this is divided by the Fourier Transform of the pulse, this manifests as large contributions at high frequencies. This is an unavoidable consequence of using a finite pulse. One may attempt to remedy this by filtering the signal at a value of

$$f_c = \frac{1}{\epsilon} \quad (2.147)$$

the inverse of the pulse width. For this example, that value is 159 Hz, approximately the value where this steep increase in the FRF begins. For accurate view of the FRF, this filtering is required, however, why this is not required for pulse reconstruction is shown below.

The reconstructed pulse was a new pulse with different magnitude, pulse width, area, and noise properties than the pulse used for calibration. Therefore, any claim of over fitting is invalid. Clearly the use of the erroneous FRF still yields excellent results for the noiseless case.

Next it is of interest to investigate the negative effects of noise and how it may degrade the results. This is shown in Figure 2.36. Once again substantial high frequency error is

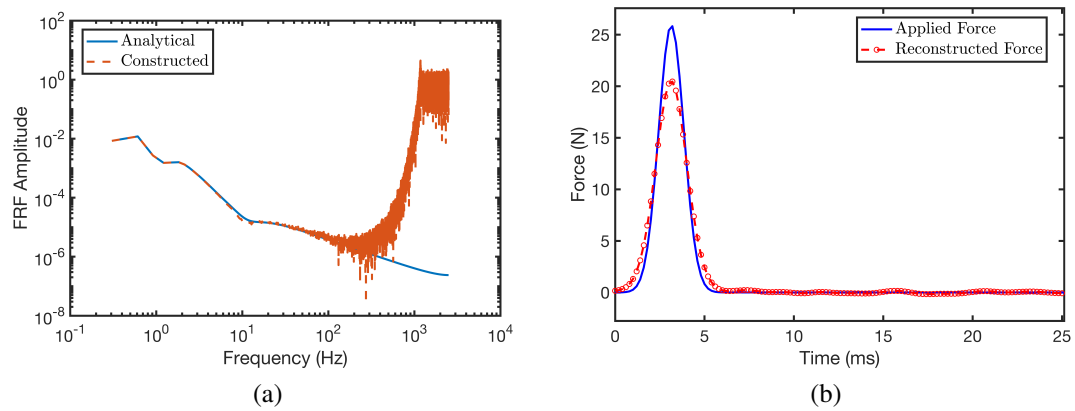


Figure 2.36: FRF solved SIMO FDIM noisy force reconstruction. FRF at DOF 5 (a) and reconstructed force (b) are both shown. SNR= 150 used for this example.

observed in the FRF due to the finite pulse. However, with the presence of noise, the pulse reconstruction is no longer unaffected. Substantial under prediction of the pulse is observed. This trend is consistent across many tests with varying sampling frequencies, pulse widths, DOFs, and noise levels. Therefore, one may conclude that noise causes unavoidable error in the FRF solved FDIM. Note that there are slight differences in the analytical FRF from Figure 2.35b and 2.36a. This is due to the random selection of system parameters during a particular numerical experiment. However, these trends are very repeatable.

Next multiple calibration tests are incorporated to investigate the repeat formulation. The hypothesis is that with more calibration inputs, a better approximation of the FRF will be obtained resulting in more accurate reconstructions. The results of the same FDIM

experiment with ten calibration tests at the same location is shown in Figure 2.37.

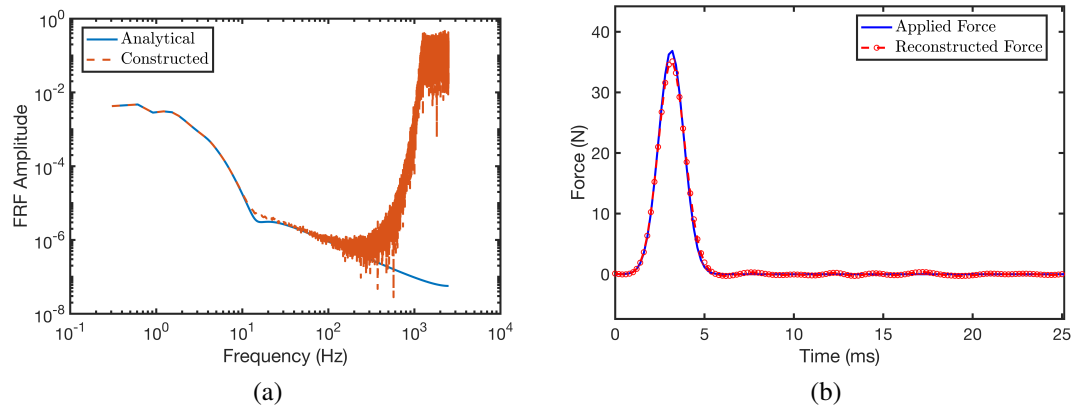


Figure 2.37: FRF solved SIMO FDIM noisy force reconstruction with ten calibration tests at same input. FRF at DOF 5 (a) and reconstructed force (b) are both shown. SNR= 150 used for this example.

No discernible accuracy increase is evident in Figure 2.37a, however, the pulse reconstruction is clearly more accurate. To more concretely observe this effect, the force reconstruction for a varying number of input calibration tests is repeated and the peak and area difference of each reconstruction is computed. These results are displayed in Figure 2.38 with varying levels of SNR.

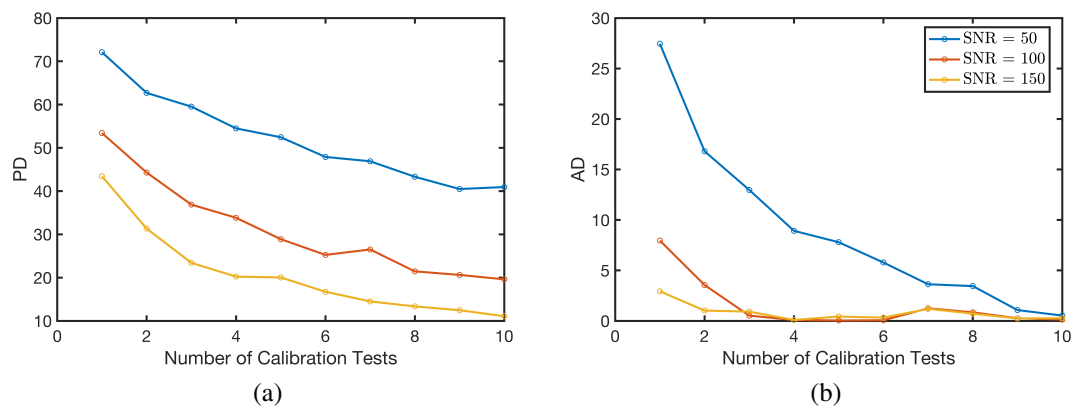


Figure 2.38: Peak (a) and Area (b) Difference versus number of calibration tests for FDIM SIMO numerical studies

As expected, the peak error reduced considerably when increasing the number of calibration tests. The most substantial accuracy increase occurs after the first few repeat tests. The influence on the area difference is more dramatic at lower SNR. Interestingly, the same accuracy with ten repeats for the SNR= 50 case is achieved as with a single test from a data set with a third the noise level. Clearly performing repeat tests can reduce the ill effects of noise.

Further increase in repeat tests for the low noise cases yields less increase in accuracy. Therefore, as in Section 2.2.3.7, a practical requirement of two to three repeat tests is ideal for high reconstruction accuracy.

### 2.3.3.5 MIMO Example

In this section the FDIM's ability to reconstruct pulses for the MIMO case is validated. The same ten DOF system discussed in the previous section is used. However, this time pulses are applied simultaneously at multiple locations. For this study all outputs (i.e.  $n = 10$ ) are considered and inputs at four locations (i.e.  $p = 4$ ). Performing the FRF solved FDIM with no repeat tests or noise, the results in Figure 2.39 are obtained.

Note the high accuracy of the reconstructions for this MIMO case study. All three simultaneously applied input pulses have been accurately reconstructed. Additionally, the hole location with no applied load was correctly reconstructed as well.

Next it is of interest to investigate the effects of noise. Adding Gaussian noise to all output data at SNR= 150, the results in Figure 2.40 are obtained. This figure reveals that the FRF solved FDIM does a very poor job at reconstructing the pulse. Both the peak and width of the reconstructed pulse are highly inaccurate.

Next, one may investigate the influence of performing multiple calibration sets on the accuracy of the reconstruction. Again the peak and area differences are used. However, as

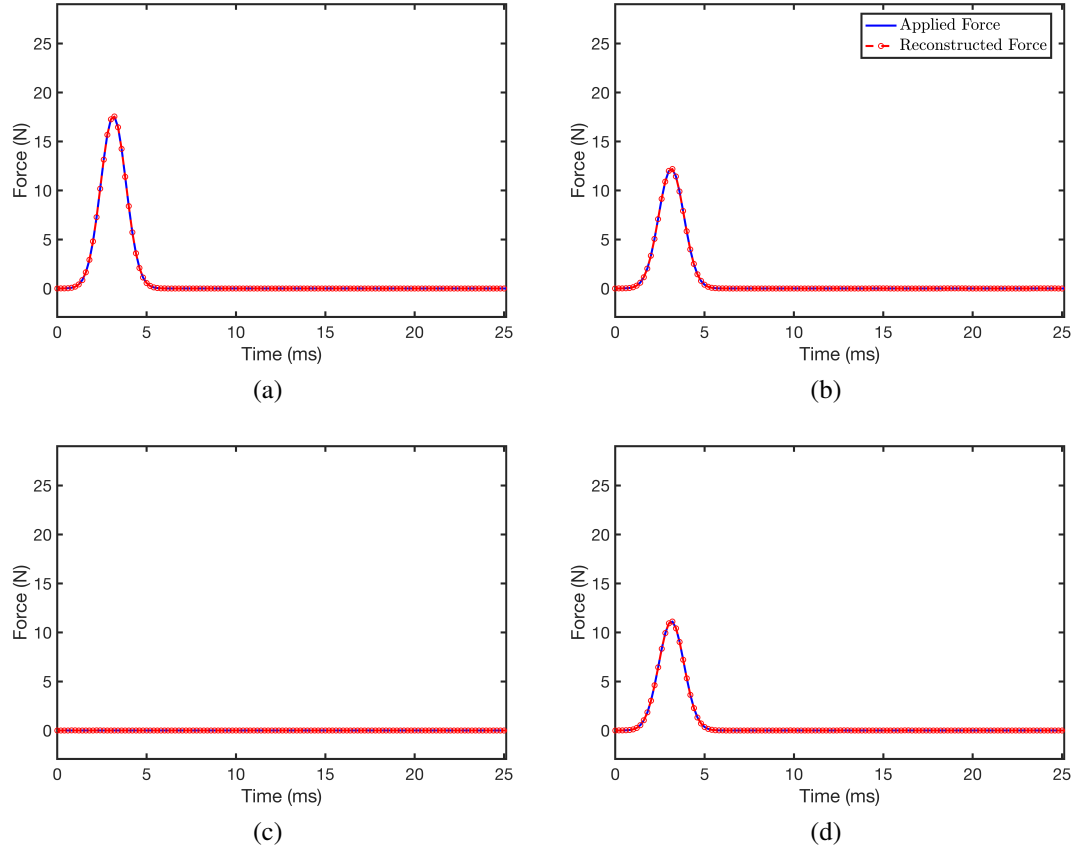


Figure 2.39: MIMO hammer pulse reconstruction for 10 DoF system. Applied force reconstruction at input nodes 2 (a), 4 (b), 6 (c), and 8 (d) are all shown. The FRF solved FDIM with no noise and  $f_s = 5$  kHz were used for this study.

in Section 2.2.3.6, the average area and peak difference were considered over all the holes where a pulse was applied. These formulae are given by Eqs. (2.126) and (2.127). The averaged peak and area differences versus number of calibration tests is depicted in Figure 2.41.

Interestingly, the results aren't nearly as drastic as in the SIMO case study. Although some improvement is observed in the peak and area difference as the number of input calibration tests increases, the effect is much smaller and never reaches a very low level of error (e.g.  $< 10\%$  AD and PD). Additionally, the MIMO case study seems much more sensitive as compared to that of the SIMO. For the high noise case, the solution occasionally

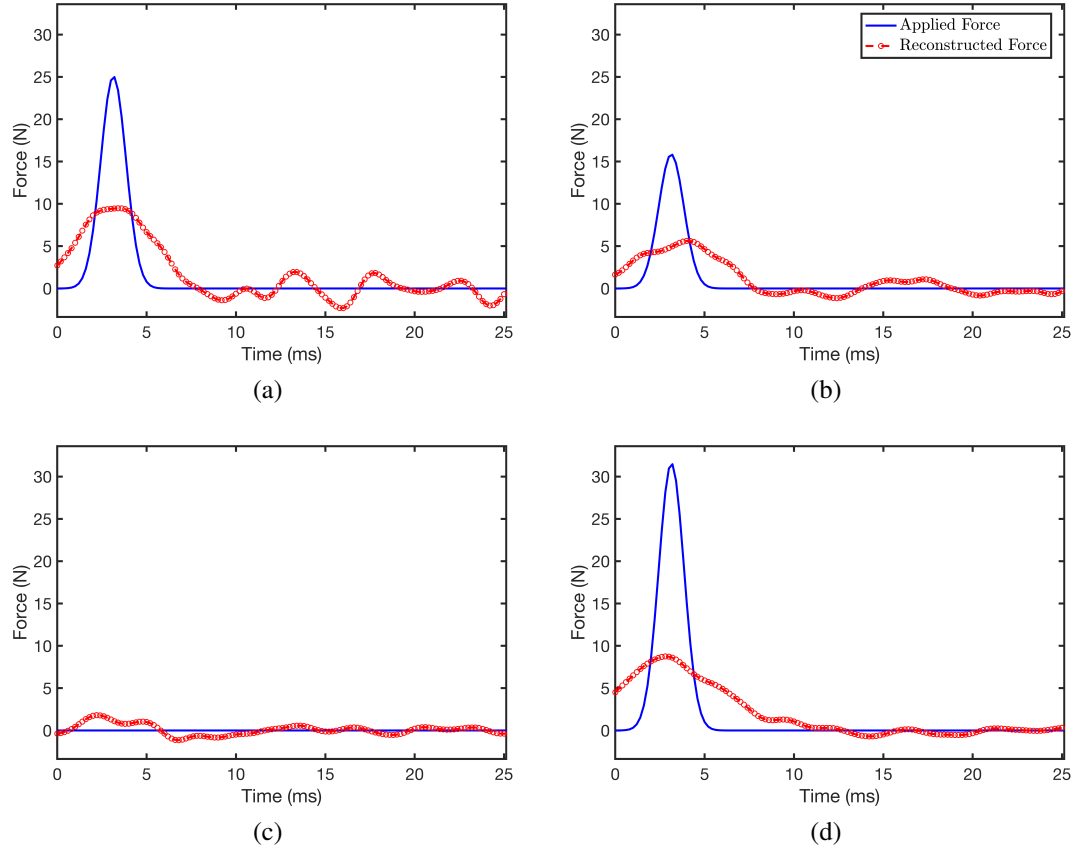


Figure 2.40: MIMO hammer pulse reconstruction for 10 DoF system. Applied force reconstruction at input nodes 2 (a), 4 (b), 6 (c), and 8 (d) are all shown. The FRF solved FDIM with  $\text{SNR} = 150$  and  $f_s = 5 \text{ kHz}$  were used for this study.

blows up. Clearly imposing the added constraint on the FRF solution (i.e. additional calibration input tests) is not enough to adequately reduce the ill conditioning in the force reconstruction solution for the MIMO case.

### 2.3.3.6 Acceleration Deconvolution

The final FDIM investigation is deconvolution of acceleration data. In Section 2.2.3.9 it was shown that the use of acceleration can prove extremely effective for the GDLM. This section is dedicated to investigating the effectiveness of acceleration deconvolution for the

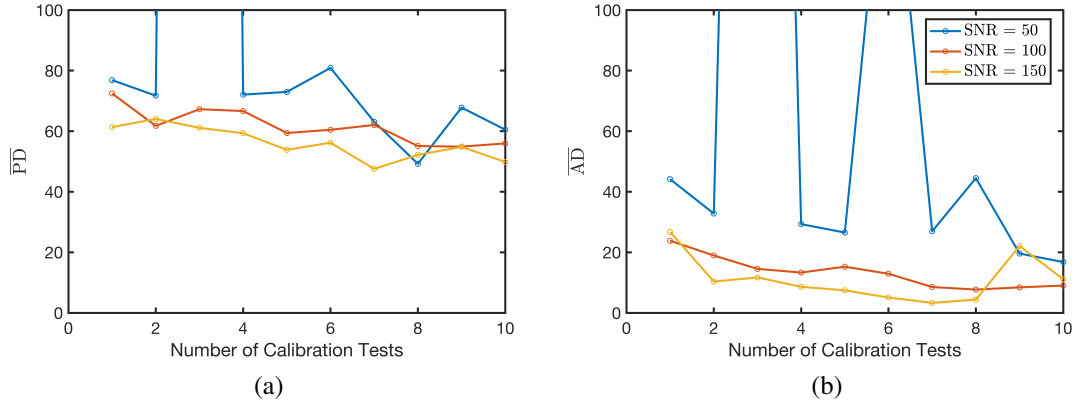


Figure 2.41: Peak (a) and Area (b) Difference averaged over each application location versus number of calibration tests for FDIM MIMO numerical studies

FDIM. This section only considers the SISO system case. However, further experimental investigations demonstrate some of the advantages for the SIMO and MIMO cases.

Consider the numerical system shown in Figure 2.9. Assume the displacement and acceleration of this mass is measured. Next, a known load such as a pulse is applied to this system and record the resultant response. The acceleration and known applied force can be used in conjunction with Eq. (2.144) to solve for the resultant acceleration FRF,  $\ddot{H}$ . For this example, consider the more simplified case where no repeat tests are used (i.e.  $p = 1$ ). An acceleration IRF construction using this approach is displayed in Figure 2.42a. Next, the FRF can be used to solve for an applied force given a measured dynamic acceleration response. An example pulse force reconstruction is displayed in Figure 2.42b. Note the excellent pulse reconstruction even with these noisy signals.

As noted in Section 2.3.2.3, this can be combined with the displacement data and reconstruct an applied load. A comparison pulse force reconstruction considering displacement-only, acceleration-only, and combined acceleration-strain deconvolution is shown in Figure 2.43.

As found in the GDLM example of acceleration deconvolution, the acceleration-only

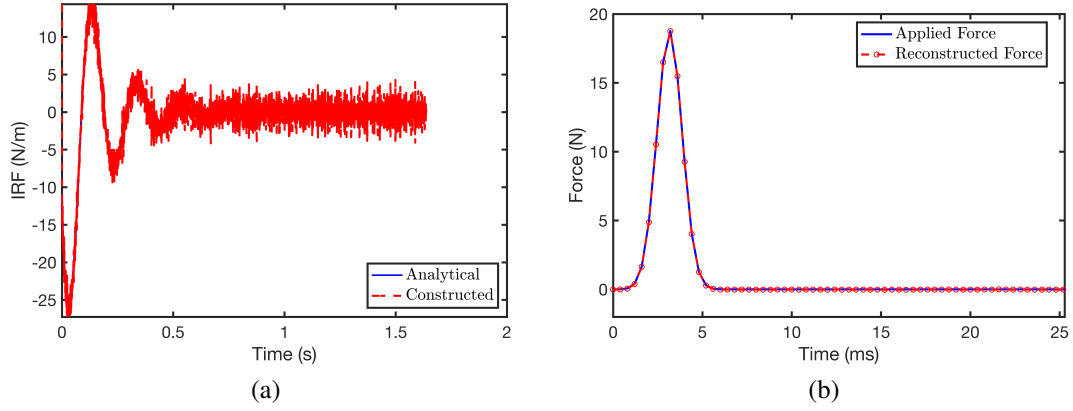


Figure 2.42: Acceleration IRF construction (a) and pulse force reconstruction (b) using FDIM acceleration deconvolution. SISO system with  $\text{SNR} = 150$  used for these studies.

and combined acceleration-displacement deconvolution far outperform the displacement-only deconvolution. All methods perform well with no added noise. Therefore, the presence of noise appears to be more detrimental to the displacement deconvolution than acceleration. Future studies should be performed to determine the cause of this difference.

#### 2.3.4 FDIM Limitations

The FDIM is an extremely computationally efficient method due to the solution of deconvolution in the frequency domain. This approach allows for a series of inversions at each frequency rather than a simultaneous inversion of a impulse response matrix on the order of the length of the signal squared. Additionally, the accuracy of this method seems very comparable with that seen in the SWAT and TDDM variants.

However, as with the previous methods, the FDIM has its drawbacks which should be noted. After review of Section 2.3.3.5, it is evident that the FDIM is less effective for the MIMO problem. For this highly over constrained problem (i.e. ten outputs and four inputs), the best achievable accuracy is about 60% peak error. Adding repeat tests helps this but the desired level of accuracy is not achieved.



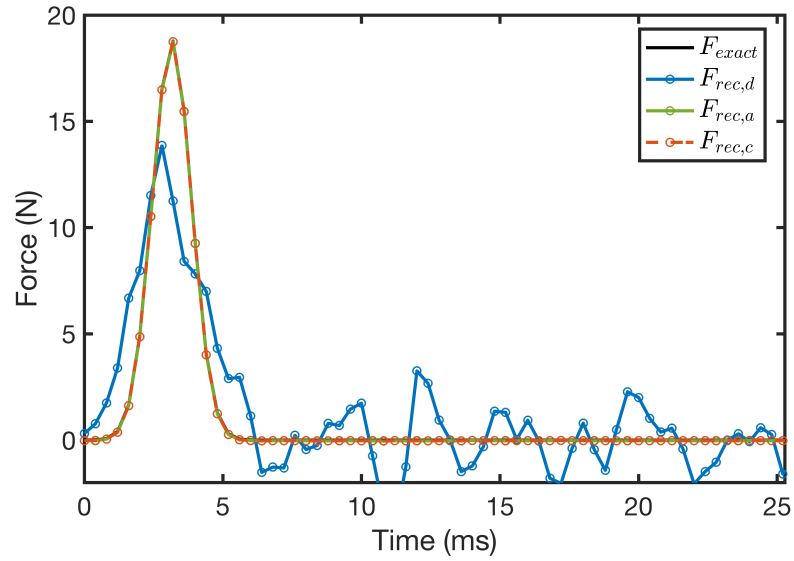


Figure 2.43: Pulse force reconstruction for acceleration-only, displacement-only, and combined acceleration-displacement deconvolution SISO example. The FDIM with  $f_s = 2500$  Hz, and  $\text{SNR} = 150$  used for this example.

Another disadvantage of this method is the general lack of modifications available to the analyst. The only modification implemented is the use of additional calibration tests. Although this improves performance, it is still not enough in some cases to properly solve the problem. Unlike in the GDLM or CMM, no large modification is available to the problem formulation (e.g. increase in constraint parameter) that can increase the conditioning of the problem to an acceptable level.

## Chapter 3: Experimental Validation on No-Flow Test Article

In this chapter, the various methodologies are validated real experimental systems. Although the methods have been validated on numerical models with noise, many complexities may arise in real systems that are not considered in idealized numerical models. Examples include nonlinearities, biased noise, and infinite DoFs. Prior to testing in a wind tunnel, it is important to demonstrate these methods on more complex, real systems to build confidence in the effectiveness of such methods.

### 3.1 Experimental Setups

Begin with an overview of the experimental setups for the bench top tests. There are a number of considerations when performing dynamic experiments. Examples include stiffness of boundary conditions, sensor connections, data acquisition, and load application. This section will overview these considerations in detail.

#### 3.1.1 Support Structures

To create a test setup that closely resembled that of a tunnel run, a similarly sized test article was developed. The fully assembled model can be seen in Figure 3.1. This test article, designed by Collopy et al[30], was chosen to maximize the number of orthogonal loading locations and simulates the approximate size, weight, and natural frequencies of typical test articles used in Tunnel 9. A steel plate is affixed to the test article that has

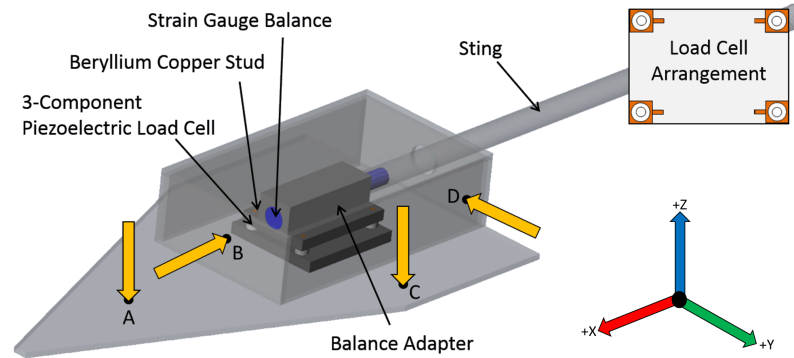


Figure 3.1: CAD representation of dynamic calibration bench top test article

mounting holes for the load cells.

The strain sensors, discussed in a later section, must be constrained between the model and sting to ensure the load travels through the sensors. For this reason, the strain sensors are mounted between the balance adapter (which connects to the sting) and the model. One may note that only a single load path exists between the model and support structure which passes through the sensors. Any other load path may inhibit the sensors performance.

The primary support structure used in most of my experimental studies is shown in Figure 3.2. This support structure is henceforth referred to as "Support Structure 1" and will be used for the majority of the experimental validation studies. This support structure is most commonly used to apply check loads for validating strain gage force balance calibrations. It is adjustable in pitch and roll via two hydraulic arms. These adjustments, in conjunction with an inclinometer allows the user to set the orientation of the model within a sixtieth of a degree.

The high speed data acquisition system (DAS) is also depicted in the left of Figure 3.2. All channels of the sensors are sent through signal conditioning boxes and then finally recorded by the DAS. This system is capable of sampling analogue signals up to a rate of 1 MHz. Additionally, a physical anti-aliasing filter of 20 kHz is available for use.

To build confidence in these methodologies, tests are performed on a second support



Figure 3.2: Calibration test article mounted on support structure 1.

structure. This is the actual structure inside of Tunnel 9. A typical sting for a similarly sized test article was used. This far longer sting will create a very different response as compared to support structure 1. Although there is no theoretical requirement for validating on the Tunnel 9 sting, these experiments will build confidence that this method works on the exact system for future integration. This structure, henceforth referred to as "Support Structure 2", is shown in Figure 3.3.

A static calibration was also performed for the piezoelectric gages. However, since pitch variation on Support Structure 1 was limited to a few degrees and availability on Support Structure 2 was limited, a static calibration on the support structure depicted in Figure 3.4 was performed.

This support structure is adjustable in pitch from 0-90°. This allows the tester to apply a purely x-direction (i.e. drag) load. This was of interest to quantify the accuracy of the static calibration in all loading directions. Since the piezoelectric strain sensor connections are unaltered during mounting on the various support structures, the static calibration should

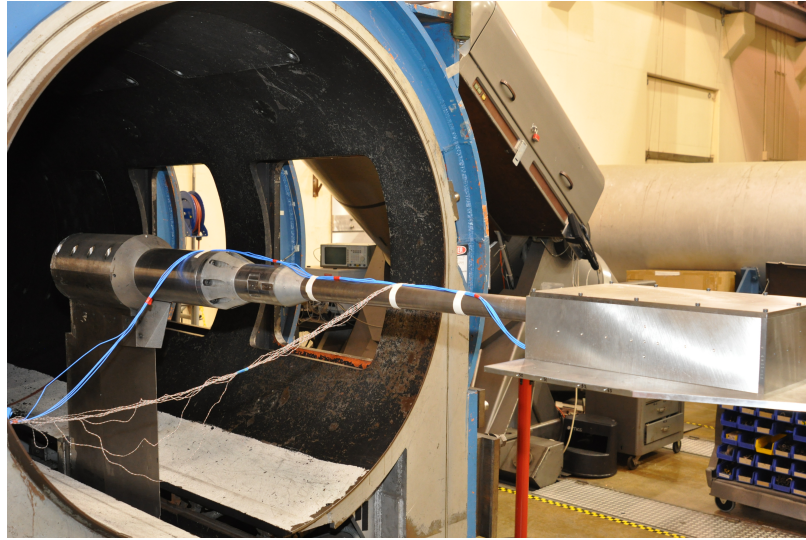


Figure 3.3: Calibration test article mounted on support structure 2.



(a)



(b)

Figure 3.4: Support structure used for static calibration with (a) and without (b) mounted test article.

hold. During mounting, an inclinometer was used to ensure the test article was oriented at zero AoA. This reduces the effects of bending deflections on various support structures.

The same data acquisition system, sensors, and test article are used in these experiments. We've simply changed the system boundary conditions by mounting the test article on various support structures.

### 3.1.2 Sensors

Unlike for static force measurement, dynamic force balances are not commercially available. Some exist but are typically not designed specifically for the wind tunnel application. For this reason, high bandwidth sensors need to be integrated directly into the test article design. A steel plate is affixed to the test article that has mounting holes for the load cells. Four piezoelectric force sensors were arranged in a rectangular formation to accurately measure all six components of forces and moments:  $F_x$  (Axial),  $F_y$  (Side),  $F_z$  (Normal),  $M_x$  (Roll),  $M_y$  (Pitch), and  $M_z$  (Yaw). Having a symmetric formation minimizes crosstalk after calibration. This is the phenomenon of undesirable signals being present on channels without having a corresponding applied load. An example of crosstalk is if a z-direction load was applied and a small signal was recovered by the y-direction sensors.

The placement of these load cells is crucial when designing a model. This is because for accurate transmission of all the force through the sensors, they have to be mounted between the sting and the model. An assembled picture of the load cell configuration can be seen in Figure 3.1. Similarly, the entire load must travel through the strain gage balance. A balance adapter was used to connect the model to the balance, with the piezoelectric load cells in between. A stud is used to constrain each load cell between the test article and balance adapter. However, this stud limits the deflection of the load cell and reduces the force transferred to the load cells. To limit the effects on the recovered force from this measurement system, beryllium-copper studs were used for their high strength and low stiffness, which means that most of the force will be transferred directly through the stiffer load cells. A sufficient preload is also required in this assembly to ensure adequate transmission of shear forces to the load cells. The manufacturer recommends at least ten times the normal force in preload as compared to the expected shear loading during testing.

The strain gage balance, colored blue in Figure 3.1, is attached to the balance adapter

with a hardened steel pushpin. Finally, the strain gage balance is firmly connected to the sting, which is constrained by the support structure of choice. One can now see that any load imparted to the test article will travel through all five of the force sensors. However, inertial loads are still present in the signal. These are created from the restoring forces in the cantilevered arrangement. A flight-worthy test article is not cantilevered and therefore, the measurement of these restoring forces is undesirable. Rather, the aerodynamic loads are the target measurement.

Nine uniaxial piezoresistive accelerometers were used to remove the inertial loading. The accelerometers were arranged in a 3-2-2-2 formation[42] to ensure accurate recovery of all directional accelerations present. The accelerometer array can be seen in Figure 3.5 and a representative example of physical placement of this array in Figure 3.1. This formation ensures that all three tangential or rotational oscillations that may be excited can be recovered.

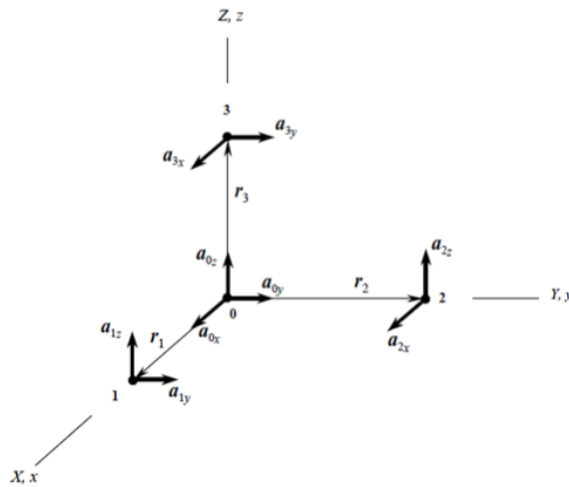


Figure 3.5: 3-2-2-2 Accelerometer Array to ensure all translational and rotational accelerations are measured.

Some relevant specifications of the load cells (Model 260A01[43]) and accelerometers (Model 56[44]) are depicted in Table 3.1. Both sensors have a very high bandwidth, making them more than suitable for the expected dynamic environment. Based on observations

Table 3.1: Sensor specifications for the load cells (left) and accelerometers (right) used in the Balance Calibration Laboratory.

	Model 260A01	Model 56
Normal Sensitivity	0.56 mV/N	0.9 mV/g
Shear Sensitivity	2.25 mV/N	-
Normal Measurement Maximum	4.45 kN	200 g
Shear Measurement Maximum	2.22 kN	-
Normal Failure Limit	5.87 kN	5000 g
Normal Broadband Resolution	0.027 N-rms	-
Shear Broadband Resolution	0.0089 N-rms	-
Upper Frequency Limit	90 kHz	2.8 kHz
Normal Lower Frequency Limit	0.01 Hz	0 Hz
Shear Lower Frequency Limit	0.001 Hz	-
Temperature Range	-54 to +121 C	-40 to +121 C

made in previous tests and numerical studies, relevant dynamics in the range of 5-1000 Hz are expected. This is well within the range of each sensor. Note that the accelerometers are uniaxial and therefore do not quote shear quantities. They do however have  $< 3\%$  transverse sensitivity so most of the response will be in reaction to the normal direction motion. The accelerometer spreadsheets unfortunately do not quote a broadband resolution value however in general this is found to be higher than desired (i.e. noisier signals than preferred). For future tests, PCB triaxial accelerometers are suggested.

For most of these experimental studies the 6-component strain gage force balance readings are not recorded. This is due to its 30 Hz upper bandwidth. This low internal resonance is far below the level of relevant dynamics. Therefore, the data beyond this limit has poor signal to noise ratio and is decidedly unusable.

Finally, it is important to measure the applied force during calibration. The most convenient way of achieving this at present is to use a modally tuned impact hammer. These hammers are typically instrumented with a piezoelectric sensor in the tip. The hammer



structure has been modally tuned to eliminate the resonant vibrations of the piezoelectric tip. Therefore, there are negligible inertial responses of the sensing element and the measured response is proportional to the applied force. Many such hammers are commercially available. For this research, the PCB Model 086C03 was chosen which has a sensitivity of 10 mV/g and a measurement range of  $\pm 2224$  N[45].

### 3.1.3 Data Acquisition

To measure all of this high bandwidth data, a high frequency data acquisition system is required. This section is dedicated to explaining the specifics of this system. All sensor channels are fed to signal conditioning units. These units power the sensors as well as allow for setting of gains and removing DC offsets.

Each channel of the piezoelectric strain sensors is fed to PCB Model 482C16 Advanced ICP signal conditioner[46]. These are capable of removing any accrued DC offset, setting gains from 0.1-200, and many other functions which are less useful for this application. The PCB Impact Hammer is similarly sent through a PCB Model 482C05 Basic ICP signal conditioner[47]. This is a simpler version the Model 482C16 that simply handles the ICP current levels. Finally the accelerometers are fed to Measurement Specialties Model 101 DC signal conditioners[48]. These are capable of setting gains from 0-999 and zeroing any DC offset.

After the data is conditioned, it is sent to a data acquisition box. The Pacific Instruments Model 6010U box[49] is used. This data acquisition system (DAS) can sample up to 32 channels at a maximum of 200 kHz, well beyond our desired limit. The sampled signal is sent through a physical 20 kHz anti-aliasing filter and digitized prior to being sent to the user.

The digitized data is then collected using the Pacific Instruments PI660-6000 software[50].

This software is compatible with the 6010U DAS and allows the user to set sampling rates and length of recorder as well as change analogue filter setting and various other options. This software also allows the user to trigger the DAS via a user supplied input or a timing pulse (as will be used in future wind tunnel experiments). Finally, this software provides a quick view of the sampled binary data prior to exportation to the desired ASCII format.

## 3.2 Experimental Results

In this section, a host of experimental results is presented to further validate the techniques formulated in this dissertation. All tests utilize data from the sensors discussed in Section 3.1.2 inside of the balance calibration test article mounted on one of the support structures discussed in Section 3.1.1.

### 3.2.1 SWAT Results

A static calibration was performed on the balance calibration test article to obtain the millivolt to elastic force scaling factors. Following this, a dynamic calibration was performed on support structure 1 to obtain the modally separated dynamic calibration matrices, used to remove the elastic force contributions from the applied force reconstruction. This section overviews the results of these two calibrations.

#### 3.2.1.1 Static Calibration Results

This section presents a validation of the static calibration methodology on piezoelectric strain sensors. Additionally, a static calibration of the 6-component strain gage force balance is presented for comparison. As discussed in Section 3.1.1, a different support structure was used for the static calibration. This was to allow drag direction loading using gravity. Alternatively, a 90-degree bend support arm may be mounted to Support Structure

1. This was unavailable during the calibration of the piezoelectric gages but was used for the 6-component strain gage force balance static calibration.

To ensure consistency with static calibration methodology used by the aerospace community, the error metrics and procedures are derived from that presented in the AIAA Recommended Practice for "Calibration and Use of Internal Strain-Gage Balances with Application to Wind Tunnel Testing"[13]. As discussed in Section 2.1.3.1, the most common error metric is the Back Calculated Residuals (BCR). To present the overall performance of a particular calibration, the AIAA Recommended Practice states that the mean, standard deviation, minimum, and maximum BCR for each measurement direction should be presented. Furthermore, it suggests the normalization of these results with an engineering unit value also be presented. Examples of this value are balance measurement maximum or applied calibration maximum. For these studies, the latter is chosen.

Before presenting the results, a discussion of the testing process aids in understanding of the final results. To begin, one must apply known static loads to the model and record the millivolt output from the sensor under investigation (i.e. the 6 component foil strain gage balance or the piezoelectric strain sensors). This is a fairly simple task and the common strategy of applying static loads via suspended weights is used. A mock up of this load application may be seen in Figure 3.6.

The test article was created with screw holes at precise locations all over the model. This allows the tester to apply a load at an exactly known location. Using the orientation of the model (obtained via an inclinometer) and the map of hole locations, one may easily compute the exact, applied forces and moments with respect to a location on the model. After the load is applied and steadied, the user may record the millivolt reading for the sensor under investigation. To obtain the static calibration matrix, one needs to assemble Eq. (2.2) and solve using Eq. (2.4).

This approach yields excellent results for classic, foil strain gage sensors which con-

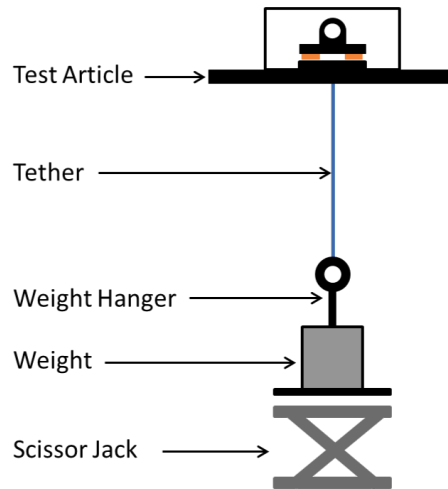


Figure 3.6: Suspended weight for static loading and drop tests.

tinuously emit a response that is proportional to the applied load. However, piezoelectric sensors act slightly different. These sensors are capacitive in nature, meaning an applied load will generate a response from the sensor which decays over time. This decay rate is a function of the piezoelectric element and is appropriately named the time constant of decay. This is a well characterized and unavoidable attribute of piezoelectric materials. However, when reviewing the static calibration methodology, one may notice a significant concern. As the weight is applied and the data becomes "steady", a drop in signal proportional to the time waited is observed.

To circumvent this concern, an average of the measured points immediately following the application of the load is considered. The measurement begins prior to load application. After data acquisition has begun, the scissor jack depicted in Figure 3.6 is used to smoothly apply the load. Finally, in post processing, the peak of each measurement is located and an average of the response over a short duration on the order of 0.25 seconds is taken. The piezoelectric strain gages used in this study[43] should lose less than 1% of their signal over this duration according to the manufacturers user's manual. Although this is small, this decay and the inability to wait until the weight is "steady" should be considered when

drawing conclusions based on the error metrics.

Finally, it should be noted that the 6 component foil strain gage force balance static calibration was performed using a calibration block rather than the weight hangers placed over the model. The use of this calibration block is standard practice by Tunnel 9 and most other users of these roll balances. The use of this precise calibration hardware surely aids in the roll balance calibration accuracy.

Figures 3.7 and 3.8 present the force and moment error, respectively calculated using Eq. (2.19). The results of the foil balance calibration (left) may be compared to that of the piezoelectric balance (right). Note that the y-axis in each have been matched for ease of comparison. A total of 135 tests were used in the foil balance calibration while 207 were used in the piezoelectric balance calibration.

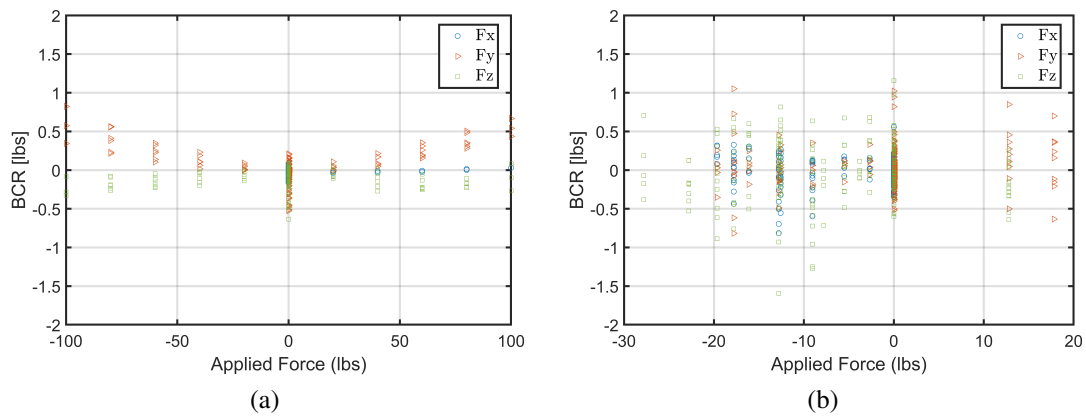


Figure 3.7: BCR of force directions for 6 component foil balance (a) and piezoelectric (b) strain gage calibration.

Upon review of Figure 3.7 it is apparent that the order of accuracy of the two calibrations is very similar. A correlation between load magnitude and accuracy is clearly evident in Figure 3.7a. A higher order calibration could be used to reduce this trend but is beyond the scope of this discussion. Upon review of the piezoelectric balance calibration, no such trend is discernible. Rather, significant scatter is observed. This can be attributed

to the error of the decay time constant and the averaging of signal near the peak. Due to unavoidable user error, small errors accrue for a given test.

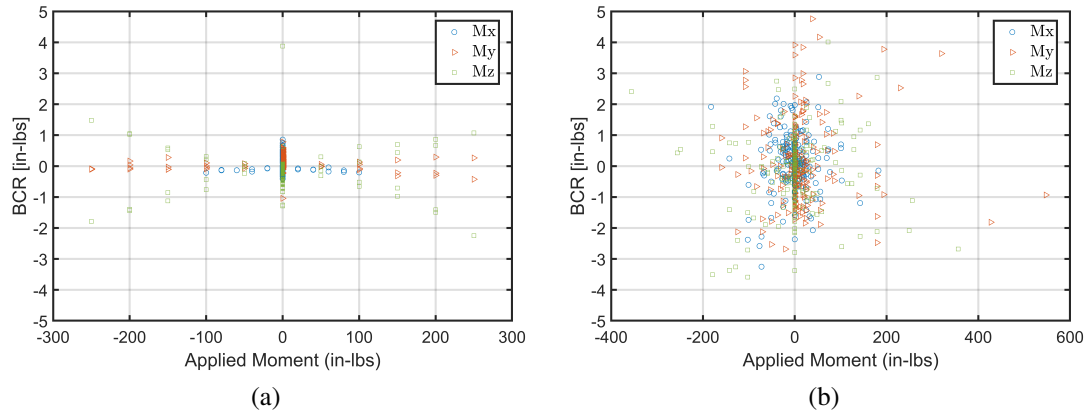


Figure 3.8: BCR of moment directions for 6 component foil balance (a) and piezoelectric (b) strain gage calibration.

Similar conclusions may be drawn for the moment BCR displayed in Figure 3.8. Additionally, the error for the piezoelectric calibration appears noticeably worse than its foil balance counterpart. Aside from the errors accumulated via signal drift and peak averaging, the imprecision of the test article dimensions could be a source of error. The calibration block used for the foil balance calibration is a very high precision machined piece of hardware. The test article has higher machine tolerances and may exhibit higher deflections during a given load application, causing additional error accumulation. Given all of these sources of error, the calibration of the piezoelectric gages is still considered to be excellent.

Finally, additional insight is gained by computing the standard deviation, mean, maximum, and minimum of these BCR values as requested by the AIAA recommended practice[13]. These values, as well as the normalized percentages and normalizing values (i.e. max applied load for a given direction) are shown in Tables 3.2 and 3.3 for the foil and piezoelectric strain gage static calibrations.

Upon review of these tables, the excellent quality of the calibrations is immediately

Table 3.2: BCR for 6-component strain gage calibration. Forces units: lbs and moment units: in-lbs.

	$F_x$	$F_y$	$F_z$	$M_x$	$M_y$	$M_z$
Standard deviation	0.0426	0.233	0.1264	0.2792	0.2234	0.6283
Average residual	-0.0196	0.0538	-0.1079	0.0448	0.1091	-0.1858
Maximum residual	0.0891	0.823	0.0879	0.8563	0.7841	3.8782
Minimum residual	-0.1664	-0.5271	-0.6333	-0.4158	-1.0427	-2.2496
Normalization value	100	100	100	100	250	250
Standard deviation	0.04%	0.23%	0.13%	0.28%	0.09%	0.25%
Average residual	-0.02%	0.05%	-0.11%	0.04%	0.04%	-0.07%
Maximum residual	0.09%	0.82%	0.09%	0.86%	0.31%	1.55%
Minimum residual	-0.17%	-0.53%	-0.63%	-0.42%	-0.42%	-0.90%

Table 3.3: BCR for piezoelectric strain gage calibration. Forces units: lbs and moment units: in-lbs.

	$F_x$	$F_y$	$F_z$	$M_x$	$M_y$	$M_z$
Standard deviation	0.1763	0.2653	0.4025	0.928	1.3579	1.2047
Average residual	-0.0228	0.0263	-0.0055	0.0982	0.1464	-0.1216
Maximum residual	0.5577	1.0522	1.1554	2.8821	4.7598	4.0111
Minimum residual	-0.8148	-0.8172	-1.5954	-3.2517	-2.682	-3.5865
Normalization value	19.6576	19.6576	27.8	182.4	547.2	356
Standard deviation	0.90%	1.35%	1.45%	0.51%	0.25%	0.34%
Average residual	-0.12%	0.13%	-0.02%	0.05%	0.03%	-0.03%
Maximum residual	2.84%	5.35%	4.16%	1.58%	0.87%	1.13%
Minimum residual	-4.14%	-4.16%	-5.74%	-1.78%	-0.49%	-1.01%

evident. Less than 1% and 2% force and moment errors are obtained for the foil balance calibration. Similarly, less than 6% and 2% force and moment errors are obtained for the piezoelectric strain gage calibration. These results are of similar order and therefore a successful calibration has been performed in both cases.

At this point, the retainment of the 6 component foil balance becomes more evident. The static force and moment measurement of these devices are superior than that of the piezoelectric balances. This is the primary motivation for the adoption of a hybrid force measurement balance as proposed.

### 3.2.1.2 Dynamic Calibration Results

After completing a static calibration, the next step of SWAT is to perform a dynamic one, where the acceleration response is considered. This section presents the dynamic calibration results and quantifies the effectiveness using modal response magnitude. For these studies, a total of 37 tests were performed across 13 hole locations. Drop tests were performed in the x, y, and z directions. Note for x and y direction (i.e. perpendicular to gravity) tests, a pulley system was used to transfer the applied load into the x or y direction. The particular orientation of this pulley is definitely a source of error as no precise orientation measurement of the pulley and tether was available.

Calibrated ten pound weights were hung at a particular location on the model using the previously made screw holes on the model and a 2.8 pound weight hanger which was fabricated for these studies. To apply a dynamic load, first one hangs the weight, steadies it, and zeros the reading on the piezoelectric load cells. After data collection begins, the weight is then removed by severing the tether with a propane blow torch. This removal of the load was found to be substantially more steady and convenient as compared to applying the weight (i.e. via dropping onto an unloaded model). It should be noted, however, that



the removal and application of a weight are mathematically equivalent.

First the original SWAT presented in Section 2.1.1 is presented. This technique is the most basic version of the SWAT where the entire time history of acceleration responses are scaled and combined with the elastic force to recover the applied forces and moments. The results of this reconstruction for a drop test applied at hole 29 are presented in Figure 3.9. To provide fair comparison with the other SWAT variants, the elastic force and acceleration contributions were low pass filtered at 200 Hz.

Hole 29 was chosen because two directional moments were applied for z-direction forces at this location. The accuracy is subjectively common when compared to the other 12 hole locations. This test is used to qualitatively discuss the effectiveness of each SWAT approach. A more quantitative analysis is presented later in this section.

The effectiveness of the static calibration is immediately evident. The scaled elastic force oscillates the applied magnitude in each direction in Figure 3.9. However, obviously using solely the static calibration is unacceptable as the elastic force (blue curve) largely overshoots the applied magnitude and continues to ring down for the entire time history. After applying the SWAT, this overshoot and subsequent oscillations are reduced considerably and the applied step load becomes more obvious. Some overshoot and higher frequency dynamics are still evident, however, the SWAT is very effective at reducing the elastic oscillations.

Next, it is of interest to see the effects of applying the modally separated SWAT. These results for the same test case are shown in Figure 3.10. As in the original SWAT, this variation has also performed adequately at removing the elastic oscillations from the statically calibrated result. However, as is most easily seen when comparing Figures 3.9e and 3.10e, the overshoot and higher frequency dynamics have been further reduced by applying the modally separated variation. For this study, the signals were filtered at 15, 25, 50, 120, and 200 Hz. These bands were chosen to isolate significant dynamics at approximately 11, 21,

33, 89, and 172 Hz. The elastic force and acceleration measurements are low pass filtered at 200 Hz as to remove all higher frequency contributions.

Finally, it is of interest to assess the performance of the modally separated SWAT with a damping matrix considered. These results for hole 29 are shown in Figure 3.11. The same frequency bands as in the modally separated SWAT variant were used for this investigation. Additionally, the velocity data was obtained using a cumulative trapezoidal integration of detrended acceleration response. Using integrated acceleration response proved more effective than differentiated strain data. The latter amplifies noise and therefore decreases performance. Again, the accuracy is increased when compared to the original SWAT. However, little to no performance gain is obvious in comparison the the modally separated variant. This is an expected result upon review of Section 2.1.3.3. Similarly to that which is shown in Figure 2.4c, our system is very lightly damped. Therefore, very small performance change between the two approaches is expected.

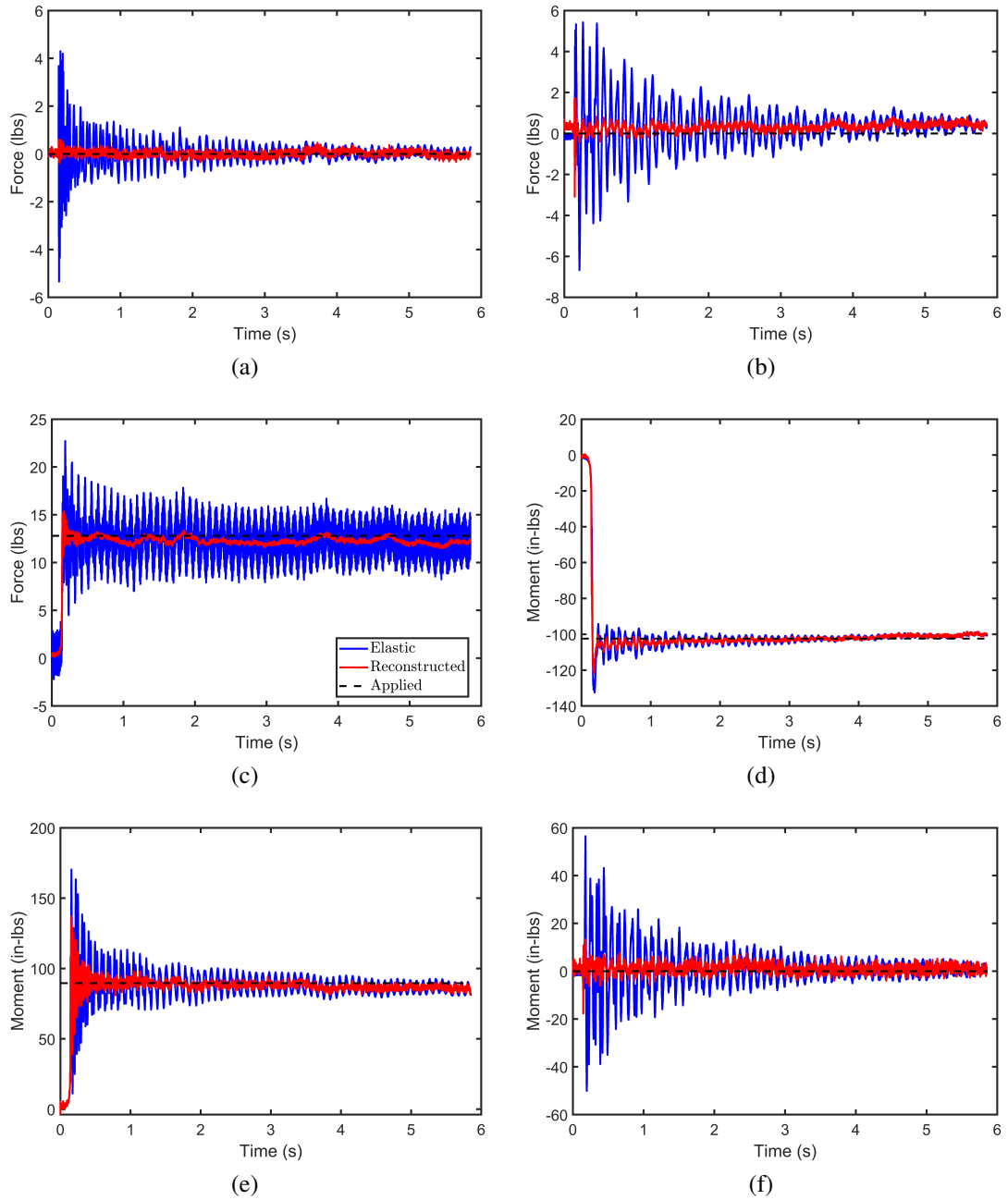


Figure 3.9: SWAT force and moment reconstruction for a 12.8 lb drop test applied at hole location 29. The original SWAT was used and  $F_x$  (a),  $F_y$  (b),  $F_z$  (c),  $M_x$  (d),  $M_y$  (e), and  $M_z$  (f) are all shown.

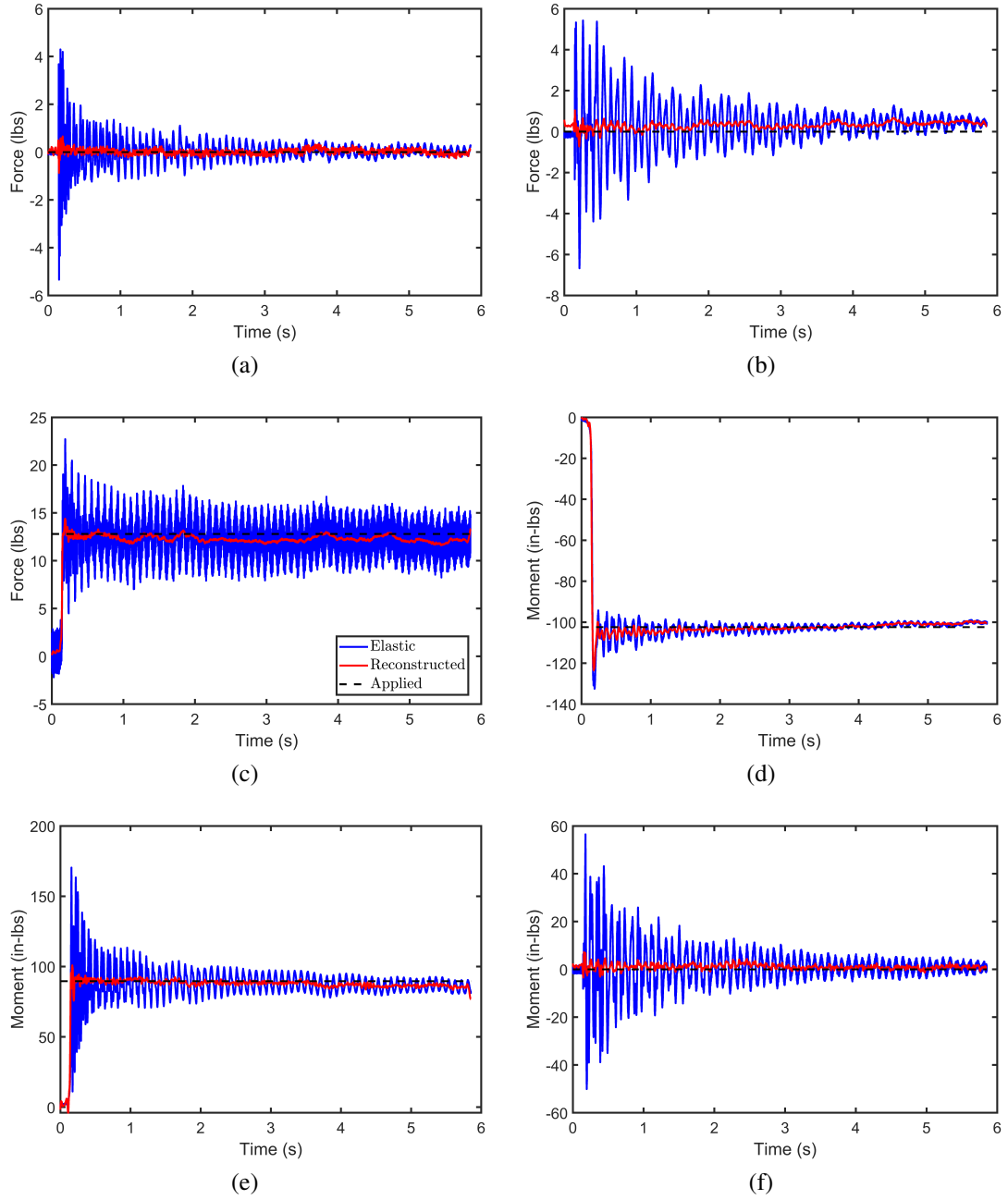


Figure 3.10: SWAT force and moment reconstruction for a 12.8 lb drop test applied at hole location 29. The modally separate SWAT was used and  $F_x$  (a),  $F_y$  (b),  $F_z$  (c),  $M_x$  (d),  $M_y$  (e), and  $M_z$  (f) are all shown.

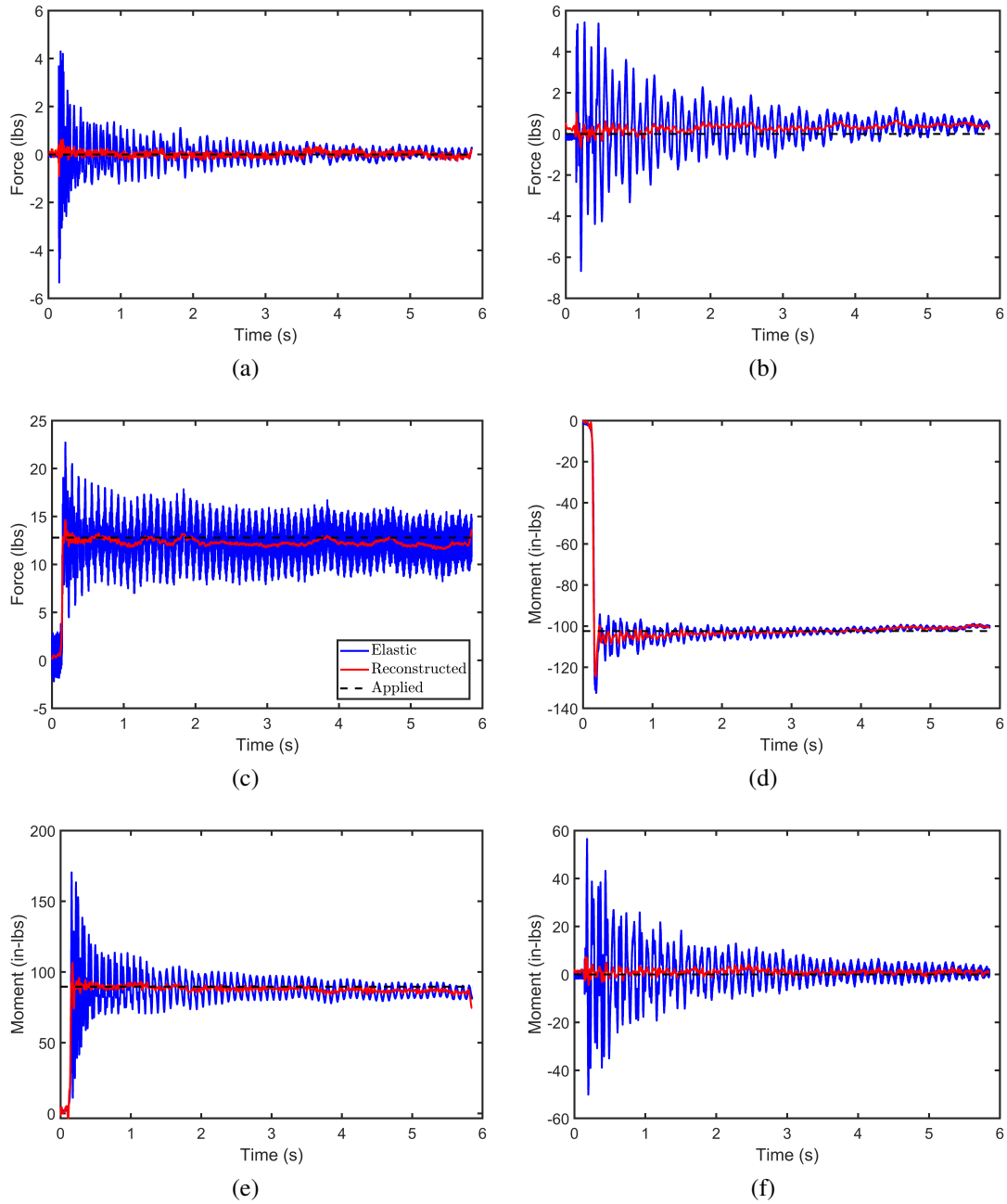


Figure 3.11: SWAT force and moment reconstruction for a 12.8 lb drop test applied at hole location 29. The modally separate with damping SWAT was used and  $F_x$  (a),  $F_y$  (b),  $F_z$  (c),  $M_x$  (d),  $M_y$  (e), and  $M_z$  (f) are all shown.

Unpacking this analysis a bit further, one may observe the Fourier transform of the z-direction for the elastic force and reconstructed force for each of the three SWAT variants. The pwelch function in Matlab was chosen to obtain a smoother (and consequently more readable) frequency response. Ten windows with 50% overlap were used to perform the Fourier transform. The result of each of the three SWAT variants versus the elastic force is displayed in Figure 3.12. Additionally, the frequencies under investigation are approximately denoted using vertical dashed lines. Immediately upon review of Figure 3.12, the previously mentioned conclusions become more obvious. The largest dynamics at approximately 10, 21, and 33 Hz are removed to a high degree for all three variants. However, at higher frequencies (e.g.  $> 40$  Hz), the original SWAT actually amplifies the higher frequency modal contribution as compared to the elastic response. The other variants however, have performed as expected and slightly reduced these contributions. Finally, little to no difference is obvious between modally separate with and without a damping matrix for this low damped structure.

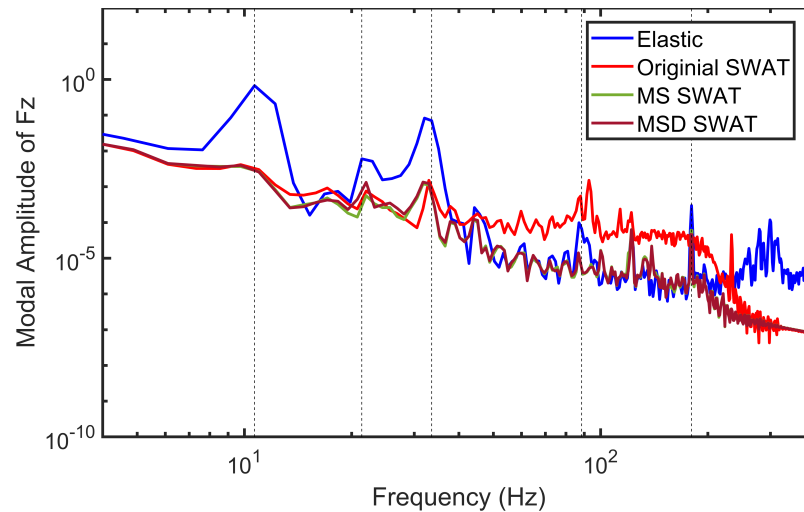


Figure 3.12: Amplitude spectra comparison for SWAT reconstruction using original, modally separate (MS), and modally separate with damping matrix (MSD).

From here it is of interest to quantify these results across all 37 tests. To do this, first

the amplitude of the Fourier transform at each of the five frequencies was collected for the elastic force and each of the three SWAT variants. One may notice small deviation in the frequency location after reconstruction and if various channels are observed. For this reason, a range of  $0.8f_i - 1.2f_i$  was searched for a peak and selected as the modal amplitude for a particular modal frequency,  $f_i$ . This prevents inadvertent biasing by selecting a trough.

Next, the modal amplitude of the reconstructed force is compared to that of the elastic force. A percentage in modal reduction (%MR) is computed as

$$\%MR = \frac{Y_i^e - Y_i^r}{Y_i^e} \times 100 \quad (3.1)$$

where  $Y$  is the amplitude of the time domain signal, the subscript denotes the frequency index of interest, and superscripts  $e$  and  $r$  denote elastic or reconstructed, respectively. The %MR for each of the five frequencies of interest and each of the six directions of force and moments for the original SWAT is presented in Table 3.4.

Table 3.4: Original SWAT modal reduction percentages averaged over all 37 tests.

$f$ (Hz)	$F_x$	$F_y$	$F_z$	$M_x$	$M_y$	$M_z$
11	99.49%	98.41%	99.73%	84.23%	99.27%	98.41%
21	99.09%	94.80%	89.01%	91.21%	94.73%	97.88%
33	98.07%	97.97%	98.14%	90.58%	90.02%	96.93%
89	98.25%	-691.37%	-559.86%	-2516.70%	-11149.61%	-3236.93%
172	-79.90%	-1316.20%	-47.54%	-16447.55%	-19355.86%	-16397.45%

The first notable observation is the extreme effectiveness of the SWAT at removing the most dominate structural modes. The first three modes of vibration are reduced by at least 80% in all directions and as high as 99% in some directions. This demonstrates the power of the SWAT at reducing modal dynamics. However, upon review of the less dominate modes (i.e. modes four and five), less effective modal reduction is observed and in most

cases, severe modal amplification. This is consistent with our qualitative observations and the specific result shown in Figure 3.12. The equal weighting of all modes in the formation of a dynamic calibration matrix causes amplification of less dominant modes. The ability to consider each mode separately, and apply appropriate scaling matrices for each is the motivation behind the modally separate SWAT.

One may also compute the percent modal reduction for the modally separate SWAT variant. These values are shown in Table 3.5. As expected, this method performs excel-

Table 3.5: Modally separate SWAT modal reduction percentages averaged over all 37 tests.

$f$ (Hz)	$F_x$	$F_y$	$F_z$	$M_x$	$M_y$	$M_z$
11	99.5%	98.9%	99.8%	83.6%	99.6%	98.9%
21	99.0%	97.7%	93.4%	91.8%	97.2%	98.8%
33	98.7%	97.5%	98.2%	95.2%	99.4%	99.0%
89	98.6%	1.1%	91.9%	12.9%	88.0%	1.7%
172	53.8%	51.6%	86.0%	51.8%	47.5%	59.8%

lently at removing the dominant modes of vibration. The reduction of modal dynamics for the first three modes are on par or better when compared with the original SWAT. However, the key improvement is obvious when observing the fourth and fifth mode. Rather than amplifying the modes, significant modal reduction is apparent for many of the directions. Some of the reduction is negligible, however, the modal dynamics were small in magnitude for these directions. Therefore one may not expect a large reduction.

Lastly, the results of modally separated SWAT with a damping matrix considered is presented. The percent modal reductions are shown in Table 3.6. Very little difference is evident between the modally separated with and without damping matrix result. Most notably, the %MR for the  $M_x$  direction of the fifth mode has increased by about 9%. All other values are very comparable.

Furthermore, one may notice decreased effectiveness of the modally separate SWAT



Table 3.6: Modally separate with damping SWAT modal reduction percentages averaged over all 37 tests.

$f$ (Hz)	$F_x$	$F_y$	$F_z$	$M_x$	$M_y$	$M_z$
11	99.5%	99.0%	99.8%	83.7%	99.6%	98.9%
21	99.1%	97.7%	87.1%	91.4%	96.6%	98.8%
33	98.7%	97.4%	98.1%	94.5%	99.3%	99.0%
89	98.4%	0.1%	91.8%	11.9%	84.8%	2.6%
172	55.1%	52.0%	88.9%	60.5%	48.4%	60.1%

(with or without damping) at the fifth mode. This highlights a practical limitation of the SWAT. At higher frequencies, the amplitude decreases considerably and improvements become difficult. Additionally, many modes are very closely spaced which makes filtering very difficult as the cut off frequency cannot be exact. Lastly, at even higher frequencies, the acceleration and strain response can become slightly out of phase due to small system delays such as electrical transfer speed and stress wave propagation. Accounting for these delays would require significant system characterization and detract from the elegant simplicity of the method. Therefore, further improvement is not considered and simply band limit the effectiveness of the SWAT. For these studies, the method is band limited at 200 Hz.

### 3.2.2 TDDM Results

This dissertation focuses on three TDDMs; a "conventional" TDDM which utilizes zero order discretization of the convolution integral at Tikhonov regularization, the CMM which uses a linear discretization and least squares inversion, and the GDLM, a generalized formulation for CMM which allows for higher order discretization. This section is devoted to validating the latter two techniques on the experimental system presented in Section 3.1.

### 3.2.2.1 SIMO CMM Experimental Results

The experiments discussed in this section were performed on Support Structure 1 described in Section 3.1.1. For clarity, a brief overview of the inputs and outputs are described here. To generate the IRFs, the dynamic strain response to input hammer pulses was recorded in each of the three directions. Ten seconds of response and input force was sampled at 25 kS/s. This data set was truncated to 50 ms after the pulse initiation to reduce computational load. The applied force was measured using a modally tuned hammer, instrumented with a piezoelectric strain sensor in the tip. Each load was applied normal to the respective surface. In order to achieve an accurate calibration, many tests were recorded at different locations and with various model alignments. One wants to encompass a large portion of the model to account for any possible loading location as well as contain the expected loading magnitude. Hammer pulse inputs were applied in all three axial directions to account for a purely x, y, or z direction applied force. Repeat tests were performed to identify outliers.

The output degrees of freedom are each direction of the individual sensors. There are four piezoelectric strain sensors, each measuring strain in three directions. This results in twelve output degrees of freedom. Since the model and sting assembly has infinite DOFs, one may choose as many input DOFs as required. For this study, 29 different input hammer locations were used. Redundant tests were performed on each location and the best quality data was selected based on signal to noise ratio. This resulted in 134 total tests across the 29 loading stations. Each of the tests was considered a different input. Four of these loading locations (A, B, C, and D) are displayed in Figure 3.1.

The reconstruction of one of the hammer pulses used to generate the IRFs can be seen in Figure 3.13. This reconstruction closely matches the measured input. For this analysis  $R_1 = R_2 = 2$ . An example output in the same direction as the applied load is displayed over

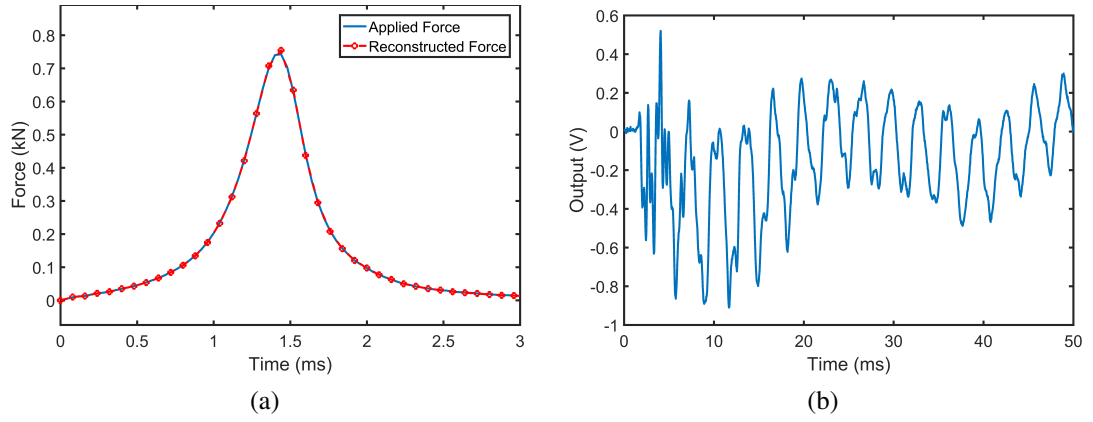


Figure 3.13: Loading Point A: z-direction impulse reconstruction (a) using  $R_1 = R_2 = 2$  compared with example unfiltered z-direction sensor output (b) for full time scale.

the whole time history used for this analysis.

To demonstrate the effectiveness of the method in all three directions, reconstructed forces at three separate locations, B, D, and C are shown in Figures 3.14, 3.15, and 3.16, respectively. The loading locations and directions for each test are depicted in Figure 3.1.

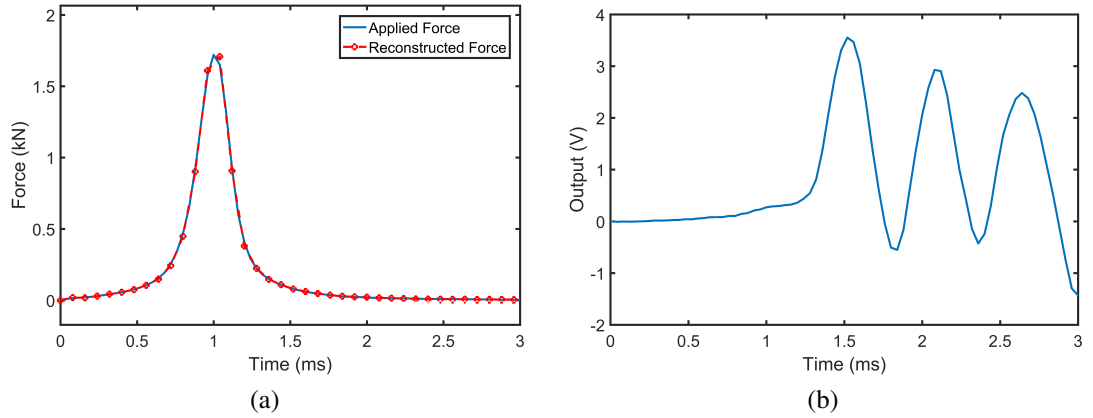


Figure 3.14: Loading Point B: x-direction impulse reconstruction (a) using  $R_1 = R_2 = 2$  compared with example unfiltered x-direction sensor output (b).

It is important to quantify the reconstruction of all input force pulses. Therefore, the peak and area differences are again considered as was done in the numerical experiments. The AD and PD are given by Eqs. (2.124) and (2.125), respectively. Since the measured

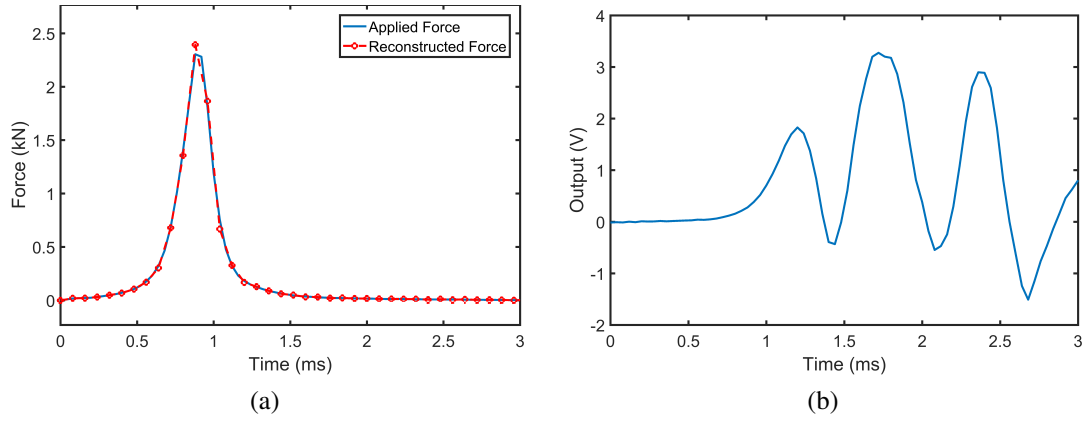


Figure 3.15: Loading Point D: y-direction impulse reconstruction (a) using  $R_1 = R_2 = 2$  compared with example unfiltered y-direction sensor output (b).

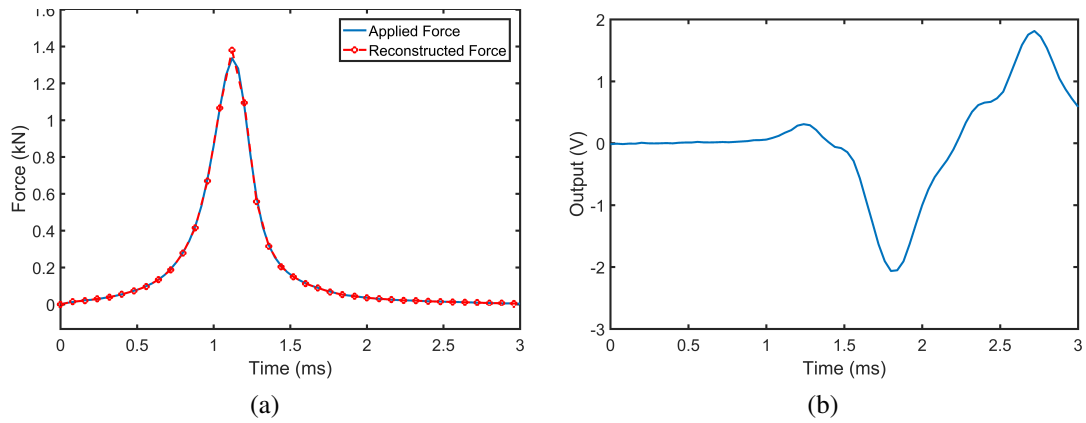


Figure 3.16: Loading Point C: z-direction impulse reconstruction (a) using  $R_1 = R_2 = 2$  compared with example z-direction sensor output (b).

and reconstructed signals have different discretizations, an  $L_p$  norm of the error is not applicable. The chosen quantities are useful for this application because area and peak value are important parameters in describing a pulse. These two quantities were computed for all tests. The average and maximum errors are shown in Table 3.7. These errors are small signifying excellent pulse reconstruction accuracy. The largest errors would likely be reduced with additional resolution.

It is also be useful to discuss why minimizing the condition number may not always be

Table 3.7: Input Pulse Reconstruction Error Analysis

	Maximum	Average
AD	0.90%	0.16%
PD	6.73%	2.94%

the optimal strategy for accurate force reconstruction. Consider the experimental data used in this section. The results presented utilize  $R_1 = R_2 = 2$ . Upon review of these results, one might wonder if the condition number is low enough. One may expect a downward trend and that our answer could be improved with an increased ratio. The average condition number for all of the tests for  $\hat{A}^T \hat{A}$  and  $\hat{B}^T \hat{B}$  can be seen in Figure 3.17 versus their respective ratios.

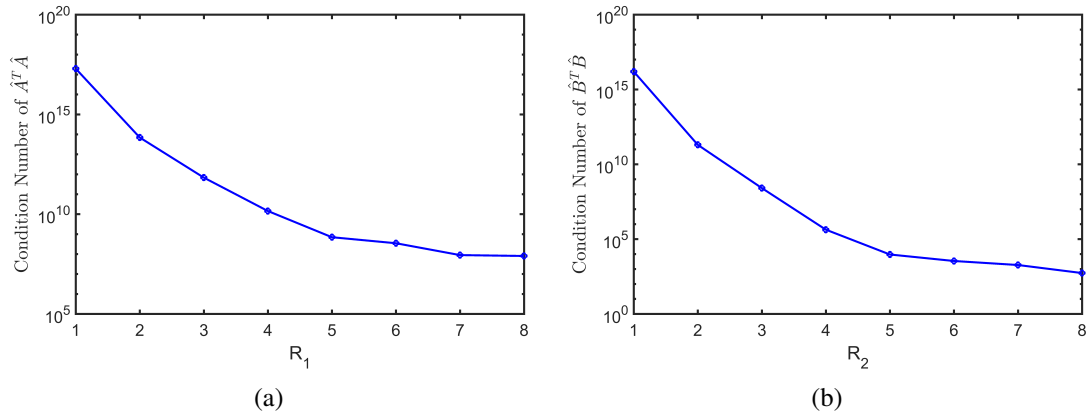


Figure 3.17: Average Condition Number for all impulse reconstructions. IRF condition number versus  $R_1$  (a) and input reconstruction condition number versus  $R_2$  (b) are both shown.

As expected, when the ratio is increased, the condition number improves for both the IRF construction and the input reconstruction problem. However, this may not result in a more accurate solution. To appreciate this, the average and max peak and area differences are plotted in Figure 3.18 versus  $R_2$ .

Clearly as  $R_2$  is increased beyond 2, the reconstruction accuracy decreases. The lack of resolution causes significant errors in both the peak and area reconstructions. For this

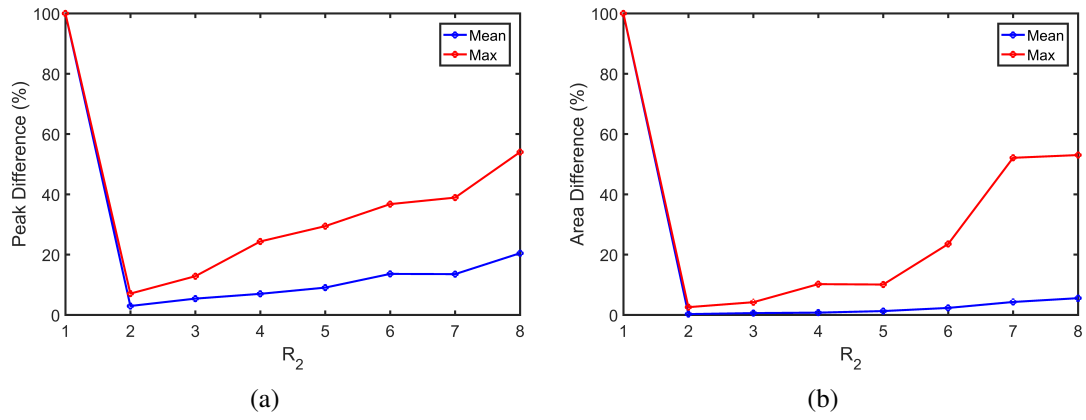


Figure 3.18: Error metrics for impulse reconstruction versus  $R_2$ . Mean and max values for peak difference (a) and area difference (b) are both shown.

case, it is desirable to keep the ratio as small as possible. Using multiple outputs has constrained the problem enough such that a higher ratio is not required. This demonstrates that resolution of input reconstruction may drive selection of ratios which may limit the flexibility in minimizing condition number. In addition, since a smaller  $R_1$  and  $R_2$  parameter resulted in an acceptable reconstruction, the SIMO case has better constrained the problem as compared to the SISO case.

Note that qualitatively similar results are found if  $R_1$  is fixed at 2 and  $R_2$  is varied. The optimal result is still at  $R_1 = R_2 = 2$ . For brevity, these results are not displayed.

### 3.2.2.2 SIMO GDLM Experimental Results

The GDLM was applied to Support Structure 2 as described in Section 3.1.1. An example hammer force reconstruction is shown in Figure 3.19. The first order case assumed linear interpolation of both the IRF and applied force to be reconstructed. The third order case assumes cubic interpolation of both the IRF and applied force to be reconstructed. The intermediate points of the third order reconstruction show a near perfect match with the measured pulse. The lack of resolution in the first order method causes a slight discrepancy

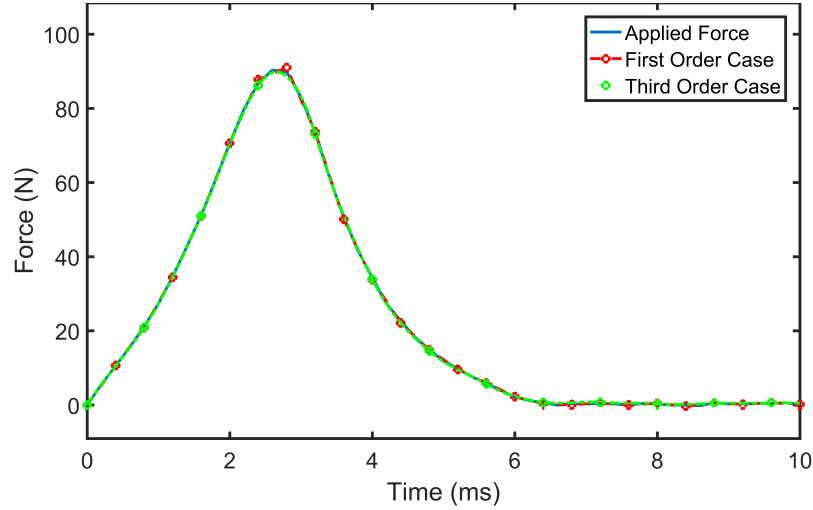


Figure 3.19: Input force reconstruction using time domain deconvolution method with first (red) and third (green) order formulations. Third order reconstruction nearly perfectly overlaps measured (blue) force. A sampling rate of 5 kHz and constraint parameters,  $\hat{R}_1 = \hat{R}_2 = 2$  were utilized for this demonstration.

at the peak of the impulse, however the reconstruction is still good.

One may note improved performance over the SISO case depicted in Figure 2.14. Although the SNR for the two investigations was comparable, the addition of multiple outputs has helped to better constrain the problem and allow for the usage of a smaller  $\hat{R}_1$  parameter.

Since 24 reconstructions are used, it is important to consider the error across all tests. Therefore, the mean and maximum peak and area errors for all reconstructions were computed for both orders. The linear method is expected to reconstruct pulses accurately for the low  $R_1$  cases. However, as  $R_1$  increases, the cubic formulation is expected to become superior.

To demonstrate this, the constraint parameters are varied and the reconstruction errors are computed. The error comparison is shown in Figure 3.20. The first and third order reconstructions display very comparable error. The third order method appears superior at reconstructing the correct area at higher  $\hat{R}_1$  values.

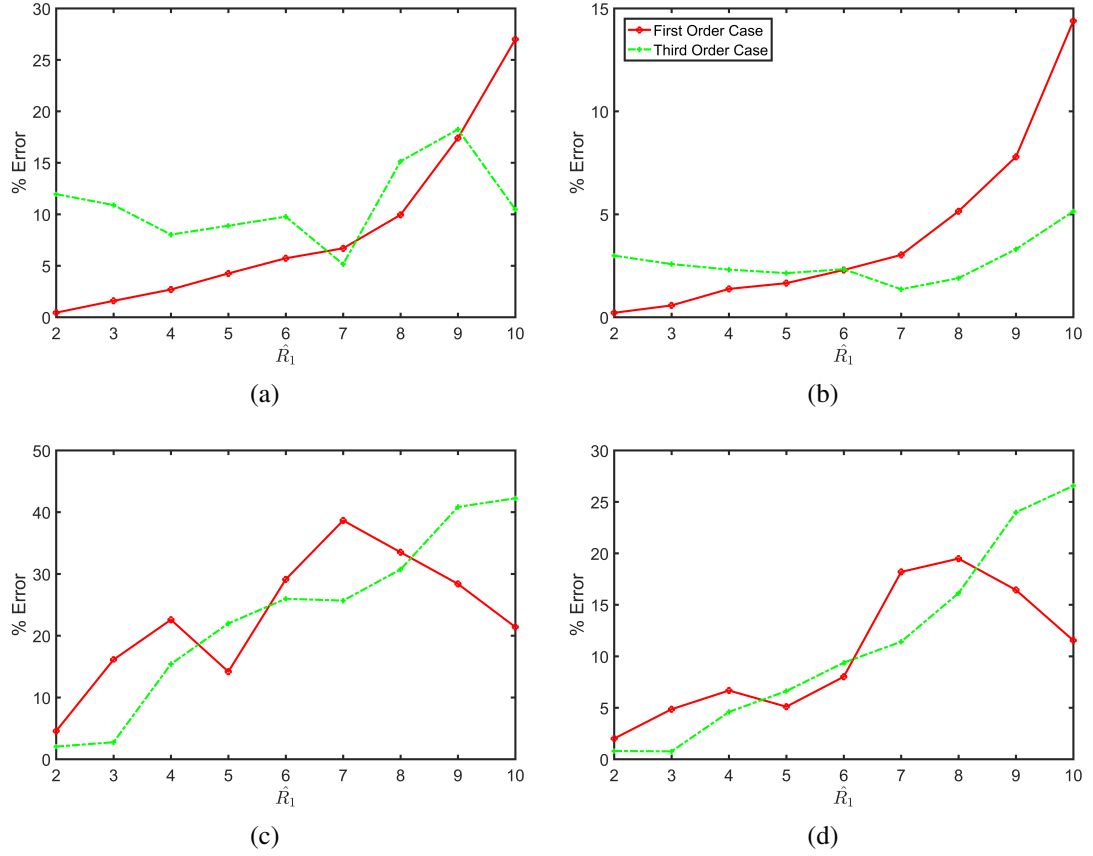


Figure 3.20: Error metrics for input force reconstruction versus  $\hat{R}_1 = \hat{R}_2$ . Maximum area (a), mean area (b), maximum peak (c), and mean peak difference (d) are all shown.

The chief problem in the inverse force reconstruction problem is the inversion of a near singular matrix. A discussion of why small singular values result in undesirable reconstructions is presented in Appendix A. To avoid noise amplification and to increase reconstruction accuracy, it is advantageous to ensure that the smallest singular values of the matrix to be inverted is not near zero. In our formulation, the matrices being inverted are  $\hat{\mathbf{A}}^T \hat{\mathbf{A}}$  for the IRF construction and  $\hat{\mathcal{B}}_i^T \hat{\mathcal{B}}_i$  for the SIMO pulse reconstruction. A concise way to compare the severity of the inversion is to compute the condition number (i.e. maximum singular value divided by minimum singular value). The smaller the condition number is, the less likely the inversion will be ill posed. Since the accuracy of the cubic method has



been shown to outclass the linear one as the constraint parameter increases, it would also be interesting to see the effect on the condition number.

The condition numbers may be seen for the IRF construction in Figure 3.21a and for the input force reconstruction in Figure 3.21b.

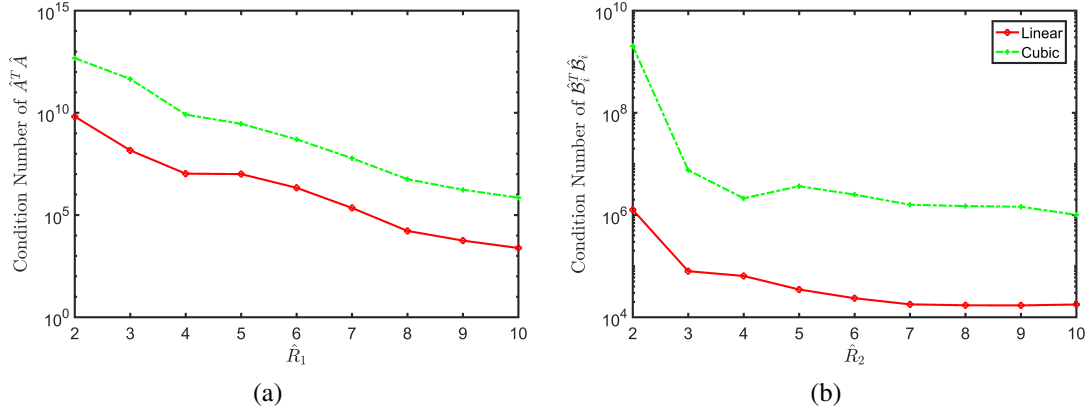


Figure 3.21: Average Condition Number for all input force reconstructions. IRF construction condition number versus  $\hat{R}_1$  (a) and input reconstruction condition number versus  $\hat{R}_2$  (b) are both shown. Both first order (red solid line) and third order (green dotted line) are shown for comparison.

It is clear to see that the first order method is better conditioned than the third order method. For any given  $\hat{R}_1$  or  $\hat{R}_2$  value, the condition number of the first order method is approximately two orders of magnitude lower.

### 3.2.2.3 MIMO GDLM Experimental Results

A SIMO force reconstruction problem is ideal. The location of the applied load is known and as is all of the information to reconstruct the force at the point. However, there may be cases where multiple input locations are of interest. In such scenarios, a MIMO formulation is required. This section provides an experimental validation of the MIMO problem for the GDLM.

For these studies, Support Structure 1 is used as much more time was allotted on this

setup to perform various experiments. Additionally, many repeat tests were with varying hammer tips. This allows for the use of the repeat formulation presented in Section 2.2.2.5. Finally, the first and third order methods are used and compared.

A dynamic calibration using the four input locations denoted in Figure 3.1 (i.e.  $p = 4$ ) and all twelve output channels of the strain sensors (i.e.  $n = 12$ ) is used to obtain the IRFs (using 5+ repeats) for each input-output pair. Then Eq. (2.105) is assembled. Solving via least squares inversion and separation of the  $u$  vector yields the force contribution at each calibration location. The capability to record a simultaneous pulse at two different locations is unavailable at this time so only single input tests are used. However, the mathematics behind this is analogous; a pulse at one location and zero at the other three is expected.

The results of this MIMO reconstruction using first and third order GDLM for a pulse applied at location C are displayed in Figure 3.22. Excellent MIMO force reconstruction is observed for this very short duration ( $<1$  ms) applied pulse. As expected, the pulse was accurately reconstructed at the input location while the other three locations display a near zero applied load.

The first and third order reconstructions yield about identical levels of accuracy. As in the numerical studies, some pulse clipping is observed from use of the first order method. The inter-point curvature of the cubic formulation allows for slightly higher accuracy at locations of large change (i.e. at start of pulse and at peak). Since this applied load is smooth, a cubic approach is recommended, however the linear results still achieve high accuracy.

One may additionally be interested in the center of moment forces and moment applied to the test article. Here the center of moment as the geometric center of the four piezoelectric strain gages in  $x$  and  $y$  (see Figure 3.1 for coordinate system) and halfway through the sensor thickness in  $z$ . With this center of moment and coordinate system one would expect a negative  $z$ -force, a negative moment about the  $x$  axis, and a very slight positive

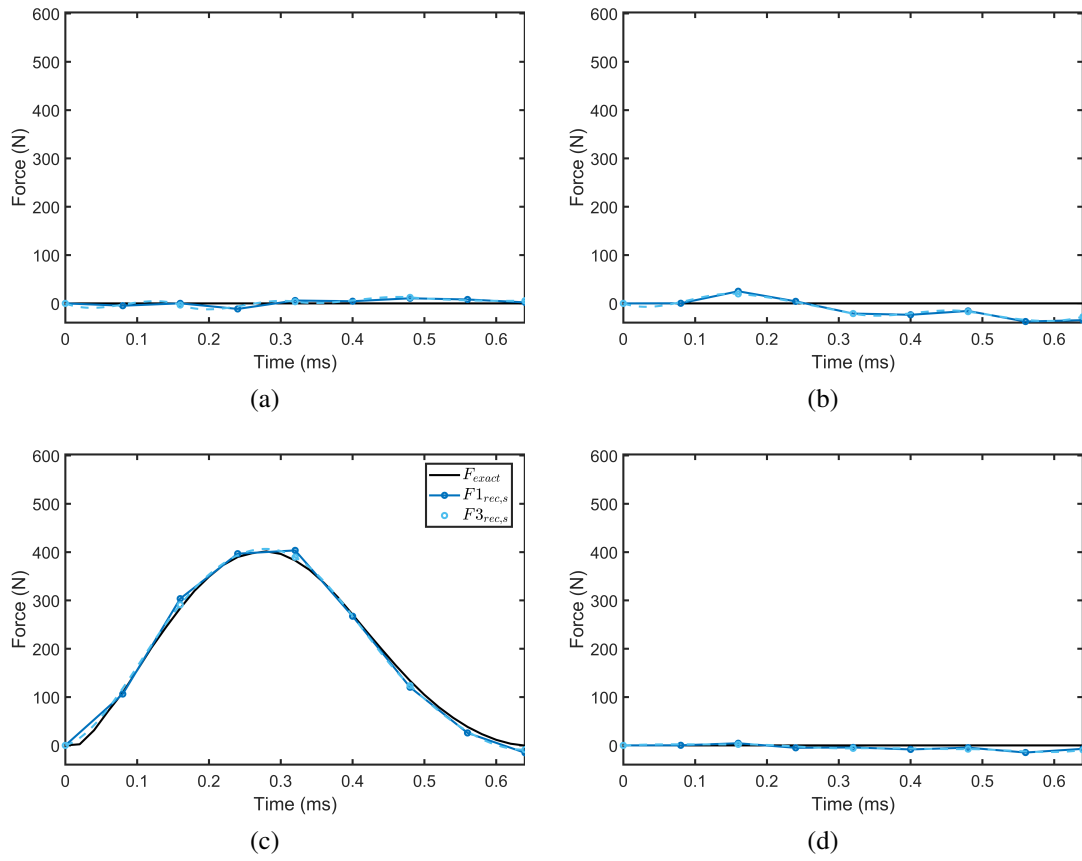


Figure 3.22: First and third order GDLM MIMO force reconstruction of point load applied at location C.  $R_1 = R_2 = 4$  and a sampling rate of 50 kHz were used. Reconstructions at hole locations A (a), B (b), C (c), and D (d) shown in Figure 3.1 are all shown.

moment about the y axis (as hole C is slightly in front of the x axis). These assumptions are affirmed when reviewing the results shown in Figure 3.23.

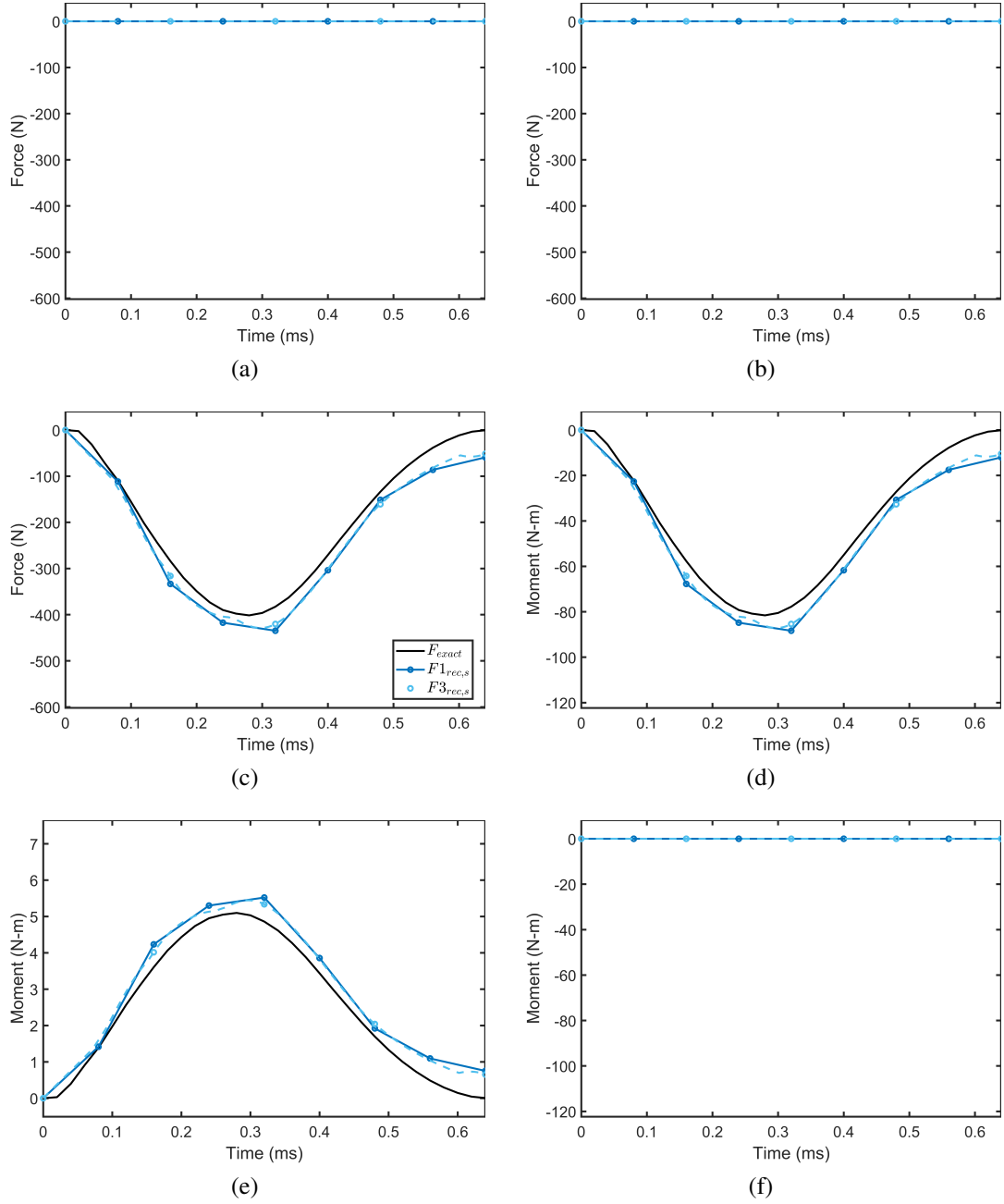


Figure 3.23: First and third order GDLM MIMO force and moment reconstruction of point load applied at location C.  $\hat{R}_1 = \hat{R}_2 = 4$  and a sampling rate of 50 kHz were used.  $F_x$  (a),  $F_y$  (b),  $F_z$  (c),  $M_x$  (d),  $M_y$  (e), and  $M_z$  (f) are all shown.

The reconstruction accuracy has declined some as compared to the point force result shown in Figure 3.22. This is to be expected as small errors from the other channels can add together and cause further error in the final forces and moments. Slight over prediction of the applied forces and moments are observed for this example.

Although this works well for the still highly over constrained case (i.e.  $n \gg p/R_2$ ) as the IRM is 12 times longer than it is wide, results will likely decline when more input locations are of interest. To investigate this claim, the above analysis is repeated with a variable number of input locations from one (i.e. the SIMO formulation) to the worst case MIMO formulation of all 16 calibration locations. To present these results in a concise manner, the maximum and average peak and area differences of the reconstruction at the input location is computed for each case. These results versus number of input locations are depicted in Figure 3.24.

The expected result is obvious upon review of this figure. The solution quality degrades as the requested number of inputs increases. Furthermore, when the number of inputs approaches and exceeds the number of outputs (i.e.  $n = 12$ ), the solution blows up and unacceptable reconstructions are obtained. As the constraint parameter is increased, the trend does not appear to change dramatically meaning there is a hard stop of  $p < n$  for this formulation. The only option is to increase the number of outputs. In the next section, the addition of acceleration measurement allowing for more input locations is shown.

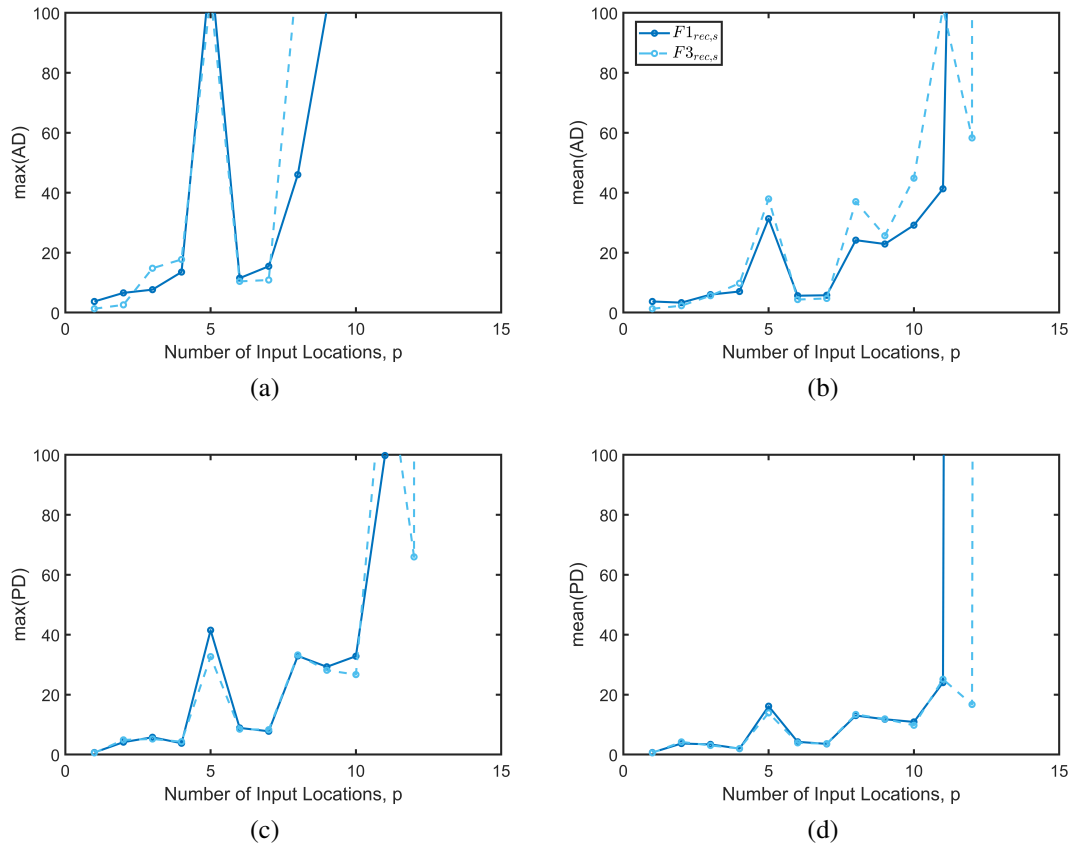


Figure 3.24: Area and peak difference of input pulse force versus number input locations using the first and third order GDLM and  $\hat{R}_1 = \hat{R}_2 = 4$ . Max area (a), average area (b), max peak (c), and average peak (d) difference are all shown.

### 3.2.2.4 Acceleration Deconvolution

In real systems, it is often far easier to obtain acceleration measurements as opposed to strain measurements. The latter typically needs to be integrated into the model design where as the former can be added as an afterthought. Additionally, the luxury of additional information can be useful in over-constraining the inversion in the event of a large constraint parameter requirement or MIMO formulation. Therefore, the acceleration-only and combined acceleration-strain approaches are validated on our Balance Calibration test article.

The same data set used in Section 3.2.2.3 was used for this study. Note that many tests were not used from that set due to saturation of the accelerometers. Future experiments could be performed with a larger dataset and more optimal accelerometers. A total of 188 hammer calibration tests were used at 15 locations in the x, y, and z direction. Eleven to fourteen tests at each location were used after the removal of the saturated datasets. As noted in the Section 2.2.3.7, two repeats should be sufficient for most cases but addition accuracy can be achieved by increasing this count.

Using Eq. (2.109) on the acceleration and strain signals, separately, the acceleration or strain IRF may be solved. Then, a random test set from the repeats is chosen as the test set. Using that test set, Eq. (2.114) is solved for the reconstructed force. Equation (2.104) may also be solved for the acceleration or strain deconvolution and compare these results to the combined expression. An example result is displayed in Figure 3.25. Note excellent agreement is shown for all three methods for the case displayed. This is characteristic of the other fourteen locations. However, an objective comparison is sought.

Again, for pulse reconstruction, the Area and Peak Differences are considered. The max and average values for strain-only (S), acceleration-only (A), and combined acceleration-strain (C) are shown in Table 3.8.

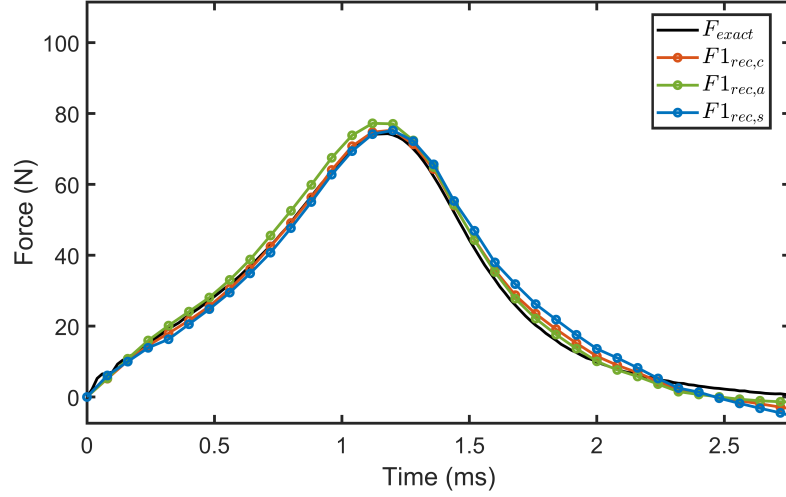


Figure 3.25: Acceleration only, strain only, and combined acceleration-strain example de-convolution result.

Table 3.8: Peak and area differences for strain only, acceleration only, and combined strain-acceleration linear GDLM force reconstruction.

	Maximum			Average		
	S	A	C	S	A	C
AD	43.5	46.09	30.14	7.32	9.26	6.66
PD	26.14	34.6	19.18	6.22	7.48	5.27

From these results it is clear that all three methods perform extremely well. The acceleration-only result is the worst. This shows that there is some advantage to using the more difficult to obtain strain measurement. However, the level of improvement is small. As expected, the combined approach yields the best results on average. Since more information is available, higher levels of accuracy are achievable. Again these improvements are small.

One of the motivations for utilizing acceleration measurements in the reconstruction problem is to further over constrain the inversion. From the above analysis, it is clear that this has a small influence for the SIMO analysis. However, the addition of acceleration measurements can prove more influential in the MIMO problem. To demonstrate this, the



MIMO analysis presented in Section 3.2.2.3 is repeated but the acceleration only, strain only, and combined acceleration-strain approaches are compared. The same peak and area differences versus number of inputs are displayed in Figure 3.26.

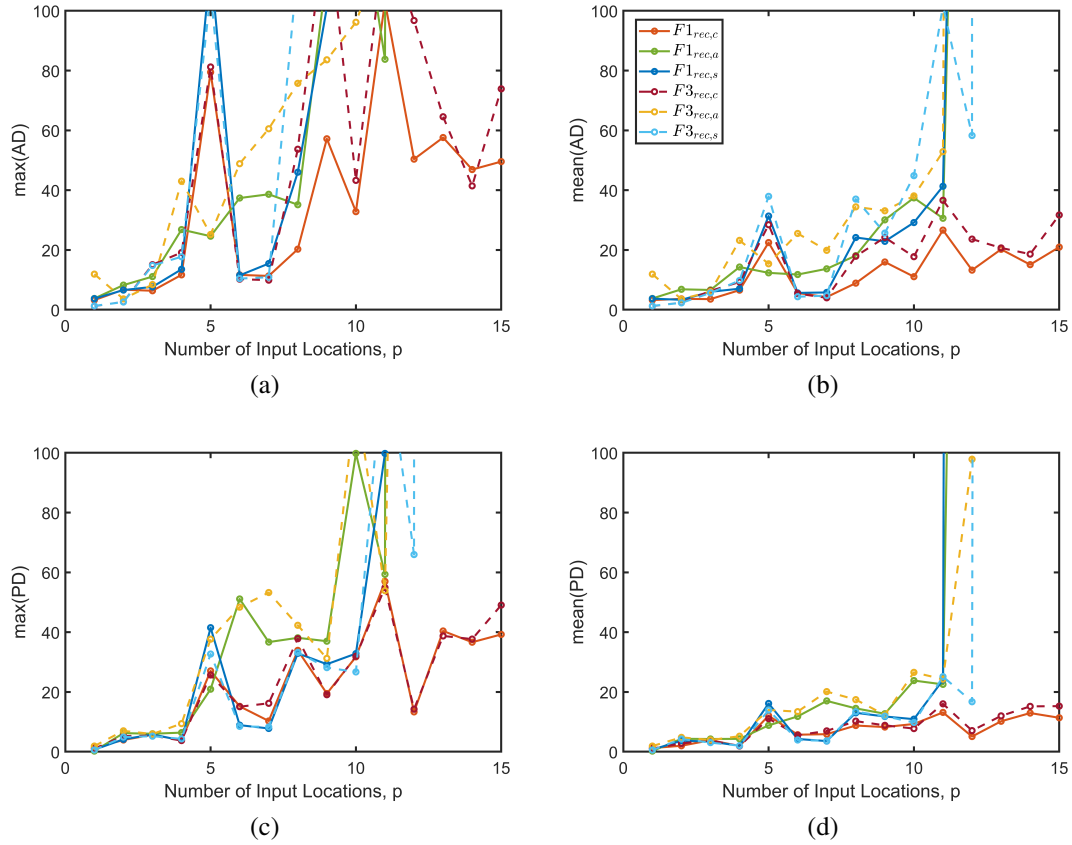


Figure 3.26: Area and peak difference of input pulse force versus number input locations using the first and third order GDLM,  $\hat{R}_1 = \hat{R}_2 = 4$  with acceleration measurements. Max area (a), average area (b), max peak (c), and average peak (d) difference are all shown.

Similarly to the previous analysis, if only acceleration channels (i.e. green and yellow curves) are considered, the result blows up as the  $p = n$  condition is approached. However, when strain and acceleration channels are simultaneously considered (i.e. red and maroon curves) one is able to increase the number of input locations (as  $n$  has doubled). Adding this information allows for a denser grid of input locations.

### 3.2.3 FDIM Results

In this section of the dissertation, the FDIM is validated on Support Structure 1. In this section only the alterations of the FDIM: the FRF solved version and using multiple input tests at the same location are of interest. The majority of this section considers strain data as the output. However, as in the presentation of the TDDM results, the acceleration response is used to quantify some trends about the method.

#### 3.2.3.1 SIMO FDIM Experimental Results

The same large dataset used in Section 3.2.2.4 is used in these studies. The luxury of using this data set is that 10-12 calibration inputs are available per hole location. As noted in the numerical studies, increasing the number of calibration inputs at a particular hole location increases the accuracy of the FDIM, so this is desirable.

Using the repeat formulation discussed in Section 2.3.2.2, a sample result shown in Figure 3.27 is obtained. As expected, excellent pulse reconstruction is observed and this

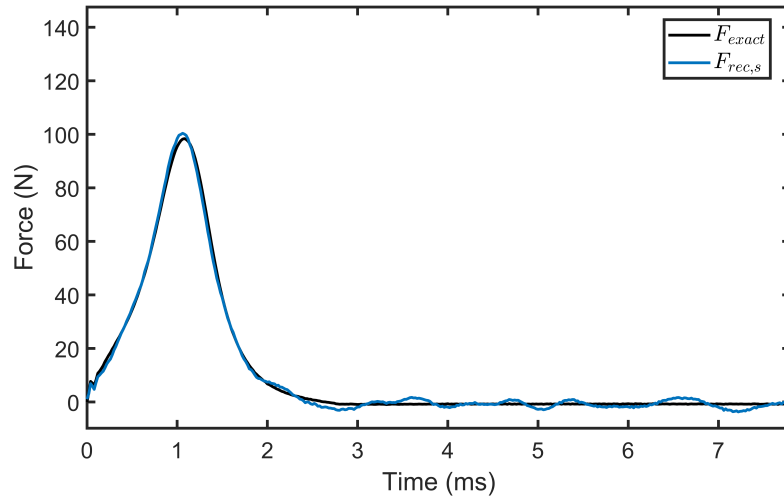


Figure 3.27: FDIM SIMO force reconstruction experimental example result. Eleven calibration input tests used for this reconstruction.

accuracy is characteristic of the other hole locations. Eleven to fourteen calibration tests were performed at each hole. As discussed in Section 2.3.3.4, adding these tests during calibration should improve reconstruction accuracy.

To further justify the need of using multiple calibration tests at a single hole, the above analysis is repeated with a varying number of calibration tests. All 188 test pulses are reconstructed at each step and the average and max of each are recorded. When plotting these error metrics, as depicted in Figure 3.28 versus the number of calibration tests used to generate the FRF, a clear trend is observed. As in Section 2.3.3.4, it is clear that additional calibration loads substantially improve the performance of this method.

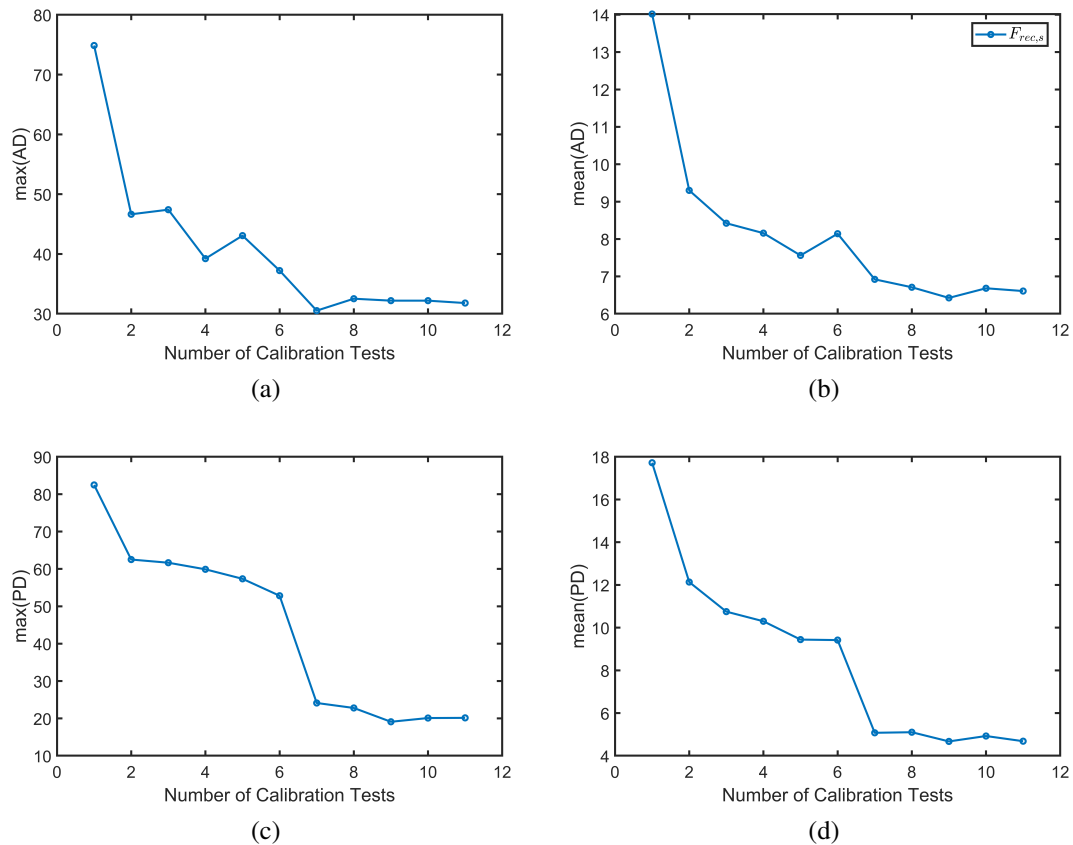


Figure 3.28: Area and peak difference of FDIM input pulse force versus number of calibration tests. Max area (a), average area (b), max peak (c), and average peak (d) difference are all shown.

### 3.2.3.2 MIMO FDIM Experimental Results

The most difficult force reconstruction case is MIMO. This section details the validation of the FDIM MIMO force reconstruction using the same data set from the previous section. The capability to supply multiple loads simultaneously is not possible on either of the test setups discussed in this dissertation. However, one may still perform a MIMO reconstruction but expect zero reconstructed load at each location other than the application location.

An example MIMO reconstruction using the hole locations depicted in Figure 3.1 is shown in Figure 3.29.

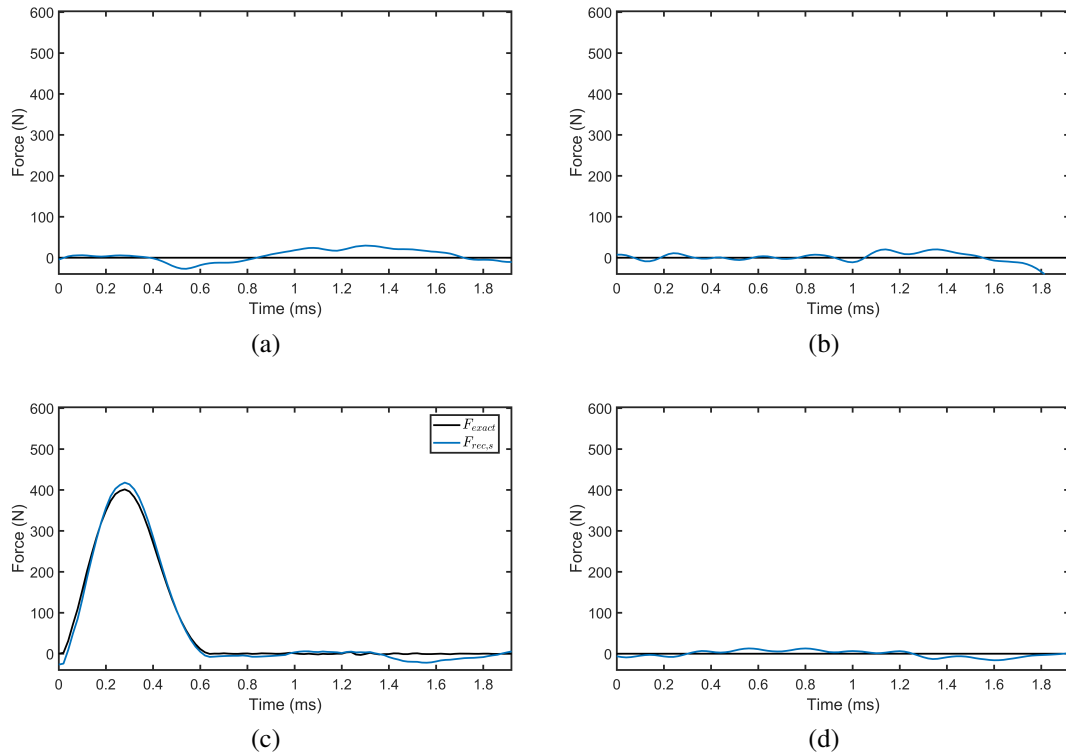
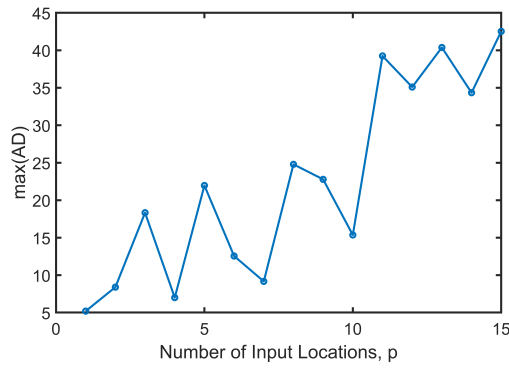


Figure 3.29: FDIM MIMO force reconstruction of point load applied at location C.  $R_1 = R_2 = 4$  and a sampling rate of 50 kHz were used. Reconstructions at hole locations A (a), B (b), C (c), and D (d) shown in Figure 3.1 are all shown.

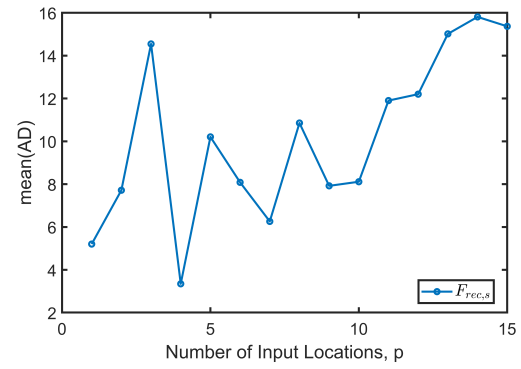
One could compute the center of moment forces and moment using the application location as was done in Figure 3.23. The intricacies of this were discussed in Section 3.2.2.3 and therefore are neglected from this analysis.

Next, it may be of interest to see the effects of number of input locations,  $p$  on the accuracy of the reconstruction. To demonstrate this, the number of input locations are varied from one to fifteen. During each study, the MIMO FDIM is used to reconstruct the force contributions at each input location as is seen in Figure 3.29. Next, the peak and area difference of the reconstruction at the application location is computed and recorded. The mean and maximum of these peak and area differences are depicted versus number of input locations in Figure 3.30.

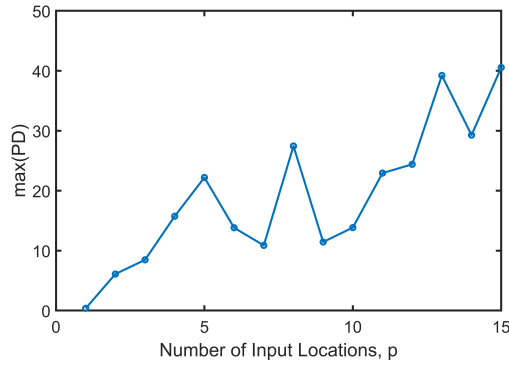
Several interesting conclusions can be drawn from Figure 3.30. First, there is a clear decline in performance as the number of input locations increases. This is expected as the inversion at each frequency becomes closer to a square matrix. This method appears extremely effective at reconstructing the pulse even when many input locations are of interest. Interestingly, even when the number of inputs exceeds the number of outputs (i.e.  $p > 12$ ), the FDIM still adequately reconstructs the input pulses. Unlike in the TDDM, a sudden drop in accuracy is not observed as  $p$  exceeds  $n$ .



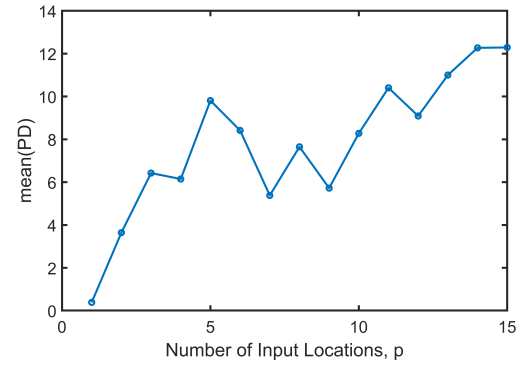
(a)



(b)



(c)



(d)

Figure 3.30: Area and peak difference of input pulse force versus number input locations using the FDIM MIMO formulation. Max area (a), average area (b), max peak (c), and average peak (d) difference are all shown.

### 3.2.3.3 Acceleration Deconvolution

As discussed previously in this dissertation, deconvolution of acceleration data is also an option for TDDMs and FDIMs. Many advantages of acceleration deconvolution exist such as ease of implementation. In this section, acceleration deconvolution and combined acceleration-strain deconvolution are validated for the experimental system.

First the SIMO case study discussed in Section 3.2.3.1 is repeated but consider strain-only, acceleration-only, and combined acceleration-strain deconvolution. An example result is shown in Figure 3.31. Note the excellent reconstruction accuracy of all three decon-

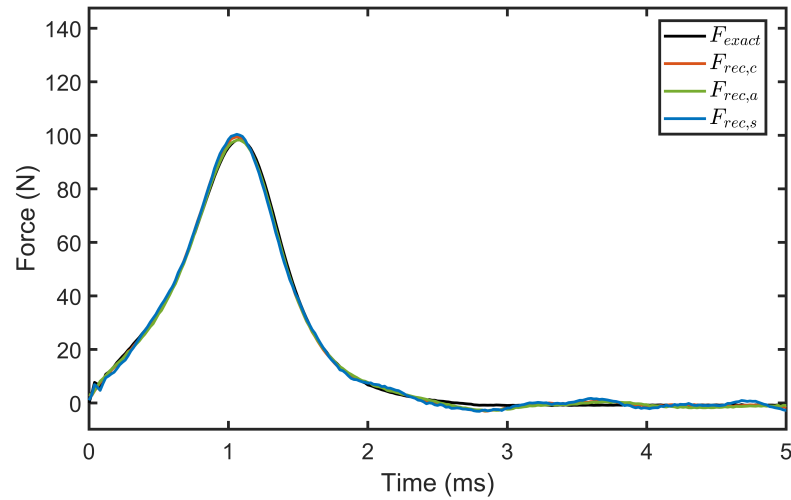


Figure 3.31: FDIM SIMO acceleration deconvolution force reconstruction experimental example result. Eleven calibration input tests used for this reconstruction.

volution variants. No obvious advantage of one method over another is observed.

It is important to quantify the accuracy across all tests. Therefore, as presented in Table 3.8, the peak and area difference for each deconvolution variant across all 188 reconstructions is computed. The maximum number of available calibration tests per hole were used. This ranges from eleven to fourteen depending on the hole location. These results are presented in Table 3.9.

Table 3.9: Peak and area differences for strain-only, acceleration-only, and combined strain-acceleration FDIM force reconstruction.

	Maximum			Average		
	S	A	C	S	A	C
AD	46.75	37.91	31.80	6.69	6.96	6.59
PD	28.12	22.90	19.55	4.76	5.55	4.64

Upon review of Table 3.9, it is clear that all three deconvolution variants perform admirably for the SIMO case study. Additionally, the results are comparable and better in some cases when compared to the results shown in Table 3.8. The FDIM with multiple calibration input solution of the FRF is extremely effective for SIMO pulse reconstruction.

Next, the study shown in Figure 3.28 is repeated. The results for acceleration-only, strain-only, and combined acceleration-strain deconvolution are shown in Figure 3.32. Again, a trend between accuracy and number of calibration inputs is observed for each deconvolution variant. Clearly, using more calibration inputs improves the accuracy of the reconstruction. Interestingly, no clear advantage is observed between the three variants.



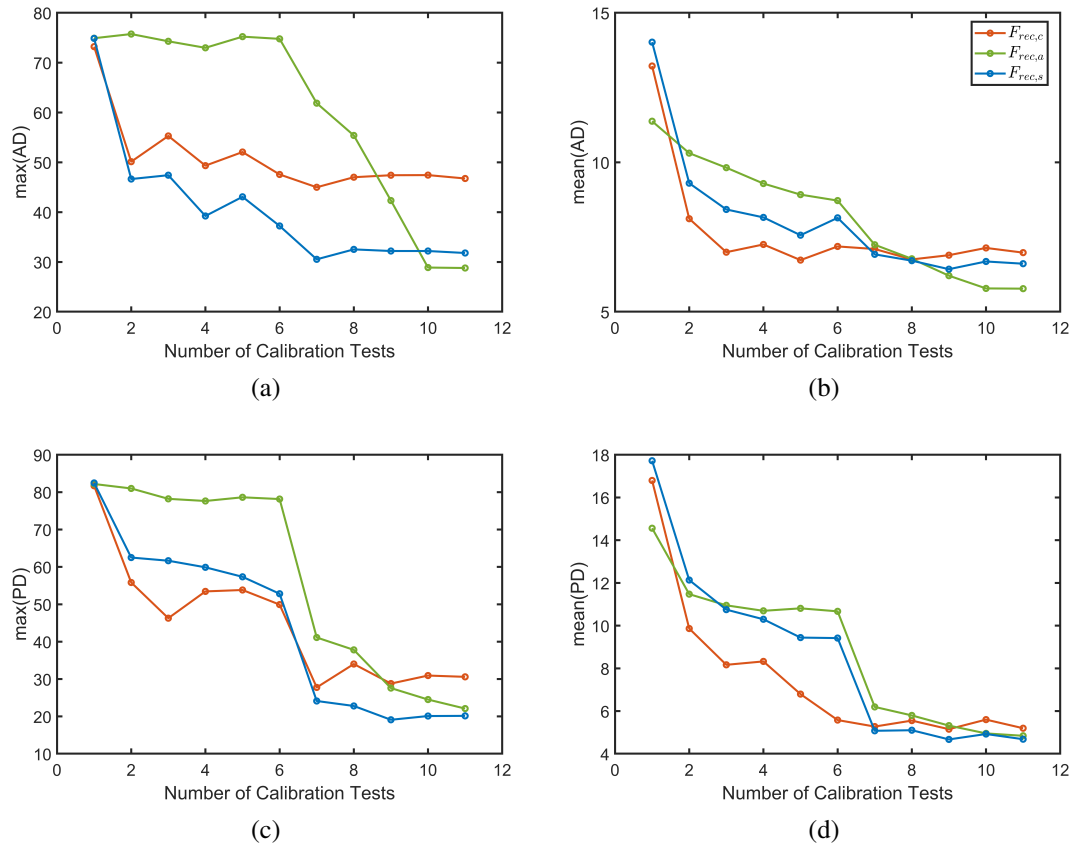


Figure 3.32: Area and peak difference of FDIM input pulse force versus number of calibration tests. Max area (a), average area (b), max peak (c), and average peak (d) difference are all shown. Acceleration-only, strain-only, and combined acceleration-strain deconvolution are all shown.

## Chapter 4: Dynamic Force Reconstruction Demonstration in Wind Tunnels

In this chapter, the developed methodologies are demonstrated on wind tunnel test articles subjected to dynamic forcing. Extensive numerical and no-flow experimental validation has been performed in this dissertation. However, there are a few concerns related to the aerodynamic forcing which are addressed in this chapter prior to the force reconstruction demonstration.

### 4.1 Aerodynamic Forcing Considerations

Dynamic aerodynamic forcing is considerably more complex than the point pulse and step loading that is primarily considered in this dissertation. This section presents some of these concerns and addresses their consequences.

#### 4.1.1 Distributed Loading

In aerodynamic forcing, the loading is no longer a point force. Instead, the flow subjects the test article to a more complex, distributed load. The previous studies in this dissertation have not considered distributed loading due to the inability to apply pressure loads to numerical lumped mass or experimental bench top models. This section presents a brief discussion of this problem and a brief numerical example to demonstrate the conclusions.

Some recent work has been performed with the objective of reconstructing a full dy-

dynamic and distributed pressure loading[51, 52]. Unfortunately, much of this work requires extensive modal identification and has yet to be validated on experimental systems. Therefore, these approaches are not attempted in this dissertation. Future work could attempt to use the datasets collected in this research to validate these methodologies.

It should be noted that the SWAT should be unaffected by distributed loading. In the SWAT (and all such variants developed in this dissertation), one is only interested in the center of moment forces and moments. Therefore, the specific form of the loading (e.g. point or distribution), is irrelevant. This section is primarily addressing the consequences on point force reconstruction methods (i.e. GDLM and FDIM).

Obviously, the GDLM and FDIM are most useful for point force application at the calibration locations. Changing the input location by even a few inches could greatly affect the dynamic response and invalidate the calibration. Furthermore, a distributed load has forcing contributions over an entire span rather than at only a particular location.

Ideally, if one knows the load is distributed, one could attempt to use the point force contributions to reconstruct the pressure loading. This is elaborated in the future work section of this dissertation. However, for these studies such analysis is not considered. Instead, the pressure load is assumed to supply a near equivalent concentrated force. This is typically done in static analyses of distributed loading. Although this is not exact for the dynamic case, it can provide a decent approximation if the area at which the dynamic pressure load acts is small.

To justify this claim, consider this numerical example performed on a finite element model (FEM) in Abaqus. This is used instead of the lumped mass numerical models because of its ability to apply distributed loads and closely match future experiments. For this study, a numerical model is generated which is very similar to that planned for the hypersonic wind tunnel investigation. This model is shown in Figure 4.1. Note the distributed pressure loading over the flap, denoted using a series of red arrows.

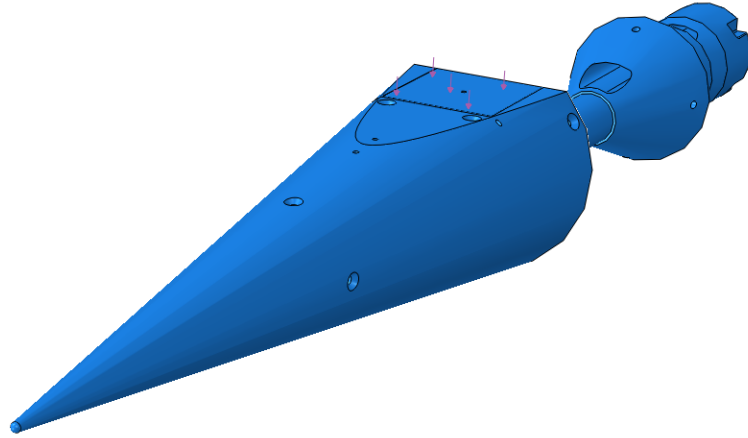


Figure 4.1: Abaqus FEM with distributed pressure loading on flap denoted by red arrows.

For this study, the assumption that the pressure loading is evenly distributed over this surface and for the duration of the loading is made. The magnitude of this distribution will rise and fall like a triangle over 40 ms. This simulates a flap deployment and retraction at the desired speed of  $1^\circ/\text{ms}$ .

To obtain the IRFs, an impulse is applied to the center of the flap. The response (both acceleration and displacement) in three directions is recorded from three nodes within the test article. This yields a total of nine acceleration outputs and nine displacement outputs, very similar to what would be obtained in a wind tunnel test. Using the TDDMs and FDIMs developed in this dissertation, the IRFs/FRFs are solved for each input-output pair.

Next, a 16 N triangle load spanning 40 ms is applied. The response at the same nodes is again recorded. Then the output is deconvolved using the IRFs/FRFs obtained in the previous step to solve for that applied triangle force. This is performed twice. Once with a concentrated force at the calibration location and once with an evenly distributed load over the flap.

The results for the first order GDLM are shown in Figure 4.2. Note the similarity between the results from the concentrated load and distributed load. The same effective

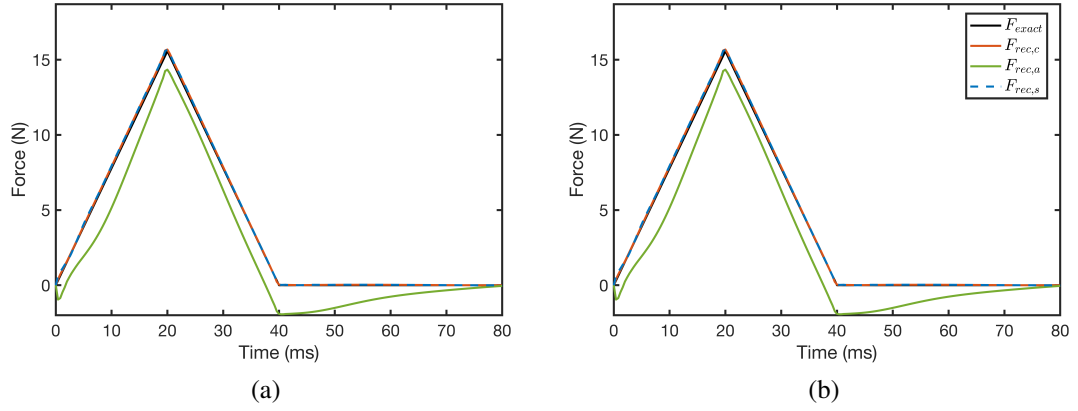


Figure 4.2: First order GDLM flap force reconstruction Abaqus numerical study using a concentrated force (a) and a distributed load (b).

result is observed. Interestingly, the acceleration-only reconstruction (green) is the worst result.

The same study can be performed with the FDIM. These results are depicted in Figure 4.3. Again, characteristically similar results are seen between the concentrated force and

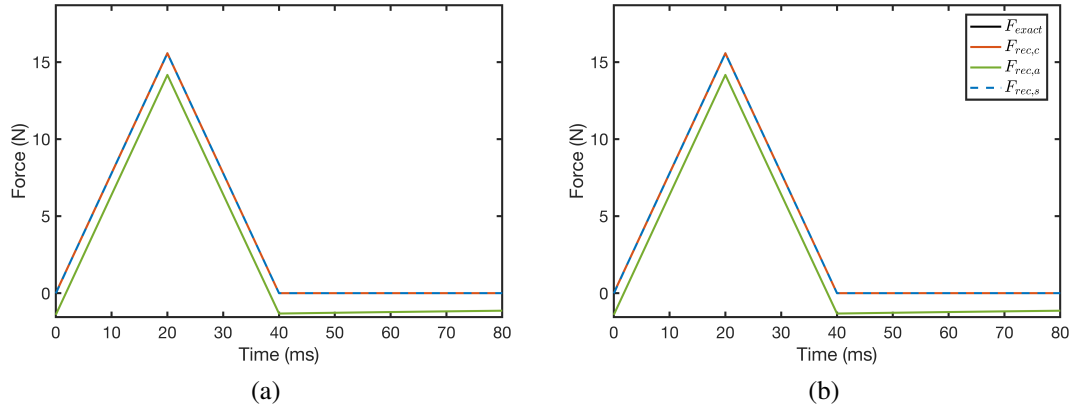


Figure 4.3: FDIM flap force reconstruction Abaqus numerical study using a concentrated force (a) and a distributed load (b).

pressure load studies. Additionally, the acceleration-only deconvolution results are worst for the FDIM as well.

### 4.1.2 Aeroelastic Effect

The purpose of this section is to investigate the effects of aeroelasticity on the force reconstruction problem. The GDLM is used as an example but the conclusions apply to all methods. First, a numerical model of a wing section is introduced. Then, a force reconstruction experiment is performed on this model.

Under the presence of a flowfield, the applied load to a model is a function of the state (e.g. displacement, rotation) of the body. This is a consequence of the directionality of the flowfield affecting the magnitude of the applied load (i.e. angle of attack alters lift and drag force). As a result, the reconstructed force is expected to exhibit oscillatory components in addition to the pulse loading or other additional loading under which the body is subjected. One should recognize, however, the difference between this aeroelastic forcing and the elastic force contribution which is obtained by only performing a static calibration.

#### 4.1.2.1 Aeroelastic System Description

Consider an aeroelastic two degree of freedom (2DOF) model. The complex motion of a wing is simplified here to only include pitch and plunge motion. Using this model, the state-dependent forcing terms should become obvious. A 2DOF wing section model, taken from Lee and Wereley's Vibrations textbook[53] can be seen in Figure 4.4. The plunge

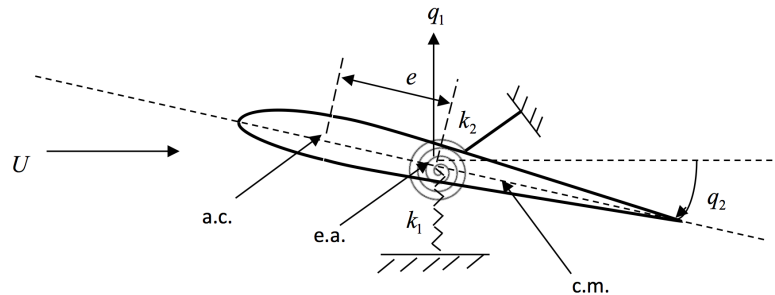


Figure 4.4: 2DOF model wing section

motion (i.e. vertical translation) is given by  $q_1$  and is resisted by the linear spring  $k_1$ , which represents the bending stiffness of the wing. The plunge motion (i.e. rotation about the elastic axis) is given by  $q_2$  and is resisted by the angular spring  $k_2$ , which represents the torsion stiffness of the wing. This is a common representation of a typical wing and is often used to approximate flutter/divergence speed for a particular wing cross-section.

The equations of motion for this system are

$$M\ddot{q}_1 - S_\alpha\ddot{q}_2 + k_1q_1 = L \quad (4.1)$$

$$-S_\alpha\ddot{q}_1 + I_\alpha\ddot{q}_2 + k_2q_2 = M_{ea} \quad (4.2)$$

where  $L$  is the effective lift force applied over the wing due to the pressure loading and  $M_{ea}$  is the moment about the elastic axis (e.a.). The variables  $M$ ,  $S_\alpha$ , and  $I_\alpha$  are the total mass, static moment of mass about the e.a., and mass moment of inertia about the e.a., respectively. These variables and the equations of motion are derived in Lee and Wereley's textbook and are omitted from this discussion for brevity.

Using quasi-steady aerodynamic theory, lift is computed as

$$L = qS \frac{\partial C_L}{\partial \alpha} \left( q_2 - \frac{\dot{q}_1}{U} \right) \quad (4.3)$$

where  $q$  is the dynamic pressure,  $S$  is the planform area of the wing,  $C_L$  is the lift coefficient for the particular air foil,  $\alpha$  is the angle of attack, and  $U$  is the air speed. The moment about the e.a. is given by

$$M_{ea} = eL + M_{ac} \quad (4.4)$$

where  $e$  is the distance from the aerodynamic center (a.c.) to the e.a. and  $M_{ac}$  is the moment

about the a.c. due to the pressure loading. The moment about the a.c. is computed as

$$M_{ac} = qSc \frac{\partial C_M}{\partial \dot{\alpha}} \dot{q}_2 \quad (4.5)$$

where  $c$  is the chord length and  $C_M$  is the moment coefficient for the particular airfoil.

Plugging Eqs. (4.3) and (4.5) into Eq. (4.4) yields

$$M_{ea} = eqS \frac{\partial C_L}{\partial \alpha} \left( q_2 - \frac{\dot{q}_1}{U} \right) + qSc \frac{\partial C_M}{\partial \dot{\alpha}} \dot{q}_2. \quad (4.6)$$

In reviewing Eqs. (4.3) and (4.6), it is clear that the applied forcing (i.e. the right hand side of Eqs. (4.1) and (4.2)) have a large dependence on the states of the system.

From here, the analyst would typically move the state dependent terms to the left hand side and calculate aeroelastic system frequencies for divergence and flutter analysis. However, this point is sufficient for this investigation.

Next, consider an additional load applied in the plunge direction at the e.a.. This could be thought of as an impulsive gust or a sudden collision with debris. This force manifests as an additional load in Eq. (4.1) as

$$M\ddot{q}_1 - S_\alpha \ddot{q}_2 + k_1 q_1 = L + F(t) \quad (4.7)$$

where, for example

$$F(t) = \frac{b}{a\sqrt{\pi}} \exp^{-(\frac{t-0.5\varepsilon}{a})^2}, \quad (4.8)$$

where  $a = 2 \cdot 10^{-3}$  controls the pulse width,  $b = \frac{1}{15}$  is a scaling constant used to select a desired area (and consequently peak magnitude), and  $\varepsilon$  is the pulse width used to shift the pulse from the  $t = 0$  axis. This simulates a steep hammer impulse force with an approximate width of 10 ms and height of 20 N.



For the purposes of numerical solution, it is useful to represent Eqs. (4.7) and (4.2) in matrix form, i.e.

$$\begin{bmatrix} M & -S_\alpha \\ -S_\alpha & I_\alpha \end{bmatrix} \begin{pmatrix} \ddot{q}_1 \\ \ddot{q}_2 \end{pmatrix} + \begin{bmatrix} k_1 & 0 \\ 0 & k_2 \end{bmatrix} \begin{pmatrix} q_1 \\ q_2 \end{pmatrix} = \begin{pmatrix} L + F(t) \\ M_{ea} \end{pmatrix} \quad (4.9)$$

or

$$\mathbf{M}\ddot{\mathbf{q}} + \mathbf{K}\mathbf{q} = \mathbf{F}. \quad (4.10)$$

We may rearrange this equation for the highest derivative i.e.

$$\ddot{\mathbf{q}} = \mathbf{M}^{-1} (\mathbf{F} - \mathbf{K}\mathbf{q}) \quad (4.11)$$

to fit the form expected by typical numerical solvers. For this and many other investigations, a fourth order Runge-Kutta (RK4) solver is appropriate to generate output data. Therefore, the built-in Matlab RK4 method: ode45 is chosen.

#### 4.1.2.2 Dynamic Calibration Discussion

The chief focus of this research is dynamic force measurement. The first step in that process is to dynamically calibrate the system under investigation. For a typical dynamic calibration, a known load must be applied and the response of the system measured. Then these two are used to form the impulse response functions (IRFs) for each input-output pair. This is commonly a pulse from an instrumented hammer, as the exact applied load is easy to measure in experiments. Now consider a practical scenario for the numerical system discussed in Section 4.1.2.1. For a tester to perform a practical calibration of this system, one must do this in a no-flow condition. The consequence of this is zero lift force and moment about the e.a., i.e.  $L = M_{ea} = 0$ .

Following this logic, two IRFs are solved,  $h_{11}(t)$  relating a plunge direction input force to a plunge direction displacement and  $h_{12}(t)$  relating a plunge direction input force to a pitch direction angular displacement. These IRFs represent the unforced dynamics of the wing system. They effectively capture the mass, static mass about the e.a., mass moment of inertia about the e.a., and the two directional stiffnesses. Therefore, any applied loading can be reconstructed which appears in the first entry of the vector on the right hand side of Eq. (4.9).

It should be noted that when using these IRFs to reconstruct dynamic forces, one will reconstruct everything in the first entry of the vector on the right hand side of Eq. (4.9). It may be the case that the user is interested in only the extra forces applied to the system (i.e.  $F(t)$ ) as would be the case for a free-flying test article. Unfortunately, this is not solved for alone. The state-dependent lift contributions are also part of the solution. A dynamic calibration in the wind-on environment at the conditions of interest would need to be performed to remove these contributions. This is obviously impractical and improbable at the moment. Therefore, the measurement of the aeroelastic loading must be accepted in addition to any extra applied loads such as gust loading.

#### 4.1.2.3 Force Reconstruction Example

The parameters for the model used in these investigations are given in Table 4.1. Note these parameters were chosen to match those used in an exercise problem in Lee and Wereleys textbook. With these parameters, the system is stable and will not diverge or flutter. Therefore, any small perturbation subjected to the system (e.g. pulse gust load) will not cause destabilization.

The calibration load in these studies is given in Eq. (4.8). For simplicity, this force is also used for the gust load in the unknown force reconstruction. Additionally, the data were

Table 4.1: Numerical system parameters for 2DOF aeroelastic model.

Variable	$M$	$S_\alpha$	$I_\alpha$	$k_1$	$k_2$	c	e	S
Value	8.7	5.4	84	$6.4 \times 10^4$	$1.3 \times 10^6$	5	0.19	150
Unit	slug	slug-ft	slug-ft <sup>2</sup>	lb/ft	lb-ft/rad	ft	ft	ft <sup>2</sup>
Variable	$\frac{\partial C_L}{\partial \alpha}$	$\frac{\partial C_M}{\partial \alpha}$	$\rho_\infty$	$q_\infty$	$U_\infty$			
Value	$1.87\pi$	0	$2.38 \times 10^{-3}$	297.1	500			
Unit	-	-	slug/ft <sup>3</sup>	psf	ft/s			

sampled at 5 kHz and the reconstruction methodology used was the cubic formulation of the GDLM.

First a dynamic calibration was performed. As discussed previously, a pulse load of approximately 20 lbs over 10 ms is simulated to strike the structure at the e.a. to ensure input excitation to DOF 1 only. This known load in conjunction with the cubic GDLM is used to solve for the pitch and plunge response IRFs with respect to this input direction. These are shown in Figure 4.5. As expected, the GDLM performs well. The analytical IRFs are

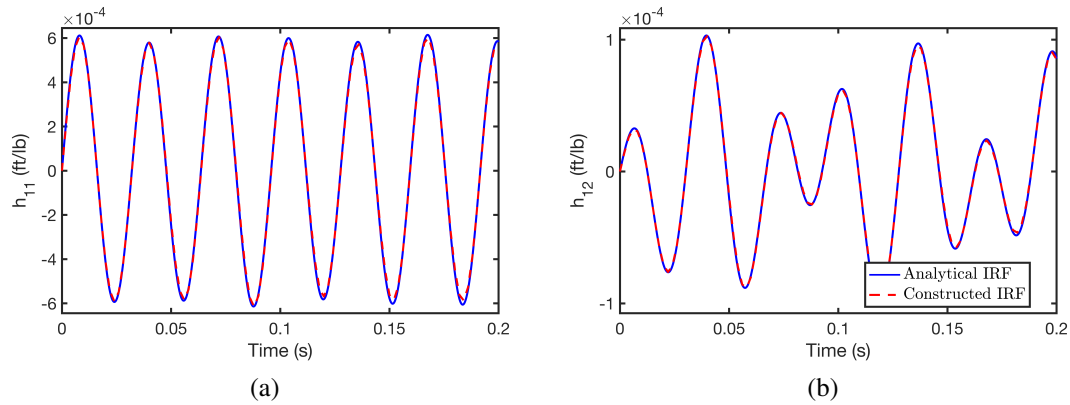


Figure 4.5: IRF construction for 2DOF wing model using  $\hat{R}_1 = 5$ . Plunge (a) and pitch (b) response IRFs both shown.

constructed with high accuracy. These IRFs can now be used in conjunction with a dynamic response to reconstruct any dynamic applied load. For example, the calibration load response may be used to reconstruct that pulse. This is shown in Figure 4.6a. As expected,

accurate reconstruction of the calibration pulse are obtained in this wind-off environment.

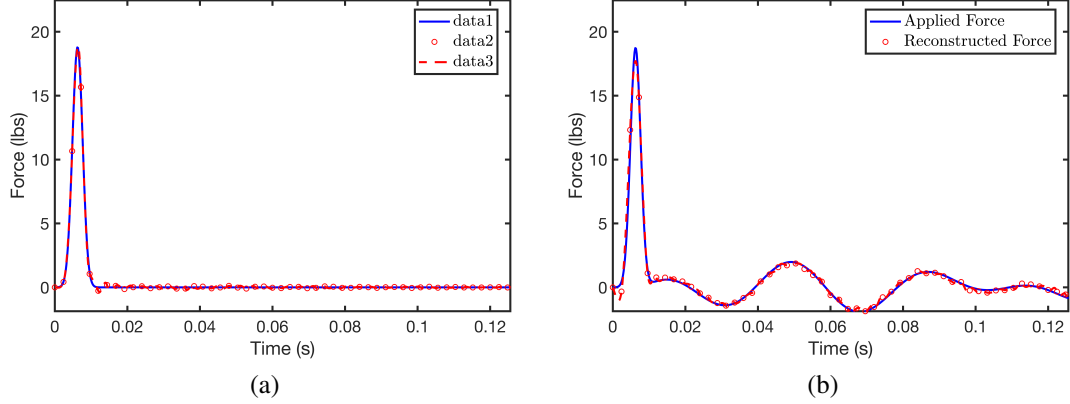


Figure 4.6: Input force reconstruction for 2DOF wing model using  $\hat{R}_1 = 5$  and  $\hat{R}_2 = 6$ . Wind-off calibration load reconstruction (a) and wind-on gust force reconstruction (b) are both shown.

Next it may be interesting to see how the GDLM performs on a wind-on time history. Using the equations of motion given by Eq. (4.10), this response is simulated. Combining this response with the IRFs obtained previously, the GDLM yields the reconstruction depicted in Figure 4.6b. As speculated, the method reconstructs the pulse gust load, as well as the state dependent lift forcing. This is represented by the subsequent oscillations following the duration of the pulse. However, as indicated by the "Applied Force" curve, this is indeed the force applied to the wind-off system. We cannot resolve purely the gust load (i.e. that shown in Figure 4.6a) using only a wind-off dynamic calibration.

This demonstrates the ability of the GDLM to reconstruct dynamic forcing on a 2DOF aeroelastic model. The presence of aeroelastic forcing is an unavoidable consequence of state dependent forcing (i.e. lift and moment being a function of angle of attack, etc.). Provided these oscillations are minimal, the experimentalist may still be able to discern an estimate of the desired, state-independent forcing contributions. To minimize the magnitude of aeroelastic force contributions, it is suggested to increase the stiffness as high as reasonable.

In subsequent wind-on experiments, the presence of this aeroelastic forcing should be considered when discerning the aerodynamic applied load. A strong recommendation is to maximize the stiffness in any ways possible. Aeroelastic forcing is an unavoidable consequence of cantilevered structures and cannot be simply removed without a wind-on dynamic calibration.

## 4.2 Transonic Demonstration

In this study the reconstruction a dynamic applied aerodynamic load in a transonic wind tunnel test is the chief focus. More specifically, the quantification of the applied forcing magnitude and frequency content of cyclic aerodynamic forcing on a small cylinder is of interest. The calibration and air-on experiments were performed at the Air Force Research Laboratory (AFRL) Wright-Patterson Air Force Base.

Assume for this study that there is an oscillating upstream flow causing the cyclic forcing. The exact cause of the forcing, and purpose of the test article, and specifics of the body undergoing forcing, are irrelevant for this study.

The GDLM and FDIM are used to reconstruct the applied loads for this case study. Acceleration response was not measured and therefore the SWAT is not applicable. A calibration data set is first obtained via striking the test article with an instrumented impulse hammer. The IRFs of the system are obtained utilizing this data. Subsequently, a validation study is performed where the calibration loads are reconstructed and compared with the measured loads obtained by the instrumented hammer. Finally, the IRFs are used to reconstruct an applied cyclic aerodynamic force.

Furthermore, a shifted formulation of the GDLM is employed to utilize the full measurement range and better compare with FDIM. Due to the cumulative nature of convolution formulation, this shifting method is required for the test time of interest.

### 4.2.1 Test Setup

For the purposes of this discussion, consider the test setup shown in Figure 4.7. The ap-

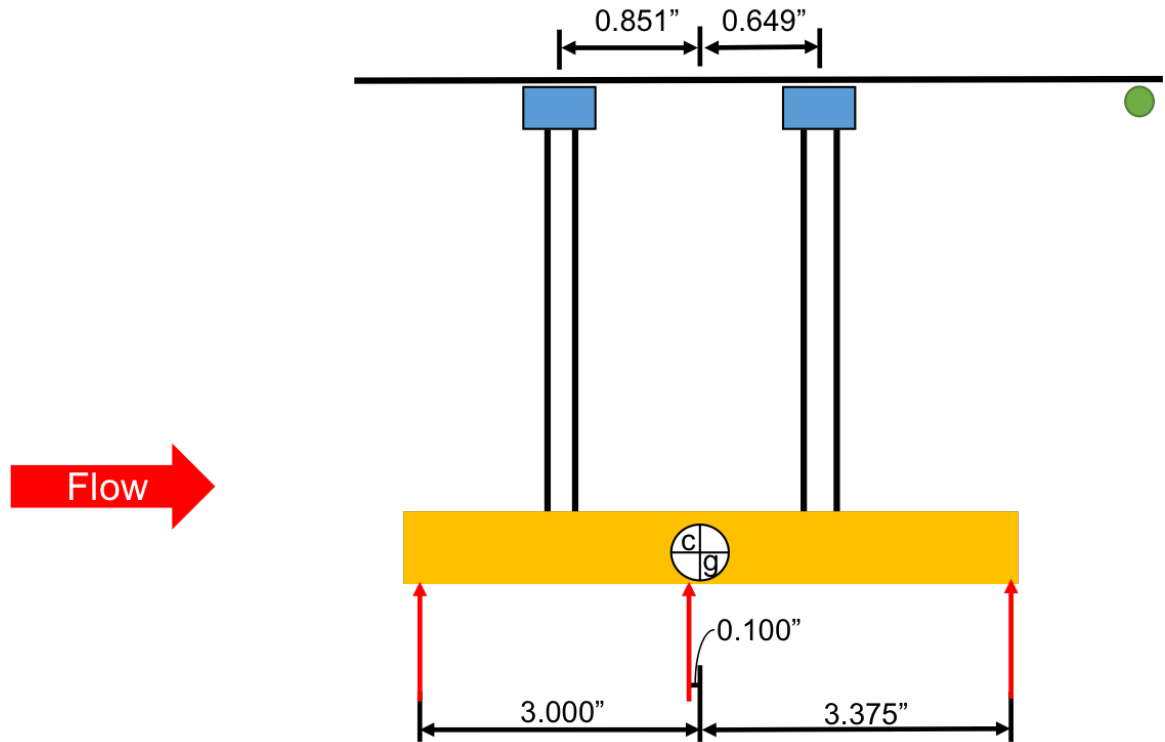


Figure 4.7: Depiction of experimental setup at AFRL. Test article (yellow), calibration load locations (skinny red arrows), piezoelectric strain sensors (blue) and high frequency pressure gages (green) are all shown with important dimensions.

plied and elastic force contributions are recorded on the strain sensors. The high frequency aerodynamic forcing causes the excitation of structural resonances in the cylinder. These structural resonances are measured by the piezoelectric strain sensors and correlate the statically calibrated force and moment measurements. This is analogous to the sting-mounted studies discussed throughout this dissertation. Additionally, a high frequency static pressure sensor is mounted in the aft end of the test setup and measures the expected applied forcing frequencies of the aerodynamic load.

There are far less sensors in this study than in the others discussed in this dissertation.

However, it is still worth mentioning their capability prior to discussing the results. There are two uniaxial strain sensors and two high frequency pressure sensors. The strain sensors are Dytran Model 1051V1[54]. The pressure sensors are Endevco Model 8507C-5[55]. The relevant specifications form these sensors are summarized in Table 4.2.

Table 4.2: Sensor specifications for AFRL transonic wind tunnel experiment. Load cells (left) and pressure sensors (right) both shown.

	Model 1051V1	Model 8507C-5
Sensitivity	112.4 mV/N	$60 \pm 20$ mV/psi
Measurement Maximum	44.5 N	5 psig
Failure Limit	890 N	100 psi
Broadband Resolution	0.62 mN-rms	0.05 mV-rms
Upper Frequency Limit	75 kHz	85 kHz
Temperature Range	-73 to +121 C	-18 to +93 C

Note that the strain sensors are uniaxial rather than triaxial as is used in other experiments in this dissertation. This limitation is suboptimal as additional output locations can improve the SIMO analysis. Furthermore, out of plane dynamics may be significant for this study. As transverse bending is the least stiff deformation path, there are likely to be significant dynamics in the transverse direction.

#### 4.2.2 Force Reconstruction Results

Acceleration measurements were not obtained for these studies. Therefore, the SWAT method is not applicable. However, a dynamic pulse force calibration was performed prior to (and after) wind tunnel testing. Therefore, the GDLM and FDIM may be applied. This section details the cyclic force reconstruction results using each method.

#### 4.2.2.1 GDLM Results

Begin with the GDLM. The air-on test data set is 8.8 seconds long sampled at 100 kS/s. Obviously, typical reconstruction would require inversion of an unreasonably large matrix. Accordingly, one may use the segmented formulation whereby a small portion of the IRF is inverted and multiplied by various segments of the output data. Next stitch the various reconstructions together to obtain the applied load over the whole time history. A more reasonable length to invert is about 100 ms for the quoted 100 kS/s sampling rate. Additionally, since it's the same IRF, one need only compute the inversion once and store it for use on subsequent output segments.

One note here is that the IRF is lower band limited to whatever segment length chosen. The theoretical lower frequency band is computed as

$$f_{\min} = \frac{1}{t_{\max}} \quad (4.12)$$

where  $t_{\max}$  is the length of the segment in seconds. However, the realizable lower frequency (i.e. the frequency where one can realistically visualize a peak in the frequency domain) is usually about an order of magnitude higher than this. Therefore for a 100 ms segment, only frequencies of about 100 Hz or more are physically realizable. Therefore, any frequency content that is reconstructed lower than this realizable lower bound should be ignored.

Fortunately, for the problem at hand, the applied forcing frequency is estimated to be approximately 1 kHz. Therefore a 100 ms segment is more than adequate to reconstruct forcing in this regime.

Additionally, recall that application of the TDDM on a system with nonzero initial conditions (i.e. a system that is not at rest) results in a small amount of error in the beginning of the reconstruction. Therefore, for additional accuracy, one may overlap the beginning of



each reconstructed segment with the end of the previous one.

To build confidence in the test setup (i.e. signal quality, system linearity, etc.), begin with a pulse force reconstruction of the input loads. Impulses were applied to the cylinder via an instrumented impulse hammer. The stiffest tip was utilized for these calibration loads to ensure high frequency dynamic excitation. The IRFs for each input-output pair are computed by measuring the applied load and the response from each of the two load cells.

With the IRFs known, the problem is reversed to reconstruct the applied calibration loads. An example force reconstruction is shown in Figure 4.8. Even with limited resolu-

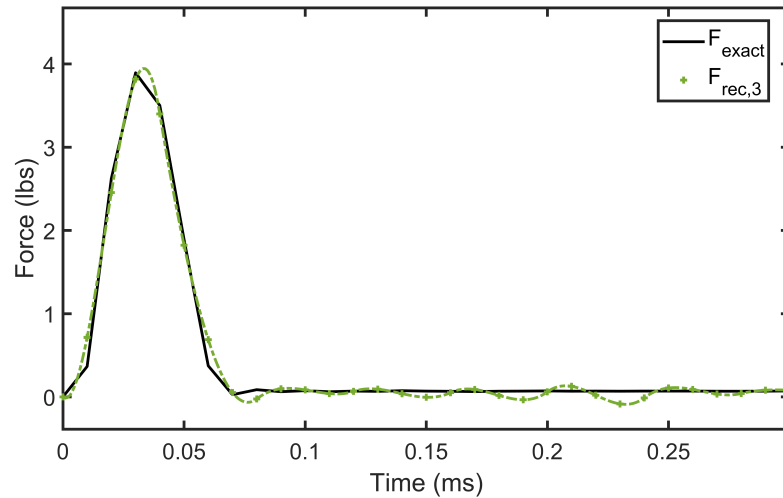


Figure 4.8: Cubic GDLM calibration pulse force reconstruction at AFRL

tion over the peak, GDLM still performs adequately at reconstructing the pulse. Six calibration sets were of high enough quality. In order to observe the overall accuracy across all six tests, the peak and area differences of all reconstructions were computed. Next, the mean and max of all peak and area differences are computed which are displayed in Table 4.3. Comparable levels of error as to that obtained from validation studies on the Balance Calibration test article are seen. Therefore, the results are of good quality one may proceed to the aerodynamic force reconstruction.

For aerodynamic testing, dynamic strain data was collected from the response of the

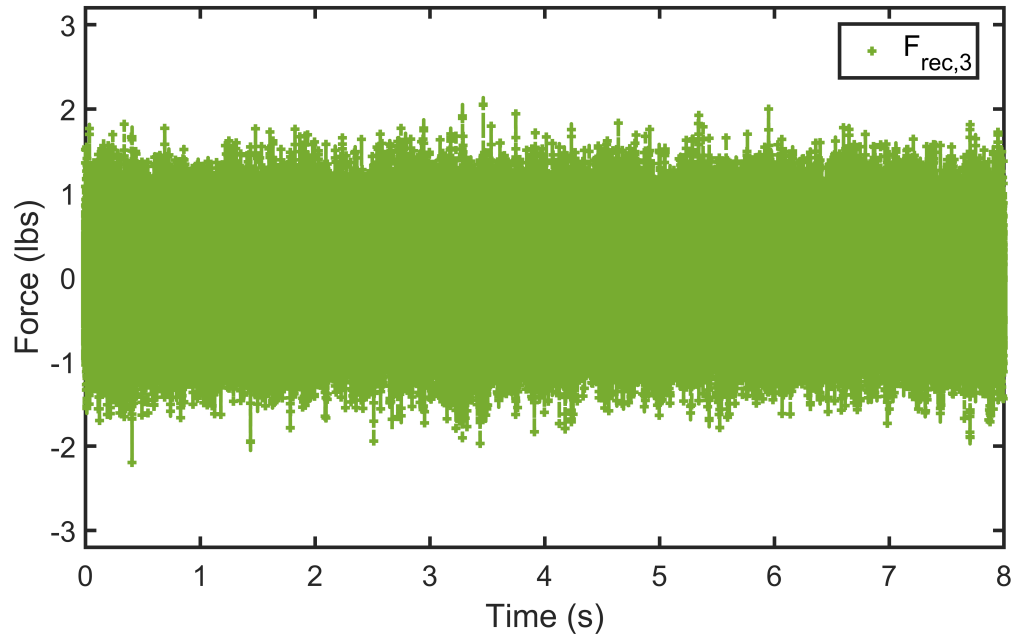
Table 4.3: Input Pulse Reconstruction Error Analysis for AFRL tests using third order GDLM

	Maximum	Average
AD	8.57	2.94
PD	11.66	5.11

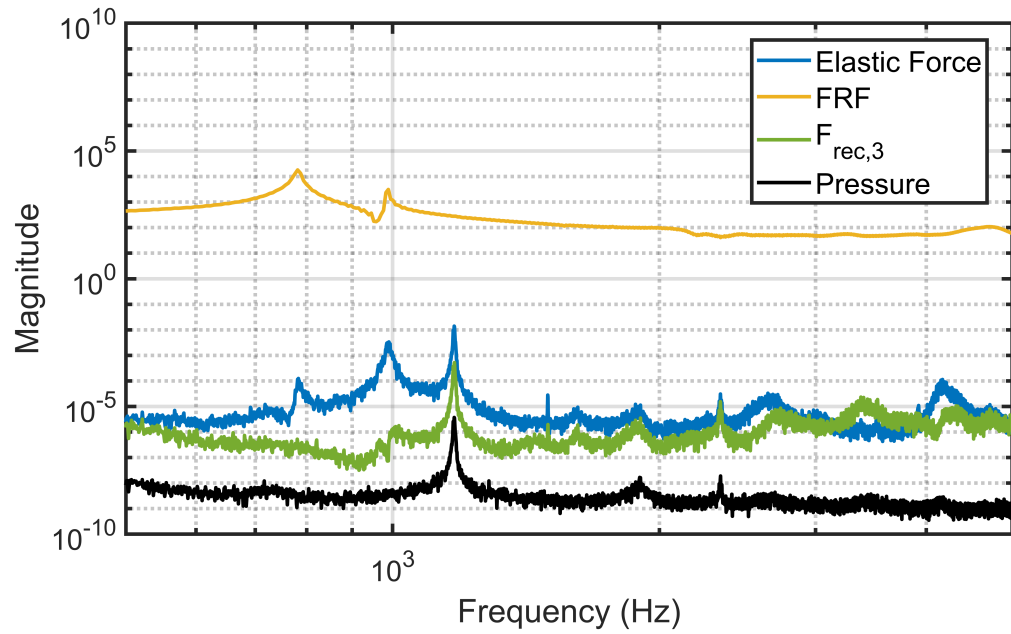
cylinder depicted in Figure 4.7 subjected to transonic tunnel conditions and an upstream oscillatory forcing. The IRFs constructed in the calibration data sets are utilized in the reconstruction of the dynamic loads. Since there are three calibration locations, a SIMO reconstruction of the load is performed at each location. Ideally, a MIMO approach would be implemented. However, recall Section 3.2.2.3 which shows that the GDLM is ill-suited for MIMO reconstruction when the number of input locations exceeds that of output locations (i.e.  $p > n$ ). Also note that the third order GDLM is considered. Since the forcing is sinusoidal, a smooth forcing is expected. Therefore, the third order method is ideal to reconstruct this load.

As mentioned, the segmented alteration was employed in order to reconstruct the entire eight second window. Figures 4.9, 4.10, and 4.11 depict the time and frequency domain force reconstructions of the wind tunnel forcing for the forward most, middle, and aft most loading stations.

The time domain plots are shown to depict the overall forcing magnitude of the aerodynamic load. There are four curves shown on each frequency domain plot: the FRF computed during calibration, the elastic force (i.e. the force computed using only static calibration), the reconstructed force using the third order GDLM, and the response from the high frequency pressure sensor during testing. Note that the FRF and pressure measurement magnitudes in the frequency plots have been altered for additional clarity.

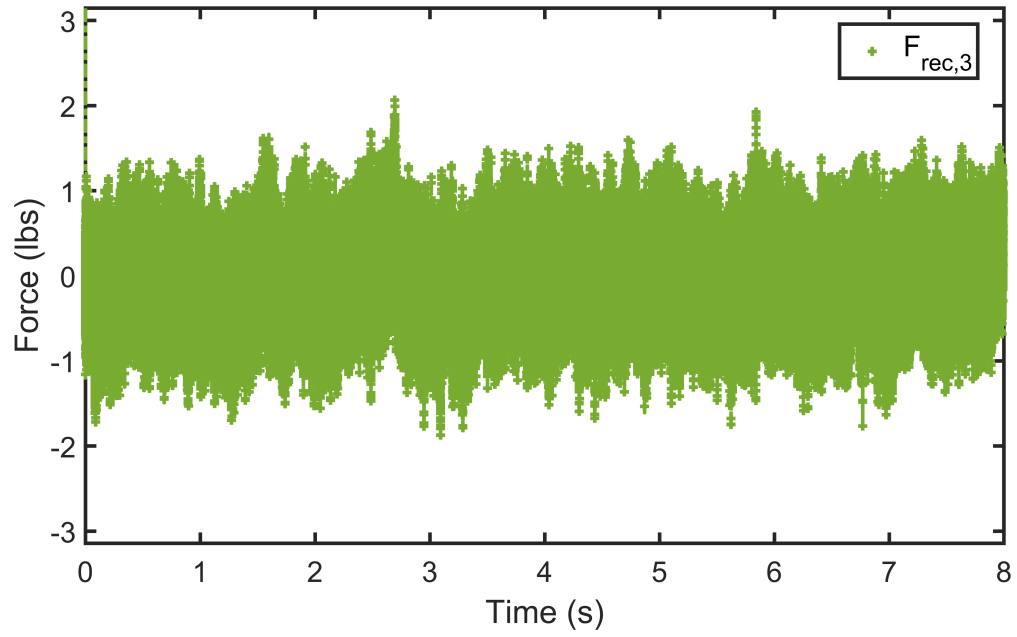


(a)

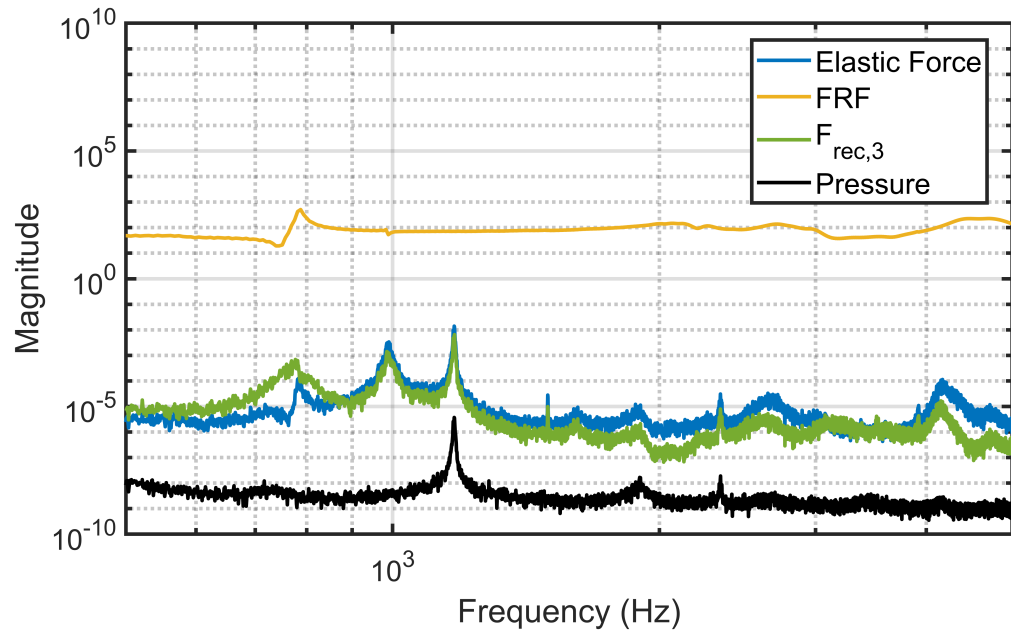


(b)

Figure 4.9: Wind tunnel force reconstruction using  $\hat{R}_1 = \hat{R}_2 = 2$  at load station 1 (forward most location). Time (a) and frequency (b) domain representations of the reconstruction are both shown.

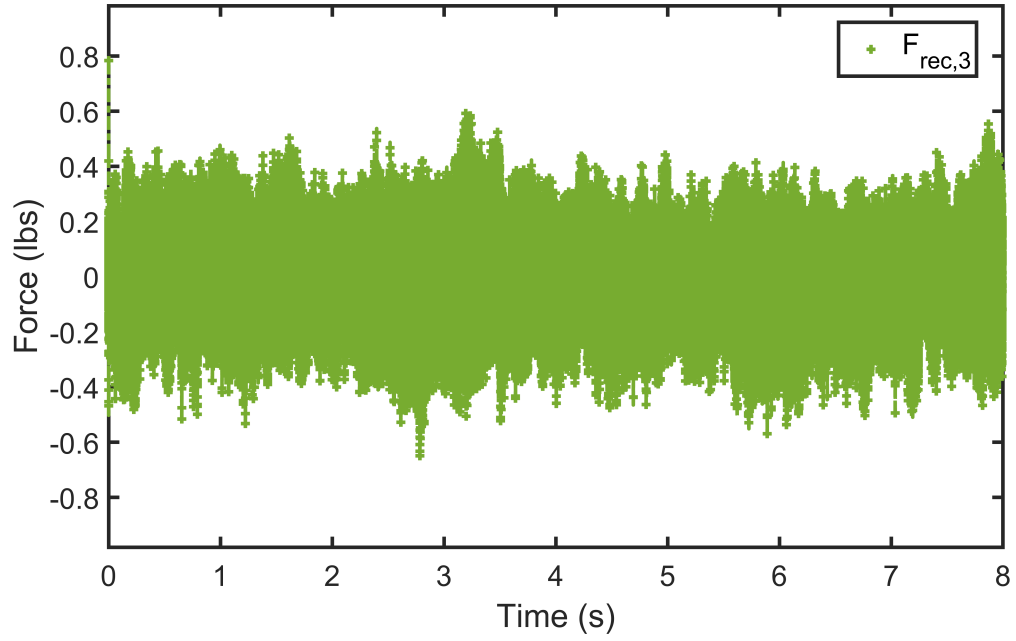


(a)

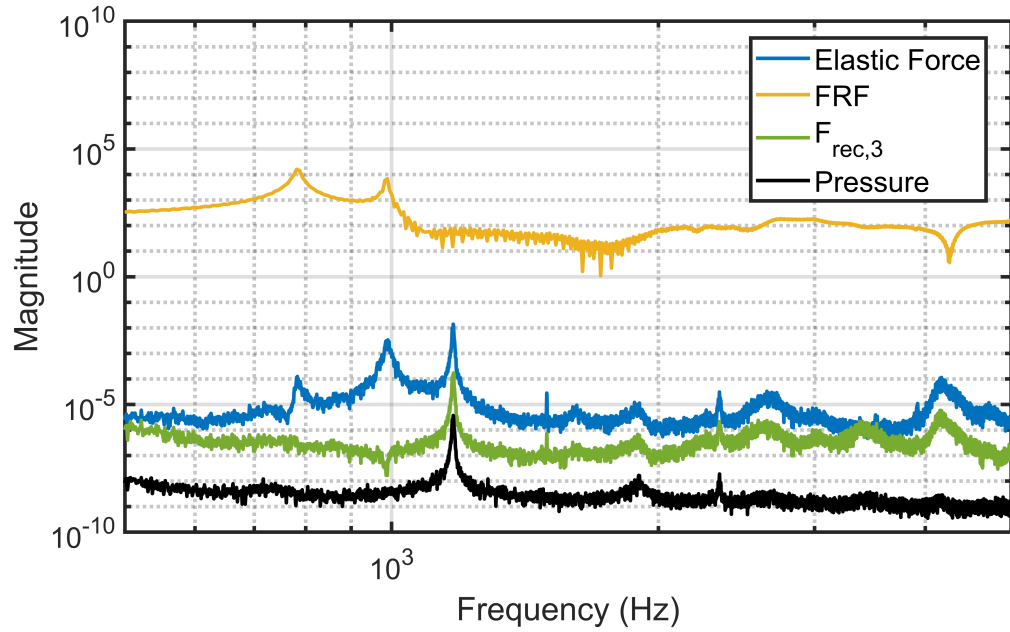


(b)

Figure 4.10: Wind tunnel force reconstruction using  $\hat{R}_1 = \hat{R}_2 = 2$  at load station 2 (middle location). Time (a) and frequency (b) domain representations of the reconstruction are both shown.



(a)



(b)

Figure 4.11: Wind tunnel force reconstruction using  $\hat{R}_1 = \hat{R}_2 = 2$  at load station 3 (aft most location). Time (a) and frequency (b) domain representations of the reconstruction are both shown.

Upon review of the plots, the following observations are evident:

1. The overall forcing magnitude decreases progressing chordwise along the cylinder. The maximum magnitude drops from 2 lbs at the forward most station to 0.6 lbs at the aft most station.
2. According to the pressure measurement, there are three clear forcing frequencies: 1174, 1904, and 2343 Hz. These are the dominant peaks in the orange curves.
3. All three loading stations were successful at reconstructing these frequencies.
4. The middle station does a poor job at removing the surrounding structural loads.
5. The forward and aft stations perform adequately at removing the 783 and 990 Hz structural modes.
6. Additional frequency content is reconstructed at 1617 and 2650 that does not appear to be present in the pressure measurement.

The first puzzling observation is that the middle station does a poor job at removing the 783 and 990 Hz structural modes. However, looking at the FRF for that station, these modes are not present. Therefore, it is likely that these modes were not excited during this calibration test. We believe this is because those two modes are likely pitching modes. A strike in the center would excite plunging modes but not pitching modes.

Another puzzling observation is that all reconstructions display additional frequency content at 1617 and 2650 Hz. Again these frequencies are not reflected in the FRFs. Because these peaks are not reflected in the pressure measurement, they are unlikely to be forcing frequencies. If these are indeed structural modes, a possible explanation may be that these are out of plane modes. Since all calibration tests were performed in the lift direction, out of plane modes would not have been excited to a large degree. A distributed

cyclic aerodynamic load however, may excite these modes. Future calibration tests should include out of plane excitation to validate this claim.

#### 4.2.2.2 FDIM Results

In this section the above analysis for the FDIM is repeated. There are several advantages to using the FDIM. First, the frequency domain characteristics such as forcing frequencies are of interest. Therefore it is natural to work in the frequency domain. Additionally, the time history is very long (i.e. eight seconds). As noted previously, the FDIM is far more efficient for long time histories as compared to TDDMs.

Begin with the same SIMO analysis performed in the previous section but with the FDIM instead of GDLM. One may expect similar results as the same data set and underlying physics are used for the two analyses. First, one may validate the pulse force reconstruction used in calibration. An example result is shown in Figure 4.12. In order

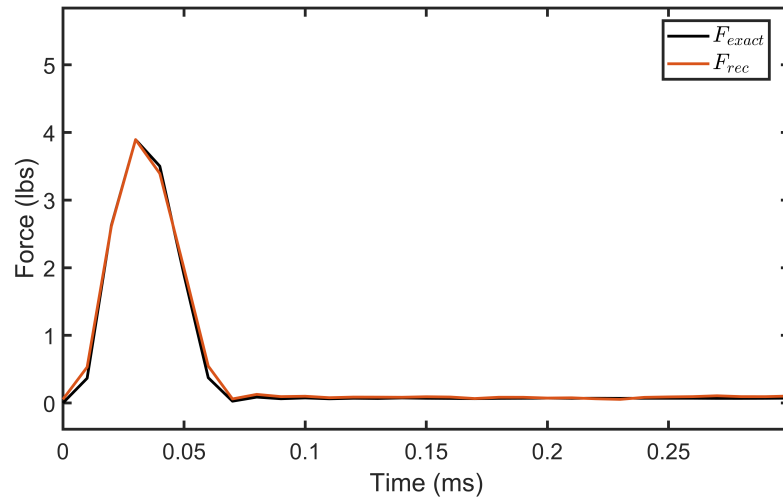


Figure 4.12: FDIM calibration pulse force reconstruction at AFRL

to observe the overall accuracy across all six tests, the peak and area differences of all reconstructions are computed. Next, the mean and max of all peak and area differences are computed which are displayed in Table 4.4. These results are extremely promising; dis-

Table 4.4: Input Pulse Reconstruction Error Analysis for AFRL tests using FDIM

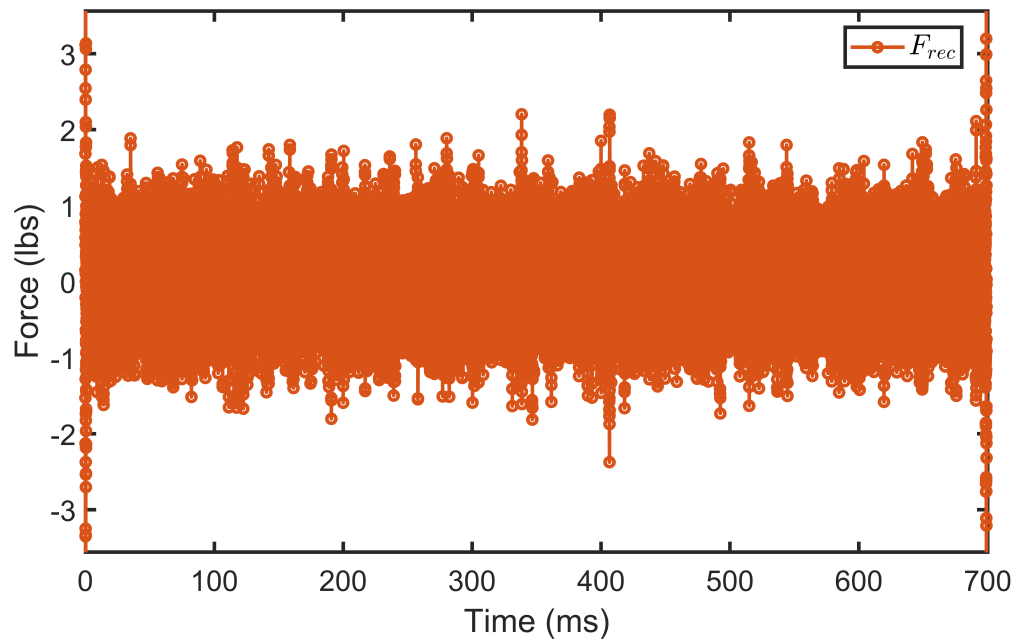
	Maximum	Average
AD	9.37	2.74
PD	7.87	1.82

playing even lower errors than seen in Table 4.3. Next, one may use the generated FRFs to reconstruct the aerodynamic forcing.

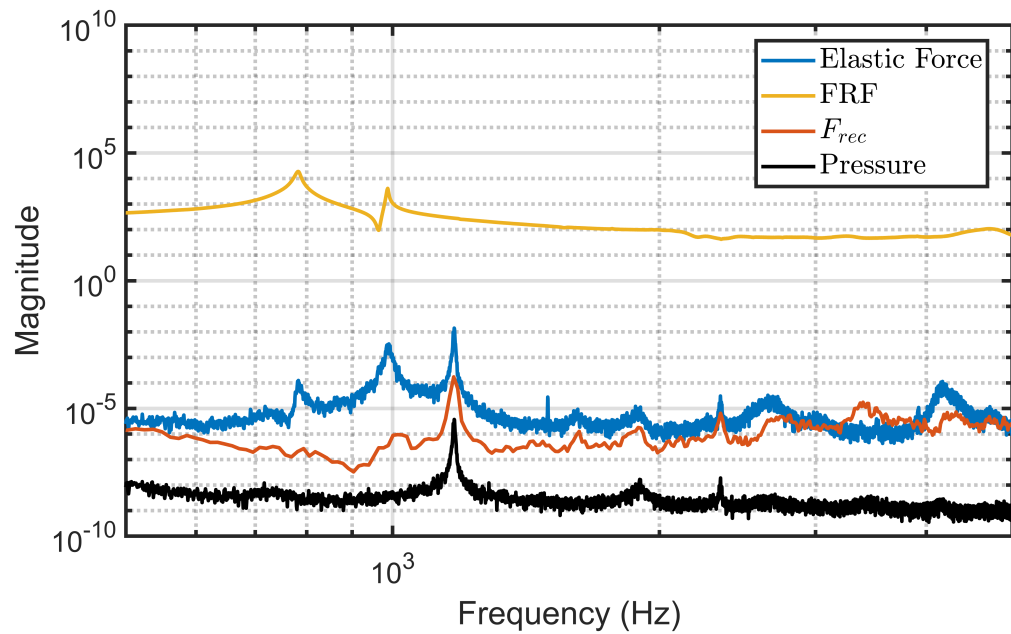
Figures 4.13, 4.14, and 4.15 depict the time and frequency domain force reconstructions of the wind tunnel forcing for the forward most, middle, and aft most loading stations.

The time domain plots are shown to depict the overall forcing magnitude of the aerodynamic load. There are four curves shown on each frequency domain plot: the FRF computed during calibration, the elastic force (i.e. the force computed using only static calibration), the reconstructed force using the FDIM, and the response from the high frequency pressure sensor during testing. Note that the magnitudes in the frequency plots have been altered for additional clarity. These results appear to agree very well with those obtained in the GDLM analysis. One may draw similar conclusions from these results.



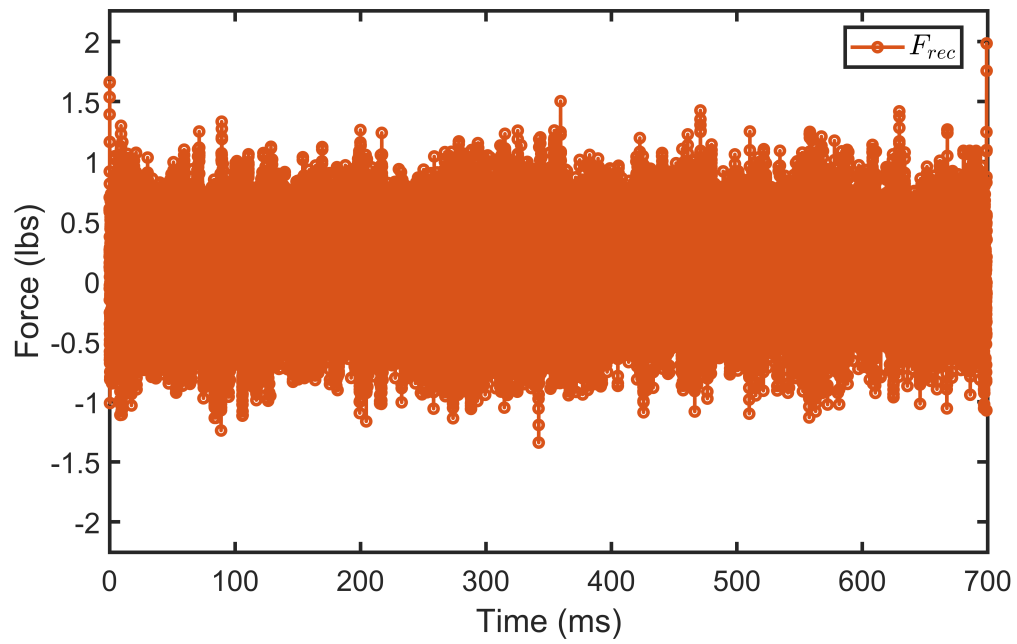


(a)

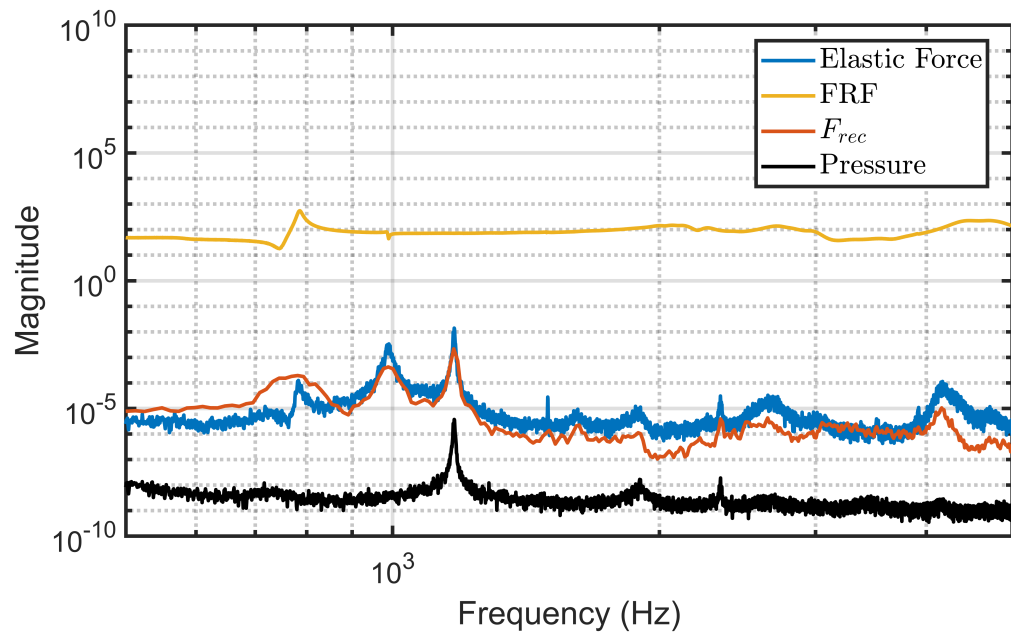


(b)

Figure 4.13: Wind tunnel force reconstruction using FDIM at load station 1 (forward most location). Time (a) and frequency (b) domain representations of the reconstruction are both shown.

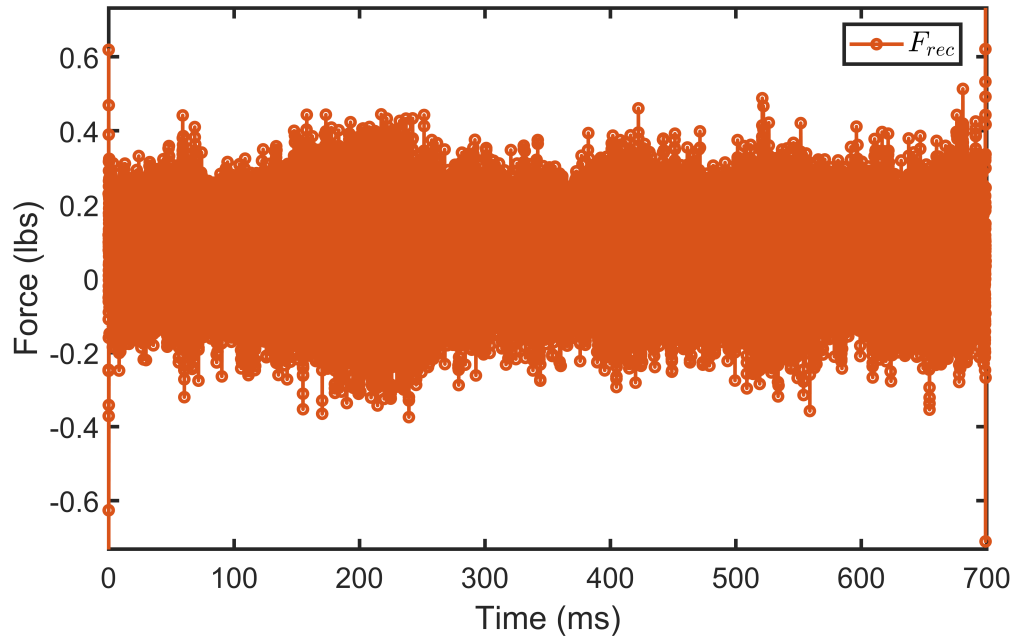


(a)

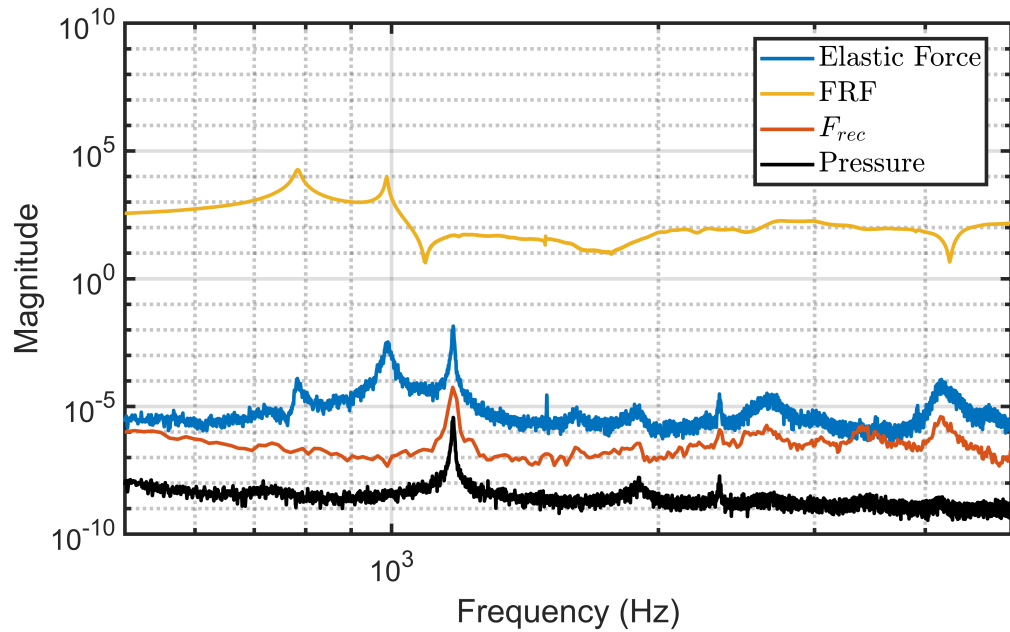


(b)

Figure 4.14: Wind tunnel force reconstruction using FDIM at load station 2 (middle location). Time (a) and frequency (b) domain representations of the reconstruction are both shown.



(a)



(b)

Figure 4.15: Wind tunnel force reconstruction using FDIM at load station 3 (aft most location). Time (a) and frequency (b) domain representations of the reconstruction are both shown.

Note that the time histories for these studies are much shorter than those in the GDLM results. This is because if multiple repeat tests are used, the shortest time history during calibration determines the maximum possible length of the FRF. This limits the overall length in this case to 0.7 seconds. Future tests could be performed with longer calibration tests.

## Chapter 5: Conclusions, Contributions, Recommendation, and Future Work

In this dissertation, a solution was sought to the problem of dynamic force measurement in AEDC Tunnel 9, a hypervelocity wind tunnel. Due to the low bandwidth of typical force measurement techniques, new approaches needed to be considered. Based on the specific restrictions and requirements of Tunnel 9, the scope of the research was narrowed to three methods: SWAT, TDDM, and FDIM. Each method has been investigated and improved with novel alterations, which are detailed in this work. The performance of each method was greatly improved by applying each alteration; often by orders of magnitude. Each method was validated both on numerical spring-mass-damper systems as well as on the Balance Calibration test article at Tunnel 9.

As for specific enhancements, the modally separated SWAT allowed for high frequency modal amplitude reduction where the conventional method showed significant, undesirable modal amplification. Furthermore, the addition of a damping matrix proved significant when the damping of the system was high.

A new TDDM was developed from first principles (i.e. convolution relationship between input and output). This reformulation allowed for simpler solution of the deconvolution problem without the need for conventional regularization of the inversion. Additionally, the segmented approach removed one of the chief weaknesses of TDDMs, the large computational requirement. By only considering a small segment of the output at a time, large time segments could be reconstructed in a more reasonable amount of time. Finally, the deconvolution of acceleration data was validated for the GDLM and shown to produce

comparable results to that of strain deconvolution. A combined acceleration-strain deconvolution was validated and yielded stable results for higher numbers of input locations.

The FDIM was also reformulated to consider direct solution of the FRF using input and output data recorded during calibration. Although this yields worse results for the simplest SISO cases, it allows for the use of multiple calibration tests. The addition of redundant calibration tests reduces the reliance of accuracy on a single test. Therefore, the influence of small user errors (e.g. application direction/location) and noise were shown to reduce significantly as the number of calibration tests increased. Again the deconvolution of acceleration data was validated, expanding the application scope for this method.

In addition to numerical and bench top validation, these techniques were also demonstrated on transonic wind tunnel experiments. These tests were used to demonstrate the segmented GDLM as well as cyclic force reconstruction for both the GDLM and FDIM. Upcoming tests are planned to demonstrate pulse control force reconstruction in a hypersonic wind tunnel.

The specific contributions to the state of the art are as follows:

1. Extension of the SWAT to improve higher frequency force reconstruction
2. Extension of the SWAT to improve force reconstruction for highly damped systems
3. Development of the CMM, a new TDDM which utilizes linear discretization and least squares inversion
4. Development of the GDLM, a generalized version of the CMM allowing for smooth reconstructions via a variable order discretization of the convolution integral
5. Validation of segmentation for TDDMs which allows for utilization of these computationally expensive methods on longer time histories

6. Utilization of multiple calibration sets to better constrain solution of the IRF in TD-DMs
7. Utilization of multiple calibration sets to better constrain solution of the FRF in FDIMs
8. Demonstration of GDLM and FDIM on transonic cyclic wind tunnel forcing experiment

As the ultimate goal is future implementation into Tunnel 9, it is important to discuss recommendations for future experiments. Although there are several benefits of recording high frequency strain data (e.g. further constraint of inversion and application of the SWAT), there are several drawbacks that should be considered. Firstly, the implementation of such sensors presents considerable design difficulty. For example, the physical size of the sensors was a challenge to implement for the upcoming tests at NASA Langley. Second, as with other strain gage balances, one must ensure that only a single load path exists between test article and support structure. This can complicate matters as the strain gage sensors must always be mounted between the two, further constraining the design possibilities. Acceleration data on the other hand is far easier to obtain. The implementation of this measurement can be an afterthought to a particular experiment, especially on large scale test articles as are used in Tunnel 9. This allows for considerable design flexibility and the ability to combine this analysis with other, more primary measurements and analyses. Furthermore, acceleration deconvolution can prove to be more effective in some very short duration cases as shown in the numerical experiments of the GDLM and FDIM.

For these practical reasons, it is my recommendation that the next investigation of this at Tunnel 9 be performed in addition to other experiments. This removes the requirement of scheduling and funding a particular experiment for this application; often a large hurdle to get over for popular DoD facilities such as Tunnel 9. If these results are acceptable and

future customers become primarily interested in dynamic force measurements, one could expand and include these high bandwidth strain sensors as well. However, if dynamic force measurement is not the primary investigation, it may prove too cumbersome to implement these sensors.

As this work is applicable to many wind tunnel facilities, a general guideline for which methods are applicable is presented here. Obviously, there are a number of factors such as tunnel size, test duration, and frequency response of interest that make an all-encompassing rule difficult or even impossible to formulate. Therefore, simple guidelines are given as a starting point for the interested experimentalist.

For large scale facilities such as Tunnel 9, the large test articles are typically sting mounted. As such, the dominant modes of vibration are typically lower frequency (e.g.  $< 100$  Hz). The SWAT is particularly useful in this frequency range as the SWAT most effectively removes these easily separable dominant modes. Additionally, the SWAT builds on techniques which most force balance engineers are familiar (i.e. static calibration) and therefore such techniques are more approachable. Of course if a higher frequency forcing is of interest, then a TDDM or FDIM may be more applicable.

For small to middle scale facilities, such as NASA Langley's Mach 6 and 10 wind tunnels[56] and AFRL's transonic wind tunnel, with long duration (e.g.  $> 10$  s), FDIMs are recommended. Generally, longer duration blow-down or continuous wind tunnels fit this category. Due to the long duration and size of these tunnels, many frequency ranges can be significant. As noted previously, the SWAT struggles at high frequencies and therefore can be less effective for significant dynamics of 200 Hz or more. Furthermore, since the duration of the usable flow is long with data generally sampled at a high rate (e.g.  $> 10$  kHz), typical TDDMs can be too computationally expensive. Although it's worth noting that the segmented GDLM formulated in this dissertation is applicable to such applications. This facility category is arguably the most flexible as the range of testing possibilities is the



most diverse. For example, if the facility is being used conventionally (i.e. constant step load suddenly applied), and the experimentalist is primarily interested in lift and drag measurement, the SWAT may be applicable. However, if a shorter duration or high frequency cyclic load is of interest, the TDDMs are more applicable.

For small scale facilities, such as the T4 free-piston shock tunnel used by University of Queensland[24], with short (e.g.  $< 10$  ms) test times, TDDMs are recommended. These can provide highly accurate force measurements on short time scales using either internal strain or acceleration measurements. Due to the high frequency dynamics relevant in these tunnels, the SWAT is ineffective as physical sensor delays on the order of hundreds of microseconds yields significant error. Additionally, due to the small scale of such facilities, it is often difficult to incorporate the various sensors required for the SWAT. FDIMs are also applicable, though their computation efficiency is not as advantageous at shorter durations.

There are a myriad of future endeavors related to this work. Many post-doctoral or follow on graduate projects could stem from this research. Specifically, uncertainty analysis, heat transfer measurement, and distributed pressure measurement are very relevant research avenues, relatively unexplored in the current field.

The most relevant topic of future research to Tunnel 9 is likely uncertainty analysis. Due to the complex solution formulation of these methods, it is often difficult to develop an uncertainty criterion. The uncertainties inherent to each measurement need be passed through the same equations (i.e. inversions), often yielding unreasonably high uncertainties due to the inversion. Additionally, for comprehensive uncertainty analysis, a separate method need be developed for each method under investigation. Scientists at NIST have recently been developing an approach for the FDIM to quantify uncertainty measurements[57]. The investigation of uncertainty of inverse problems is definitely an area of relevant future research.

Heat transfer measurement is also a relevant application to aerodynamic wind tunnel

measurement. Typically, a 1D heat transfer assumption is made and the analytical properties of each layer/substrate is assumed[58–60]. However, this can cause significant difficulties if the system properties are challenging to obtain. Interestingly, a convolution relationship exists between temperature and applied heat transfer[61]. Therefore, provided the system remains LTI, one may attempt to apply the GDLM or FDIM to this problem as well.

Distributed, dynamic pressure measurement is also a relevant topic of future research. Often in aerodynamic testing, the distribution of pressure applied to the test article surface is of more interest than a particular point force contribution. Therefore, the solution of a distributed pressure field over a test article surface would be extremely insightful. Pressure sensitive paint (PSP) provides this but requires an oxygen flow and conflicts with TSP. Based on preliminary numerical experiments, it is possible to reconstruct a dynamic pressure field given a sufficiently dense grid of reconstructed point forces. However, much future work would need to be performed to validate this method on an experimental system. Additionally, the required input force spacing density is currently unknown.

The scope of future work could also expand beyond the field of aerodynamics. Many physical processes can be related via the convolution integral (e.g. acoustics). Therefore, these methods could be applied in many other fields where the convolution relationship is applicable.

Additionally, a hypersonic wind tunnel demonstration is planned at NASA Langley Research Center in the near future. Due to scheduling difficulties, this study was not included in the dissertation. However, it will be published in future works.

As interest in control of hypersonic test articles continues to grow, so too will the need for measurement of dynamic forces applied in wind tunnels. It is this authors hope that this dissertation serves as an approachable starting point for the scientist interested in implementing one of these techniques.

## Appendix A: Ill-Posed Problem Explanation

In this section we give proof that small singular values become large errors during inversion. Consider the following arbitrary matrix equation

$$\mathbf{y} = \mathbf{A}\mathbf{u} \quad (\text{A.1})$$

where  $\mathbf{y}$  and  $\mathbf{u}$  are  $N \times 1$  vectors and  $\mathbf{A}$  is an  $N \times N$  matrix relating the two. Such is the case in discretized convolution problems. Next, consider the singular value decomposition (SVD) of matrix  $\mathbf{A}$ , i.e.

$$\mathbf{A} = \mathbf{U}\mathbf{S}\mathbf{V}^T = \sum_{i=1}^N \mathbf{u}_i \sigma_i \mathbf{v}_i^T \quad (\text{A.2})$$

where  $\mathbf{U}$ ,  $\mathbf{S}$ , and  $\mathbf{V}$  are  $N \times N$  matrices,  $\mathbf{S}$  is a diagonal matrix of singular values, and  $\mathbf{U}$  and  $\mathbf{V}$  are orthogonal matrices (i.e.  $\mathbf{U}^{-1} = \mathbf{U}^T$ ).

Additionally, consider a measured output as

$$\mathbf{y}_m = \mathbf{y}_e + \mathbf{n} \quad (\text{A.3})$$

where the subscripts  $m$  and  $e$  stand for measured and exact, respectively. The last term,  $\mathbf{n}$  is a vector of noise points i.e.

$$\mathbf{n} = \frac{\text{std}(\mathbf{y}_e)}{\text{SNR}} \bar{\mathbf{n}} \quad (\text{A.4})$$

where std is the standard deviation, SNR is the signal to noise ratio and  $\bar{\mathbf{n}}$  is a Gaussian

distribution of points with a standard deviation of one. This is consistent with our definition of SNR and allows the user to set the noise level as some fraction of the exact signal.

As is commonly done with inverse problems, we wish to invert  $\mathbf{A}$  and premultiply  $\mathbf{y}_m$  to solve for  $\mathbf{u}$ , i.e.

$$\mathbf{u}_{\text{rec}} = \mathbf{A}^{-1} \mathbf{y}_m = \mathbf{A}^{-1} (\mathbf{y}_e + \mathbf{n}). \quad (\text{A.5})$$

The first term, is the exact input i.e.  $\mathbf{u}_e = \mathbf{A}^{-1} \mathbf{y}_e$ , however, the latter term is a source of error. Recalling the SVD of  $\mathbf{A}$ , we may define a noise contribution to the input as

$$\mathbf{u}_n = \mathbf{A}^{-1} \mathbf{n} = \sum_{i=1}^N \frac{\mathbf{u}_i^T \mathbf{n} \mathbf{v}_i}{\sigma_i}. \quad (\text{A.6})$$

In this form, it is clear that very small singular values (e.g.  $< 10^{-10}$  or so) become extremely large errors in the reconstructed input,  $\mathbf{u}_{\text{rec}}$ .

If we plug Eq. (A.4) into Eq. (A.6) we see that this error also grows as the signal to noise ratio decreases. Furthermore, if any singular value is equal to zero, the answer tends to infinity.

## Appendix B: Properties of Convolution

### B.1 Commutativity

In this section, I will prove the commutativity property of the continuous convolution, i.e.

$$u * h(t) = h * u(t) \quad (\text{B.1})$$

where  $*$  is the convolution operation. For clarity, the continuous convolution equation is mirrored here

$$y(t) = \int_{-\infty}^{\infty} h(t - \tau)u(\tau) d\tau \quad (\text{B.2})$$

where the more general expression spanning all time (infinity bounds) is used.

Begin by defining the new variable

$$x = t - \tau. \quad (\text{B.3})$$

We may express Eq. (B.2) in terms of this new variable by noting  $\tau = t - x$  and  $d\tau = -dx$  as

$$y(t) = \int_{\infty}^{-\infty} h(x)u(t - x)(-dx) \quad (\text{B.4})$$

or swapping the bounds (and by doing so, multiplying by -1) as

$$y(t) = \int_{-\infty}^{\infty} h(x)u(t - x) dx. \quad (\text{B.5})$$

Finally, one may note that the selection of the integration variable  $x$  is arbitrary. Therefore, we may switch back to our original notation of  $\tau$  and we obtain

$$y(t) = \int_{-\infty}^{\infty} h(\tau)u(t - \tau) d\tau \quad (\text{B.6})$$

thus proving the commutativity property of the continuous convolution.

## B.2 Fourier Transform

In this section, I will prove that applying a Fourier Transform to a continuous convolution integral results in a multiplication of the frequency domain counterparts of the convolved signals, i.e.

$$\mathcal{F}\{h * u(t)\} = H(\omega) \cdot U(\omega) \quad (\text{B.7})$$

where capital variable signify frequency domain counterparts of the lower case time domain variables.

Begin with the definition of the continuous Fourier Transform, i.e.

$$\mathcal{F}\{f(t)\} = \int_{-\infty}^{\infty} \exp^{-2\pi i \omega t} f(t) dt. \quad (\text{B.8})$$

We may plug the continuous convolution (i.e. Eq. (B.2)) into Eq. (B.8) as

$$\mathcal{F}\{h * u(t)\} = \int_{-\infty}^{\infty} \exp^{-2\pi i \omega t} \left[ \int_{-\infty}^{\infty} h(t - \tau)u(\tau) d\tau \right] dt. \quad (\text{B.9})$$

We may switch the order of integration as

$$\mathcal{F}\{h * u(t)\} = \int_{-\infty}^{\infty} \left[ \int_{-\infty}^{\infty} \exp^{-2\pi i \omega t} h(t - \tau) dt \right] u(\tau) d\tau \quad (\text{B.10})$$

where  $u(\tau)$  is kept out of the first integral as it is not a function of  $t$ . Next, we may display the exponential term as

$$\exp^{-2\pi i \omega t} = \exp^{-2\pi i \omega(t-\tau+\tau)} = \exp^{-2\pi i \omega(t-\tau)} \cdot \exp^{-2\pi i \omega \tau}. \quad (\text{B.11})$$

Plugging this result back into Eq. (B.10) and moving the second term outside the integral results in

$$\mathcal{F}\{h * u(t)\} = \int_{-\infty}^{\infty} \left[ \int_{-\infty}^{\infty} \exp^{-2\pi i \omega(t-\tau)} h(t-\tau) d\tau \right] \exp^{-2\pi i \omega \tau} u(\tau) d\tau. \quad (\text{B.12})$$

Define the new variable given in Eq. (B.3) which results in

$$\mathcal{F}\{h * u(t)\} = \int_{-\infty}^{\infty} \left[ \int_{-\infty}^{\infty} \exp^{-2\pi i \omega x} h(x) dx \right] \exp^{-2\pi i \omega \tau} u(\tau) d\tau. \quad (\text{B.13})$$

Finally, one may evaluate each integration separately as each contain unique variables, i.e.

$$\mathcal{F}\{h * u(t)\} = \left[ \int_{-\infty}^{\infty} \exp^{-2\pi i \omega x} h(x) dx \right] \int_{-\infty}^{\infty} \exp^{-2\pi i \omega \tau} u(\tau) d\tau \quad (\text{B.14})$$

and recalling our definition of the Fourier transform results proves Eq. (B.7).

### B.3 Differentiability

In this section, I will prove the differentiability of the convolution integral, i.e.

$$\frac{d}{dt} y(t) = \frac{d}{dt} h * u(t) \quad (\text{B.15})$$

or in compact notation as

$$\dot{y}(t) = \dot{h} * u(t) \quad (\text{B.16})$$

where the dot signifies a time derivative. Obviously, using the commutative property of the convolution, we could apply the time derivative to the function  $u(t)$  instead. However, applying the derivative to  $h(t)$  is more useful for the applications discussed in this dissertation.

This property is most easily derived using the inverse Fourier Transform, i.e.

$$f(t) = \int_{-\infty}^{\infty} \exp^{2\pi i \omega t} F(\omega) d\omega \quad (\text{B.17})$$

which transforms frequency domain signals back to the time domain. Evaluating the time derivative of Eq. (B.17) we obtain

$$\dot{f} = \frac{d}{dt} \int_{-\infty}^{\infty} \exp^{2\pi i \omega t} F(\omega) d\omega = 2\pi i \omega \int_{-\infty}^{\infty} \exp^{2\pi i \omega t} F(\omega) d\omega. \quad (\text{B.18})$$

Hence the Fourier Transform of the time derivative of an arbitrary function is

$$\mathcal{F} \left\{ \dot{f}(t) \right\} = 2\pi i \omega F(\omega). \quad (\text{B.19})$$

Returning to Eq. (B.16), we may apply the Fourier Transform to gain additional insight, i.e.

$$\mathcal{F} \left\{ \dot{y}(t) \right\} = 2\pi i \omega \mathcal{F} \{ y(t) \} = 2\pi i \omega \mathcal{F} \{ h * u(t) \} = 2\pi i \omega H(\omega) \cdot U(\omega). \quad (\text{B.20})$$

Performing an inverse Fourier Transform results in Eq. (B.16).

One may also note that this operation is repeatable so long as a differential exists. Therefore, we may repeat this operation to prove

$$\ddot{y}(t) = \ddot{h} * u(t) \quad (\text{B.21})$$



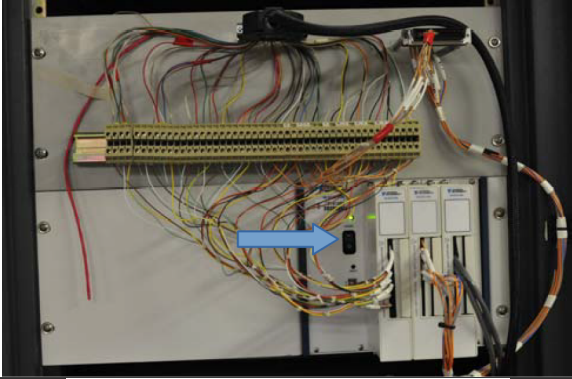

and all subsequent time derivatives.


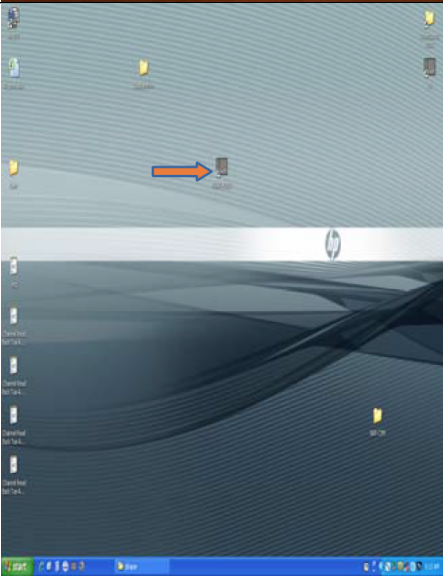

## Appendix C: Standard Operating Procedures

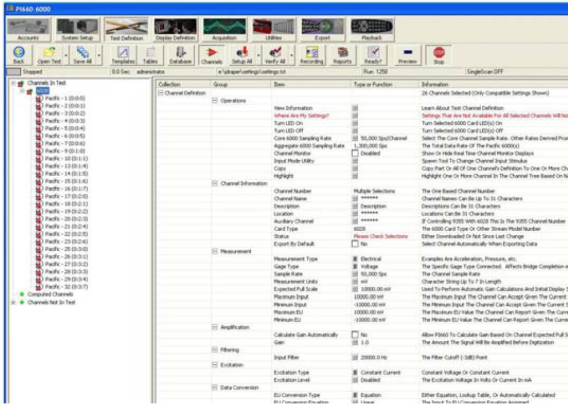
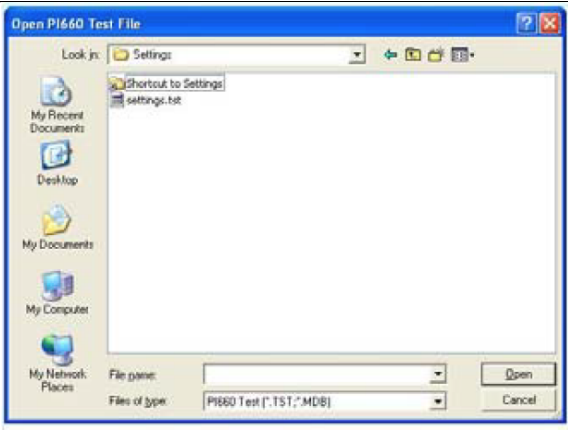
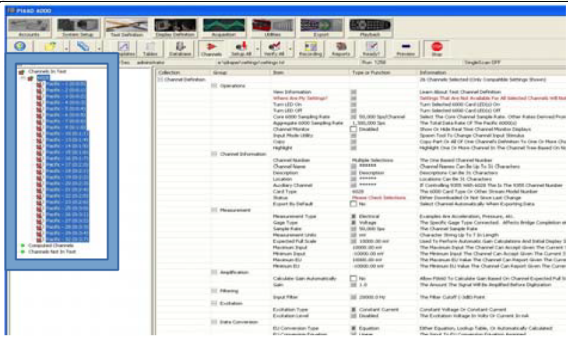
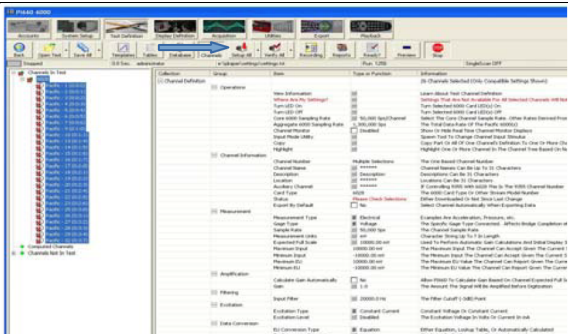
The purpose of this appendix is to aid future researches in properly collecting data and performing static and dynamic calibrations for the various methods discussed in this dissertation. These standard operating procedures (SOPs) are most useful for experiments in the AEDC White Oak Balance Calibration Laboratory. However, the methods could still be followed with slightly different hardware at another facility.



### C.1 Data Acquisition

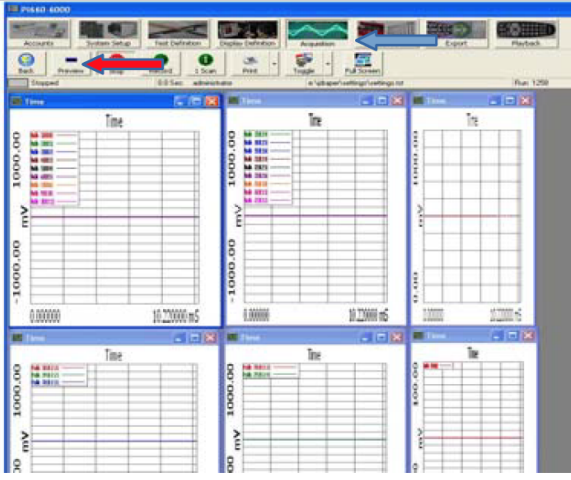

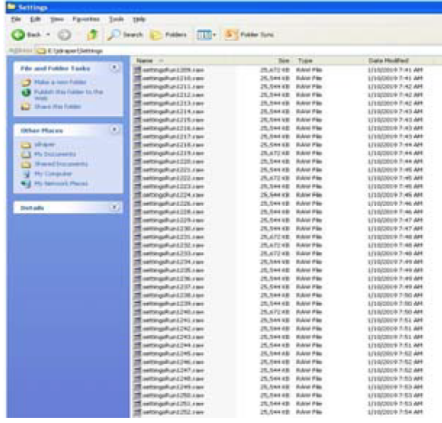
This appendix contains step-by-step instructions for collecting data in the AEDC White Oak Balance Calibration Laboratory. In particular, the data acquisition of Model 260A01 strain gages and Model 52 accelerometers using Model 482c16 and Model 101 DC signal conditioners, respectively. For different sensors, signal conditioners, or testing location, the following process may vary.

Step Number	Description	Illustration
1	Turn on pedal box.	 <p>A photograph showing the internal wiring of a pedal box. A blue arrow points to a small black switch, likely the power switch, located among a dense array of colorful wires connected to a terminal block.</p>
2	<p>Turn on data acquisition boxes.</p> <p>Note: Pictured are for the Model 260A01 (left) and Model 52 Accelerometers (right).</p>	 <p>A photograph showing two stacks of data acquisition boxes on a white shelf. The left stack consists of four blue-faced units, and the right stack consists of three blue-faced units. Below the stacks, on a lower shelf, is a larger silver-faced unit, likely a power supply or a central processing unit. Numerous cables are visible connecting the units.</p>

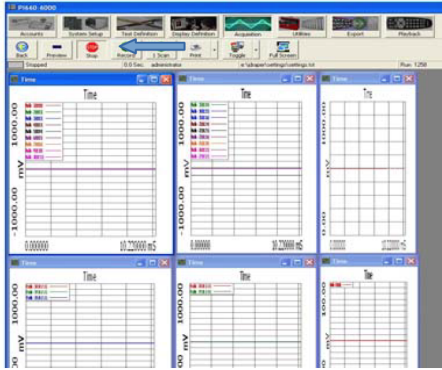
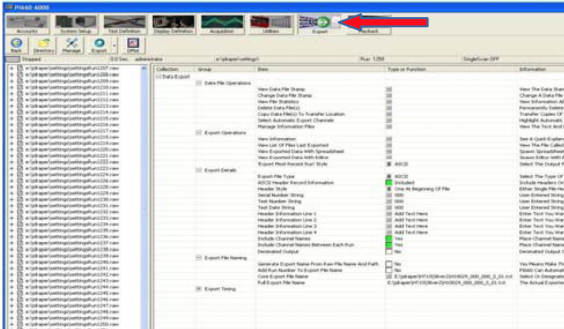
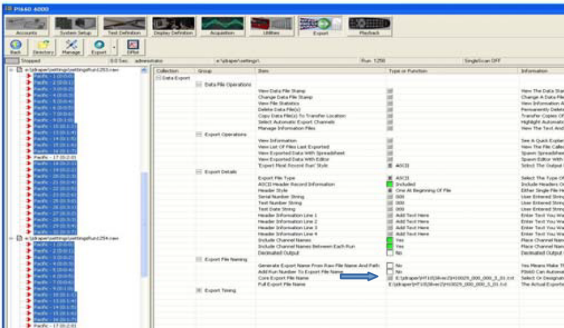
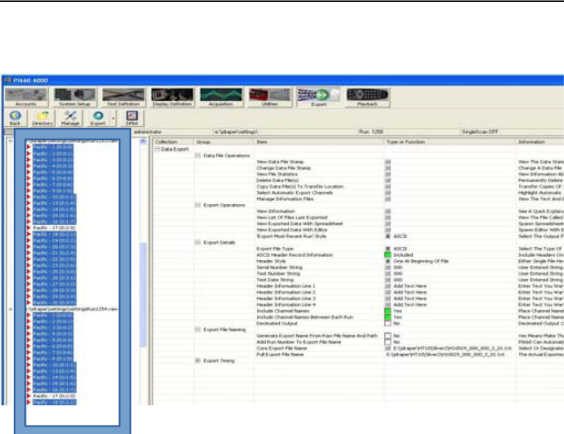
3	Turn on computer and plug in hard drive.	
4	Open program in center of desktop called PI660-6000.	
5	On the top menu click "Log In".	

6	<p>Navigate to the test definition tab and select the "Open Test" module.</p>	
7	<p>Navigate to the settings folder on the hard drive and open settings.txt</p>	
8	<p>Click the "+" next to 6028. Then click on 6028 to select all the sub items.</p>	
9	<p>On the top menu click the "Setup All" module.</p>	

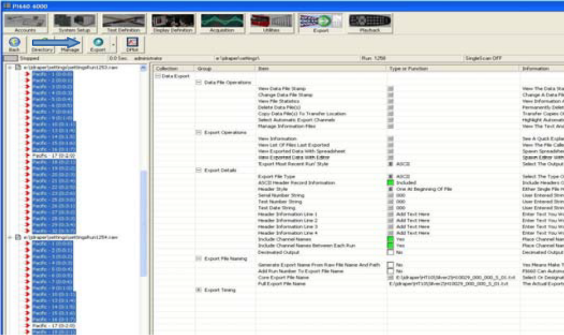
10	<p>Zero the strain sensors. Do this by hitting enter, navigate to zero, then hit enter again. Click the down arrow when channel is selected to select all. Then, click the right/left arrow and click the up arrow to select autozero. Click enter and wait for the autozero process to finish. This is when the screen goes back to showing the gains of each signal (e.g. 10 10 10 10).</p>	 <p>The image shows a PCB Piezotronics Model 482C Series Sensor Signal Conditioner. The front panel features a digital display showing 'Chan All AUTOZERO'. Above the display are four status indicators for channels 1 through 4, each with 'OPEN', 'SHORT', and 'OVERLOAD' labels. Below the display are navigation buttons: a power button, left and right arrows, up and down arrows, and an 'ENTER' button. The unit is black with a silver faceplate.</p>
11	<p>Zero the accelerometers. Do this by clicking on each channel button, then hitting zero. The arrows show the channel select and zero buttons.</p>	 <p>The image shows a Measurement Systems Model 191 DC Signal Conditioner Amplifier. The front panel has a large color display showing a menu with 'SET AMPLIFIER GAIN' and 'MY EXCITATION VOLTAGE'. Below the display are buttons for 'Enter', 'Ch. 1 Select', 'Ch. 2 Select', 'Ch. 3 Select', 'Short Cal', and 'Reset Zero'. Red arrows point to the 'Ch. 1 Select' and 'Reset Zero' buttons. The unit is black with a silver faceplate.</p>

12	<p>Navigate to the acquisition tab on the computer and click preview to preview the sensor output.</p>	
13	<p>To run a test, hit the pedal to begin recording. If previewing, under the acquisition tab, the selected button will change from preview to record. When the recording is over it will change back to preview.</p>	
14	<p>To delete a test in the event of an error, open up the file explorer and inside the external HD directory navigate to jdraper/settings. Here, the most recent raw data file can be deleted.</p>	



15	<p>If previewing and finished taking data, click "Stop" on the top menu.</p>	
16	<p>To export data, navigate to the export tab.</p>	
17	<p>In export settings, select the output folder.</p>	
18	<p>On the left menu, select all channels to export except channel 17. This is because channel 17 contains data from the pedal which is not needed. In addition, multiple tests can be exported at the same time and renamed later.</p>	

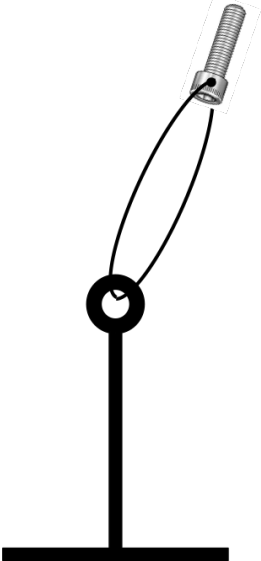


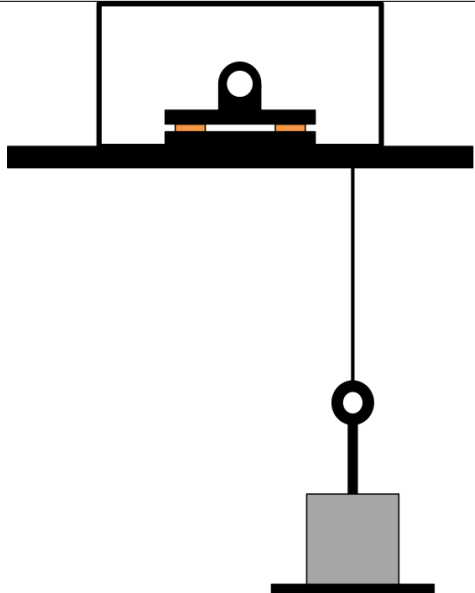

19	Click export to export the data in text format. Rename the files as necessary.	
----	--	--

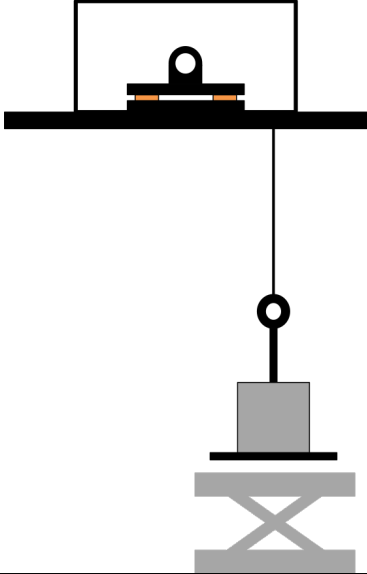

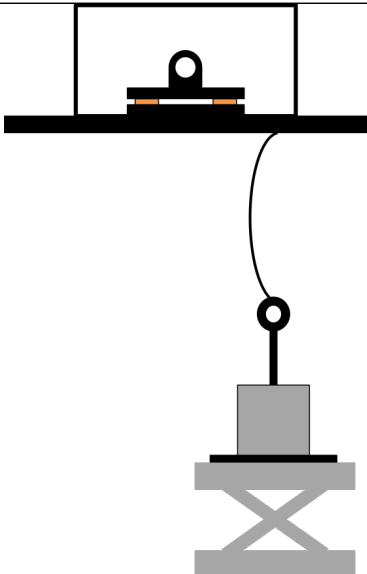
## C.2 Static Calibration

This section details the static calibration of the piezoelectric strain sensors. Since these sensors are capacitive in nature, they exhibit non-negligible drift after a sensor is loaded. Due to this drift, typical calibration methodologies are not applicable as the user cannot wait a long period of time for the signal to steady. To circumvent this challenge, the method used here is to remove the weight from the test article. This is significantly smoother and faster than applying the weight.

As a note, it is often recommended to fully encompass the loading envelope with the static calibration. For example, if 10 pounds of normal force is expected, it may be useful to perform calibrations from 0 to 20 pounds in as fine an increment as desired. The SOP for each loading orientation and magnitude is presented below.

Step Number	Description	Illustration
1	Thread fishing line through weight hanger and screw with through hole in screw head.	
2	Zero orientation of model such that gravity is coincident with the desired loading direction (e.g. 0° pitch and roll yields pure z-direction force). An inclinometer is recommended for this step.	

3	Insert screw into hole location of interest and load desired weight onto weight hanger.	
4	Steady weight such that swinging is minimized.	
5	Zero reading from strain sensors. To do so, on each strain gage signal conditioner select "ZERO" from the main menu. Scroll to "ALL" for the "Channel" option and choose the "Autozero" option. Wait until screen returns to original state.	
6	Ensure data acquisition system is primed (see data acquisition SOP for more explicit instructions).	

7	<p>Place scissor jack below weight hanger.</p> <p>This will remove the weight, a steadier alternative to placing the weight.</p>	
8	<p>Trigger data acquisition by pressing pedal.</p>	
9	<p>Shortly ( 1 second) after data acquisition initiation, raise scissor jack and smoothly remove weight until tension in fishing line is released.</p>	

10	Wait until data collection has finished (default recording time is 10 seconds) and remove screw from hole of interest.	
11	Repeat steps 2-10 for each loading orientation/magnitude of interest.	

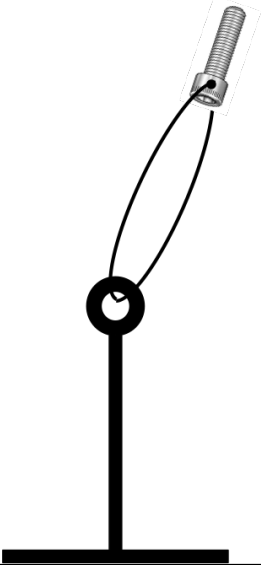
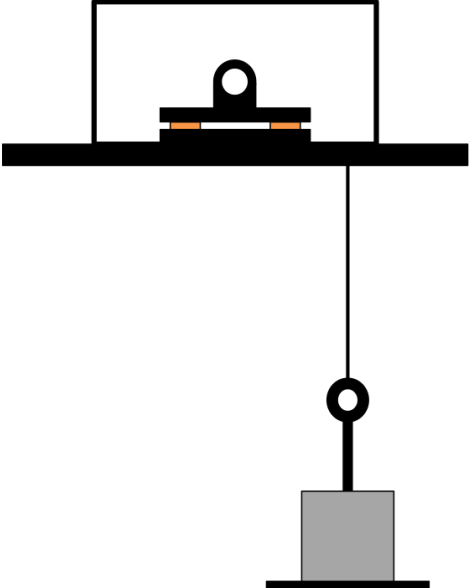
### C.3 Dynamic Calibration


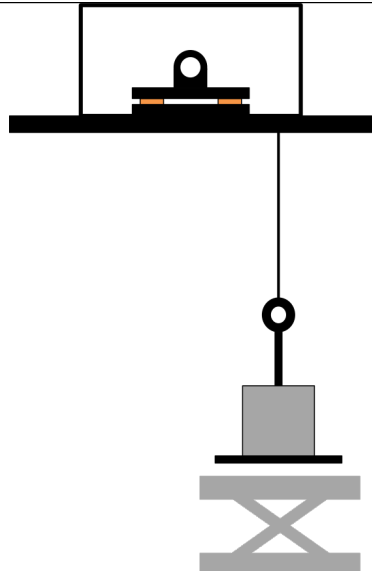
This section details the dynamic calibration for each of the methods. Different calibration methodologies are utilized for the SWAT and TDDM/FDIM approaches. As such, a separate SOP is presented for the two variants.


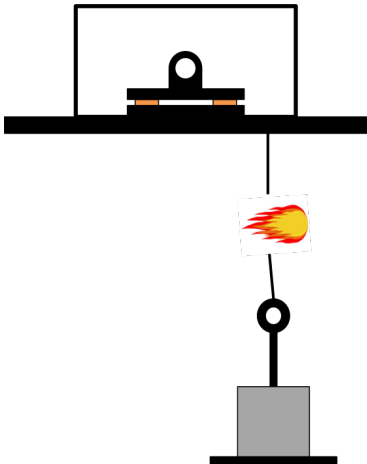
#### C.3.1 SWAT - Drop Testing

The dynamic calibration methodology used for the SWAT is very similar to static calibration. The primary difference is the step is *dynamically* applied rather than *statically*. So instead of a scissor jack smoothly removing the weight, a blowtorch or other severing mechanism is used to sharply remove the weight. The SOP for SWAT dynamic calibration is presented below.

Step Number	Description	Illustration
----------------	-------------	--------------

1	Thread fishing line through weight hanger and screw with through hole in screw head.	
2	Zero orientation of model such that gravity is coincident with the desired loading direction (e.g. $0^\circ$ pitch and roll yields pure z-direction force). An inclinometer is recommended for this step.	
3	Insert screw into hole location of interest and load desired weight onto weight hanger.	

4	Steady weight such that swinging is minimized.	
5	Zero reading from strain sensors. To do so, on each strain gage signal conditioner select "ZERO" from the main menu. Scroll to "ALL" for the "Channel" option and choose the "Autozero" option. Wait until screen returns to original state.	
6	Ensure data acquisition system is primed (see data acquisition SOP for more explicit instructions).	
7	Place scissor jack below weight hanger. This will remove the weight, a steadier alternative to placing the weight.	



8	Trigger data acquisition by pressing pedal.	
9	Shortly ( 1 second) after data acquisition initiation, sever the tether to release the weight. Typically, a propane blow torch is used for this application as it is the quickest and smoothest method. Scissors could also be used but often impart unwanted oscillations to the applied load.	
10	Wait until data collection has finished (default recording time is 10 seconds) and remove screw from hole of interest.	
11	Repeat steps 1-10 for each loading orientation/magnitude of interest.	


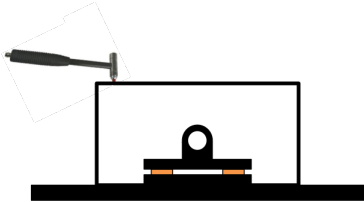
### C.3.2 TDDM/FDIM - Hammer Testing

Dynamic calibration for the TDDM and FDIM is slightly different than for the SWAT. The reasoning behind this is the exact applied load during calibration must be known for these methods. If a step load was used, the exact magnitude, rise time, and any possible oscillations are not known which can cause errors in the constructed IRF/FRF. Since impulse hammers directly measure dynamic loads, the tester can record a more accurate applied



load. The SOP for hammer test dynamic calibration is detailed below.

Step Number	Description	Illustration
1	<p>Ensure that the hammer is plugged in to the Model 482C05 signal conditioner and the desired tip is securely attached.</p> <p>The user may want to wait a few minutes after plugging in the hammer as the signal tends to drift slowly towards zero as it's first plugged in.</p>	
2	<p>Zero orientation of model such that gravity is coincident with the desired loading direction (e.g. 0° pitch and roll yields pure z-direction force). An inclinometer is recommended for this step.</p>	
3	<p>Zero reading from strain sensors. To do so, on each strain gage signal conditioner select "ZERO" from the main menu. Scroll to "ALL" for the "Channel" option and choose the "Autozero" option. Wait until screen returns to original state.</p>	

4	Ensure data acquisition system is primed (see data acquisition SOP for more explicit instructions).	
5	Trigger data acquisition by pressing pedal.	
6	Shortly ( 1 second) after data acquisition initiation, strike the surface with the impulse hammer. Try to apply the strike as orthogonally to the surface as possible. User orientation error is a possible source of error. Additionally, retract the hammer as quickly as possible. Double pulses are a common error of hammer testing and can sometimes be avoided by quickly retracting the hammer.	
7	Wait until data collection has finished (default recording time is 10 seconds) and remove screw from hole of interest.	
8	Repeat steps 2-7 for each loading orientation, hammer tip, and loading magnitude of interest.	

## Bibliography

- [1] Keith C. Lynn, Sean A. Commo, and Peter A. Parker. Wind-Tunnel Force Balance Characterization for Hypersonic Research Applications. *Journal of Aircraft*, 49(2): 556–565, March 2012. ISSN 0021-8669, 1533-3868. doi: 10.2514/1.C031567. URL <http://arc.aiaa.org/doi/10.2514/1.C031567>.
- [2] Keith C. Lynn, Kenneth G. Toro, David T. Chan, Sundareswara Balakrishna, and Drew Landman. Enhancements to the National Transonic Facility Semispan Force Measurement System. *Journal of Aircraft*, 52(6):1736–1755, November 2015. ISSN 0021-8669, 1533-3868. doi: 10.2514/1.C032942. URL <http://arc.aiaa.org/doi/10.2514/1.C032942>.
- [3] Ray Rhew, Jon Bader, Timothy Marshall, Marcus Skelley, and Mark Woike. Partnership for the Revitalization of National Wind Tunnel Force Measurement Capability. In *47th AIAA Aerospace Sciences Meeting including The New Horizons Forum and Aerospace Exposition*, Orlando, Florida, January 2009. American Institute of Aeronautics and Astronautics. ISBN 978-1-60086-973-0. doi: 10.2514/6.2009-1514. URL <http://arc.aiaa.org/doi/10.2514/6.2009-1514>.
- [4] J. L. Grunnet. Factors affecting the magnitude of jet interaction forces. *Journal of Spacecraft and Rockets*, 8(12):1234–1235, December 1971. ISSN 0022-4650, 1533-6794. doi: 10.2514/3.30370. URL <http://arc.aiaa.org/doi/10.2514/3.30370>.
- [5] Mitsuru Kurita, Tsuyoshi Inoue, and Yoshiaki Nakamura. Aerodynamic interaction due to side jet from a blunted cone in hypersonic flow. American Institute of Aeronautics and Astronautics, August 2000. doi: 10.2514/6.2000-4518. URL <http://arc.aiaa.org/doi/10.2514/6.2000-4518>.
- [6] Stuart Laurence, Jan Martinez Schramm, Sebastian Karl, and Klaus Hannemann. An Experimental Investigation of Steady and Unsteady Combustion Phenomena in the HyShot II Combustor. American Institute of Aeronautics and Astronautics, April 2011. ISBN 978-1-60086-942-6. doi: 10.2514/6.2011-2310. URL <http://arc.aiaa.org/doi/10.2514/6.2011-2310>.

- [7] Stuart Laurence, Hiroshi Ozawa, Damien Lieber, Jan Martinez Schramm, and Klaus Hannemann. Investigation of Unsteady/Quasi-Steady Scramjet Behavior using High-Speed Visualization Techniques. American Institute of Aeronautics and Astronautics, September 2012. ISBN 978-1-60086-931-0. doi: 10.2514/6.2012-5913. URL <http://arc.aiaa.org/doi/10.2514/6.2012-5913>.
- [8] Andrew Lazur, J. Sawyer, Brian Sullivan, and Larry Hudson. Hypersonic vehicle control surface development. In *9th International Space Planes and Hypersonic Systems and Technologies Conference*, Norfolk, VA, U.S.A., November 1999. American Institute of Aeronautics and Astronautics. doi: 10.2514/6.1999-4864. URL <http://arc.aiaa.org/doi/10.2514/6.1999-4864>.
- [9] Nathan Falkiewicz, Carlos Cesnik, Michael Bolender, and David Doman. Thermoelastic Formulation of a Hypersonic Vehicle Control Surface for Control-Oriented Simulation. In *AIAA Guidance, Navigation, and Control Conference*, Chicago, Illinois, August 2009. American Institute of Aeronautics and Astronautics. ISBN 978-1-60086-978-5. doi: 10.2514/6.2009-6284. URL <http://arc.aiaa.org/doi/10.2514/6.2009-6284>.
- [10] John F. Lafferty, Joseph J. Coblish, Eric Marineau, Joseph D. Norris, Inna Kurits, Daniel R. Lewis, Michael Smith, and Michael Marana. The Hypervelocity Wind Tunnel No. 9; Continued Excellence Through Improvement and Modernization. American Institute of Aeronautics and Astronautics, January 2015. ISBN 978-1-62410-343-8. doi: 10.2514/6.2015-1340. URL <http://arc.aiaa.org/doi/10.2514/6.2015-1340>.
- [11] Inna Kurits, Joseph Norris, and Pratik Bhandari. Temperature-Sensitive Paint Calibration Methodology Developed at AEDC Tunnel 9. In *49th AIAA Aerospace Sciences Meeting including the New Horizons Forum and Aerospace Exposition*, Orlando, Florida, January 2011. American Institute of Aeronautics and Astronautics. ISBN 978-1-60086-950-1. doi: 10.2514/6.2011-851. URL <http://arc.aiaa.org/doi/10.2514/6.2011-851>.
- [12] J. Sanchez and H. Benaroya. Review of force reconstruction techniques. *Journal of Sound and Vibration*, 333(14):2999–3018, July 2014. ISSN 0022460X. doi: 10.1016/j.jsv.2014.02.025. URL <http://linkinghub.elsevier.com/retrieve/pii/S0022460X14001527>.
- [13] Internal Balance Technology Working Group, editor. *Recommended Practice: Calibration and Use of Internal Strain-Gage Balances with Application to Wind Tunnel Testing (AIAA R-091-2003)*. American Institute of Aeronautics and Astronautics, Inc., Washington, DC, January 2003. ISBN 978-1-56347-645-7 978-1-56347-646-4. doi: 10.2514/4.476464. URL <http://arc.aiaa.org/doi/book/10.2514/4.476464>.

- [14] Eric C. Marineau. Force Measurements in Hypervelocity Flows with an Acceleration Compensated Piezoelectric Balance. *Journal of Spacecraft and Rockets*, 48(4):697–700, July 2011. ISSN 0022-4650, 1533-6794. doi: 10.2514/1.A32047. URL <http://arc.aiaa.org/doi/10.2514/1.A32047>.
- [15] Eric Marineau, Matthew MacLean, E. Mundy, and Michael Holden. Force Measurements in Hypervelocity Flows with an Acceleration Compensated Strain Gage Balance. *Journal of Spacecraft and Rockets*, 49(3):474–482, May 2012. ISSN 0022-4650, 1533-6794. doi: 10.2514/1.A32041. URL <http://arc.aiaa.org/doi/10.2514/1.A32041>.
- [16] John W. Draper, Sung Lee, and Eric C. Marineau. Development and Implementation of a Hybrid Dynamic Force Measurement System at AEDC Tunnel 9. American Institute of Aeronautics and Astronautics, January 2017. ISBN 978-1-62410-453-4. doi: 10.2514/6.2017-1593. URL <http://arc.aiaa.org/doi/10.2514/6.2017-1593>.
- [17] Matthew Allen and Thomas Carne. Comparison of Inverse Structural Filter (ISF) and Sum of Weighted Accelerations (SWAT) Time Domain Force Identification Methods. In *47th AIAA/ASME/ASCE/AHS/ASC Structures, Structural Dynamics, and Materials Conference & 14th AIAA/ASME/AHS Adaptive Structures Conference & 7th*, Newport, Rhode Island, May 2006. American Institute of Aeronautics and Astronautics. ISBN 978-1-62410-040-6. doi: 10.2514/6.2006-1885. URL <http://arc.aiaa.org/doi/abs/10.2514/6.2006-1885>.
- [18] S. J. Laurence, C. S. Butler, J. Martinez Schramm, and K. Hannemann. Force and Moment Measurements on a Free-Flying Capsule in a Shock Tunnel. *Journal of Spacecraft and Rockets*, 55(2):403–414, March 2018. ISSN 0022-4650, 1533-6794. doi: 10.2514/1.A33820. URL <https://arc.aiaa.org/doi/10.2514/1.A33820>.
- [19] Niranjana Sahoo, D.R. Mahapatra, G. Jagadeesh, S. Gopalakrishnan, and K.P.J. Reddy. Design and analysis of a flat accelerometer-based force balance system for shock tunnel testing. *Measurement*, 40(1):93–106, January 2007. ISSN 02632241. doi: 10.1016/j.measurement.2006.03.016. URL <https://linkinghub.elsevier.com/retrieve/pii/S0263224106000650>.
- [20] Jim Crafton, Scott Stanfield, Nikolay Rogoshchenkov, Steve Palluconi, and Ryan F. Schmit. Measurement of Unsteady Forces on a Store in a Cavity Using Dynamic Pressure-Sensitive Paint. In *2018 Aerodynamic Measurement Technology and Ground Testing Conference*, Atlanta, Georgia, June 2018. American Institute of Aeronautics and Astronautics. ISBN 978-1-62410-561-6. doi: 10.2514/6.2018-3318. URL <https://arc.aiaa.org/doi/10.2514/6.2018-3318>.
- [21] Marvin E. Sellers and Michael Nelson. Development of Unsteady Pressure Sensitive Paint Measurement Capability at Arnold Air Force Base. In *2018 Aerodynamic Measurement Technology and Ground Testing Conference*, Atlanta, Georgia, June

2018. American Institute of Aeronautics and Astronautics. ISBN 978-1-62410-561-6. doi: 10.2514/6.2018-4051. URL <https://arc.aiaa.org/doi/10.2514/6.2018-4051>.
- [22] Edward T. Schairer, Rabindra D. Mehta, and Michael E. Olsen. Effects of Pressure-Sensitive Paint on Experimentally Measured Wing Forces and Pressures. *AIAA Journal*, 40(9):1830–1838, September 2002. ISSN 0001-1452, 1533-385X. doi: 10.2514/2.1860. URL <http://arc.aiaa.org/doi/10.2514/2.1860>.
- [23] David J. Mee, William J. T. Daniel, and John M. Simmons. Three-component force balance for flows of millisecond duration. *AIAA Journal*, 34(3):590–595, March 1996. ISSN 0001-1452, 1533-385X. doi: 10.2514/3.13108. URL <http://arc.aiaa.org/doi/10.2514/3.13108>.
- [24] D. J. Mee. Dynamic calibration of force balances for impulse hypersonic facilities. *Shock Waves*, 12(6):443–455, May 2003. ISSN 0938-1287, 1432-2153. doi: 10.1007/s00193-003-0181-6. URL <http://link.springer.com/10.1007/s00193-003-0181-6>.
- [25] Matthew Robinson and Klaus Hannemann. Short Duration Force Measurements in Impulse Facilities. In *25th AIAA Aerodynamic Measurement Technology and Ground Testing Conference*, San Francisco, California, June 2006. American Institute of Aeronautics and Astronautics. ISBN 978-1-62410-029-1. doi: 10.2514/6.2006-3439. URL <http://arc.aiaa.org/doi/10.2514/6.2006-3439>.
- [26] Luke J. Doherty, Michael K. Smart, and David Mee. Measurement of Three-Components of Force on an Airframe Integrated Scramjet at Mach 10. American Institute of Aeronautics and Astronautics, July 2015. ISBN 978-1-62410-320-9. doi: 10.2514/6.2015-3523. URL <http://arc.aiaa.org/doi/10.2514/6.2015-3523>.
- [27] S. R. Sanderson and J. M. Simmons. Drag balance for hypervelocity impulse facilities. *AIAA Journal*, 29(12):2185–2191, December 1991. ISSN 0001-1452, 1533-385X. doi: 10.2514/3.10858. URL <http://arc.aiaa.org/doi/10.2514/3.10858>.
- [28] Christina Ngo, Jessica Powell, and James C. Ross. Inverse Force Determination on a Small Scale Launch Vehicle Model using a Dynamic Balance. In *55th AIAA Aerospace Sciences Meeting*, Grapevine, Texas, January 2017. American Institute of Aeronautics and Astronautics. ISBN 978-1-62410-447-3. doi: 10.2514/6.2017-1405. URL <http://arc.aiaa.org/doi/10.2514/6.2017-1405>.
- [29] Jared A. Grauer and Matthew J. Boucher. Frequency-Domain Deconvolution for Flight Dynamics Applications. In *2018 Atmospheric Flight Mechanics Conference*, Atlanta, Georgia, June 2018. American Institute of Aeronautics and Astronautics.

- ISBN 978-1-62410-557-9. doi: 10.2514/6.2018-3157. URL <https://arc.aiaa.org/doi/10.2514/6.2018-3157>.
- [30] Arianne Collopy, Sung Lee, and Eric C. Marineau. Development of Dynamic Force Measurement Capabilities at AEDC Tunnel 9. American Institute of Aeronautics and Astronautics, January 2014. ISBN 978-1-62410-256-1. doi: 10.2514/6.2014-0983. URL <http://arc.aiaa.org/doi/10.2514/6.2014-0983>.
- [31] PCB Model 356a32, . URL <https://www.pcb.com/Products.aspx?m=356A32>.
- [32] Static-Dynamic\_transducer.pdf, . URL [https://www.kulite.com/assets/media/2017/05/Static-Dynamic\\_Transducer.pdf](https://www.kulite.com/assets/media/2017/05/Static-Dynamic_Transducer.pdf).
- [33] A N Tikhonov. On the solution of ill-posed problems and the method of regularization. page 5.
- [34] C Groetsch, W. *The theory of Tikhonov regularization for Fredholm equations of the first kind*. Pitman Publishing Limited, 1984. ISBN 0-273-08642-1.
- [35] Thomas Schuster, Bernadette Hahn, and Martin Burger. Dynamic inverse problems: modelling regularization numerics. *Inverse Problems*, 34(4):040301, April 2018. ISSN 0266-5611, 1361-6420. doi: 10.1088/1361-6420/aab0f5. URL <http://stacks.iop.org/0266-5611/34/i=4/a=040301?key=crossref.13fc65da3c8fd4e4b71d41c45d1127f5>.
- [36] Per Christian Hansen. Analysis of Discrete Ill-Posed Problems by Means of the L-Curve. *SIAM Review*, 34(4):561–580, December 1992. ISSN 0036-1445, 1095-7200. doi: 10.1137/1034115. URL <http://epubs.siam.org/doi/10.1137/1034115>.
- [37] Per Christian Hansen and Dian Prost O’Leary. The Use of the L-Curve in the Regularization of Discrete Ill-Posed Problems. *SIAM Journal of Scientific Computation*, 14(6):1487–1503, November 1993.
- [38] J.W. Draper, S.W. Lee, and E.C. Marineau. Numerical construction of impulse response functions and input signal reconstruction. *Journal of Sound and Vibration*, 432:259–271, October 2018. ISSN 0022460X. doi: 10.1016/j.jsv.2018.06.041. URL <https://linkinghub.elsevier.com/retrieve/pii/S0022460X18304036>.
- [39] J.W. Draper III and S.W. Lee. Smooth construction of impulse response functions and applied loads using a time domain deconvolution method. *Journal of Sound and Vibration*, 443:430–443, March 2019. ISSN 0022460X. doi: 10.1016/j.jsv.2018.11.050. URL <https://linkinghub.elsevier.com/retrieve/pii/S0022460X18308149>.

- [40] E. Jacquelin, A. Bennani, and P. Hamelin. Force reconstruction: analysis and regularization of a deconvolution problem. *Journal of Sound and Vibration*, 265(1): 81–107, July 2003. ISSN 0022460X. doi: 10.1016/S0022-460X(02)01441-4. URL <http://linkinghub.elsevier.com/retrieve/pii/S0022460X02014414>.
- [41] John W. Draper and Sung Lee. Development of Hypersonic Wind Tunnel Force Measurement using Deconvolution of Acceleration Data. In *AIAA Scitech 2019 Forum*, San Diego, California, January 2019. American Institute of Aeronautics and Astronautics. ISBN 978-1-62410-578-4. doi: 10.2514/6.2019-0940. URL <https://arc.aiaa.org/doi/10.2514/6.2019-0940>.
- [42] Philippe Cardou and Jorge Angeles. Linear Estimation of the Rigid-Body Acceleration Field From Point-Acceleration Measurements. *Journal of Dynamic Systems, Measurement, and Control*, 131(4):041013, 2009. ISSN 00220434. doi: 10.1115/1.3117209. URL <http://DynamicSystems.asmedigitalcollection.asme.org/article.aspx?articleid=1476047>.
- [43] PCB Model 260a01, . URL <https://www.pcb.com/Products.aspx?m=260A01>.
- [44] Measurement Specialties Model 52 Accelerometer, . URL <https://www.mtasia.co.jp/product/acceleration/accelerometer/material/52.pdf>.
- [45] PCB Model 086c03, . URL <http://www.pcb.com/products.aspx?m=086C03>.
- [46] PCB Model 482c16, . URL <http://www.pcb.com/products.aspx?m=482C16>.
- [47] PCB Model 482c05, . URL <http://www.pcb.com/products.aspx?m=482C05>.
- [48] Measurement Specialties Model 101 DC Signal Conditioner Users Manual, . URL <https://www.manualslib.com/manual/730919/Measurement-Computing-101.html#manual>.
- [49] Model 6010u, Enclosure 4-Slot, USB Data & Control Interface On Pacific Instruments Inc., . URL <http://catalog.pacificinstruments.com/item/signal-conditioning-enclosures/6010u-4-slot-usb-data-control-interface-enclosures/1762>.
- [50] PI660usermanual.pdf, . URL <http://nees.buffalo.edu/training/Pacific/PI660UserManual.pdf>.
- [51] Kun Li, Jie Liu, Xu Han, Xingsheng Sun, and Chao Jiang. A novel approach for distributed dynamic load reconstruction by spacetime domain decoupling. *Journal of Sound and Vibration*, 348:137–148, July 2015. ISSN 0022460X. doi: 10.1016/j.jsv.2015.03.009. URL <https://linkinghub.elsevier.com/retrieve/pii/S0022460X15002278>.



- [52] Kun Li, Jie Liu, Xu Han, Chao Jiang, and Dequan Zhang. Distributed dynamic load identification based on shape function method and polynomial selection technique. *Inverse Problems in Science and Engineering*, 25(9):1323–1342, September 2017. ISSN 1741-5977, 1741-5985. doi: 10.1080/17415977.2016.1255740. URL <https://www.tandfonline.com/doi/full/10.1080/17415977.2016.1255740>.
- [53] Sung Lee and Norman Wereley. *Introduction to Vibration in Engineering*. Cognella Inc, first edition, 2017.
- [54] Dytran Model 1051 Specification Sheet, . URL [https://www.dytran.com/images/product\\_pdf/1051V1\\_ds.pdf](https://www.dytran.com/images/product_pdf/1051V1_ds.pdf).
- [55] Endevco Piezoresistive pressure transducer Model 8507c, . URL [https://buy.endevco.com/amfile/file/download/file\\_id/6641/product\\_id/2628/](https://buy.endevco.com/amfile/file/download/file_id/6641/product_id/2628/).
- [56] Karen T. Berger, Kevin E. Hollingsworth, Shelia A. Wright, and Shann J. Rufer. NASA Langley Aerothermodynamics Laboratory: Hypersonic Testing Capabilities. In *53rd AIAA Aerospace Sciences Meeting*, Kissimmee, Florida, January 2015. American Institute of Aeronautics and Astronautics. ISBN 978-1-62410-343-8. doi: 10.2514/6.2015-1337. URL <http://arc.aiaa.org/doi/10.2514/6.2015-1337>.
- [57] Nicholas Vlajic and Ako Chijioke. Traceable calibration and demonstration of a portable dynamic force transfer standard. *Metrologia*, 54(4): S83–S98, August 2017. ISSN 0026-1394, 1681-7575. doi: 10.1088/1681-7575/aa75da. URL <http://stacks.iop.org/0026-1394/54/i=4/a=S83?key=crossref.d9c8fac527e60d9d059aaf2f9ae18c28>.
- [58] Joseph Coblish, Stuart Coulter, and Joseph Norris. Aerothermal Measurement Improvements using Coaxial Thermocouples at AEDC Hypervelocity Wind Tunnel No. 9. American Institute of Aeronautics and Astronautics, January 2007. ISBN 978-1-62410-012-3. doi: 10.2514/6.2007-1467. URL <http://arc.aiaa.org/doi/10.2514/6.2007-1467>.
- [59] Tianshu Liu, Zemin Cai, Jianhuang Lai, Justin Rubal, and John Sullivan. Analytical Methods for Determination of Heat Transfer Fields from Temperature Sensitive Paint Measurements in Hypersonic Tunnels. American Institute of Aeronautics and Astronautics, January 2009. ISBN 978-1-60086-973-0. doi: 10.2514/6.2009-736. URL <http://arc.aiaa.org/doi/10.2514/6.2009-736>.
- [60] Brian Hollis. User’s Manual for the One-Dimensional Hypersonic Experimental Aero-Thermodynamic (1dheat) Data Reduction Code. NASA Contractor Report 4691, NASA Langley Research Center; Hampton, VA, United States, August 1995.
- [61] M. L. G. Oldfield. Impulse Response Processing of Transient Heat Transfer Gauge Signals. *Journal of Turbomachinery*, 130(2):021023, 2008. ISSN 0889504X. doi:

10.1115/1.2752188. URL <http://Turbomachinery.asmedigitalcollection.asme.org/article.aspx?articleid=1467707>.